Structural and Mutational Characterisation of Human Retinoschisin

A thesis submitted to the University of Manchester for the degree of Doctor of Philosophy (PhD) in the Faculty of Biology, Medicine and Health

2016

Ewan Phillip Ramsay

School of Biological Sciences
Division of Cell Matrix Biology and Regenerative Medicine

List of Contents

Word Count: 54,740

List of Figures

List of Tables

List of Abbreviations

Å	Angstrom
A_{280}	Absorbance at 280nm
AAV	Adeno-associated viral vector
AMOG	Adhesion molecule on glia
AOX1	Alcohol oxygenase 1
ART	Algebraic reconstruction
ATP	Adenosine triphosphate
AUC	Analytical ultracentrifugation
BCM	Barycentric mean fluorescence
BMGY	Buffered glycerol complex medium
BMMY	Buffered methanol complex medium
CAI	Carbonic anhydrase inhibitor
C_c	Chromatic aberration
CCD	Charge-coupled device
CCF	Cross correlation function
cGMP	Cyclic guanosine monophosphate
cm	Centimetre
CMV	Cytomeglavirus
CRX	Cone-rod homeobox
C_s	Spherical aberration
CTF	Contrast transfer function
CTP	Cytosine triphosphate
Da	Dalton
DAMMIF	Dummy atom model minimisation fast
DAMMIN	Dummy atom model minimisation
DDR	Discoidin domain receptor
DHA	Docosahexanoic acid
D_{max}	Maximum dimension
DMEM4	Dulbecco's modified eagles medium 4
DMSO	Dimethylsulfoxide
DQE	Detector quantum efficiency

DS	Discoidin
Dscam	Down syndrome cell adhesion molecule
DSF	Differential scanning fluorimetry
dSTORM	Direct stochastic optical reconstruction microscopy
DTT	Dithiothreitol
PVDF	Polyvinylidene fluoride
e^-	Electron
eBIC	Electron bio-imaging centre
EBNA	Epstein barr virus nuclear antigen
ECM	Extracellular matrix
EDTA	Ethylenediaminetetracetic acid
EM	Electron microscopy
EMAN	Electron micrograph analysis
EOM	Ensemble optimisation
ERG	Electroretinogram
ExPASY	Expert Protein Analysis System
f/f_0	Perrin factor
FBS	Feotal bovine serum
FDR	False discovery recovery
FEG	Field emission gun
FRC	Fourier ring comparator
FSC	Fourier shell correlation
GABA	Gamma-aminobutyric acid
GCL	Ganglion cell layer
GPCR	G-protein coupled receptor
GTP	Guanosine triphosphate
HEK-293	Human embryonic kidney 293 cells
HEPES	4-(2-hydroxyethyl)-1-piperazineethanesulfonic acid
HRP	Horseradish peroxidase
I(0)	Forward scattering intensity
I(q)	Scattering intensity
INL	Inner nuclear layer

IPL	Inner plexiform layer
kb	Kilobase
kDa	Kilodalton
LaB_6	Lanthanum hexaboride
LAT	Linker for activation of T-cells
LB	Luria-bertani
LDS	Lithium dodecylsulfate
LOVD	Leiden open variation database
L-VGCC	L-type voltage gated calcium ion channels
M	Molar
MALS	Multi-angle light scattering
MAGI	Membrane-associated guanylate kinase, WW and PDZ domain-containing proteins
MAPS	Monolithic activated pixels
MCS	Multiple-cloning site
Megf10	Multiple epidermal growth factor-like domains protein 10
Megf11	Multiple epidermal growth factor-like domains protein 11
mg/ml	Milligrams per millilitre
mGluR6	Metabotropic glutamate receptor 6
ML	Maximum likelihood
ml	Millilitre
mM	Millimolar
MOPS	3-(N-morpholino)propanesulfonic acid
MOR	Modifier of retinoschisin
MWCO	Molecular weight cut-off
NFL	Nerve fibre layer
ng	Nanogram
nm	Nanometre
NMR	Nuclear magnetic resonance
NSD	Normalised spatial discrepancy
^{o}C	Degrees centigrade
OD600	Optical density at 600nm
ONL	Outer nuclear layer

OPL	Outer plexiform layer
ORF	Open reading frame
P(r)	Pair distribution function
PALM	Photoactivatable localisation microscopy
PBS	Phosphate buffered saline
PCR	Polymerase chain reaction
pI	Isoelectric point
PMCA	Plasma membrane Ca2+ ATPase
pmol	Picomoles
PNGaseF	Peptide-N-Glycosidase F
PSD-95	Postsynaptic density of 95 kDa
PSF	Point spread function
q	Scattering vector
RELION	Regularized likliehood optimisation
R_{ex}	Conformational exchange term
R_g	Radius of gyration
R_h	Hydrodynamic radius
RPE	Retinal pigment epithelium
RS	Ray sum
S^2	Generalized order parameter
SARM1	Sterile
SART	Simultaneous iterable reconstruction technique
SASA	Solvent accessible surface area
SAXS	Small angle X-Ray scattering
SD-OCT	Spectral domain optical coherence tomography
SDS-PAGE	Sodium dodecyl sulfate polyacrylamide gel electrophoresis
SEC	Size exclusion chromatography
SIRT	Simultaneous reconstruction technique
SLN	Solid lipid nanoparticles
SNR	Signal to noise ratio
TAE	Tris-acetate EDTA buffer
TBST	Tris buffered saline tween-20

TEM	Transmission electron microscopy
Tm	Melting temperature
TMEM16B	Transmembrane protein 16B
TRPM1	Transient receptor potential cation channel subfamily M member 1
TSPO	Translocator protein
TTP	Thymidine triphosphate
U	Units of enzyme activity
UPR	Unfolded protein response
UV	Ultraviolet
XLRS	X-linked retinoschisis
YPD	Yeast peptone dextrose
ε	Molar extinction coefficient
λ	Wavelength
µg/ml	Micrograms per millilitre
µl	Microgram
µM	Micromolar
τe	Local correlational time
χ^2	Chi-squared

Abstract

University of Manchester

Ewan Ramsay

Doctor of Philosophy (PhD)

Structural and Mutational Characterisation of Human Retinoschisin

X-Linked Retinoschisis (XLRS) is a currently incurable, progressive retinal degeneration that affects approximately 1:20,000 males. Sufferers have a loss of retinal structure and visual acuity, leading to blindness. The condition is caused by mutation of the RS1 gene encoding the retinal-specific protein retinoschisin. Retinoschisin is critical in maintaining the normal, ordered retinal architecture, with deletion in mice models leading to loss of both structure and visual processing, analogous to XLRS sufferers. However, re-introduction of retinoschisin using adeno-associated viral vectors leads to complete rescue in these models.

Despite the importance of retinoschisin in maintaining retinal architecture, the mechanism by which it maintains this structure remains unknown. As a result, this study aimed to structurally characterise retinoschisin and XLRS-associated point mutants R141H and H207Q to gain insight into the mechanism of retinoschisin action. To this end, retinoschisin was expressed and purified from HEK 293-EBNA cells and the structure of both monomeric and octameric retinoschisin was investigated using Small-Angle X-Ray Scattering (SAXS) and Cryo-electron microscopy (Cryo-EM).

Monomeric retinoschisin was found to adopt an elongated structure that allowed for the tight association of the subunits into a planer propeller structure. However, in solution conditions the octamer also stably self-assembled into a dimer of octamers, for which the structure was solved using cryo-EM. This allowed for construction of a quasi-atomic model, enabling mapping of XLRS-associated point mutations on the complex. Two major classes of mutation were identified, in the intra-octamer and inter-octamer interfaces, suggesting a mechanism of pathology for these mutants. Observation of clustered conservative mutations at the inter-octamer interface suggested the dimer of octamers may be physiologically relevant. Furthermore, comparison of the R141H mutant to the wild-type revealed an additional mutated site in the propeller tips. Here, R141H was suggested to induce a small conformational change and alter an interaction site. Another mutant, H207Q, however, induced a destabilization of the assembled retinoschisin molecule.

In conclusion, we purified and structurally characterised human retinoschisin, identifying a new hexadecameric oligomer. The structure of this allowed for identification of distinct classes of mutations on the assembled molecule and a hypothesis of the mechanism of retinoschisin action in the retina.

Declaration

No portion of the work referred to in this thesis has been submitted in support of an application for another degree or qualification of this or any other university or other institute of learning.

Copyright Statement

The following four notes on copyright and the ownership of intellectual property rights must be included as written below:

I. The author of this thesis (including any appendices and/or schedules to this thesis) owns certain copyright or related rights in it (the "Copyright") and s/he has given The University of Manchester certain rights to use such Copyright, including for administrative purposes.

II. Copies of this thesis, either in full or in extracts and whether in hard or electronic copy, may be made only in accordance with the Copyright, Designs and Patents Act 1988 (as amended) and regulations issued under it or, where appropriate, in accordance with licensing agreements which the University has from time to time. This page must form part of any such copies made.

III. The ownership of certain Copyright, patents, designs, trade marks and other intellectual property (the "Intellectual Property") and any reproductions of Copyright works in the thesis, for example graphs and tables ("Reproductions"), which may be described in this thesis, may not be owned by the author and may be owned by third parties. Such Intellectual Property and Reproductions cannot and must not be made available for use without the prior written permission of the owner(s) of the relevant Intellectual Property and/or Reproductions.

IV. Further information on the conditions under which disclosure, publication and commercialisation of this thesis, the Copyright and any Intellectual Property University IP Policy (see http://documents.manchester.ac.uk/display.aspx?DocID=24420), in any relevant Thesis restriction declarations deposited in the University Library, The University Library's regulations (see http://www.library.manchester.ac.uk/about/regulations/) and in The University's policy on Presentation of Theses.

Acknowledgements

First of all, I would like to thank my supervisor Professor Clair Baldock for all the help and advice she gave me during this project.

I would like to thank all the members of the Baldock lab for their day-to-day help and support during my degree.

I also thank Professor Robert Ford for being my advisor during this project.

I would like to thank Dr. Alan Roseman, Dr. Richard Collins, Dr. Thomas Jowitt and Ms. Diana Ruiz for their help and advice throughout my degree.

Finally, I would like to thank my family and my girlfriend Mariavittoria for years of love and support during my project.

The work described here was funded by the Wellcome Trust as part of the Wellcome Trust Centre for Cell Matrix Research at the University of Manchester.

1 Introduction

1.1 The Structure and Function of the Retina

Sight is believed to account for around 80% of all sensory inputs in humans, therefore, a complex and efficient apparatus has evolved to capture and process this stimulus (Hildebrand and Fielder 2011). The retina, essential for the perception of light stimuli and the generation of sight relies on a highly regular, layered laminar sheet structure around 200µm thick (Masland 2012) with distinct cell populations in each 'band' (Figure 1.1) to detect and process the incoming stimuli.

At the base of this structure (in the back of the eye) are the rod and cone photoreceptor cells supported by the Retinal Pigment Epithelium (RPE) which forms a tight, regular structure to regulate the extracellular environment of the eye (Hildebrand and Fielder 2011). The RPE serves multiple functions including the phagocytosis of damaged photoreceptor discs and recycling of the photopigment 11-cis-retinaldehyde (Hildebrand and Fielder 2011). This is facilitated by a specialized extracellular matrix (ECM) termed the interphotoreceptor matrix which attaches the photoreceptors to the RPE (Al-Ubaidi, Naash et al. 2013, Ishikawa, Sawada et al. 2015). The photoreceptors, with a combined population of 110 million cells in the human retina, form a layer on top of this known as the Outer Nuclear Layer (ONL) (Hildebrand and Fielder 2011). The photoreceptors are classified into two distinct kinds in the human retina, with both rod (high-sensitivity, black-and-white vision) and cone (100 fold less sensitive than the rod cells, but allow for high acuity colour vision) cells. These cells are not distributed equally in the retina, with the cone cells concentrated in a central structure known as the fovea, and rod cells found throughout the periphery. Light detection is mediated by the integral membrane complex opsin in the outer segment, which has bound an 11-cis-retinaldehyde molecule. Absorption of a photon of light by this molecule induces a trans-isomerisation which leads to activation of the G-protein transducin, which in turn activates a cyclic guanosine monophosphate (cGMP) phosphodiesterase, reducing the intracellular cGMP levels. This, in turn, leads to closure of the open Na^+ cation channels, leading to hyperpolarization and activation of the photoreceptor (Hildebrand and Fielder 2011, Hoon, Okawa et al. 2014).

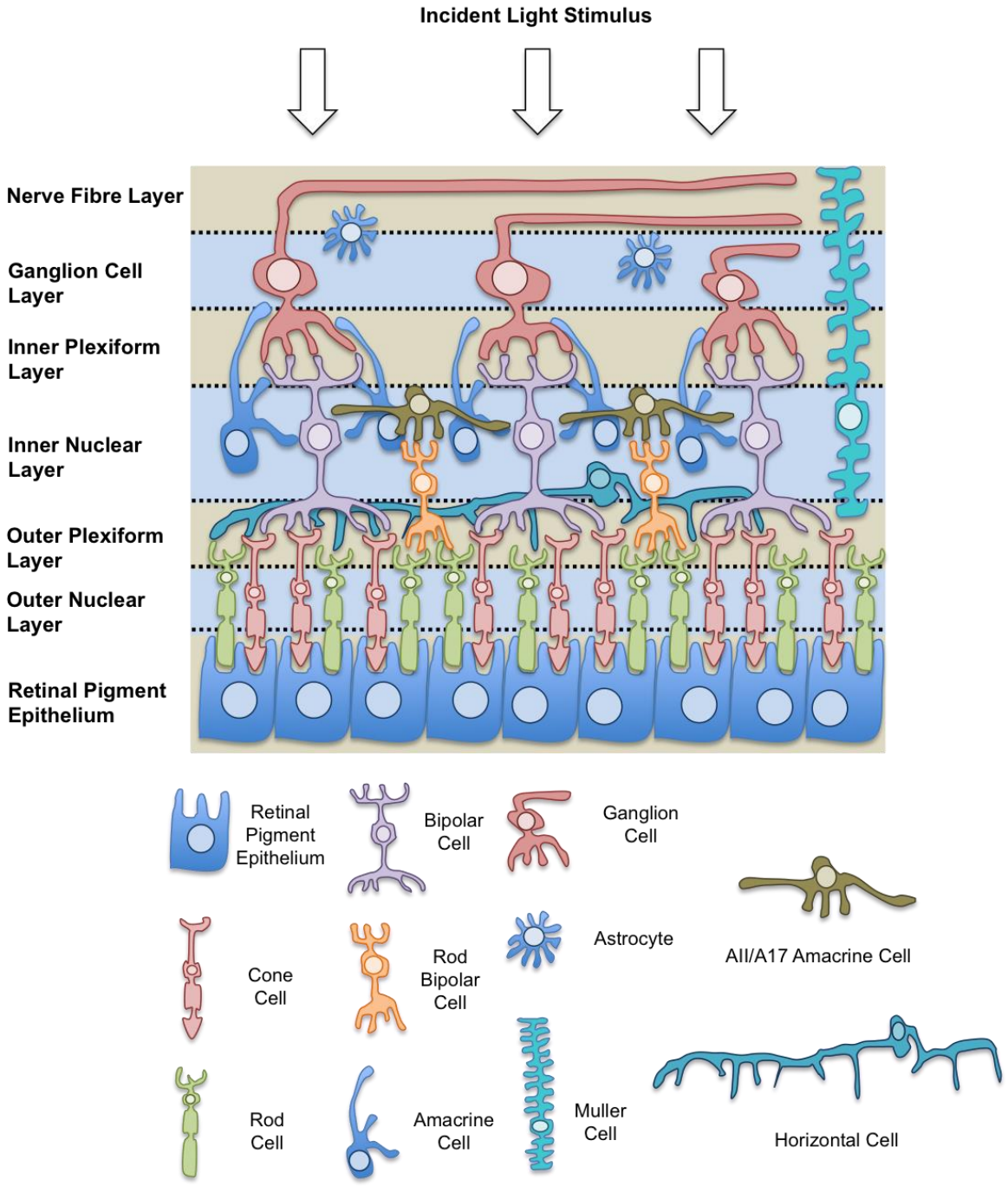

Figure 1.1 – The laminar structure of the human retina. Shown are the major cell types forming the highly compartmentalised, laminar structure of the retina. Incident light stimulus is detected at the base of the structure by the rod and cone photoreceptors with the visual processing carried out by the synaptic connections between the neurons depicted. The major cell types are shown, with multiple different types of each cell present in the retina.

Photoreceptors synapse with another secondary neuron in the outer plexiform layer (OPL) known as the bipolar cells (using glutamate as the neurotransmitter), with as many as 12 bipolar cell types identified extending into the inner nuclear layer (INL) (Masland 2012) (Figure 1.1). Some bipolar cells show specificity to either rods or cones, with some showing even higher specificity (such as the S-cone bipolar cells which contact solely S-cones for the detection of blue light) (Hildebrand and Fielder 2011).

Under dark conditions, the photoreceptors are continuously signalling to the bipolar cell using glutamate, with the activation of the photoreceptor reducing glutamate release. This then leads to different cellular responses from the bipolar cells. Indeed, the visual processing carried out by these cells can be split into two categories, ON (where photoreceptor activation induces bipolar cell depolarization and activation) and OFF (where photoreceptor activation leads to hyperpolarization and inactivation). This splits the output into two parallel processing streams for cone cells, with rod cells signalling only through the ON pathway (Hildebrand and Fielder 2011, Hoon, Okawa et al. 2014). However, synapsing with the photoreceptors in the OPL are additional cells such as the horizontal cells which receive inputs from multiple photoreceptors and feed these inputs into the bipolar cells or signal back to photoreceptors themselves. This generates complex networks which allow for processes such as normalization of the image to account for changes in brightness across the visual field (Masland 2012). The signal is then passed to the retinal ganglia on the surface of the retina (found in the ganglia cell layer (GCL)) through synapses in the inner plexiform layer (IPL) (Figure 1.1). Here the presence of a diverse class of amacrine cells (of which 30 types have been so far identified) allows for further signal processing (Hildebrand and Fielder 2011, Masland 2012). Indeed, amacrine cells have multiple excitatory and inhibitory interactions with ganglia, bipolar cells and even other amacrine cells. These interactions allow for complex processing, such as motion detection and integration of different signals and other specific functions. For example, the AII and A17 amacrine cells in the INL transmit signals from rod-bipolar cells through to the cone-bipolar cells, allowing for the rods to transmit visual information to the ganglia (Hoon, Okawa et al. 2014). This message is then transmitted from the ganglia to the optic nerve through the nerve fibre layer (NFL). These interactions are highly complex, involving an array of neurotransmitters such as Gamma-aminobutyric acid (GABA), glycine, acetylcholine, dopamine and other peptide neurotransmitters, in contrast to the glutaminergic signalling at the OPL (Hildebrand and Fielder 2011).

Aside from these visual components, the retina also houses a host of supportive cells such as the muller cells (which work to maintain the internal conditions of the retina to allow for visual processing), astrocytes (glial cells which support the ganglia) and microglia (which can infiltrate the retinal structure and are phagocytic). Overall, it is estimated that there are over 60 distinct cell types in the human retina (Hildebrand and Fielder 2011, Masland 2012) (Figure 1.1).

This functionality of the retina is dependent upon the maintenance of a highly ordered structure. Indeed, many pathologies show a degradation of this structure, such as the ‘rosette’ structural abnormalities observed in the ONL during retinoblastoma, diabetic retinopathy or retinitis pigmentosa (Hoon, Okawa et al. 2014).

1.2 X-Linked Retinoschisis – A Loss of Retinal Order

1.2.1 X-Linked Retinoschisis Presentation

One of the most common conditions which leads to loss of retinal structure is X-Linked Retinoschisis (XLRS). First described in two brothers by Haas in 1898, XLRS was later shown to show sex-linked inheritance. Currently, XLRS is one of the most prevalent macular degenerations in males (George, Yates et al. 1995, Tantri, Vrabec et al. 2004, Sikkink, Biswas et al. 2007), with an estimated worldwide frequency of 1:5000 to 1:20,000 and 'hotspots' of increased prevalence such as Finland where XLRS is the most common X-Linked condition (Tantri, Vrabec et al. 2004). The vast majority of all sufferers are males, however, recently a few cases of females with XLRS have been reported, with the lowered incidence in females due to the X-linked recessive inheritance of this disorder (Mendoza-Londono, Hiriyanna et al. 1999, Rodriguez, Rodriguez et al. 2005, Saldana, Thompson et al. 2007, Saleheen, Ali et al. 2008, Ali and Seth 2013, Staffieri, Rose et al. 2015).

The most prominent phenotype is a progressive loss of visual acuity throughout life, with the rate of vision deterioration accelerating in the fourth decade (Sikkink, Biswas et al. 2007, Molday, Kellner et al. 2012). XLRS has a very high (approximately 98%) penetrance however presents as a highly variable condition, even amongst siblings in affected families (Molday, Kellner et al. 2012). In the worst cases, XLRS leads to severe visual impairment and even blindness with juvenile onset (George, Yates et al. 1995, Prasad, Wagner et al. 2006). However, conversely, other XLRS sufferers have only minor symptoms, with others still only having pigment abnormalities without any affect on vision (Kellner, Brummer et al. 1990, Renner, Kellner et al. 2008). Also, significant variability is observed in the progression of the disease. Whilst progressive loss of sight is reported for sufferers, conversely, there have been many reports of patients for whom the disease does not show significant deterioration over time (Kellner, Brummer et al. 1990, Roesch, Ewing et al. 1998, Apushkin, Fishman et al. 2005).

Alongside these clinical presentations, XLRS sufferers are also at elevated risk of complications which can lead to complete loss of sight. Between 5-22% of patients suffer retinal detachment with an additional 4-40% of sufferers experiencing vitreous haemorrhage in the retina (Tantri, Vrabec et al. 2004). Despite the affect that this disorder has on public health and the progressive nature of the disease, currently there is no cure or effective treatment for the condition.

1.2.2 XLRS Pathophysiology

The progressive sight loss is associated with a series of both structural and functional alterations in the retina. The most prominent of these is splitting of the outer retinal layers from the inner retina in a process known as 'schisis' (George, Yates et al. 1995, Tantri, Vrabec et al. 2004, Sikkink, Biswas et al. 2007). This then generates large, fluid-filled cavities known as 'schisis cavities' which can be imaged in two dimensions using spectral domain optical coherence tomography (SD-OCT) (Xu, Molday et al. 2009, Yu, Ni et al. 2010) (Figures 1.2A and B). Such SD-OCT studies have also observed capillaries crossing unsupported through these cavities, explaining the increased incidence of retinal haemorrhage in sufferers (Tantri, Vrabec et al. 2004). However, different classes of schisis events are observed in the XLRS retina. The most striking and common schisis observed is the foveal schisis, present in the majority of cases and so is used as a major diagnostic indicator (George, Yates et al. 1995). The formation of the foveal cysts causes a distinctive 'spoke-wheel' or star-shaped schisis with several schisis striae radiating from the central schisis. This schisis, however is most pronounced in young patients with collapse of the schisis into older age (George, Yates et al. 1995, Menke, Feke et al. 2011, Molday, Kellner et al. 2012).

The impact on the retinal structure also appears to affect the vectorial nerve transmission required for sight. The electrical response of the retina after a light stimulus is measured using the Electroretinogram (ERG), which is used for diagnosis. With respect to XLRS, two main regions of the ERG are considered, the a-wave (this is the initial, negative potential caused by activation of photoreceptor cells) and the b-wave (which monitors the function of the ON-bipolar cells following activation by photoreceptors) (Sikkink, Biswas et al. 2007). Characteristically, XLRS-sufferers show a reduced bipolar cell activity with a lower b-wave response compared to an unaffected retina, suggesting impaired ON-bipolar cell stimulation (Alexander, Barnes et al. 2001, Khan, Jamison et al. 2001, Shinoda, Ohde et al. 2001) (Figure 1.2C). This suggests that communication between photoreceptors and bipolar cells may be compromised. However, consistent with the observations of variability in the age of onset, severity and disease progression, significant variability is observed in ERG responses. For example, whilst many sufferers show a negative response, this varies significantly in severity, with some patients showing completely preserved b-waves (Eksandh, Andreasson et al. 2005, Renner, Kellner et al. 2008, Vincent, Robson et al. 2013). As a result, for diagnosis, ERG measurements are combined with structural observations using SD-OCT (Renner, Kellner et al. 2008).

Although the a-wave appears to be preserved in the XLRS retina (Khan, Jamison et al. 2001), recent studies have highlighted an impact upon the photoreceptors during the course of the disease. XLRS appears to be associated with progressive photoreceptor

death. Indeed, mice models of XLRS (see section 1.2.4) show reduced photoreceptor light sensitivity and retarded development followed by thinning of this cell layer (Weber, Schrewe et al. 2002, Janssen, Min et al. 2008, Genead, Pasadhika et al. 2009, Ziccardi, Vijayasarathy et al. 2012).

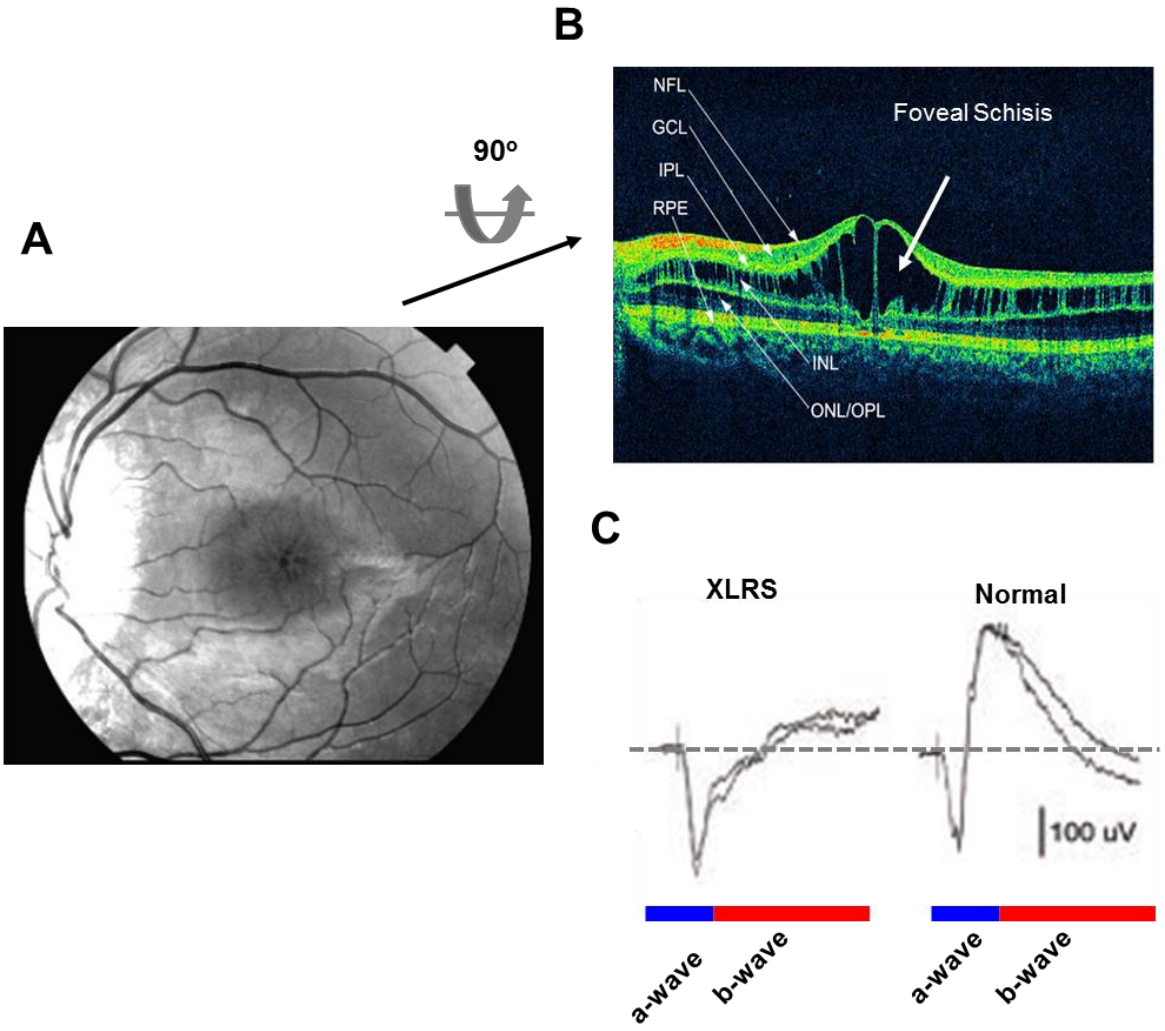

Figure 1.2 – The XLRS retina. Shown are the major symptoms of the XLRS disease state. (**A**) The central, stellate foveal schisis, and (**B**) the formation of the schisis cavity and splitting of retinal cell layers observed by SD-OCT. (**C**) 'Negative' ERG profile showing a lack of b-wave formation in the XLRS patient. Adapted from: Sikkink (2007), and Yu (2010).

Consistent with the thinning of the cell layer, an increase in photoreceptor apoptosis was observed in XLRS mice models, with apoptosis peaking at P18 (Gehrig, Janssen et al. 2006). Apoptosis correlated with an upregulation of pro-inflammatory cytokines (such as interleukin-1) and pro-inflammatory caspases (Gehrig, Janssen et al. 2006, Gehrig, Langmann et al. 2007). Furthermore, there was an increase in the number of activated microglia infiltrating the photoreceptor layer, suggesting that both the induction inflammatory responses and the invasion of activated microglia may be responsible for the large-scale cell death (Gehrig, Janssen et al. 2006). Indeed, activated microglia were

observed in the retina before the onset of cell death. Also, when these microglia were characterised in XLRS mice models they were shown to have increased expression of Egr1 (which induces pro-inflammatory mediator expression) (Langmann, Ebert et al. 2009), Dap12 (involved in neuronal phagocytosis) (Weigelt, Ernst et al. 2007), STAP-1 (which increases the activation of microglia) (Stoecker, Weigelt et al. 2009) and AMWAP (involved in alternative macrophage activation pathways) (Karlstetter, Walczak et al. 2010). Furthermore, these microglia were found to upregulate the mitochondrial Translocator protein (TSPO) which increased production of interleukin-6, the chemoattractant CCL2 and nitric oxide synthase, contributing to a pro-inflammatory microglial phenotype (Karlstetter, Nothdurfter et al. 2014). Indeed, treatment of XLRS mice models with docosahexanoic acid (DHA), which attenuated the activated phenotype of isolated microglia *in vitro,* significantly reduced photoreceptor apoptosis in XLRS mice models (Ebert, Weigelt et al. 2009). Therefore this suggests that during the course of the disease there is an induction of a chronic inflammatory response in the photoreceptor cell layer, which may in turn contribute to the progressive sight loss reported in patients.

1.2.3 XLRS Genetics – Uncovering Retinoschisin

Early studies into the cause of XLRS had suggested that the disease state was caused by loss of Muller cell function (George, Yates et al. 1995). These cells, a major supportive glial cell type, straddle the entire length of the retina and regulate the function of many cells both during development and in adulthood (George, Yates et al. 1995, Hildebrand and Fielder 2011). Early observations of the mizou phenomenon in XLRS retinae (a change in colour of the retina due to defective removal of potassium released from activated photoreceptor cells) suggested a failure of Muller cell function in these retinae (Dejong, Zrenner et al. 1991). To identify the genetic lesion which leads to the hereditary disease, a number of studies sought to identify the affected gene on the X-chromosome. In the first of these studies, Wieacker et al. localized the 'XLRS-locus' to within 25 centimorgans (cM) of the Xg blood group markers (Wieacker, Wienker et al. 1984). Further efforts refined this position to a 1000kb stretch between the markers DXS418 and DXS999 (Alitalo, Karna et al. 1987, Huopaniemi, Rantala et al. 1997). Using this, Sauer et al. employed a positional cloning strategy to finally identify the causative gene, the RS1 gene, found at Xp22.2 which contained a single open reading frame (ORF) for the protein retinoschisin (Sauer, Gehrig et al. 1997). This protein was small, 224 amino acids in length and 24kDa in molecular weight with sequence analysis suggesting a lack of any glycosylation (Sauer, Gehrig et al. 1997).

The identification of retinoschisin suggested that XLRS was a monogenic disorder, with mutation of a single factor responsible for the disease state. Indeed, currently 198 mutations associated with the development of XLRS have been identified in this gene,

encompassing missense mutations, splice-site mutations, insertions and deletions (den Dunnen, Kraayenbrink et al. 1998, Pimenides, George et al. 2005, Molday, Kellner et al. 2012)

1.2.4 The Importance of Retinal Architecture – Insights from the Rs1h Mouse Knockout

Indeed, the importance of retinoschisin in the maintenance of normal retinal architecture was highlighted through retinoschisin knock out mice models. Knockout of the highly homologous murine retinoschisin (Rs1h, which shares 96% sequence identity with the human protein) led to the generation of an XLRS phenotype (Weber, Schrewe et al. 2002). The mice have schisis cavities, thinning of the photoreceptor cell layer with a loss of photoreceptor cell number and a characteristic negative ERG profile, suggestive of a loss of visual processing capacity in these mice (Weber, Schrewe et al. 2002). Furthermore, a two-stage disease was observed in the ERG profiles, with bipolar cell activity first affected (observed by the reduced b-wave) followed by a decline in the a-wave, which correlated with the loss of photoreceptor cells (Weber, Schrewe et al. 2002). Additionally, such studies allowed for a more comprehensive analysis of the effect of loss of retinoschisin in the retina. Deletion of retinoschisin was found to disrupt the normal, laminar compartmentalisation of cells, with loss of alignment between the columnar photoreceptor cells and mislocalisation of both bipolar cells and photoreceptors (Zeng, Takada et al. 2004, Min, Molday et al. 2005, Kjellstrom, Bush et al. 2007, Janssen, Min et al. 2008, Park, Wu et al. 2009).

In addition, re-introduction of wild-type retinoschisin into $Rs1h^{-/y}$ mice using modified Adeno-Associated Viral (AAV) vectors led to complete structural and functional rescue. For instance, reintroduction of retinoschisin under control of the photoreceptor-specific opsin promoter caused a reversal of retinal degeneration in these mice. Strong photoreceptor expression was observed following treatment, correlating with a two-fold increase in cell numbers and recovery of the ERG profile, suggesting a rescue of the neurotransmission in these retinas (Min, Molday et al. 2005, Janssen, Min et al. 2008). Furthermore, other mice models showed a re-ordering of the retinal cell layers and resolution of schisis cavities, with the improvements persisting for the lifetime of the mice (up to 16 months) (Kjellstrom, Bush et al. 2007). Furthermore, greatest rescue was observed when retinoschisin expression was specifically re-introduced to photoreceptors (Byrne, Ozturk et al. 2014). Together, these observations strongly suggested that retinoschisin was both essential and sufficient to maintain normal retinal architecture and photoreceptor-bipolar cell neurotransmission.

Despite this strong correlation between retinoschisin and XLRS, the high variability observed in symptoms had led to the suggestion that additional genetic modifiers may alter the outcome and severity of the disease and as a result the genetic background must be considered in these mice studies. Using an $Rs1h^{-/y}$ mouse model, Johnson et al. identified an allele in a single site on chromosome 7, known as the 'Modifier of Retinoschisis (MOR)' locus, which was able to rescue the retinoschisis phenotype in a recessive manner (Johnson, Aoyama et al. 2008). This locus was later identified as the tyrosinase locus, with inactivation of this gene allowing for retinoschisis rescue. The authors attributed this effect to a possible alteration of dopamine metabolism which may indirectly affect retinal structure (Johnson, Cole et al. 2010). However, these findings suggest complexities in the XLRS condition that offer further opportunities to explore the variability observed in this disease.

1.3 Retinoschisin – An Essential Structural Component of the Retina

1.3.1 The Expression of Retinoschisin

Consistent with the importance of retinoschisin in maintaining retinal architecture, retinoschisin has a retinal-specific expression profile. The lack of expression of retinoschisin from Muller cells dramatically shifted the focus of the disease, from the Muller cells to the photoreceptors in the outer retina (Molday, Kellner et al. 2012). Analysis of the RS1 gene sequence showed two highly conserved binding sites in the RS1 promoter and an additional site in the first intron for the Cone-Rod Homeobox (CRX) transcription factor, a transcription factor found solely in photoreceptor cells (Gehrig, Warneke-Wittstock et al. 1999, Langmann, Lai et al. 2008, Kraus, Karlstetter et al. 2011). Indeed, CRX does appear to drive expression from this promoter, with overexpression of CRX driving expression of RS1 promoter-luciferase reporter constructs in both HEK293 and *Xenopus laveis* cells *in vitro.* Mutation of the CRX sites in these systems led to a 70% loss of retinoschisin expression (Langmann, Lai et al. 2008). Moreover, this *in vitro* approach identified an additonal CpG island sequence approximately 3kb upstream of the RS1 locus which enhanced retinoschisin expression in this system (Kraus, Karlstetter et al. 2011).

The observation that retinoschisin expression is driven by photoreceptor-specific factors was consistent with the observed expression of retinoschisin in mice. *In situ* hybridization of RS1 antisense riboprobes in mice retinal sections revealed strong signals from the photoreceptor cell layer with deletion of these photoreceptor cells in the *rd/rd* mouse model leading to loss of RS1 mRNA signal (Grayson, Reid et al. 2000, Molday, Hicks et al. 2001). This observation was supported by the expression of retinoschisin in WERI-Rb1 cells *in vitro*, which represent an immortalized precursor to the photoreceptor cell

(Grayson, Reid et al. 2000, Kitamura, Gribanova et al. 2011). However, closer analysis of the *rd/rd* mice using RT-PCR against the RS1 locus was able to detect weak expression, suggesting another minor expressing cell type (Molday, Hicks et al. 2001). This signal was found to be due to the bipolar cells still present, with immunofluorescence microscopy showing bipolar cell staining after 4 weeks of culture (Molday, Hicks et al. 2001). Such retinoschisin expression was not observed for Muller cells (Reid, Yamashita et al. 2003).

However, whilst this expression pattern is well established in the adult retina, retinoschisin expression is different during retinal development. Immunolabelling of mice retinae at different stages of development showed retinoschisin expression was seen in each layer as waves of developmental expression (Takada, Fariss et al. 2004). Expression is first detected in the retinal ganglion cell layer at postnatal day 1 (P1) with expression then detected in the mid retina at P3, and photoreceptor based expression established in the outer retina at between P12 and 14. This expression tracks the sequential maturation of each cell layer during development, with expression in the retinal ganglion cell and inner retinal layers diminishing following expression in photoreceptor cells (Takada, Fariss et al. 2004). Together, these data suggest that retinoschisin expression is under complex regulation and may be important for the development as well as the maintenance of the retina.

Despite the characterisation of retinoschisin being largely focused on the retina, retinoschisin expression has also been observed in other cell types. Expression was observed in the pineal gland; however, deletion of retinoschisin gave no phenotype in this tissue (Takada, Fariss et al. 2006). Furthermore, Huopaniemi et al. detected retinoschisin expression in the uterus, where it was proposed that retinoschisin may mediate implantation of the blastocyst into the uterine wall (Huopaniemi, Fellman et al. 1999).

1.3.2 Localisation of Retinoschisin in the Retina

In contrast to the apparent strict regulation of retinoschisin expression, the localisation of the protein is ubiquitous in the retina, being found in all cell layers (Molday, Hicks et al. 2001, Takada, Fariss et al. 2004). Following expression in the photoreceptor and bipolar cells, retinoschisin is secreted and is then thought to diffuse throughout the retina. Reid et al. have suggested that Muller glial cells (which span the length of the retina) are able to actively transport retinoschisin across the retinal cell layers (Reid and Farber 2005). However, this has been disputed. Following observation of retinoschisin expression during development in inner cell layers, Takada et al. argue that the retinoschisin observed here is due to local production and not long-range transport (Takada, Fariss et al. 2004). However, despite the wide distribution of retinoschisin, it appears enriched in the outer

retina with high levels of retinoschisin immunostaining observed on photoreceptors and at the synapse between the photoreceptors and bipolar cells, where expression appears concentrated (Grayson, Reid et al. 2000, Molday, Hicks et al. 2001, Reid, Yamashita et al. 2003, Ou, Vijayasarathy et al. 2015).

Retinoschisin was found to label the membranes of photoreceptors and bipolar cells cultured *in vitro* with permeablization of the cells (which non-specifically removed peripherally attached plasma membrane proteins) leading to loss of retinoschisin staining (Reid, Yamashita et al. 2003). Indeed, retinoschisin was found in purified photoreceptor membrane fractions and was found to associate with the membranes of WERI-Rb1 cells (Wang, Zhou et al. 2006). This was further supported by immunogold labeling of retinoschisin in mice retinal sections which showed a distinct membrane localisation on the inner segment of photoreceptor cells, with clustering on adjacent basolateral membranes of adjacent photoreceptors (Vijayasarathy, Takada et al. 2007). Taken together, these data suggest that retinoschisin exists as a peripheral membrane protein distributed throughout the retina.

1.3.3 The Retinoschisin Protein

The retinoschisin sequence, consists of four distinct regions (Sauer, Gehrig et al. 1997). The first is a signal sequence allowing for secretion. During secretion, this sequence was found to be cleaved in two positions, producing two distinct isoforms which differ in length by two residues (Vijayasarathy, Gawinowicz et al. 2006). This region is followed by the Rs1 domain, a 39 residue, cysteine-rich sequence with little sequence homology to any known protein (Molday, Kellner et al. 2012) (Figure 1.3A). The Rs1 domain is immediately followed by the discoidin domain (DS), which represents the major functional region of the retinoschisin sequence. This region makes up approximately 75% of the retinoschisin sequence (Wu and Molday 2003, Molday 2007). The final section is a small 5 residue extension protruding from the DS domain (Sauer, Gehrig et al. 1997) (Figure 1.3A).

The DS domain (also known as the F5/8 type C domain) was first characterised in the amoeba *Dictyostelium discoidin* as a lectin domain with strong affinity for galactose which allowed for cell migration and aggregation (Poole, Firtel et al. 1981), with lectin binding also observed for the retinoschisin DS domain (Dyka, Wu et al. 2008). The domain is widespread, found in over 100 eukaryotic and 300 prokaryotic proteins complexing with a wide range of ligands from small molecules such as saccharides and phospholipids to large protein assemblies such as collagen I (Baumgartner, Hofmann et al. 1998, Kiedzierska, Smietana et al. 2007, Lin, Huai et al. 2007, Vander Kooi, Jusino et al. 2007, Carafoli, Bihan et al. 2009). In each case, these interactions are important for many

biological processes including blood coagulation (Macedo-Ribeiro, Bode et al. 1999, Pratt, Shen et al. 1999), heart development and fertilization (Kiedzierska, Smietana et al. 2007).

Such is the importance of these domains, they have been intensively investigated, with many structures for related domains solved using X-ray crystallography and NMR spectroscopy (Macedo-Ribeiro, Bode et al. 1999, Pratt, Shen et al. 1999, Lee, Kreusch et al. 2003, Lin, Huai et al. 2007, Vander Kooi, Jusino et al. 2007, Carafoli, Bihan et al. 2009). The wealth of structural information available has allowed for homology modelling of the retinoschisin DS domain, with many models constructed (Fraternali, Cavallo et al. 2003, Wu and Molday 2003, Wang, Zhou et al. 2006, Sergeev, Caruso et al. 2010, Wu and Liu 2012). Analysis of these structures and sequences has revealed a highly conserved common structure for these domains, with the core of the domain consisting of an eight-stranded antiparallel β-sandwich, which forms multiple hydrophobic contacts required to stabilize the domain. However, the major stabilizing interaction in the discoidin domain is a disulphide bond formed between the N and C-termini of the domain between two highly conserved cysteine residues (in the retinoschisin DS domain this is between C63 and C219) (Figure 1.3B). Indeed, this is critical to discoidin domain folding, allowing for the formation of a highly globular shape (Sergeev, Caruso et al. 2010).

Alongside this highly conserved core structure, the discoidin domain also has three projecting loops or 'spike' regions (termed spikes 1, 2 and 3), which are found at one end of the molecule (Kiedzierska, Smietana et al. 2007) (Figure 1.3B). These structures form the major interaction interface of the domain for its known ligands, and in contrast to the β-sandwich core, the sequence of the loops are highly variable (Kiedzierska, Smietana et al. 2007). This variability allows for each discoidin domain to complex with a different ligand whilst having a highly similar core structure. For instance, the loops of the discoidin domains in the coagulation factors V and VIII contain a hydrophobic motif which interacts with phosphatidylserine and inserts into the plasma membrane of platelets during blood coagulation (Macedo-Ribeiro, Bode et al. 1999, Pratt, Shen et al. 1999). However, through alteration of the spike sequence, the discoidin domains found in the discoidin domain receptors (DDRs) instead bind collagen I (Carafoli, Bihan et al. 2009). Indeed, the spikes found in retinoschisin are important for ligand binding. Introduction of an R141S mutation into spike 3 of the retinoschisin DS domain led to a loss of galactose binding (Dyka, Wu et al. 2008). However, unique to retinoschisin is an additional disulphide bond formed between C110 in spike 2 and C142 in spike 3. *In silico* modelling of a homology model of the DS domain suggested that the presence of this bond masks a hydrophobic aggregation motif (Wu and Liu 2012). Indeed, expression of the C110Y mutant in HEK-293 cells lead to the formation of high molecular weight aggregates which were retained in the endoplasmic reticulum (ER) (Gleghorn, Trump et al. 2010).

1.3.4 Oligomerisation of Retinoschisin

Retinoschisin, however is not secreted as a monomer but instead assembles into a disulphide-stabilised homo-octameric complex in the ER which is then secreted (Molday, Hicks et al. 2001, Wu and Molday 2003, Wu, Wong et al. 2005, Kitamura, Gribanova et al. 2011). This octamerisation is dependent on the regions flanking the DS domain, with disulphide linkages formed between C59 in the Rs1 domain and C223 in the C-terminal extension, which appear to form a 'ring' of stabilizing disulphide bonds. Mutation of these residues led to secretion of retinoschisin dimers and monomers (Wu and Molday 2003, Wu, Wong et al. 2005) which implicated an additional disulphide in dimerization. A further mutation of C40 to generate the C40S/C59S/C223S triple mutant prevented all oligomerisation, resulting in retinoschisin secreted as a monomer. However, a single mutation of C40 did not prevent octamer formation (Wu and Molday 2003, Wu, Wong et al. 2005). Therefore a model for retinoschisin assembly was proposed with homotypic C40-C40 bonds in adjacent Rs1 domains linked together to allow for dimerization alongside C59-C223 bonds for full assembly of the octamer (Wu, Wong et al. 2005) (Figure 1.3C). The octamer appeared to be the functional oligomer, with mutation of the residues required for octamerisation associated with the development of XLRS (den Dunnen, Kraayenbrink et al. 1998, Gehrig, White et al. 1999, Hiriyanna, Bingham et al. 1999).

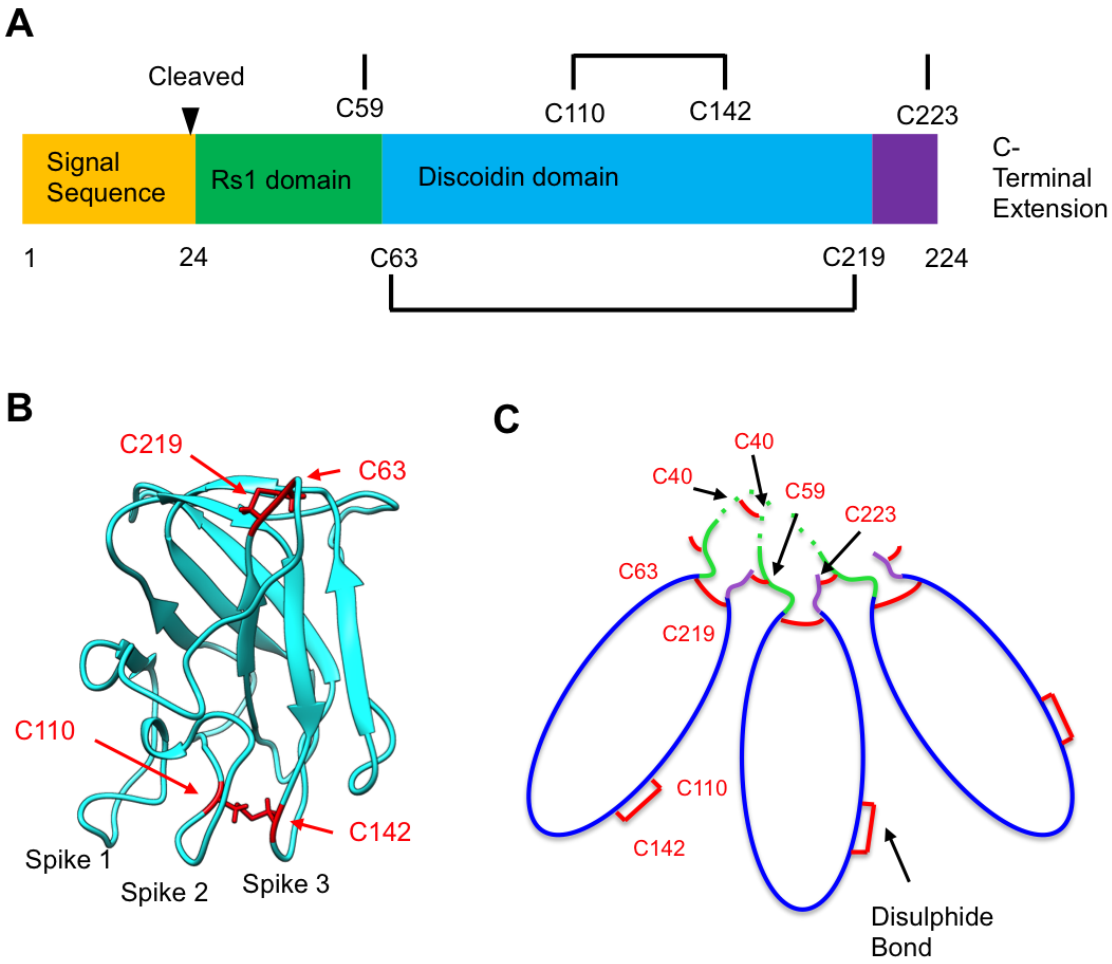

Figure 1.3 – Retinoschisin domain structure and model of oligomerisation. (**A**) Schematic showing the domain organisation of retinoschisin. Disulphide bonds are indicated. (**B**) Constructed homology model of the retinoschisin discoidin domain. Shown are the identified disulphide bonds required for folding. (**C**) Current model for the octamerisation of the retinoschisin protein. Shown are the residues and disulphide bonds important in both domain folding and oligomerisation (red). Sequence colouring corresponds to (**A**), showing the positions of the Rs1 domain, discoidin domain and C-terminal extension.

1.3.5 Distinct Types of Mutation Lead to XLRS

Mutation of this assembled complex leads to the development of XLRS with the disease-associated missense mutations able to be classified into distinct groups. The largest of these groups are the mutations that lead to incorrect folding and intracellular retention of the retinoschisin molecule. These are found throughout the sequence, however, appear to be concentrated in the discoidin domain and represents the most common mechanism of pathology, with most point mutations analysed to date leading to intracellular retention (Wang, Waters et al. 2002, Wu and Molday 2003, Iannaccone, Mura et al. 2006, Wang, Zhou et al. 2006, Dyka and Molday 2007, Walia, Fishman et al. 2009, Gleghorn, Trump et al. 2010, Vijayasarathy, Sui et al. 2010). Indeed, such mutations have been observed to form large aggregates which accumulate in the ER, however do not induce the unfolded protein response (UPR), suggesting that the main pathology is due to the null phenotype with respect to retinoschisin production (Gleghorn, Trump et al. 2010). The high number and even cover of point mutations across the sequence which cause misfolding of the

discoidin domain suggests that the domain is very sensitive to any changes in amino acid identity at a number of positions. Another, distinctly smaller class first identified by Wang et al. are those found in the signal sequence. Both L12H and L13P prevent entry into the ER, generating a null phenotype by preventing entry of retinoschisin into the secretory system (Wang, Waters et al. 2002).

However, whilst intracellular retention represents a major pathological mechanism, other XLRS-associated mutants have been identified which retain secretion. One class of these mutants affects the residues required for higher order assembly. Both C59 and C223 mutations have been associated with the development of XLRS and whilst these mutants are still secreted, they no longer form octamers (Wu, Wong et al. 2005). As a result, this suggests that octamerisation is important for retinoschisin function. However, another class of mutants is still secreted as octamers. This class contains only a handful of currently characterised mutations (for example R141H, R141G, H207Q and R209H) and may represent alterations of functional sites within the retinoschisin molecule, forming non-functional octameric complexes (Wang, Zhou et al. 2006).

1.4 Towards the Mechanism of Retinoschisin Function

Whilst the importance of retinoschisin in the maintenance of retinal architecture has been well established, the mechanism it uses to maintain the cellular structure remains elusive. As a result, numerous studies have concentrated on the identification of binding partners to gain functional insight into the retinoschisin complex. To date numerous binding partners to retinoschisin have been identified.

1.4.1 Phosphatidylserine

The first proposed interaction for retinoschisin was with the membrane phospholipid phosphatidylserine to explain the peripheral membrane localisation of retinoschisin. Initially, retinoschisin was found to co-purify with phosphatidylserine phospholids through electrostatic interactions (Vijayasarathy, Takada et al. 2007). Further atomic force microscopy analysis suggested that retinoschisin was found in ordered membrane phases, requiring phosphatidylserine and calcium for the interaction (Kotova, Vijayasarathy et al. 2010). Molecular dynamics simulations suggested this membrane interaction was mediated via residues Y89, W92 and I144 in the spike regions of the discoidin domain (Fraternali, Cavallo et al. 2003). However, later experiments were unable to reproduce the observed lipid binding using both immobilized phospholipids and purified membrane vesicles *in vitro* (Molday, Wu et al. 2007, Friedrich, Stohr et al. 2011). Furthermore, it was suggested that the interaction with phosphatidylserine may not be physiologically relevant as this lipid is mostly found on the inner leaflet of the plasma

membrane (Molday, Kellner et al. 2012). Therefore, this proposed interaction remains tenuous and further validation is required.

1.4.2 Na/K-ATPase-SARM1 Complex

The first protein binding partner to be identified for retinoschisin was a retinal-specific Na/K-ATPase found in the photoreceptor membrane (Molday, Wu et al. 2007). This channel actively maintains the membrane potential though export of Na^+ and import of K^+ ions. The channels are found in many tissues and have a common structure, formed from a heterodimeric complex consisting of an α and β-chain (Kaplan 2002). The α-chain is a 10 transmembrane helix integral membrane protein which forms the pump and has ATPase activity. However, the α-chain is strongly associated with the β-chain, which is a chaperone that trafficks the α-chain to the plasma membrane (Kaplan 2002). The β-chain is considerably smaller, containing a single pass transmembrane helix with a large, disulphide-stabilised and glycosylated ectodomain (Kaplan 2002, Morth, Pedersen et al. 2007).

Multiple isoforms of each chain exist for the Na/K-ATPase, however, of interest is the β2 isoform which is highly expressed in retinal tissues and present on photoreceptor membranes together with the α3 subunit (Blanco and Mercer 1998). This isoform was initially characterised as the Adhesion Molecule on Glia (AMOG) which was required for interactions between neurons and glia (Antonicek, Persohn et al. 1987). Further characterisation identified AMOG as a novel β2 isoform of the Na/K-ATPase channel subunit, sharing 56% sequence homology with the 'housekeeping' β1 subunit (Gloor, Antonicek et al. 1990). Interestingly, deletion of this subunit did not affect the *in vitro* channel activity in extracts from murine retinas, however, histological analysis of the retinas from β2 knockout mice showed significant cellular degeneration and apoptosis due to activation of an intrinsic death program (Magyar, Bartsch et al. 1994, Molthagen, Schachner et al. 1996). Therefore, this suggested that the Na/K-ATPase subunit may have a role in retinal adhesion.

Both retinoschisin and the retinal specific α3β2 Na/K-ATPase co-immunoprecipitated and co-localised together in mice retina (Molday, Wu et al. 2007). Indeed, using a β2 mouse knockout, retinoschisin localisation to photoreceptor membranes was shown to require the Na/K-ATPase subunit, with expression of these components in HEK293 cells sufficient to drive retinoschisin association with the cell surface (Friedrich, Stohr et al. 2011). Together, these studies suggested that retinoschisin may stably associate with the Na/K-ATPase subunit, giving the β2 subunit its observed adhesive properties. However, the nature of the interaction is not known. It has been proposed that retinoschisin may bind to the

glycans attached to the subunit, however this is yet to be confirmed (Molday, Wu et al. 2007). Moreover, the intracellular signalling molecule Sterile Alpha and TIR motif containing protein (SARM1) forms a complex with the retinal Na/K-ATPase (Molday, Wu et al. 2007). This small protein is involved in the inhibition of innate immune signalling (O'Neill and Bowie 2007) but has also been observed to interact with syndecan-2 which is known to regulate the morphology of neuronal cells (Chen, Lin et al. 2011). This raises the potential that retinoschisin binding may activate an intracellular signalling cascade which may be important in the maintenance of retinal architecture.

1.4.3 L-Type Voltage Gated Ion Channels

Retinoschisin has also been found to interact with another photoreceptor ion channel. Using both co-immunoprecipitation and mammalian two-hybrid assays, retinoschisin was shown to bind to L-type voltage gated ion channels (L-VGCCs) (Shi, Jian et al. 2009). L-VGCCs are membrane permeable, calcium specific ion channels which regulate numerous processes such as muscle contraction, secretion, gene expression and neurotransmission (for example in the retina). The channel consists of four subunits, the α_1, $\alpha_2\delta$, β and Υ, producing a 400kDa complex in the plasma membrane (De Waard, Gurnett et al. 1996). The α_1 subunit is the largest subunit, of around 190-250 kDa consisting of multiple membrane spanning helices. This subunit consists of a tetramer of a 6 helical bundle, which together form the membrane-spanning pore (Wu, Yan et al. 2015). As a result, this subunit is the main functional component, containing also the voltage-sensing capability, ion selectivity and the binding sites for pharmacological inhibition. The remaining auxiliary subunits modulate the activity of α_1 through altering trafficking, activation and inactivation and channel gating kinetics (Davies, Hendrich et al. 2007, Buraei and Yang 2013).

In the retina both the CaV 1.3 and CaV 1.4 α_1 subunits are expressed on both cone and rod photoreceptors and are important in neurotransmission between the photoreceptor and bipolar cell, with deletion of this channel causing reduced ERG b-wave in mice models (Mansergh, Orton et al. 2005). L-VGCCs are found in the presynaptic membrane on the photoreceptor and regulate the production of glutamate in the dark state (Pardue and Peachey 2014). In the signalling to ON-bipolar cells, the glutamate diffuses and binds to the G-protein coupled receptor (GPCR), the metatrobic glutamate receptor (mGluR6), on the bipolar cell membrane (Nomura, Shigemoto et al. 1994, Xu, Dhingra et al. 2012) which then activates the bound heterotrimeric G-protein $G_{\alpha 0 \beta \Upsilon}$ (Dhingra, Lyubarsky et al. 2000) which then binds and inactivates the non-specific cation channel Transient receptor potential cation channel subfamily M member 1 (TRPM1). This channel depolarizes and activates the bipolar cell (Morgans, Zhang et al. 2009, Koike, Obara et al. 2010, Peachey,

Pearring et al. 2012). Stimulation with light leads to a reduction in glutamate release, which in turn stimulates TRPM1-mediated depolarization and neurotransmission.

Retinoschisin was found to bind to the N-terminus of CaV1.3, with the R141G mutant leading to loss of the normal circadian control of this channel and altered channel gating kinetics (Shi, Jian et al. 2009). This suggests that retinoschisin may be exerting a regulatory influence upon the channel. However, this may also represent a feedback loop as L-VGCCs in the retina regulate the circadian production of retinoschisin, which is lost upon inhibition of the L-VGCC channel (Ko, Liu et al. 2008). Furthermore, retinoschisin has been shown to be important in maintaining the synaptic localisation of this channel (Ou, Vijayasarathy et al. 2015). Together, these observations suggest that binding partners at the photoreceptor membrane may allow retinoschisin to have an additional function and potentially regulate its own production.

1.4.4 Retinal Extracellular Matrix

Whilst the focus for the identification of binding partners has been focused on membrane binding partners, additional interacting partners have been identified in the extracellular matrix. Steinier-Champliaud et al. identified the extracellular matrix component β2-laminin as a potential interacting partner (Steiner-Champliaud, Sahel et al. 2006). This suggests that retinoschisin may be able to facilitate cell-matrix interactions, but this still remains poorly studied.

1.4.5 Differential Models for Retinoschisin Function

Currently, two competing models exist to explain the mechanism by which retinoschisin maintains retinal structure. The first model proposes that retinoschisin is an adhesion protein which directly maintains cell adhesion, maintaining retinal structure. Indeed, the discoidin domain is closely associated with many such adhesion events and deletion of retinoschisin leads to both retinal schisis (Weber, Schrewe et al. 2002) and loss of close association of adjacent photoreceptors, suggesting an adhesive function (Vijayasarathy, Takada et al. 2007). However, conversely it has been suggested that retinoschisin may regulate retinal structure through regulation of intraocular pressure. In this model, retinoschisin regulation of ion channels would allow for this regulation, with its loss leading to a build-up of fluid and intraocular pressure which triggers a schisis event, leading to the development of XLRS (Molday, Kellner et al. 2012). Currently, the lack of data prevents any definitive description of retinoschisin action in the retina.

1.5 The Development of XLRS Therapeutics

Despite the lack of functional information regarding retinoschisin, efforts have been made to develop therapeutics for XLRS. Detailed below are the two major approaches which have been adopted for retinoschisin treatment.

1.5.1 Carbonic Anhydrase Inhibitors

The presence of schisis cavities in the XLRS retina has led to the use of carbonic anhydrase inhibitors (CAIs) in the treatment of XLRS. Indeed, CAIs such as dorzolomide and acetozolomide have proven useful in the treatment of macular oedema, where inhibition of carbonic anhydrase in the RPE leads to both acidification of the retina and increased fluid extrusion, lowering intraocular pressure (Wolfensberger 1999). This suggested a possible role in the correction of the schisis cavities formed during XLRS.

Many case studies have reported that both acetazolomide and dorzolomide treatment have been successful in correcting schisis cavities, reducing photoreceptor cell layer thinning and improving visual acuity. For example Apushkin et al. reports improvement in foveal thickness in 7 out of 8 patients in the study, with Walia et al. reporting success in CAI treatment of XLRS irrespective of the class of disease-associated mutation (Apushkin and Fishman 2006, Walia, Fishman et al. 2009). However, whilst these CAIs have been effective in preventing schisis cavities, any improvement in visual acuity has been small with variable responses to treatment (Genead, Fishman et al. 2010, Khandhadia, Trump et al. 2011). Furthermore, a number of studies have reported no improvement in visual acuity after treatment despite correction of retinal splitting and even cases where CAIs have had no effect (Ali and Seth 2013). Also, Zhour et al. reported a lack of corrective effect of CAIs in resolving the retinoschisis seen in the Rs1h$^{-/y}$ mouse model (Zhour, Bolz et al. 2012). As a result, this suggests that CAIs may not be an effective treatment for XLRS or effectiveness may be influenced by other factors.

1.5.2 Retinoschisin Gene Therapy

The successful re-introduction of wild-type retinoschisin using AAV vectors in the Rs1h$^{-/y}$ mouse model has spurred efforts to develop a therapeutic for patients. Pre-clinical evaluations confirmed that the vectors are well tolerated in both mice and *Cynomolgus macaques* with no antibodies detected against retinoschisin and vector DNA only detected in the eye (Ye, Budzynski et al. 2015, Ye, Conlon et al. 2015). Following this, a phase I clinical trial for the use of recombinant AAV vectors for the treatment of XLRS is currently underway (https://clinicaltrials.gov/ct2/show/NCT02416622?term=xlrs&rank=2)..

However, additional approaches towards gene therapy of XLRS have been recently developed. Solid Lipid Nanoparticles (SLNs) have been developed for the introduction of the wild-type retinoschisin construct (Delgado, del Pozo-Rodriguez et al. 2012). Both dextran and hyaluronan-based vectors facilitated endocytosis of the construct, with treatment of photoreceptors *in vitro* using these constructs inducing retinoschisin expression (Apaolaza, Delgado et al. 2014). Injection of SLNs containing wild-type retinoschisin constructs also leads to a reduction in photoreceptor loss and schisis resolution in the $Rs1h^{-/y}$ mouse model (Apaolaza, Del Pozo-Rodriguez et al. 2015), suggesting that such non-viral gene therapy vectors may be of therapeutic use.

However, reintroduction of wild-type retinoschisin in the knockout mice models is in the absence of endogenous retinoschisin, while patients express mutant forms of retinoschisin which could potentially interact with the wild-type protein. Using a HEK 293-EBNA cell system, wild-type retinoschisin was co-expressed with mutant retinoschisin to mirror the situation in patient photoreceptors. For mutants which retained retinoschisin, wild-type retinoschisin co-expressed with the mutant assembled correctly and was secreted, suggesting that gene therapy is a viable option in this situation, which describes a large number of currently characterised mutations (Dyka and Molday 2007). However, co-expression with the R141H mutant (which retains octameric secretion) led to co-assembly of wild-type and mutant protein, generating chimeras which could still be non-functional (Dyka and Molday 2007). As a result, in the development of gene therapy, it may be important to consider the causative mutation in the patient.

1.6 Biophysical Characterisation of Retinoschisin

With the current efforts towards developing treatments for XLRS, it is becoming increasingly important to gain a fuller picture of the mechanism of retinoschisin action and the effects of particular causative mutations to inform these studies. As a result, this study aims to structurally characterise both the retinoschisin monomer and octamer. To this end, two principle techniques were employed. Small Angle X-Ray Scattering (SAXS) was used to biophysically characterise the monomer with Cryo-Electron Microscopy (Cryo-EM) employed to determine the structure of the fully assembled octameric complex.

1.7 Small Angle X-Ray Scattering

SAXS allows for a detailed analysis of multiple parameters of protein structure such as size, molecular weight, molecular volume and the presence of flexibility, whilst also allowing for determination of the low resolution (approximately 2nm resolution) reconstruction of the molecular structure (Jacques and Trewhella 2010, Rambo and Tainer 2011, Rambo and Tainer 2013, Kikhney and Svergun 2015). In this approach, a pure solution of monodisperse protein molecules are illuminated by a beam of collimated

and focused X-rays. The X-rays propagate through space as a plane wave, with interaction with the electron cloud in each of the atoms (scattering centres) generating additional secondary wavelets which are scattered with respect to the transmitted radiation (Jacques and Trewhella 2010, Mertens and Svergun 2010). The scattering event is elastic and coherent, this therefore generates patterns of interference which carry information of the protein internal structure to the detector, allowing for interrogation of the molecular structure. However, within the illuminated solution, both solute (protein) and solvent molecules will cause elastic scattering and, as a result, the total scatter (p) is equal to the sum of all scattering events. Therefore, in order to detect the protein in solution the scattering of the solvent must be subtracted (using a solvent-only control) from the total scattering, with the resulting difference in scattering (Δp) representing the signal from the protein molecules (Putnam, Hammel et al. 2007, Mertens and Svergun 2010) (Figure 1.4A).

The detector during the SAXS experiment is placed at a scattering angle (2θ) and records the scattering in two dimensions from very low angle scattering (which carries the lowest resolution information) to higher angle scattering (which contains more information regarding the structure of the protein) (Jacques and Trewhella 2010, Mertens and Svergun 2010) (Figure 1.4A). The scattering here is isotropic through the two dimensions due to the chaotic tumbling of the protein molecules in solution, which ultimately limits the resolution of the technique (Jacques and Trewhella 2010). However, the isotropic nature of the elastic scattering allows for rotational averaging of the signal and data reduction, generating a one-dimensional scatter profile for the protein molecule (Mertens and Svergun 2010). Here, the logarithm of the intensity of the scattering (LogI(q)) is plotted against the scattering vector (q) with units of 1/Å, defined as:

$$q = \frac{4\pi sin\theta}{\lambda}$$

where 2θ is the angle between the scattered and incident radiation at which the scattering pattern was measured and λ is the wavelength of incident radiation (Jacques and Trewhella 2010, Mertens and Svergun 2010) .The scattering vector allows for expression of the scattering intensity at different spatial frequencies, with higher values of q (up to 0.4-0.5) representing higher resolution information. The typical one-dimensional scatter curve shows high scattering intensity at low angles (low q values) which is reduced at increasing q values due to the difficulty in discerning the protein signal from the solvent at increasing resolutions (Rambo and Tainer 2011).

Many model-independent, informative measures of protein structure can be extracted directly from the one-dimensional scatter profile. Analysis of this one-dimensional scatter curve at very low scatter angles (low q values) shows the Guinier region of the curve. Conversion of this region to a Guinier plot (LogI(q) vs. q^2) generates a straight line where the gradient is equal to:

$$-\frac{Rg^2}{3} \cdot q^2$$

where q is the scattering vector and R_g is the radius of gyration (Mertens and Svergun 2010, Rambo and Tainer 2013). The radius of gyration value represents a size parameter for the protein molecule, it describes the average root-mean-square distribution of all the lengths present in the molecule projecting out from the centre of mass of the molecule weighted by their scattering density (Mertens and Svergun 2010). Larger proteins have larger R_g values, with the opposite true for more compact proteins. Straight line fitting in the Guinier region allows for determination of this value by exploiting the relationship between R_g and the gradient of the Guinier region (Figure 1.4B).

Extrapolation of the linear region to the y-intercept yields the forward scattering intensity (I(0)), or the scattering at zero angle (Mertens and Svergun 2010). This value represents the scattering density of the molecule per unit volume. Therefore, comparison of this value to the I(0) value for known standards such as Bovine Serum Albumin (BSA) allows for determination of the approximate molecular weight of the protein (Mertens and Svergun 2010) (Figure 1.4B). However, this measure is affected by a number of potential effects. For determination of I(0), the concentration of both the protein and standard must be accurately known. Also, the presence of aggregation or intermolecular repulsion can lead to an increase or decrease in the scattering intensity respectively at very low q values, which can lead to altered I(0) measurements, and therefore, protein samples must first be assessed for concentration and the presence of aggregates prior to SAXS analysis (Jacques and Trewhella 2010).

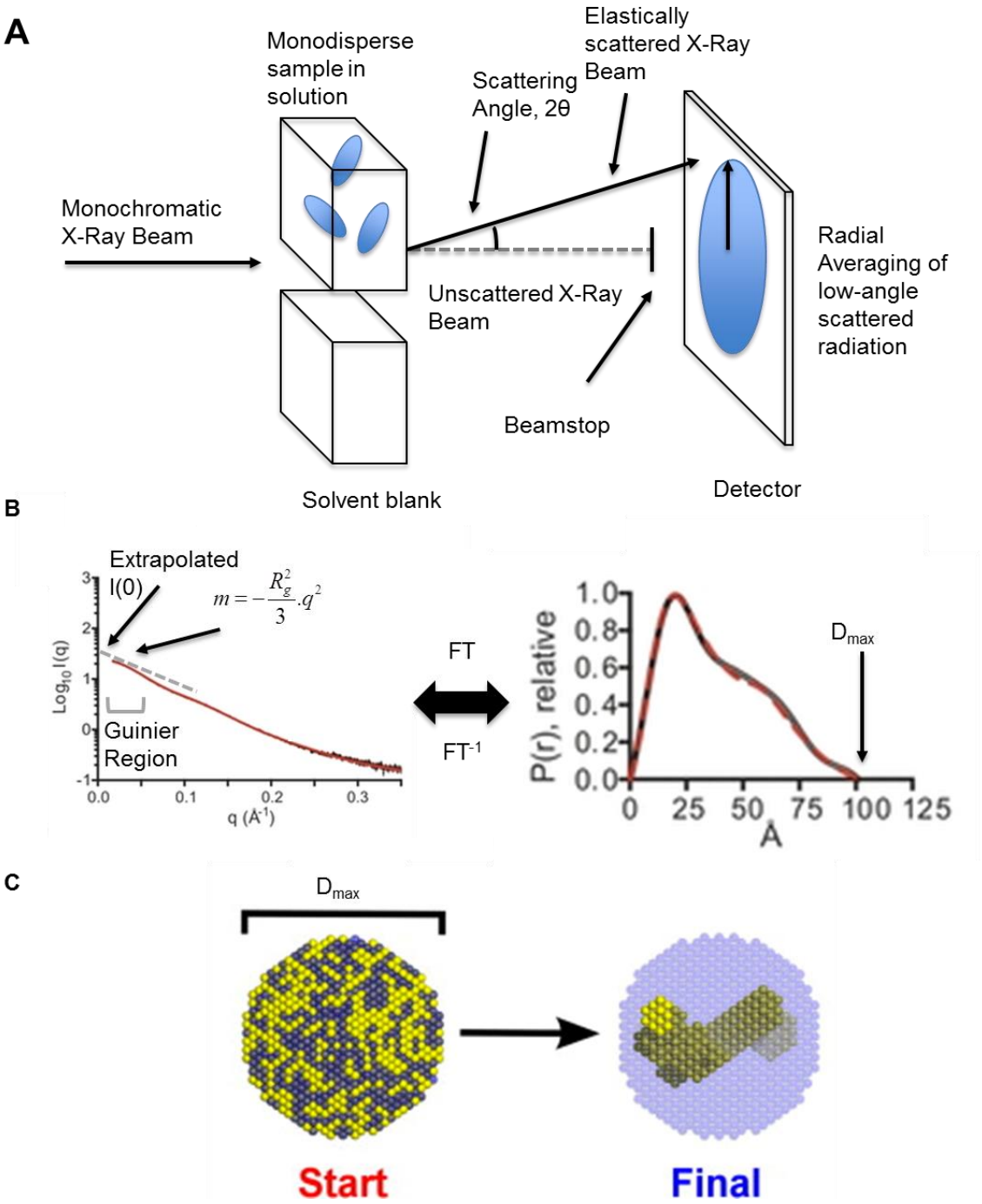

Figure 1.4 – Protein structural determination using SAXS. (**A**) A purified, monodisperse protein sample is illuminated by monochromatic X-rays, with the protein low angle scatter detected and rotationally averaged to generate the one-dimensional SAXS curve. (**B**) Determination of the R_g and I(0) from the SAXS curve, with Fourier transform producing the pair-distribution function, from which D_{max} is calculated. (**C**) The model-independent variables determined in previous steps is used in DAMMIN and DAMMIF programs to calculate the low-resolution volumetric model of the protein molecule. Adapted from: Mertens et al (2010).

Further transformation of the one-dimensional SAXS profile allows for interrogation of the folded character of the protein sample. Plotting of $q^2I(q)$ against q produces a Kratky plot, which can be used to determine the folding state of the protein (Mertens and Svergun 2010). Typically, in the Kratky plot, folded and rigid globular proteins show a peak at low q followed by a return to near baseline for the signal at high q values. However, for intrinsically disordered, unfolded or flexible proteins the signal rises throughout the q

range (Jowitt, Murdoch et al. 2010, Mertens and Svergun 2010, Rambo and Tainer 2011). This analysis has been built on, with the generation of R_g-normalized kratky plots $((I(q)/I(0))(qR_g)^2$ against qR_g) which allows for the globularity of the protein fold to be analysed. In this analysis, a peak in the position (1.1, $\sqrt{3}$) is indicative of a spherical protein. Displacement of the peak away from this point is suggestive of an extended conformation, allowing for the elongation of the protein fold to be assessed (Durand, Vives et al. 2010).

Potentially the most informative transformation of the one-dimensional scatter curve is the pair-distance distribution function or P(r). The P(r) function is a measure of the probability of finding a given intramolecular distance r (P(r)) plotted against the real-space intramolecular distance (Putnam, Hammel et al. 2007, Mertens and Svergun 2010, Kikhney and Svergun 2015). This generates a distinctive real-space profile for each protein, the shape of which informs the shape of the protein molecule. Furthermore, the x-intercept of this function represents the distance at which the probability of observing larger distances drops to zero. This value is known as the maximum dimension (D_{max}), which effectively gives a measure of the absolute size of the protein molecule (Mertens and Svergun 2010) (Figure 1.4B). However, to confirm that the calculated P(r) accurately represents the SAXS profile, an inverse Fourier transform of this distribution is carried out to generate a regularized scatter profile, which can be compared to the experimental data (Jacques and Trewhella 2010).

Together, these analyses allow for characterisation of the protein molecule. Furthermore, using the values determined, the low resolution solution structure of the protein molecule can be modelled *ab initio*. Such analyses were originally performed by comparison of the scattering profile with the theoretical scattering from geometrical shapes (Mertens and Svergun 2010). However, Svergun et al. have developed an extensive bead-modelling software suite which works to recapitulate *in silico* the observed scattering profile using a series of beads. In this approach, adopted by the program Dummy Atom Model Minimisation (DAMMIN), a 'search volume' is defined by the measured D_{max} of the protein. This volume is populated with beads or 'dummy atoms' which are randomly assigned as solvent or protein and the simulation is randomized to scramble the positions of the beads. Following this, an iterative process is adopted where the theoretical scattering profile of the protein bead model is calculated and compared to the experimental profile. After each round, the model is changed and compared again, with the program working to minimize the difference between the calculated and experimental profiles to recapitulate the protein structure (Svergun 1999). This allows for low resolution analysis for the protein structure, with subsequent improvements in the DAMMIN Fast (DAMMIF) program

allowing for up to a forty-fold increase the speed of processing (Franke and Svergun 2009) (Figure 1.4C).

However, with such bead modelling approaches, the random 'seed' used as a starting point for the iterative calculation can influence the result. Indeed, the bead modelling approach is unable to give a full, unambiguous solution for any given experimental SAXS profile (Mertens and Svergun 2010). As a result, multiple simulations are run simultaneously using different random start points and the results of each individual *ab initio* model compared using the DAMAVER software suite (Volkov and Svergun 2003). This compares, averages and filters the individual *ab initio* models to generate an averaged model which recapitulates the protein structure.

These low resolution envelope structures provide information on the solution structure of the protein molecule and can be compared to high resolution structures through rigid-body modelling (using SASREF). For flexible proteins, an ensemble of dynamic conformations of the protein structure in solution can be extrapolated (using, for example Ensemble Optimisation). As a result, SAXS is a versatile technique for probing the solution state of protein molecules (Mertens and Svergun 2010, Kikhney and Svergun 2015).

1.8 Cryo-Electron Microscopy (Cryo-EM) and Single Particle Analysis

For many years now, cryo-EM has been a powerful technique for the characterisation of structures over many scales. EM has been previously used to structurally analyse entire cells or organelles (using for example tomography or serial sectioning) to individual proteins and macromolecular complexes (using single particle analysis) which have been resistant to analysis by more traditional techniques such as X-Ray Crystallography or Nuclear Magnetic Resonance (NMR) spectroscopy. However, single particle analysis using cryo-EM requires a number of steps from sample preparation, imaging and processing to allow for three-dimensional structure determination.

1.8.1 Sample Preparation for Electron Microscopy

Electrons are readily scattered by many molecules, including air and as result the electron microscope must be maintained under a tight vacuum to allow for imaging. However, this also means that the protein must be stabilized in a state to allow for imaging under such conditions (Orlova and Saibil 2011). Currently, there are two principal methods to stabilize protein samples for imaging. The first of these preparations is negative-stain, widely used in the 1960s (Brenner and Horne 1959), with this sample preparation allowing for the first three-dimensional single particle reconstruction of the T4 bacteriophage tail (De Rosier and Klug 1968). This technique effectively substitutes the solvent with a dilute solution of

heavy metal salts such as uranium acetate and is dried. The salt stains the entire grid except for the protein molecules and as a result, individual protein particles can be imaged according to exclusion of the heavy metal stain. This technique produces good contrast and allows for the size, shape and symmetry of the particle to be imaged with relative ease using small quantities of material. However, the non-physiological state is prone to the generation of flattened or dehydrated particles and can also break apart fragile multi-protein complexes and ultimately limits the resolution of reconstruction to around 20Å (Orlova and Saibil 2011). Therefore, development of a technique that preserved the native arrangement was required. Following a series of electron diffraction studies, Taylor and Glaser showed that freezing the samples under cryo conditions maintained a native structure with the high-resolution information protected (Taylor and Glaeser 1974, Taylor and Glaeser 1976). Following this, Dubochet et al. developed a rapid freezing method where the sample was plunge-frozen in liquid ethane cooled by liquid nitrogen (Adrian, Dubochet et al. 1984, Dubochet, Adrian et al. 1988). Such rapid cooling prevented the formation of ice crystals, trapping the protein in a vitrified state which allowed for imaging of the particles. This method allowed for imaging without staining at near-native conditions with the potential for higher resolution structures and a more isotropic orientation of the particles in the vitrified solution. Therefore, the improved sample conditions heralded the cryo-EM technique which is used extensively today for structural characterisation of protein complexes.

1.8.2 The Transmission Electron Microscope

The imaging of such solid-state samples requires both focusing, scattering and detection of electrons. These functions are performed by the transmission electron microscope (TEM).

There are many commonly used sources of electrons in the electron microscope. Thermal emission of electrons can be carried out using a heated Tungsten filament or a Lanthanum Hexaboride (LaB_6) crystal. However, the most recently developed electron source is the Field Emission Gun (FEG). This is a sharpened tungsten crystal, which generates more coherent electrons to allow for higher resolution structural determination (Orlova and Saibil 2011) (Figure 1.5A).

The emitted electrons are then accelerated in a vacuum using voltages ranging from 100-300 kV. During this acceleration, the electrons are passed through a lens system which focuses the electrons and magnifies the resulting image. First, the emitted electrons (which are divergent) are converted into a parallel beam by the condenser lens, this is followed by the objective lens which magnifies the image after the beam has passed

through the sample and then intermediate and projector lenses which further magnify the image. Alongside the lens system, there are also a series of apertures which remove high-angle scattered electrons (Orlova and Saibil 2011).

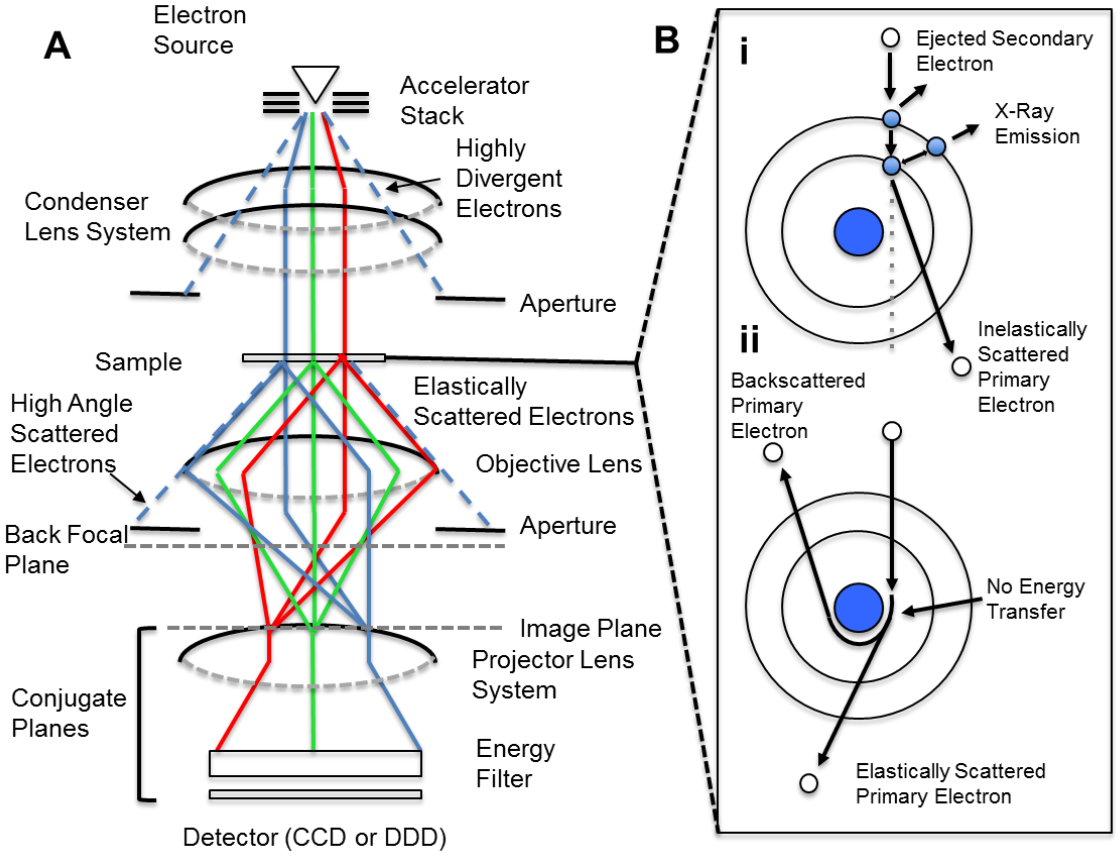

Figure 1.5 – Image formation and electron interactions in the electron microscope. (**A**) A schematic of the electron microscope showing the electron source, lens system, sample and elastic scattering of electrons, energy filter and detector. (**B**) (**i**) The inelastic and (ii) elastic scattering events between an incident electron and the sample produced during illumination. Adapted from: Orlova et al (2011).

The lens system, however, is not perfect and this affects the imaging of the sample. A number of aberrations exist, such as spherical aberration (C_s) where that electrons at the periphery are focused more than those passing through the centre, this is corrected for during image processing. Additionally, electrons with longer wavelengths are focused more readily, so generating planes of differently focused electrons, which is known as chromatic aberration (C_c). These electrons (alongside inelastically scattered electrons, see below) can be removed before detection using an energy filter, which only allows electrons of a certain energy to pass through to the detector, with the lower energies of these electrons preventing passage (Orlova and Saibil 2011) (Figure 1.5A).

Initially, the image was detected using photographic film, however, the convenience and improved signal to noise ratio (SNR) at low resolutions of another class of detectors, the charge-coupled devices (CCDs), led to their widespread adoption in TEM imaging

(Sander, Golas et al. 2005, Suloway, Pulokas et al. 2005). In CCD detectors, the electron strikes a scintillator which converts the electrical signal to photons which travel through an array of wells that convert the photons back to into a small electrical charge. The pixel charges are serially transferred to a readout which digitally produces the image (Orlova and Saibil 2011).

Despite the convenience of use of these detectors, they have limited imaging capacity. The detector quantum efficiency (DQE) (a measure of the efficiency that the detector records the signal, with a perfect detector giving a DQE of 1) is low, at only approximately 0.1 (Bai, McMullan et al. 2015). The limitations of the CCD have stimulated the development of a new class of detectors called the monolithic active pixel sensors (MAPS) which are more commonly known as direct electron detection devices (DDDs) (Faruqi and Henderson 2007). These consist of a radiation-hardened membrane which has the electronics fabricated directly onto them. As a result, the striking of the electron can be directly sensed (McMullan, Clark et al. 2009). Furthermore, the detectors are thin (around 50 μm thick) which minimises the scattering of electrons back up through the detector (back-scattering) which contributes to noise (McMullan, Faruqi et al. 2009) (Figure 1.5B). This has allowed for much higher DQE and therefore higher signal-to-noise imaging using the DDDs. These detectors have also had other benefits, allowing for high resolution imaging which will be discussed in section 1.8.7.

1.8.3 Sample-Electron Interactions and Image Formation

Interactions of the focused electron beam with the sample are complex, with multiple different interactions observed in the electron microscope. Some the incident beam passes straight through the sample and does not interact, with a small portion interacting with the sample. In the microscope, there are two types of interactions observed, elastic and inelastic scattering. Inelastic scattering is caused by a collision between the incident electron and an outer shell electron of the scattering centre, or by interaction with an inner energy level, which leads to energy transfer into the sample. This interaction is damaging, rapidly causing radiation damage through bond breakage, secondary scattering events, X-ray emission and free-radical generation. These inelastic scattering events produce the absolute resolution limit of cryo-EM through radiation damage. Therefore, to reduce this, imaging of biological specimens is done under 'low-dose' mode, with samples typically exposed to around 1-40 electrons/$Å^2$ (Orlova and Saibil 2011) (Figure 1.5B).

However, there are also elastic scattering events where the incident electron is scattered by the sample but does not transfer energy to the sample. Here, the electron emerges at a scattering angle with the same energy as before the event. In this case, the scattering is

produced due to the constructive interference of the secondary wavelets generated during the elastic scattering event, with constructive interference generating waves at multiple scattering angles with respect to the unscattered wave (Figure 1.5B). The scattering angles are dependent on the distance between the scattering centres, with low angle scatter due to features at lower spatial frequencies and increasing scatter angles generated by scattering of higher spatial frequency features (Orlova and Saibil 2011). The focusing of the objective lens following this scattering causes the scattered waves to interact with the unscattered component, however, due to the initial scattering event and the excess path length, the scattered radiation is phase shifted with respect to the unscattered beam, generating phase contrast. This phase contrast is made visible in the image by inducing amplitude contrast when it is recombined with the unscattered beam, with increased contrast caused by spherical aberration and defocusing of the microscope (Erickson and Klug 1970, Danev and Nagayama 2010).

Such image formation in the microscope however does not allow for the transfer of information at all spatial frequencies. The alternating pattern of constructive and destructive interference between the scattered waves with different path lengths (caused by scattering of components of different spatial frequencies) and unscattered radiation leads to regions of both positive and negative contrast in the image and frequencies where there is no information transfer. This generates a sinusoidal function of alternating positive and negative contrasts in the image known as the contrast transfer function (CTF) (Orlova and Saibil 2011). The CTF also decays at higher spatial frequencies. This is caused by envelope functions which are the result of many imperfections in the microscope such as lens aberrations, current instabilities, microscope instabilities, beam incoherence and radiation damage of the sample. Therefore, the CTF describes the image formation in the electron microscope and the complex blurring of the image, with the real space equivalent being the point spread function (PSF), defined as the blurred microscope image of a single point (Mindell and Grigorieff 2003, Orlova and Saibil 2011, Cheng 2015).

The CTF is affected by the focus of the microscope, with defocusing altering the envelopes leading to a CTF with greater information transfer at low spatial frequencies and a loss at higher frequencies, with the opposite true closer to focus (Cheng 2015). As a result, this allows for correction of this CTF by merging of CTFs carried out at different defocuses which effectively ‘fills in’ the missing information, allowing for complete information transfer into the image. Further CTF correction can be performed such as ‘phase-flipping’ which inverts the contrast of the negative contrast frequencies in the image (Orlova and Saibil 2011).

1.8.4 Image Processing and Analysis

Following recording of images, image processing allows for structural analysis of the molecules. Due to the low signal to noise ratio of individual images and the requirement for even sampling of all the dimensions of the molecule, multiple particles must be boxed off and selected from the micrographs. Following selection, the particle stack must be aligned to improve the signal to noise. This alignment can be performed using the cross-correlational function (CCF). Particles are normalized (to allow for accurate comparison using the CCF) and aligned with a reference image using peaks in the CCF function, which allows for all the particles to be brought into register (Orlova and Saibil 2011).

However, this aligned stack of images has within it many different projections of the particle structure seen from different angles due to the isotropic distribution of the particle in the vitreous ice. As a result, these views must be separated and each 'class' averaged together to give a higher SNR view of the particle structure. This is known as class averaging and allows for a two-dimensional representation of the protein structure (Orlova and Saibil 2011).

Reference-free classification requires clustering of similar images to define each class and therefore a pixel-by-pixel comparison of each particle. However, this is computer intensive and so the data is reduced and a statistical method used to classify the data. In these methods, each particle image is defined as a 'point' in *n*-dimensional space which accounts for all the pixel intensity values of that particle. Multivariate statistical analysis (MSA) can then be used to identify the greatest differences in the data set and these are defined as 'principal components' in the data, with the ends of these principal component vectors being the Eigen images which represent the biggest variations in the data (Vanheel and Frank 1981). Definition of classes and evaluation of image similarities can be done using one of two methods. Hierarchical clustering starts with a single cluster and works to generate the required number of classes by maximizing inter-class variation and minimizing intra-class variation, generating clusters of points which define each class (van Heel 1984). The other method, K-means clustering, starts by generating random points (K-means), which define clusters and then assigns all the nearest particles to each cluster. The program then iteratively refines the population of each cluster to minimize the sum of all intra-cluster variations, generating each class (Orlova and Saibil 2011).

1.8.5 Angle Assignment and Three-Dimensional Reconstruction

Whilst this allows for analysis of the particle structure using two-dimensional projections, to determine the particle structure in three-dimensions, the relative orientations of these projections must be known. There have been many methods proposed for angle

assignments using both computational and experimental approaches. Computationally, angle assignment can be carried out using common lines in reciprocal space. Common lines theorem shows that for each pair of two-dimensional Fourier transforms which are different projections for the same model, both will have a common line or one-dimensional projection between them. Identification of at least three of these lines between projections allows for complete angle assignment for all orientations (Crowther, Amos et al. 1970).

Experimentally, angles can be assigned using tilt pairs, where the same field of particles is imaged when untilted and then again at high tilt. Alignment between the fields allows for tracking of individual particles (Radermacher, Wagenknecht et al. 1987). However, the limitation of the microscope to collecting data at tilts only up to around 60 degrees, generates a 'missing cone' which distorts the resulting three-dimensional reconstruction (Orlova and Saibil 2011). To overcome this limitation, another method termed orthogonal tilt reconstruction has been developed. Here, particles are imaged at both 45 and -45 degrees tilt, which generates a series of images around the common axis with prevents the 'missing cone' effect (Leschziner and Nogales 2006).

Following angular assignment the three-dimensional structure of the particle can be reconstructed using either reciprocal or real-space methods. In reciprocal space, the three-dimensional structure can be calculated using Fourier inversion. In this method, the first used for three-dimensional reconstruction, a three-dimensional Fourier transform is built from two-dimensional Fourier transforms (which represent projections of the three-dimensional volume). Therefore, an inverse Fourier transform of the three-dimensional Fourier transform constructed by these two-dimensional 'slices' will generate the density map of the structure (De Rosier and Klug 1968). Another method, carried out in real space, is also commonly used for reconstruction and is known as back-projection. In this method, projections (which have assigned angles) are stretched back in space (in the direction of that projection) along lines known as ray sums (RS). The density in each pixel of the reconstruction is the sum of all the ray sums which intersect and pass through that point. However, this method can generate blurred or noisy reconstructions, with additional filtering needed to prevent these effects (Harauz and Ottensmeyer 1983).

The three-dimensional map represents the structure of the particles imaged, however, the reconstruction can be refined to higher resolutions. Indeed, software packages such as EMAN (Ludtke, Baldwin et al. 1999, Tang, Peng et al. 2007) can generate an initial model which is then further refined to generate a final reconstruction. This refinement follows an itertive scheme, where the particles are first compared to the projections of the three-dimensional structure to generate classes to which angles are assigned allowing for three-dimensional reconstruction, which generates the references for the next iteration (in a

procedure known as projection matching). This comparison is known as multi-reference refinement, with a number of methodologies available to compare the projections to the particles. One such commonly used comparator is the cross correlational coefficient (CCF), with the similarity between the two objects assessed during both translational and rotational searches. The particle is then assigned to the reference which provides the greatest CCF, which is followed by averaging of each individual class. Each particle therefore contributes to a single class. This technique allows for accurate alignment, classification and three-dimensional structural refinement and closely resembles a least-squares approach, in which the error between the data and the references is iteratively reduced during the refinement. However, with this approach, correct class assignment may be prevented by high noise levels in the cryoEM images. An alternative approach was developed in 1998 by Sigworth, known as Maximum Likelihood (ML) (Sigworth 1998, Sigworth, Doerschuk et al. 2010). ML instead refines the class averages and three-dimensional structure to maximize the probability that the model represents the data. In this approach, during comparison between the class averages and model projections, probabilities are calculated for all orientations for each particle and the particles then contribute to each class weighted against that probability, instead of being assigned to a single class (Sigworth 1998, Sigworth, Doerschuk et al. 2010, Scheres 2012, Scheres 2016). However, in this approach, ML is able to produce different models which agree equally well with the data. As a result, an additional regularization step is applied in which model parameters are estimated from the experimental data in advance, complementing the data and leading to a single, optimal solution (Scheres 2012, Scheres 2012). It has been reported that this ML approach is better able to cope with the low SNR values of cryoEM data, generating optimal robust classifications and reconstructions (Scheres, Valle et al. 2005). Indeed, the ML approach has been reported to prevent another phenomenon observed in other types of reconstruction, known as overfitting. This is the inclusion of noise into the data set which leads to incorrect high resolution estimations, to which the CCF approach is vulnerable. Indeed, using both a least-squares and regularized ML approach to refine an GroEL data set, the least squares approach gave a much higher resolution estimation which was not supported by the structures observable in the map and was not observed in the ML approach (Scheres and Chen 2012).

A number of software packages are available for this structural refinement using both least-squares or ML approaches. Packages such as EMAN, SPIDER (Frank, Radermacher et al. 1996), IMAGIC (van Heel, Harauz et al. 1996) and FREALIGN (Grigorieff 2007) offer a least squares approach for structural refinement, with either real-space or Fourier space three-dimensional reconstructions. Another widely used package for reconstruction is known as Regularised Likelihood Optimisation (RELION) which instead employs an ML approach for efficient three-dimensional reconstruction. In addition

RELION also allows for the three-dimensional classification of structural heterogeneity in particle sets using a starting reference model. Here, generation of a defined number of models with initially random differences between them allows for competitive ML-based projection matching. If the individual states are sufficiently different and discontinuous in nature, then even subtle differences between groups of particles can be determined for the global particle structure or even local regions. This further enhances the reconstruction resolution by generating more homogenous sets of particles for refinement. Such approaches have allowed for high resolution analysis of flexible and dynamic multi-protein complexes (Scheres, Gao et al. 2007, Scheres 2010, Scheres 2016).

1.8.6 Resolution Estimations

Following refinement of the three-dimensional structure, resolution assessment is carried out using the Fourier shell correlation (FSC) which is a measure of the consistency of two models generated from half of the data set in Fourier shells of spatial frequency. The maps will be highly consistent at low spatial frequencies (giving values close to 1) but will progressively decline at increasing spatial frequencies. The global resolution of the map is then interpreted at an FSC value known as a criterion. These criteria are levels of FSC set at different signal to noise ratios. Commonly used is 0.5 where there is good signal to noise ratio, however this is often an underestimation of the map resolution, as when the half reconstructions are merged, the noise is reduced. Therefore, often in a 'gold-standard' refinement where two models are independently refined using projection matching of half the data and then combined, the FSC value of 0.143 can be used to report the resolution (Rosenthal and Henderson 2003).

However, FSC resolution estimation produces a single, global resolution value for the map. This assessment of resolution suffers from the incorporation of noise and masking artefacts which can lead to artificially increased resolution estimations (Scheres and Chen 2012, Scheres 2012, Kucukelbir, Sigworth et al. 2014). Furthermore, a global resolution ignores potentially interesting fluctuations in model resolution which may be relevant to protein function. As a result, ResMap assesses the local resolution distribution of the map. In ResMap, each three-dimensional voxel in the unfiltered map is assessed for the presence of a signal that is statistically significant above the noise observed in the map. In each case, the signal is processed through a false discovery recovery (FDR) procedure, with the highest detected resolution (above p=0.05 significance) selected as the resolution for that voxel in the map. For this, ResMap steadily samples through the resolution range tested, from highest to lowest resolutions, with voxels passing this procedure assigned the highest resolution and voxels which do not meet this requirement tested at decreasing resolutions (Kucukelbir, Sigworth et al. 2014).

1.8.7 Recent Developments in Cryo-EM

Previously, the theoretical limit for single particle analysis was far from being attained using traditional cryo-EM technology. Henderson showed that electron microscopy was capable of high resolution reconstruction, even on proteins as small as 100 kilodaltons (kDa), with the limit of the technique caused by suboptimal imaging (Henderson 1995). However, in recent years, cryo-EM has undergone a 'resolution revolution', with the development of new technological and computational advances allowing cryo-EM to reach ever higher resolutions (Kuhlbrandt 2014, Bai, McMullan et al. 2015). This has allowed for the first time cryo-EM structural analysis to atomic resolution, with new *de novo* atomic models being built and refined using cryo-EM determined electron density. Indeed, a number of studies have achieved resolutions between 3-4Å (Liao, Cao et al. 2013, Bai, Yan et al. 2015, Nguyen, Galej et al. 2016), with the structure of lactate dehydrogenase solved to approximately 2.2Å resolution (Bartesaghi, Merk et al. 2015). This has allowed for the first time atomic level characterisation of challenging proteins that could not be determined by X-ray crystallography or NMR spectroscopy.

One major reason for this improvement is the new DDD cameras. Alongside the improved DQE and reduced backscattering, these cameras are also capable of recording movies with multiple frames. This has, in turn, allowed for electron dose fractionation (selecting a subset of the best frames which represent very low dose imaging) and the ability to correct for beam-induced particle movement, which blurs high resolution features, through correlation of the entire image stack (Brilot, Chen et al. 2012, Campbell, Cheng et al. 2012, Li, Mooney et al. 2013). Furthermore, movie refinement and particle polishing have allowed for the effects of radiation damage on the high and low resolution features to be corrected, further improving the resolution (Scheres 2014). Also, new gold substrates have been developed which also work to reduce beam-induced motion on the grid, allowing for improved imaging conditions (Russo and Passmore 2014).

Further improvements are being developed to improve imaging by inducing additional phase contrast using phase plates inserted into the microscope to generate observable particles without the need for defocusing. This produces stronger contrast and improved signal to noise ratios at focus and low defocus values which has the potential to allow further high resolution features to be extracted from particles and improve reconstructions (Danev and Nagayama 2010, Danev and Baumeister 2016).

1.9 Aims

Exploiting these techniques, this study aimed to structurally characterise the different oligomers of retinoschisin and the effects that XLRS-associated mutations have on this

structure. In doing so, we aimed to provide insight into the potential mechanism of retinoschisin function in the retina. Whilst retinoschisin has been established as a crucial factor in the maintenance of retinal structure, the precise function that it serves is still elusive. It is becoming increasingly important to investigate this, with the concerted effort currently underway for the treatment of XLRS using both carbonic anhydrase inhibitors and gene therapy approaches. Indeed, structural and functional insight may provide information required for improved therapeutic design or alternative treatment strategies. Relating to the gene therapy efforts, it has been previously suggested that the R141H mutation may be refractory to such treatment. As a result, identification of other mutations which may pose a similar challenge could be informative for this treatment.

Indeed, mutational studies may be highly informative on the function of retinoschisin. Of particular interest are those mutations which retain the ability to be secreted as octamers (such as R141H, R141G, H207Q and R209H). These mutations appear to generate a non-functional yet fully assembled retinoschisin, suggesting an alteration of a 'functional site'. Investigation into such a site may provide insight into how retinoschisin functions in the retina by pinpointing important residues and structures in the protein. Therefore, adopting a structural approach, this study aimed to address two key questions:

1. What is the structure of the retinoschisin monomer and octamer and are there any conformational changes observed upon oligomerisation?
2. What are the effects of XLRS-associated mutations (specifically those which retain octameric secretion) on the retinoschisin structure and can these be related to a model of retinoschisin function?

To address these questions, the specific aims of the project were:

1. To express and purify both monomeric and octameric retinoschisin in the HEK293-EBNA and *Pichia pastoris* cell system in sufficient quantities to allow for structural analysis.
2. To use both hydrodynamic analysis and SAXS to investigate the structure of the retinoschisin monomer and the Rs1 domain.
3. To employ cryo-EM to solve the structure of the fully assembled octamer state and use this information to build a quasi-atomic structure to identify important residues in complex formation.
4. To investigate the effects of both the R141H and H207Q mutations which are secreted as octamers to attempt to identify both the mechanism of pathology for these mutants and any potential functional sites in the retinoschisin octamer.

2 Materials and Methods

2.1 Materials

2.1.1 Plasmid Vectors

For mammalian expression, the pCEP-Pu/Ac7 vector (Appendix 1) was used (Life Technologies). A variant of the pCEP4 mammalian expression vector (Life Technologies), the pCEP-Pu/Ac7 allowed for selection via the acquisition of puromycin resistance by transformed cells. Bacterial transformants were selected using the ampicillin resistance conferred to bacteria upon transformation with this plasmid. Secretion of the expressed protein was enabled by the presence of the BM40 signal sequence in the open reading frame, which was subsequently cleaved before secretion of the mature, folded protein.

Yeast expression was carried out using the pPICZAα expression vector (Appendix 2). Selection in both bacteria and *Pichia pastoris* yeast was by resistance to zeocin antibiotic. Secretion of the protein product in this vector used the α-factor signal sequence which is also cleaved prior to protein secretion.

2.1.2 Mammalian Expression Cells

Human Embryonic Kidney (HEK)-293 cells containing the Epstein-Barr Virus Nuclear Antigen I (HEK293-EBNA) were a stock cell line in the lab prior to the start of this project (Troilo, Zuk et al. 2014). HEK293-EBNA cells previously stably transfected with pCEP-Pu/Ac7 containing wild-type retinoschisin C-terminally tagged with a thrombin cleavage site (LVPRGS) and His_6 tag were generated by Dr. Tom Owens prior to the commencement of this project.

2.2 Molecular Biology and Construct Generation

2.2.1 Generation of Mutant Constructs

Sequences for the R141H and H207Q XLRS-associated mutants for mammalian expression were purchased as Gene Strings (Life Technologies). Gene sequences encoded the 5' NheI restriction site, protein coding segment, C-terminal thrombin cleavage site, His_6 tag, stop codon and 3' XhoI restriction site (Appendix 3). Similarly, constructs for the *Pichia pastoris* yeast expression system were obtained as gene strings. Sequences encoding wild-type retinoschisin and the C40S/C59S/C223S retinoschisin sequence were generated with the 5' EcoRI sequence, protein coding segment, C-terminal His_6 tag followed by the 3' SacII restriction site. Sequences were codon optimized for expression in *Pichia pastoris* (Appendix 4). Codon optimization was carried out using the manufacturers software as an automated process. Gene String constructs were received as purified linear DNA with the specified sequence.

2.2.2 Polymerase Chain Reaction Amplification of Constructs

To allow for In-Fusion HD cloning of the insert into the expression vector, primers which were homologous to the ends of the insert and 15 base pairs of the vector sequence which flanked the desired insertion site within the vector were generated. These were used to amplify the insert using the polymerase chain reaction (PCR), allowing for insertion of these homologous regions onto the 5' and 3' ends of the inserts. Table 2.1 summarizes the primers used during PCR amplification of inserts for cloning into the pCEP-Pu/Ac7 and pPICZAα vectors.

Construct	Primer Direction	Primer Sequence (5'-3' Orientation)
R141H/H207Q RS1 pCEP-Pu/Ac7 Vector	Forward Primer (5'-3')	**5'-** GCAGCCCCGCTAGCCTCTACCGA GGAT**- 3'**
	Reverse Primer (3'-5')	**5'-** CCTTGCCGGCCTCGAGCTCGAGT CAATGGTGGTGATGGTGGTGGCT**- 3'**
C40S/C59S/C223S RS1 pPICZAα Vector	Forward Primer (5'-3')	**5'-** GGCTGAAGCTGAATTCTCTACTGA AGATGAAGGTGAGGAC **- 3'**
	Reverse Primer (3'-5')	**5'-** AAGCTGGCGGCCGCCGCGGTTAG TGGTGGTG-**3'**
WT Discoidin Domain pPICZAα Vector	Forward Primer (5'-3')	**5'-** GGCTGAAGCTGAATTCTGTCCATA CCACAAGCCATTGGGT**-3'**
	Reverse Primer (3'-5')	**5' -** AAGCTGGCGGCCGCCGCGGTTA GTGGTGATGGTGATGGTGGCTG CCTCTGGGCACCAGACACTCCA ACAACTCCATTCTGATAGCGAT **- 3'**

Table 2.1 – Primers used for the generation of the R141H and H207Q retinoschisin pCEP-Pu/Ac7 construct and the C40S/C59S/C223S retinoschisin and wild-type discoidin domain pPICZAα constructs. Different sequences present within each primer are highlighted. Blue denotes the regions homologous with the flanking vector regions for In-Fusion HD cloning, red denotes the restriction site present, green denotes the stop codon, pink the His_6-tag and black denotes the regions which are complementary with the insert.

For high fidelity PCR amplification of the insert using these primers KAPA HiFi HotStart DNA polymerase (KAPA Biosystems) was used for amplification. The PCR reaction was performed in a total volume of 50µl with 20ng of gene string template DNA, 200pmol of both forward and reverse primer, 25µl of 2x KAPA HiFi Hotstart Readymix (containing 0.3mM of ATP, TTP, CTP and GTP, 2.5mM Magnesium Chloride and 1U of KAPA HotStart DNA polymerase) and 18µl of sterile water.

PCR amplification was carried out according to manufacturers instructions with the following protocol:

1. An initial denaturation step	95°C	3 minutes
2. A second denaturation step	98°C	20 seconds
3. An annealing step	55°C	15 seconds
4. DNA Polymerase Extension step	72°C	1 minute (1minute/kb extension)

Steps 2 to 4 were cyclically repeated for 35 cycles to allow efficient amplification of the gene string template. This was followed by a final extension step at 72^{o}C for 2 minutes to complete the PCR reaction.

2.2.3 Restriction Double Digest of Vector Sequences

Double digest of the multiple cloning site (MCS) for both the pCEP-Pu/Ac7 and the pPICZAα vector was carried out prior to the DNA ligation reaction. The mammalian pCEP-Pu/Ac7 vector was digested using NheI-HF (New England Biolabs) and XhoI (New England Biolabs) restriction enzymes with the yeast pPICZAα vector cut using a combination of EcoRI-HF (New England Biolabs) and SacII (New England Biolabs) restriction enzymes. Between 5-10µg of purified vector was incubated with 40U of each enzyme. Each reaction was performed in 1x CutSmart Buffer (New England Biolabs) (50mM Potassium Acetate, 20mM Tris-Acetate, 10mM Magnesium Acetate, 0.1mg/ml Bovine Serum Albumin, pH 7.9) and the final reaction volume made to 50µl using sterile water. The resulting reaction mixture was incubated for 2 hours at 37^{o}C to ensure full digestion of the vector.

2.2.4 Agarose Gel Electrophoresis

Separation of DNA by electrophoresis was carried out in 1% (w/v) agarose gels. Gels were prepared through addition of 1% (w/v) agarose (Bioline) to 100ml of TAE buffer (2M Tris Buffer, 1M acetic acid and 0.5mM EDTA, pH 8.0) and dissolved by heating in a microwave. Following heating, the solution was cooled and 0.005% (v/v) SafeView nucleic acid stain (NBS Biologicals Ltd.) added. Samples were loaded into the wells alongside Hyperladder I DNA standard (Bioline) to allow for estimation of DNA fragment length. Electrophoresis was carried out at room temperature; 120V for 40 minutes and DNA visualized using visible spectrum blue light.

2.2.5 Purification of DNA from Agarose Gels

DNA was purified from the agarose gel using the QIAqucik Gel Extraction Kit (Qiagen) following the manufacturers instructions. DNA bands were excised from the gel, transferred to a sterile microfuge tube and the gel sample was immersed in a volume of QG buffer 3-fold greater than the weight of the excised gel fragment and incubated at 50^{o}C for 10 minutes. Following dissolution of the gel fragment, 1 volume of isopropanol was added to the solution and the sample passed through a QIAquick spin column (Qiagen) by centrifugation at 10 000 *xg*. Immobilised DNA in the spin column was washed

once using 750µl PE buffer (Qiagen) and eluted from the column using 20µl of DNAse-free sterile water.

2.2.6 In-Fusion Ligation of Inserts

DNA ligation was carried out using the ClonTech In-fusion HD cloning kit according to the manufacturers instructions. Briefly, the ligation reaction contained 2µl of 5x In-Fusion HD Enzyme Premix incubated with 200ng of purified PCR amplified insert and 200ng of restriction-digested vector. The final volume of the reaction was adjusted to 10µl using sterile water. The reaction mixture was then incubated at 50^{o}C for 15 minutes.

2.2.7 XL-10 Transformation of Ligation Mixtures and Selection of Positive Clones

The resulting ligation mixture was transformed into XL-10 Gold competent *Escherichia coli* bacteria (Agilent Technologies). 50µl of cell suspension was defrosted slowly at 4^{o}C and incubated on ice for 10 minutes with 5-7µl of ligation mixture. The DNA-bacteria mixture was heat-shocked at 42^{o}C for 45 seconds and then incubated on ice for a further 5 minutes. Cells were spread on Luria-Bertani (LB)-Agar plates (1% (w/v) tryptone, 0.5% (w/v) yeast extract, 170mM NaCl, 1.5% (w/v) agar, pH 7.5) supplemented with 100µg/ml ampicillin antibiotic for pCEP-Pu/Ac7. For pPICZAα-transformation, bacteria were grown on low salt LB-Agar (1% (w/v) tryptone, 0.5% (w/v) yeast extract, 85mM NaCl, 1.5% (w/v) agar, pH 7.5) supplemented with 25µg/ml zeocin antibiotic (Melford Laboratories). Cells were grown at 37^{o}C overnight to allow for antibiotic selection.

2.2.8 Growth of Bacterial Overnight Cultures

Colonies were picked from LB-agar plates and grown in LB media supplemented with 100µg/ml ampicillin antibiotic for pCEP-Pu/Ac7 transformed bacteria. Bacteria colonies transformed with pPICZAα were grown in low salt LB media supplemented with 25µg/ml zeocin antibiotic. Cells were grown overnight under rotation at 37^{o}C.

2.2.9 Miniprep Purification of Expression Vectors

Expression constructs were purified from the bacteria using the QIAprep Spin Miniprep Kit (Qiagen) according to the manufacturers instructions. A 10ml volume of overnight bacterial culture was pelleted by centrifugation at 10 000 *xg.* The cells were resuspended in a 250µl of buffer P1 (with RNase added) and 250µl of buffer P2 added. After 5 minutes, the reaction was quenched using 350µl of buffer N3. Cell debris was removed by centrifugation at 10 000 *xg* for 10 minutes and the resulting supernatant passed through a QIAprep spin column (Qiagen). The spin column was washed once with 750µl of PE

buffer and the purified construct eluted from the column using 20µl of DNAse-free sterile water.

2.2.10 DNA Sequencing of Expression Vectors

DNA sequencing reactions were prepared in a total volume of 10µl containing 5µM of forward sequencing primer and approximately 500ng of purified plasmid DNA. For sequencing of mammalian pCEP-Pu/Ac7 constructs, the pCEP forward sequencing primer was used (5'- AGAGCTCGTTTAGTGAACCG -3'). Sequencing of the pPICZAα vector used the 5'AOX1 sequencing primer (5' – GACTGGTTCCAATTGACAAGC – 3') which annealed in the 5' AOX1 promoter region, upstream of the open reading frame. These samples were sent to GATC Biotech (Cologne, Germany) using the LIGHTrun service for sequencing.

2.3 Recombinant Protein Expression in the HEK-293 EBNA Mammalian Cell Expression System

2.3.1 HEK-293 EBNA Cell Culture

Untransfected HEK293-EBNA cells were cultured initially in T75 and T225 culture flasks (Corning) using 10ml and 25ml of growth media (Dulbecco's Modified Eagles Media 4 (DMEM4) supplemented with 10% (v/v) Feotal Bovine Serum (FBS) and 1% (v/v) Penicillin Streptomycin Mixture) (Sigma). Cells were grown for 48 hours at 37^{o}C with 5% CO_2, until confluent. For passage, cells were washed in 10ml (for T75 cultures) or 25ml (for T225 cultures) of Phosphate Buffered Saline (PBS – Sigma) and detached by incubation at 37^{o}C with 2ml or 5ml (for T75 or T225 cultures respectively) trypsin-EDTA solution (Sigma). Trypsin was deactivated through addition of a 4-fold higher volume of growth media. The resulting suspended cells were seeded at a 1:5 dilution for further growth.

2.3.2 HEK-293 EBNA Transfection and Selection

Confluent HEK293-EBNA cells were diluted 1:40 in growth media and 1ml added to each well of a 6-well tissue culture plate. Cells were further supplemented with 1ml of growth media and were grown overnight at 37^{o}C with 5% CO_2 to 80% confluency. For transfection, 1µg of purified plasmid DNA was pre-incubated with 100µl of serum-free media (DMEM4 mixed in a 1:1 ratio with F12-HAMS supplemented with 5% (v/v) of Penicillin/Streptomycin mixture) and 5µl PLUS-reagent at room temperature for 15 minutes. Alongside this, an additional 100µl of serum-free media was incubated with Lipofectamine Plus reagent (Life Technologies) for 15 minutes. The DNA-Lipofectamine solutions were mixed for a further 15 minutes prior to addition to the cells. During this

preparation, cells were washed with 1ml of pre-warmed PBS and 800µl of serum-free media added. The Lipofectamine-DNA mixture was added directly to the cells, yielding a final volume of 1ml, which was incubated at 37^{o}C, 5% CO_2 for 3 hours. After incubation, cells were centrifuged at 1000 *xg* and resuspended in 5ml of growth media in a T25 cell culture flask (Corning). After growth, cells were subsequently passaged (as previously described in section 2.3.1) using trypsin into a larger T75 flask (Corning). After growth to 100% confluency, cell growth media supplemented with 2µg/ml puromycin was added to select for transformed cells.

2.3.3 Transfected HEK-293 EBNA Cell Storage

Following stable transfection of HEK-293 EBNA cells with the pCEP-Pu/AC7 vector, stocks were produced and stored for future work. A 100% confluent culture of transfected cells were treated with trypsin (as previously described), with the resuspension of the trypsin-cell suspension being carried out using freezing media (50% (v/v) DMEM-4, 40% (v/v) FBS, 10% DMSO and 1% (v/v) Penicillin/Streptomycin mixture). Aliquots (1ml) of the cell suspension were made and cells frozen.

2.3.4 HEK-293 EBNA Expression of Recombinant Protein

Previously stored HEK-293 EBNA cultures, cells were thawed rapidly at 37^{o}C and resuspended in 9ml of growth media in a T75 culture flask. Cells were grown at 37^{o}C with 5% CO_2 until 100% confluency was reached and the media then replaced with growth media supplemented with 2µg/ml puromycin to select for transformed cells. Cell population was increased through transfer of the cell population to a T225 culture flask followed by a HYPERflask or NUNC Triple Layer Flask. Once confluent, the media was changed to serum-free media.

2.3.5 Media Harvest and Processing

Conditioned media from confluent cells was removed every 72 hours and replaced with fresh media. Collected media was stored at -20^{o}C until required and thawed at room temperature overnight. Media was initially filtered using Whatmann No. 1 filter paper, then using a Millipore 0.65µm DVPP filter (under vacuum conditions) to remove finer particulate matter. Media was subsequently dialysed overnight into 10mM Tris pH 7.4, 150mM NaCl at 4^{o}C using VIS8 10000 MWCO dialysis membrane (Medicell International Ltd.).

2.4 Retinoschisin Expression in the *Pichia pastoris* X-33 Yeast Cell Expression System

2.4.1 Production of Electro-competent Pichia pastoris Cells

Stable transformation of the recombinant retinoschisin used the *Pichia pastoris* X-33 strain (Life Technologies). *P. pastoris* cells were initially grown on Yeast extract Peptone Dextrose (YPD) Agar plates (1% (w/v) yeast extract, 2% (w/v) peptone, 2% (w/v) D-glucose and 2% (w/v) agar) at 30^{o}C for 72 hours. A single colony was selected and grown in a 5ml liquid YPD culture overnight at 30^{o}C under rotation. This small overnight culture was used to inoculate a larger 500ml culture of YPD media. This was grown overnight to a cell density of approximately 5-7x10^{7} cells/ml. Cell were centrifuged at 3000 *xg* and the pellet resuspended in 100ml of YPD containing 200mM HEPES pH 8.0. Following resuspension, Dithiothreitol (DTT) was added to a final concentration of 25mM and cells incubated for 15 minutes at 30^{o}C. After incubation, 200ml of ice-cold 1M sorbitol was added to the cell suspension and the cells collected immediately by centrifugation at 3000 *xg* at 4^{o}C. This sorbitol resuspension and centrifugation step was repeated with the resulting cell pellet a further two times with decreasing volumes (100ml followed by 20ml) of 1M sorbitol. Following this step, the cell pellet was finally resuspended in 1ml of ice-cold 1M sorbitol, generating a highly turbid cell suspension of electro-competent cells at a density of approximately 1x10^{9} cells/ml.

2.4.2 Linearization of the pPICZAα Construct

For transformation, 1-5µg of pPICZAα construct was linearized with SacI-HF (New England Biolabs). The pPICZAα construct was incubated with 40U of SacI-HF enzyme in CutSmart buffer (New England Biolabs) and the volume adjusted to 50µl using sterile water. The reaction mixture was incubated for 2 hours at 37^{o}C.

The linearized construct was then purified from the reaction mixture using a QIAquick PCR Purification Kit (Qiagen) according to the manufacturers instructions. Briefly, a 5-fold greater volume of buffer PB was added to the restriction digest reaction mix. The resulting solution was passed through a QIAquick under centrifugation and the column washed in 750µl of buffer PE. The linearized DNA construct was subsequently eluted in DNAse-free sterile water.

2.4.3 Transformation of Electro-competent Pichia pastoris Cells

Pichia pastoris cells were transformed with linearized pPICZAα construct using electroporation. To this end, 1µg of linearized vector was incubated with 40µl of electro-competent *P. pastoris* cells (at a density of approximately 1x10^{9} cells/ml) on ice and mixed

gently for 10 mins. Cell-DNA suspension was transferred into a 0.2cm BioRad Micropulser electroporation cuvette and the cell suspension pulsed (using the BioRad micropulser) once for 5 milliseconds using the *Pichia pastoris* setting according to the manufactutrer's instructions. Electroporated cells were immediately resuspended in 1ml of ice-cold YPD media containing 1M sorbitol and transferred to a sterile microfuge tube.

2.4.4 Selection and Confirmation of Transformation

Electroporated colonies were spread on YPD-Agar plates supplemented with 1M sorbitol and 100µg/ml of zeocin antibiotic (Melford Laboratories) and grown at 30^{o}C for 48 hours. Colonies were picked and re-streaked on YPD-Agar plates containing 100µg/ml of zeocin and grown for a further 48 hours at 30^{o}C.

Zeocin-resistant colonies were grown overnight in 5ml of YPD media at 30^{o}C under rotation. Genomic DNA was isolated using a phenol-cholorform genomic DNA extraction. Cells were collected by centrifugation at 5000 *xg* and the pellet resuspended in 1ml of EB solution (containing 1M Sorbitol, 1mM EDTA and 30mM DTT). Then centrifuged and resuspended in 500µl of EB solution supplemented with 1mg/ml lyticase from *Arthrobacteur luteus* (Sigma). The reaction was incubated at 37^{o}C for 1 hour and the reaction quenched through addition of 55µl of STOP buffer (100mM Tris, 3M NaCl, 20mM EDTA, pH 7.5). DNA was extracted by addition of 500µl of 1:1 Phenol:Choloform mixture (Sigma) and mixed. Cell debris was removed through centrifugation and the top aqueous phase of the mixture transferred to a fresh microfuge tube. Another 500µl of Phenol:Cholorofom mixture was added to the aqueous phase and the centrifugation step repeated. The resulting aqueous phase was transferred to a new microfuge tube and 400µl of choloform added. The mixture was agitated then centrifuged as before. The top aqueous phase was transferred to another microfuge tube. To this, 100% ethanol was added and mixed with the aqueous phase to precipitate the DNA. The precipitated DNA was pelleted by centrifugation at 10 000 *xg* for 15 minutes at room temperature and the supernatant removed. The resulting DNA pellets were air-dried at room temperature then frozen at -20^{o}C. Following thawing of the frozen pellet, the DNA was resuspended in 20µl of sterile water and stored at -20^{o}C.

To confirm the presence of the expression cassette the 5' AOX1 forward primer (see previous) and 3' AOX1 reverse primer (5'-GCAAATGGCATTCTGACATCC-3') were used to amplify the AOX1 locus in the genomic DNA extracts using the PCR outlined in section 2.2.2. PCR amplification was carried out for 40 cycles with a final extension step of 7 minutes at 72^{o}C as a final step. As a control, the blank pPICZAα vector was also amplified to allow for detection of the band shift through comparison. PCR products were run on a

1% agarose gel at 120V for 45 minutes (see section 2.2.4). Sequences were confirmed using DNA sequencing from the 5' AOX1 forward primer (see section 2.2.10). Transformed cells with the correct sequence were grown in 5ml of YPD media overnight and 1ml of culture was transferred to a cryovial (Thermo-Fisher), sterile DMSO added to a final concentration of 10% (v/v) and frozen at -80^{o}C. For expression of the construct, the cells were grown on YPD plates supplemented with 100µg/ml of zeocin antibiotic. Cells were grown at 30^{o}C for 48-72 hours.

2.4.5 Growth and Retinoschisin Expression in Pichia pastoris

A streak of multiple transformed colonies inoculated 50ml of Buffered Glycerol Complex Media (BMGY) (1% (w/v) yeast extract, 2% (w/v) peptone, 1.34% (w/v) yeast nitrogen base, 100mM potassium phosphate pH 6.0 and 1% (v/v) glycerol). Cells were grown overnight at 30^{o}C at 180rpm rotation and subsequently transferred to 500ml BMGY media. Cells were grown for 12-18 hours at 30^{o}C and 180rpm until the optical density at 600nm (OD_{600}) was greater than 5. Cells grown in BMGY were collected through centrifugation at 3000 *xg* and the cell pellet resuspended in 4l of Buffered Methanol Complex Media (BMMY) (1% (w/v) yeast extract, 2% (w/v) peptone, 1.34% (w/v) yeast nitrogen base, 100mM potassium phosphate pH 6.0 and 0.5% (v/v) methanol). The BMMY media was divided equally into 500ml volumes in baffled 2l culture flasks at an initial OD_{600} between 1 and 2 (in each 500ml culture) and cells grown at 30^{o}C and 180rpm for 96 hours with methanol injected into the culture every 24 hours to maintain a constant concentration of 0.5% in the induction media. Cells were pelleted, supernatant collected and cleared by filtration and then dialysed as detailed in section 2.3.5.

2.5 Protein Purification from Processed Media

2.5.1 Nickel Affinity Protein Purification

Media from both HEK293-EBNA and *P. pastoris* expression systems underwent the same purification procedure. Media was purified using a His-Trap FF 5ml column (GE Healthcare), which had been washed and pre-equilibrated with 10 column volumes of 'Binding Buffer' (20mM Tris pH 8.0, 500mM NaCl, 25mM Imidazole). Using an AKTA prime FPLC system, media was passed over the column at 15ml/min. The column was then washed with 100ml of Binding Buffer at 5ml/min. 50ml of Elution Buffer (20mM Tris pH 8.0, 500mM NaCl, 500mM Imidazole) was passed over the column at 0.5ml/min and 1ml elute fractions collected and monitored using the absorbance at 280nm (A_{280}). Peak fractions observed in the A_{280} spectrum were pooled and further concentrated using a Vivaspin-6 centrifugal concentrator 10 000 MWCO (Sartorius) to 1.0ml volume.

2.5.2 Size Exclusion Chromatography (SEC)

Concentrated sample was injected onto a Superdex 75 10/300L column controlled by an AKTA purifier system. The column was initially equilibrated using 30ml of 10mM Tris pH 7.4, 150mM NaCl. 1ml of sample was injected onto the column and passed at 0.5ml/min in 10mM Tris pH 7.4, 150mM NaCl. Eluted volume was collected in 0.5ml fractions with protein elution monitored using A_{280}.

2.6 Assessment of Protein Purity and Protein Identification

2.6.1 Sodium Dodecyl Sulphate Polyacrylamide Gel Electrophoresis (SDS-PAGE)

Concentrated (4x) LDS NuPAGE Buffer (Life Technologies) was diluted 1:4 into the sample. The sample was loaded onto a 4-12% NuPAGE SDS-PAGE gel (Life Technologies). Electrophoresis was carried out at 180V at room temperature for 1 hour with 50mM MOPS, 50mM Tris, 0.1% (v/v) SDS, 1mM EDTA, pH 7.7 running buffer in an X-Cell Surelock Minicell electrophoresis system (Life Technologies). Assessment of molecular weight was performed using Seeblue Plus2 pre-stained protein standard (Thermo-Fisher) with protein visualized using Instant Blue (Expedion) as directed by the manufacturer instructions.

2.6.2 Western Blotting

SDS-PAGE gels were transferred to a nitrocellulose membrane (Whatmann) at 35V for 70 minutes at room temperature using an X-Cell Surelock Minicell system (Life Technologies). Protein transfer was performed in Tris-glycine transfer buffer (96mM Tris-HCL, 780mM glycine, 0.075% (v/v) SDS with 20% (v/v) methanol). Immediately after transfer, the membrane was blocked at room temperature with 5% (w/v) milk solution. Blots were probed with a monoclonal mouse anti-His_6 antibody (MAB050, R&D Systems) diluted 1:1000 in 5% (w/v) milk solution in TBST overnight at 4^oC. Following this washed three times in TBST and incubated with an anti-mouse HRP-conjugated secondary antibody (R&D Systems) at 1:4000 dilution in 5% (w/v) milk solution in TBST for 1 hour at room temperature. Blots were then further washed three times using TBST solution. Visualization of the blot was performed using Uptilight US Chemiluminescence ECLmax solution (Interchim) and the ChemiDoc Imaging System (BioRad).

2.6.3 Mass Spectrometry Protein Identification

Samples were submitted to the University of Manchester Mass Spectrometry Core Facility (Michael Smith Building, University of Manchester, Oxford Road, M13 9PL). Protein bands

were excised from SDS-PAGE, trypsin digested and analysed using the HCT Ultra (Bruker Daltonics).

2.6.4 Mass Spectrometry Intact Mass Determination

Intact mass determination of purified retinoschisin protein was performed at the University of Manchester Mass Spectrometry Core Facility (Michael Smith Building, University of Manchester, Oxford Road, M13 9PL). Protein sample was submitted to the service in a 20µl volume of 10mM Tris pH 7.4, 150mM NaCl buffer at 0.3mg/ml concentration.

2.6.5 Protein Concentration Determination

UV absorbance of protein solutions was measured using a Nanodrop-1000 spectrophotometer (Nanodrop) at 280nm wavelength. Protein concentration was estimated using the Beer-Lambert Law (A=εcl) where A is absorbance at 280nm wavelength, ε is the molar extinction coefficient ($M^{-1}cm^{-1}$), c is equal to the concentration in mols and l is the path length of the measurement (cm). An extinction coefficient of 63 535 M^{-1} cm^{-1} was calculated from the protein sequence using the Protparam programme available on the ExPasy website (http://web.expasy.org/protparam/).

2.7 Biophysical Characterisation

2.7.1 Multi-Angle Light Scattering (MALS)

Octamer samples of 0.5ml volume were analysed using a Superdex200 10/300GL column (GE Healthcare) and monomer samples analysed using a Superdex75 10/300GL. Columns were run at 0.75ml/min in 10 mM Tris pH 7.4, 150 mM NaCl and passed through a Wyatt DAWN Heleos II EOS 18-angle laser photometer coupled to a Wyatt Optilab rEX refractive index detector. Resulting hydrodynamic radii and molecular mass measurements were analysed using Astra 6.

2.7.2 Analytical Ultracentrifugation (AUC)

Both wild-type and R141H retinoschisin octamer and monomer samples (0.1mg/ml) were analysed using a XL-A centrifuge (Beckman). Samples in 10mM Tris pH 7.4, 150mM NaCl were centrifuged simultaneously at 45, 000rpm in an An60Ti-4 Hole rotor at 20^{o}C with the sedimenting boundary monitored at 230nm every 180 seconds for 250 scans. Data was analysed using continuous model-based distribution of Lamm equation solutions (C(s)) using the Sedfit software suit (Schuck 2000). Resulting apparent sedimentation

coefficients were corrected for solvent conditions using Sednterp, giving R_h and f/f_0 values for each construct (Laue, Shah et al. 1992).

2.7.3 Small Angle X-Ray Scattering (SAXS)

Data were collected at BM29 beamline, European Synchotron Radiation Facility, Grenoble, France. Data for wild-type retinoschisin monomer and C40S/C59S/C223S retinoschisin monomer were collected at 1.9 and 1.1 mg/ml, respectively with a BioSAXS automatic sample changer. In contrast, data were collected on the discoidin domain (50 µl at 1mg/ml) using inline SEC-SAXS with a Superdex200 Increase 3.2/300 at 0.1ml/min in 10mM Tris pH 7.4, 150mM NaCl, with protein elution monitored using A_{280}. For both SEC-SAXS and batch mode, data were collected using the Pilatus 1M detector at a 2.8m distance, using a q-range between 0.01 and 5 nm^{-1}. Data were reduced using in-house software and buffer subtraction and analysis was performed using the ScÅtter software package (http://www.bioisis.net/). Volumetric bead modelling of the SAXS data was carried out using the DAMMIF (Dummy Atom Model Minimisation Fast) program in the ATSAS package (Franke and Svergun 2009). Initially, 17 runs of DAMMIF were carried out. The resulting models were compared to generate an averaged and filtered model using the DAMAVER software suite in ATSAS (Volkov and Svergun 2003).

2.7.4 Negative-Stain Electron Microscopy and Image Processing

Carbon coated 400 mesh copper grids (Electron Microscopy Sciences) were glow discharged at 25mA for 25 seconds using a K100X Glow Discharger (EMITECH). After glow discharging, 3µl of 20µg/ml of purified wild-type or R141H octamer was adsorbed onto the surface of the grid for 60 seconds. Following adsorption, the grid was washed with 60µl of 2% Uranyl Acetate solution and blotted dry. The sample was analysed using a FEI Tecnai 12 Biotwin electron microscope equipped with a tungsten filament (for the wild-type data) or a LaB_6 (for the R141H and H207Q data sets) electron source operating at 120kV. Images were recorded under low dose conditions, using the FEI low dose mode available in the FEI Tecnai 12 electron microscope. Low dose imaging allows for imaging of the sample at the desired defocus value without pre-exposure of the sample through focusing of the beam onto the sample. The sample is only exposed by the beam upon image capture. This is important as it both prevents the destruction of high frequency features (particularly in unstained specimens) and the artefactual redistribution of stain in negatively stained samples (Unwin 1974, Orlova and Saibil 2011). In the low dose imaging, the grid was first searched at low magnification (3200x) in the search mode which allowed for searching of the grid whilst exposing the sample to a very low electron dose spread across a large grid area. Following identification of a suitable area, the microscope was focused at higher magnification (67,000x) using the focus option, which

moved the beam onto an adjacent area, preventing pre-exposure of the sample. The microscope was focused on the carbon support, allowing for selection of the correct defocus for imaging. This was then followed by exposure mode, which moved the beam back to the previously unexposed region of interest and an exposure taken at a nominal magnification of 23 000x onto a 2,048 x 2,048 pixel Charge Coupled Device (CCD) camera, giving a sampling of 3.5Å/pixel at the specimen level for wild-type and R141H particle sets, with H207Q particles imaged with a sampling of 2.8 Å/pixel. During this low dose mode imaging, search, focus and exposure parameters were stored to allow for efficient imaging of multiple grid areas. Due to observed particle anisotropy, images were recorded with 0^o, 5^o and 10^o α-tilts at between -0.5µm and -5µm defocus range to generate the wild-type particle set.

Micrographs were analysed using the EMAN 2.0 software suite (Tang, Peng et al. 2007). Particles were manually picked using *e2interactiveboxer.py* using a box size of 33nm for wild-type and R141H particle sets and 35nm for H207Q octamer particles. Particles were subsequently Contrast Transfer Function (CTF) corrected and a particle set generated, containing 6665, 10,108 and 1985 particles for wild-type, R141H and H207Q octamers respectively. Sets were subsequently aligned and averaged using the reference-free classification functionality in the *e2classaverage.py* program to generate class sum images used to interrogate the structure. Due to observed particle anisotropy it was not possible to generate a three-dimensional angular reconstruction.

2.7.5 Preparation of Grids for Cryo-EM Analysis

C-Flat 2-2 copper grids were initially glow discharged at 25mA for 25 seconds using a K100X Glow Discharger (EMITECH). 3µl of protein (0.1mg/ml) was adsorbed onto the grid for 1 minute at 100% humidity. Using a FEI Vitribot, grids were blotted dry for 8 seconds and plunge frozen into liquid ethane. Grids were immediately transferred to liquid nitrogen for imaging. For wild-type, R141H and H207Q retinoschisin, grid preparation was carried out at the same protein concentration, in the same buffer onto C-Flat 2-2 grids using this protocol.

2.7.6 Direct Electron Detection Device (DDD) Cryo-EM Microscopy

The wild-type retinoschisin octamer was imaged (using low dose) in an FEI Tecnai F30 coupled with a Gatan Quantum K2 Summit direct electron counting camera. Images were recorded at 59 000x nominal magnification, giving a pixel size of 0.8Å/pixel at the specimen level. 120 movie mode images were recorded in which the sample was irradiated with a total dose of $25e^-/Å^2$ for 25 frames at 0.1 second/frame over a defocus range of –1µm to –4µm. For the R141H retinoschisin octamer, images were recorded at

the electron Bio-Imaging Centre (eBIC) using an FEI Titan Krios equipped with a Gatan Quantum K2 Summit detector. Images were recorded (using a low dose protocol) with EPU (FEI) at 105 000x nominal magnification in EFTEM, giving a pixel size of 1.29 Å/pixel at the specimen level. A 20eV energy-selecting slit was used for zero-loss imaging and seven second exposures were fractionated into 500ms frames using a dose rate of $5e^-$ /pixel/second for a total dose of $40e^-/Å^2$. A defocus range between -1 to -4.5µm was used to record 1200 movie mode images which were subsequently used for structural analysis.

2.7.7 DDD Image Analysis

Movie exposures were stacked and particle drift corrected using the MotionCorr program (Li, Mooney et al. 2013). 120 movie mode images where collected for the wild-type data set, with 1200 movie mode images collected for the R141H mutant. First and last 6 frames were discarded from further evaluation in the wild-type data set, with only frames 2-8 (giving a half total dose of $20e^-/Å^2$) were selected for the R141H mutant. Wild-type images were 2x2 Fourier binned in MotionCorr to 1.6Å/pixel and unbinned data (1.29Å/pixel) used for R141H structural analysis. The motion corrected micrographs were analysed using EMAN2.0 software suite. Particles were selected using *e2interactiveboxer.py* using a box size of 21nm for the wild-type and 33nm for R141H molecules, generating particle sets of 14,614 and 13,343 particles for wild-type and R141H data sets respectively. To build an initial model used for RELION processing, picked particles were CTF-corrected using *e2ctf.py* and analysed in two dimensions using reference-free class averaging facilitated by the *e2classaverage.py* functionality in EMAN2.0. 130 classes were generated for each particle set, showing clear two stacked octameric rings. These reference-free class averages were used to generate a D8 symmetrical initial model in EMAN2.0 which was further refined using *e2refine.py.* Using phase-flipped particles, the model was subject to 6 refinement iterations using D8 symmetry and the Fourier Ring Correlation (FRC) comparator with 40% of the lowest quality particles discarded by the refinement procedure to minimize the effects of poor quality particles and the final model produced. This model was used as a reference for three-dimensional classification in RELION 1.4.

Further data analysis was performed using RELION 1.4 (Scheres 2012). As in EMAN2.0, particles were CTF-corrected but this time using CTFFIND4 (Mindell and Grigorieff 2003). Particles were classified using RELION 1.4 for 25 iterations, generating final class averages of the data set. Both wild-type and mutant data sets underwent 5 rounds of class averaging to minimize particle heterogeneity and remove ‘bad’ or damaged particles (discarding 11,829 and 5614 particles for wild-type and R141H particle sets, respectively). At an intermediate stage before further analysis, particles were centered using the python script recenter.py before further refinement was performed (Rawson, Iadanza et al. 2016).

Wild-type particles were three-dimensionally classified into 2 classes using C8 symmetry for wild-type particle set, generating classes for the octamer (1320 particles) and dimer of octamers (1465 particles). No single stack octamers were observed following class averaging of the R141H particle set. Therefore D8 symmetry was used for three-dimensional classification into two classes. Variation was only observed in the disordered central region, which was subsequently masked out during refinement using a soft-Gaussian mask generated in RELION 1.4, therefore a single D8 symmetrical three-dimensional class (class 2) was refined against the entire particle set which had shown high homogeneity in the discoidin domain regions of the protein (containing 7056 particles). Refinement of each class against the particles which clustered into it produced identical structures at lower resolution (Appendix 5).

Taking a single three-dimensional class as an initial model in each instance, three-dimensional refinement was carried out using RELION refine3D starting from a 30Å filtered initial model generated during the initial three-dimensional classification procedure from the EMAN reference. Refinement was followed by post-processing, with the R141H map further improved at this stage through addition of the Gatan K-2 Summit detector Modulation Transfer Function at 300kV. The final resolution for each map refined in RELION 1.4 was determined using the Fourier Shell Correlation (FSC) at the 0.5 and 0.143 criterion.

2.7.8 ResMap Local Resolution Calculation

Local resolution in resulting maps was further analysed using ResMap-H2 (Kucukelbir, Sigworth et al. 2014). Unfiltered half models generated during the refine3D refinement procedure in RELION 1.4 were input as split models and the local resolution variation across the map calculated. Evaluation of the local resolution distribution was performed using UCSF Chimera (Pettersen, Goddard et al. 2004).

2.7.9 Homology Modelling

A homology model of the retinoschisin discoidin domain (both wild-type and R141H mutant) was constructed using the Phyre2 Protein Fold Recognition Server (Kelley, Mezulis et al. 2015). The sequence of the retinoschisin both the wild-type and R141H mutant Discoidin domain (residues 63-219) were input in intensive mode. Six sequences were used to model the domain; coagulation factor V chain b (1SDD), epithelial discoidin domain-containing receptor 1 chain a (4AG4), coagulation factor VIII light chain (3CDZ), galactose-binding domain-like discoidin domain (1CZS), chain b, coagulation factor VIII (2R7E) and neuropilin 1 chain b (4DEQ). Known disulphide bonds were inserted and the model energy minimized using the UCSF Chimera suite (Pettersen, Goddard et al. 2004).

2.7.10 Model Fitting and Quasi-Atomic Model Generation

Domain fitting was carried out using DockEM for both the wild-type and R141H structures (Roseman 2000). Cryo-EM determined wild-type and R141H maps were Fourier filtered using the Mapfilter2 program in the DockEM software suite, filtering the wild-type and R141H maps to 9.5Å and 4.5Å respectively to prevent over-fitting. The wild-type and R141H discoidin domain homology models were converted to electron densities (filtered to the same resolution as their respective maps) representing the original atomic model using the goMakedensity.com script available in the DockEM software package. For wild-type docking, the atomic model density was filtered to 9.5Å, with filtering to 4.5Å used for fitting to the R141H structure. The fitting was carried out as a global search of the entire density of the map, searching at 4^{o} angular increments. Fits were ranked according to the correlation value calculated for the fit of the search object to the map and the number of standard deviations this value was above the mean correlation across the 200 fits calculated during the search. To confirm handedness of each model, fitting the discoidin domain homology model to both the initial hand produced and the opposing hand was performed, with the correlation values and the statistical significance of the fits compared. Furthermore, fits were visually inspected using UCSF Chimera.

2.7.11 FlexEM Flexible Fitting into the R141H Hexadecamer Structure

Flexible fitting of the R141H Discoidin domain homology model was carried out using the FlexEM program (Topf, Lasker et al. 2008). The rigidly fitted domain was subject to 4 rounds of molecular dynamics simulated annealing refinement to a map at 4.2Å resolution, followed by energy minimization in UCSF Chimera. The flexibly fitted subunit was then further optimized through symmetrical fitting to preserve the eight-fold symmetry in the subsequent quasi-atomic model. The final correlation value at 4.2Å resolution was measured using UCSF Chimera.

2.7.12 PDBePISA Interface Analysis

Two models were selected from the intra-octamer and inter-octamer interface between 2 fitted Discoidin domains within the hexadecameric retinoschisin structure. The interfaces between each subunit were identified using the PDBePISA webserver (Krissinel and Henrick 2007) (http://www.ebi.ac.uk/pdbe/pisa/) that identified residues involved in the interface according to the proportion of surface area each residue had buried in the interface.

2.7.13 OPTIM Denaturation and Aggregation Analysis

Monitoring of protein stability using barycentric mean fluorescence (BCM) measurements and aggregation (using static light scattering at 473nm wavelength) was carried out using the OPTIM1000 (Avacta Analytical). 9µl of 0.1mg/ml protein solution in 10mM Tris, 150mM NaCl at pH7.4 was placed in an OPTIM microcuvette and the protein initially incubated at 20^{o}C. Temperature was increased at 1^{o}C intervals to 90^{o}C, with the intrinsic fluorescence of the sample between 330 and 350nm monitored to observe protein unfolding. Simultaneously the light scattering of the protein at 473nm wavelength monitored to identify the onset of aggregation.

2.7.14 Differential Scanning Fluorimetry (DSF)

Measurements were carried out using a 96-well, white, low profile plate (Bio Rad) loaded into a CFX96 Real Time PCR Detection system (Bio Rad). Measurements were made in a total volume of 10µl consisting of 9µl of wild-type or R141H octamer or monomer at 0.1mg/ml concentration with 1µl of Sypro Orange (Life Technologies) at a final concentration of 10x. Samples were equilibrated at 20^{o}C for 2 minutes and then temperature incrementally increased by 1^{o}C and equilibrated for 30 seconds prior to the measurement. The cycle concluded with a final denaturation hold at 100^{o}C for 2 mins. All fluorescence measurements were carried out in the HEX channel and T_m was calculated using the CFX manager software (Bio Rad).

2.7.15 Intrinsic Fluorescence Spectroscopy

Intrinsic fluorescence measurements were carried out on 12µg of purified wild-type and R141H retinoschisin monomers at 0.1mg/ml in 120µl of 10mM Tris pH7.4, 150mM NaCl at 20^{o}C. Three-dimensional spectra were measured using a Horiba Fluoromax flourimeter (Horiba). Wavelengths ranging from 240nm to 305nm were used for excitation and emission spectra recorded between 310nm and 420nm. Scanning through both the excitation and emission spectra was performed at 2nm increments. Two-dimensional spectral comparison was performed at 295nm excitation wavelength to minimize the effect of tyrosine fluorescence upon the comparison.

3 Results Chapter 1: Nano-scale Structure of the Retinoschisin Monomer

In order to structurally characterise retinoschisin and gain insight into both the assembly and the effects of XLRS-associated mutations on the structure, wild-type retinoschisin monomer structure was first investigated. To this end, retinoschisin was purified from a HEK293-EBNA stably expressing cell line and subsequently characterised using both hydrodynamic measurements (including size-exclusion chromatography multi-angle light scattering (SEC-MALS), analytical ultracentrifugation (AUC)) and Small-Angle X-Ray Scattering (SAXS).

3.1 Expression and Purification of Wild-Type Retinoschisin

The study of retinoschisin structure was performed using a recombinant retinoschisin construct (Figure 3.1A). Expression was driven in the pCEP-Pu/AC7 expression vector in the HEK293-EBNA cell line using the Cytomeglavirus (CMV) forward promoter. The construct was secreted using the BM40 signal sequence which was subsequently cleaved, producing retinoschisin containing the N-terminal Rs1 domain, discoidin domain and small C-terminal extension. To allow for detection and purification of the retinoschisin protein, the sequence was tagged with a His_6-tag at the extreme C-terminus, after a thrombin cleavage site (LVPRGS). Retinoschisin was purified from the media using nickel-affinity chromatography. Shown in figure 3.1B, nickel affinity chromatography was able to bind a protein of approximately 25 kDa, which was not removed by the washing procedure. An additional band is observed in the elute fraction migrating between 150 and 250 kDa, which may potentially represent an assembled octameric complex of retinoschisin. Sequence analysis revealed a lack of N-linked glycosylation sites in the retinoschisin sequence (Sauer, Gehrig et al. 1997) with close agreement observed between the determined molecular weight and the mass derived from the protein sequence. In order to confirm that the species did not show any N-linked glycosylation, PNGaseF digestion of the retinoschisin monomer under both reducing and non-reducing conditions was performed. Shown in figure 3.1C, treatment of retinoschisin with PNGaseF did not lead to a mass change in the protein, confirming the absence of glycosylation. Finally, to confirm the identity of the expressed protein, tryptic-digest mass-spectrometry was performed on the species migrating at approximately 25 kDa. Mass spectrometry (Figure 3.1D) confirmed the identity of the species as retinoschisin with high confidence and 54% peptide sequence coverage, confirming the successful expression and purification of retinoschisin.

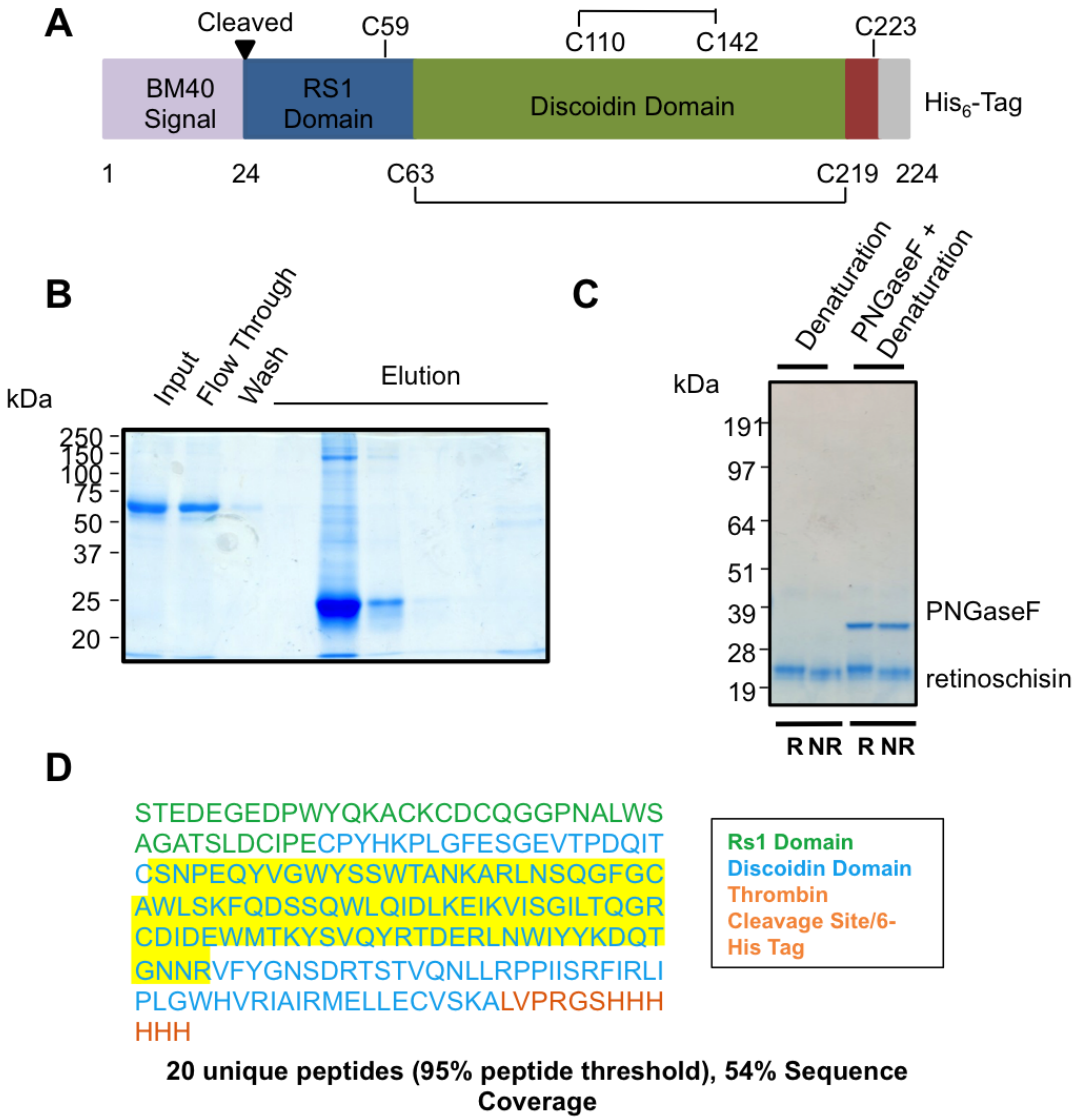

Figure 3.1 – Purification of wild-type retinoschisin from HEK293-EBNA cell system. (**A**) Schematic of the retinoschisin construct used, showing the positions of the domains. Intramolecular disulphides are marked with a (-) and residues required for disulphide-mediated octamerisation are marked. (**B**) Coomassie-stained reducing SDS-PAGE of Ni-NTA purification of recombinant, wild-type retinoschisin showing input, flow through, wash and elution fractions. (**C**) PNGaseF digestion of purified retinoschisin monomer. SDS-PAGE was carried out under reducing (R) and non-reducing (NR) conditions to ensure protein denaturation. (**D**) Tryptic-digest mass spectrometry identification of the major purified species, confirming retinoschisin identity. Shown in yellow are the peptides observed during mass spectrometry analysis.

Previously, retinoschisin had been demonstrated to be secreted *in vivo* as a disulphide-stabilised octameric complex, with loss of this complex associated with the development of XLRS (Wu, Wong et al. 2005). In order to determine if the purified construct was able to assemble into this state, thus producing a functional protein analogous to that found *in vivo*, the oligomerisation of the construct was investigated. SDS-PAGE analysis under both reducing and non-reducing conditions confirmed that in the absence of β-mercaptoethanol (β-MeOH), retinoschisin was secreted from the HEK293-EBNA cell system as three principal species migrating at approximately 200, 40 and 20 kDa, consistent with the expression of monomeric, dimeric and octameric species. Addition of the β-MeOH reducing agent caused a loss of these higher species, with only a single

band at approximately 25 kDa, suggesting that formation of these higher order oligomers was dependent upon disulphide-bonding (Figure 3.2A). Furthermore, reduction of the monomeric species induced an upward band-shift for this protein, suggesting that the presence of the disulphide bonds within the monomer allowed the retinoschisin sequence to fold into a more compact conformation, as has been previously reported (Wu, Wong et al. 2005). Such disulphide–dependent folding (between C63 and C219) has previously been shown important in the folding of the retinoschisin discoidin domain (Wu and Liu 2012). Anti-His_6 western blotting confirmed that all species observed contained a His-tag, suggesting that they are formed solely from recombinantly expressed retinoschisin (Figure 3.2B) with SEC-MALS analysis confirming the presence in solution of three distinct species with molecular weight of approximately 200, 54 and 27kDa respectively. This is in good agreement of the predictions from sequence of the mass of octamer, dimer and monomer species of retinoschisin (Figure 3.2C). Together, these data confirm the expression, secretion and purification of retinoschisin octamer, dimer and monomer species. The disulphide-dependent folding and oligomerisation observed further suggested that the protein folded in a native manner, producing a functional retinoschisin variant which was consistent with the retinoschisin observed *in vivo*.

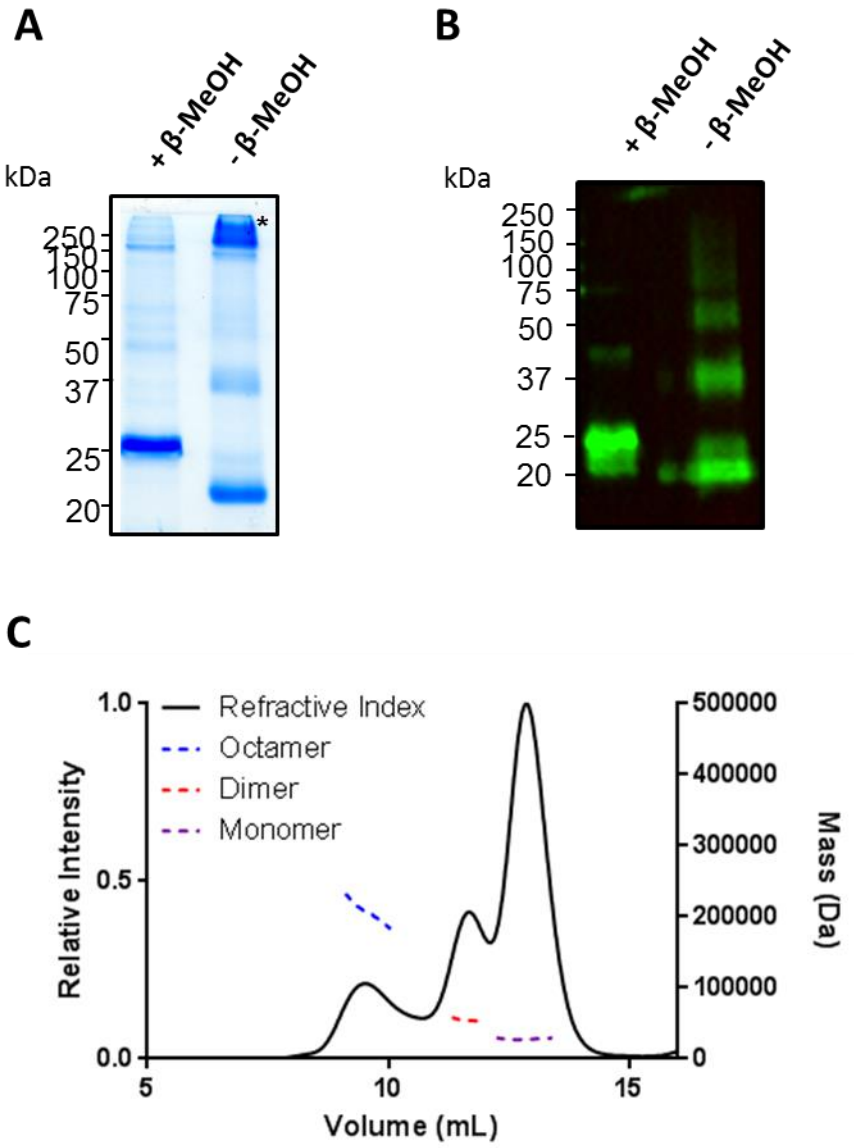

Figure 3.2 – Purified retinoschisin forms disulphide-dependent dimers and octamers. (**A**) Coomassie-stained SDS-PAGE analysis of Ni-NTA affinity chromatography-purified retinoschisin. Samples were run in the presence (+) or absence (-) of β-mercaptoethanol (β-MeOH). Disulphide-dependent higher order oligomer formation is highlighted by (*). (**B**) Anti-His western blotting analysis of Ni-NTA affinity chromatography purified retinoschisin in the presence (+) or absence (-) of β-mercaptoethanol (β-MeOH). (**C**) SEC-MALS purification of Retinoschisin, showing separation of Octamer, Dimer and Monomer oligomers with molecular weights of approximately 200 kDa, 54 kDa and 27 kDa respectively.

3.2 The Solution Structure of the Wild-Type Retinoschisin Monomer

3.2.1 Hydrodynamic Analysis of the Wild-Type Retinoschisin Monomer

Purification of the retinoschisin monomer allowed for insight into the organization of the protein sequence and the structure retinoschisin adopts in solution. Initially, the protein was characterised hydrodynamically using SEC-MALS (Figures 3.3Ai and Aii) and AUC (Figures 3.3Bi and Bii). Together, these analyses were consistent, reporting similar

molecular mass estimates and Hydrodynamic Radii (R_h) of 2.8nm and 2.4nm for SEC-MALS and AUC respectively. Together, with an f/f_0 value (Perrin factor) of 1.21 determined via AUC (Figure 3.3Bii), suggesting a globular protein fold.

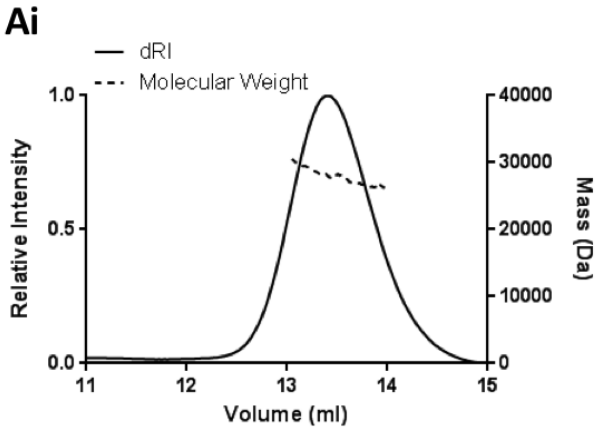

Aii

Molecular Weight (kDa)	27
Hydrodynamic Radius (nm)	2.8
Polydispersity	1.002

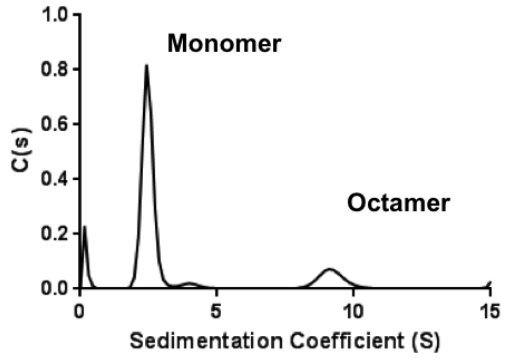

Bii

Molecular Weight (kDa)	25
Sedimentation Coefficient ($S_{(20,w)}$)	2.6
Hydrodynamic Radius (nm)	2.4
f/f_0	1.21

Figure 3.3 – Hydrodynamic analysis of purified wild-type retinoschisin monomer. (**Ai**) SEC-MALS analysis of wild-type retinoschisin monomer. (**Aii**) Extracted hydrodynamic values from SEC-MALS analysis. (**Bi**) Sedimentation velocity AUC analysis of wild-type retinoschisin monomer analysed using model-based continuous distribution (C(s)). (**Bii**) Hydrodynamic parameters obtained from AUC analysis.

3.2.2 SAXS of the Wild-Type Retinoschisin Monomer

To further investigate the structure of the retinoschisin monomer sequence, SAXS analysis was employed. The one-dimensional scatter profile of the log of the intensity of X-Ray scatter (LogI(q)) expressed in reciprocal space as a function of the scattering vector q ($Å^{-1}$) is shown in figure 3.4A for purified retinoschisin monomer. Due to high noise in the high q range, reliable points between $0.025Å^{-1}$ and $0.23Å^{-1}$ q were used for subsequent SAXS analyses.

The Guinier region for retinoschisin was highly linear (Figure 3.4Bi) as shown by the low residuals recorded for the fitted line (Figure 3.4Bii). Such straight-line character is also indicative of a monodisperse system, with no observed aggregation or repulsive interactions in the low q region of the curve. This analysis reported an R_g value of 31.6Å, a relatively large value for a 24 kDa single-domain protein, suggesting an elongated state.

This shape was further analysed using a dimensionless Kratky plot (Figure 3.4C). The R_g-normalized Kratky plot for the retinoschisin monomer reveals the peak in the low q range, confirming the folded character of the protein (Figure 3.4C). However, this peak in the normalized analysis does not occur at the 1.1 vs. $\sqrt{3}$ crosshairs. A peak at this point is indicative of a spherical protein system, with the displacement of the peak in the retinoschisin Kratky plot away from this point suggestive of an extended conformation (Durand, Vives et al. 2010).

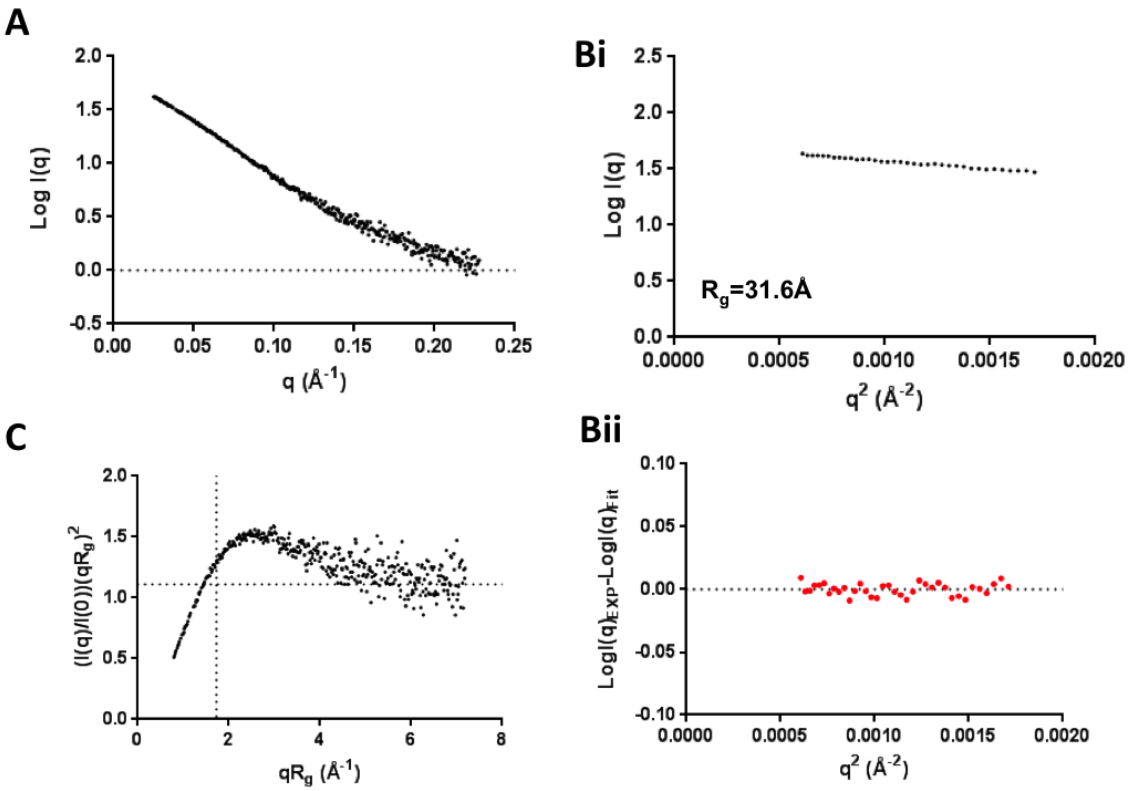

Figure 3.4 – SAXS analysis of purified wild-type retinoschisin monomer. (**A**) One-dimensional SAXS profile showing the log of X-ray scattering intensity (LogI) as a function of the scattering vector q. (**Bi**) Guinier plot (LogI vs. q^2) of the low q region, showing a Radius of Gyration (R_g) value of 31.6 Å for the wild-type retinoschisin monomer. (**Bii**) Plotted residuals ($LogI(q)_{EXP}$-$LogI(q)_{FIT}$) for the Guinier region. (**C**) Normalized Kratky plot ($(I(q)/I(0))(qR_g)^2$ vs. qR_g) showing a folded peak. Shown are the cross-hairs for globularity of the protein fold (1.1 vs. √3), this plot suggests a folded, elongated structure.

3.2.3 Shape Determination and Volumetric Modelling of Wild-Type Retinoschisin Monomer from SAXS Analysis

Further structural parameters were extracted from the SAXS experiment. A Fourier transform of the scatter profile allows for the range of different intramolecular distances and their relative proportions to be determined. This pair distance distribution function (P(r)) allows for the determination of the D_{max} or the maximum dimension of the protein molecule (the point at which the probability of finding any greater lengths within the molecule drops to zero) (Putnam, Hammel et al. 2007, Mertens and Svergun 2010). The P(r) distribution calculated for the retinoschisin wild-type monomer using the GNOM

functionality (Svergun 1992) in the ATSAS suite (Figure 3.5A) revealed a D_{max} of 108Å, with the P(r) shape suggesting the presence of a single globular region attached to a smaller yet more extended section, as shown by the tail in the P(r) with a smaller proportion of larger molecular dimensions. Inverse Fourier transform of the P(r) distribution revealed a regularized scatter profile which agreed well with the experimental scatter profile (Figure 3.5B). Further structural analysis employed *ab initio* volumetric automated bead modelling to reconstruct the scatter profile. Employing DAMMIF (Dummy Atom Model Minimization Fast) (Franke and Svergun 2009) using 17 iterations, the final averaged and filtered model revealed a globular yet elongated character with a single flat globular region attached to a smaller, more extended region (Figure 3.5C). For the 17 iterations, the Normalized Spatial Discrepancy (NSD) (Volkov and Svergun 2003) was 0.5855 (<0.7) indicative of a unique solution and unambiguous result. Furthermore, the theoretical scatter curve (Figure 3.5Di, shown in red) fitted well with the experimental data, revealing small, symmetrical residuals between the fit and the experimental data over the q range used with a X^2 value of 0.71 (Figure 3.5Dii). To further corroborate the observed structure, HYDROPRO solution modelling was performed on the SAXS DAMMIF bead model (de la Torre, Huertas et al. 2000). HYDROPRO analysis predicted a sedimentation coefficient of 2.3S for the DAMMIF model. This is highly similar to the sedimentation coefficient observed for AUC experiments, therefore suggesting the SAXS model recapitulates the low resolution solution structure of the retinoschisin monomer.

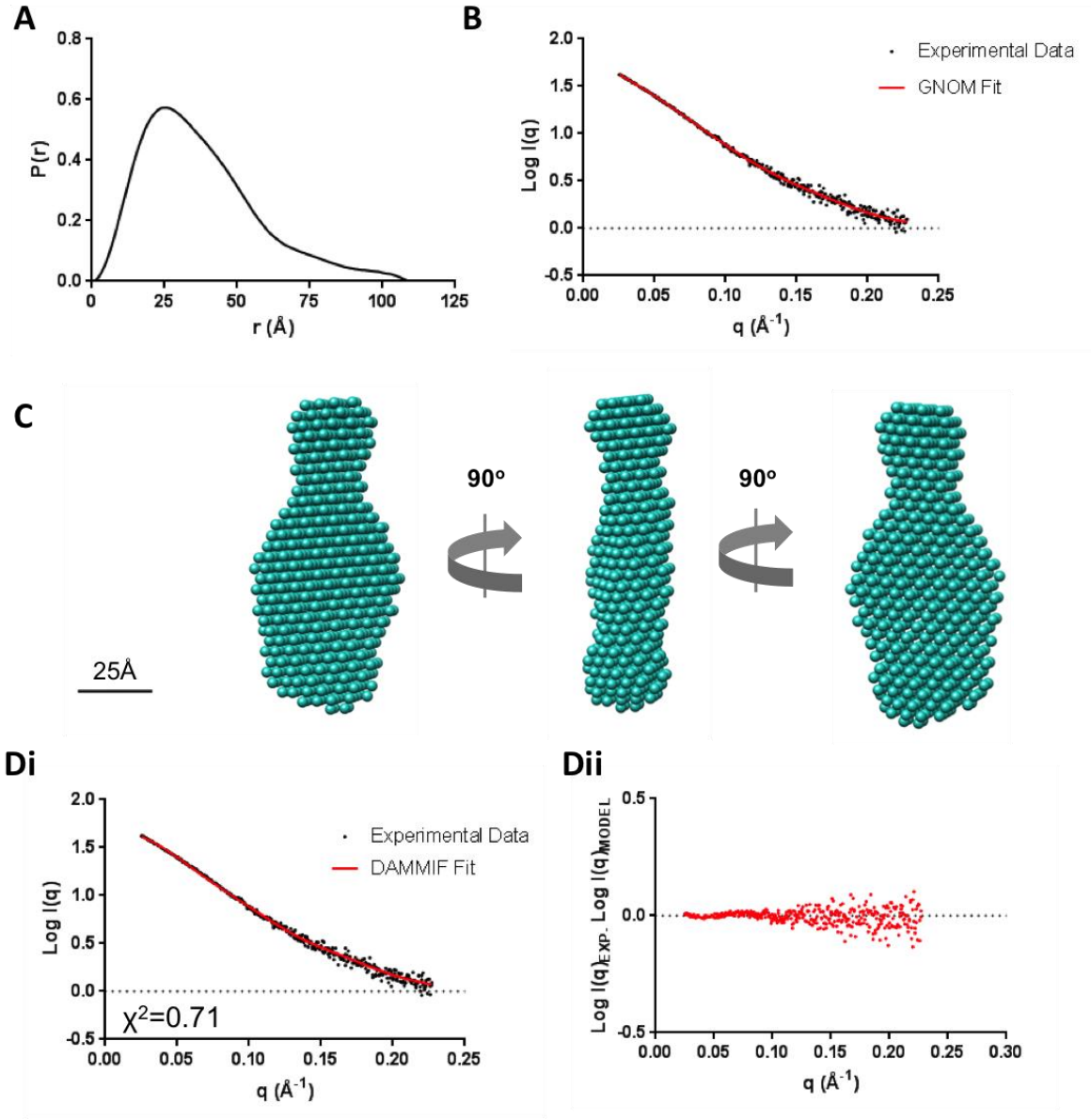

Figure 3.5 –SAXS structural determination of the wild-type retinoschisin monomer. (**A**) Pair-distance distribution function (P(r)) of the retinoschisin monomer, showing the probability of given intramolecular distances being present within the protein. The D_{max} (the maximal distance observed for the protein) is shown by the x-intercept at P(r)=0. Monomeric retinoschisin is shown to have a D_{max} value of 108Å. (**B**) The one-dimensional retinoschisin monomer scatter curve with the GNOM P(r) normalized fit overlayed. (**C**) DAMMIF volumetric bead modelling predicts the low resolution molecular shape of the retinoschisin monomer. (**Di**) Normalized DAMMIF fit overlayed the one-dimensional SAXS scatter profile, showing a χ^2 fit to the data of 0.71. (**Dii**) Plotted residuals of the normalized DAMMIF fit to the SAXS scatter profile.

3.3 The Solution Structure of the C40S/C59S/C223S Retinoschisin Monomer

3.3.1 Expression and Purification of the C40S/C59S/C223S Retinoschisin Monomer

The overexpression of retinoschisin led to the production of octameric, dimeric and monomeric species (Figure 3.2). This raised the possibility that the monomeric species represented a population of oligomerisation incompetent molecules due to non-native intramolecular disulphide linkages formed between the cysteine residues in the Rs1 domain and was therefore an artefactual structure of the expression system. To

investigate this possibility the C40S/C59S/C223S retinoschisin triple mutant was expressed in the *Pichia pastoris* yeast expression system. Previously, it had been shown that the C59 and C223 residues were critical for the disulphide-mediated octamerisation of the complex, with the triple mutant C40S/C59S/C223S secreted from mammalian cells solely as monomers (Wu, Wong et al. 2005). As the structure of this molecule was independent of potential disulphide oligomerization of the octamerising cysteine residues, a similar structure between the wild-type and triple mutant constructs would suggest that the observed structure was intrinsic to the protein and not produced artificially by aberrant disulphide bond formation.

C-terminally His_6-tagged C40S/C59S/C223S retinoschisin (Figure 3.6A) was inserted into the pPICZAα yeast expression vector with sequencing confirming the insertion of the three required mutations with respect to the wild-type sequence (Appendix 4). Secreted protein was purified from the conditioned media using Ni-NTA affinity chromatography. Shown in figure 3.6B, reducing SDS-PAGE analysis of elute fractions recovered from this purification observed a species migrating at approximately 28 kDa not observed in the wash or flow-through fractions. However, an additional band was observed migrating at 39 kDa. Western blotting against the recombinant His_6 tag revealed a reactive species at approximately 25 kDa in the elute fractions, with the larger eluting species not His-reactive, suggesting that it is a higher molecular weight contaminant (Figure 3.6C). Whilst these results suggested the successful expression of C40S/C59S/C223S retinoschisin from the *P. pastoris* expression system, there appeared to be high degree of contamination. As a result, SEC purification using the Superdex75 SEC-column of the His-purified elutes was carried out to improve the purity of the protein sample. SEC separation showed three main peaks, with the most prominent peak at an elution volume of 14ml, eluting at the same volume as observed for the wild-type monomer (Figures 3.6D and 3.3A). Reducing SDS-PAGE analysis of the peak fractions in the region marked on figure 3.6D, identified a species migrating at around 25 kDa corresponding to the peak eluting at 14ml, as observed for wild-type retinoschisin monomer (Figure 3.1B). The additional peak eluting at approximately 10-12ml consisted of a contaminant protein migrating between 28 and 39 kDa, with the later eluting peak representing smaller protein contaminants, possibly caused by degradation of the retinoschisin protein (Figure 3.6E).

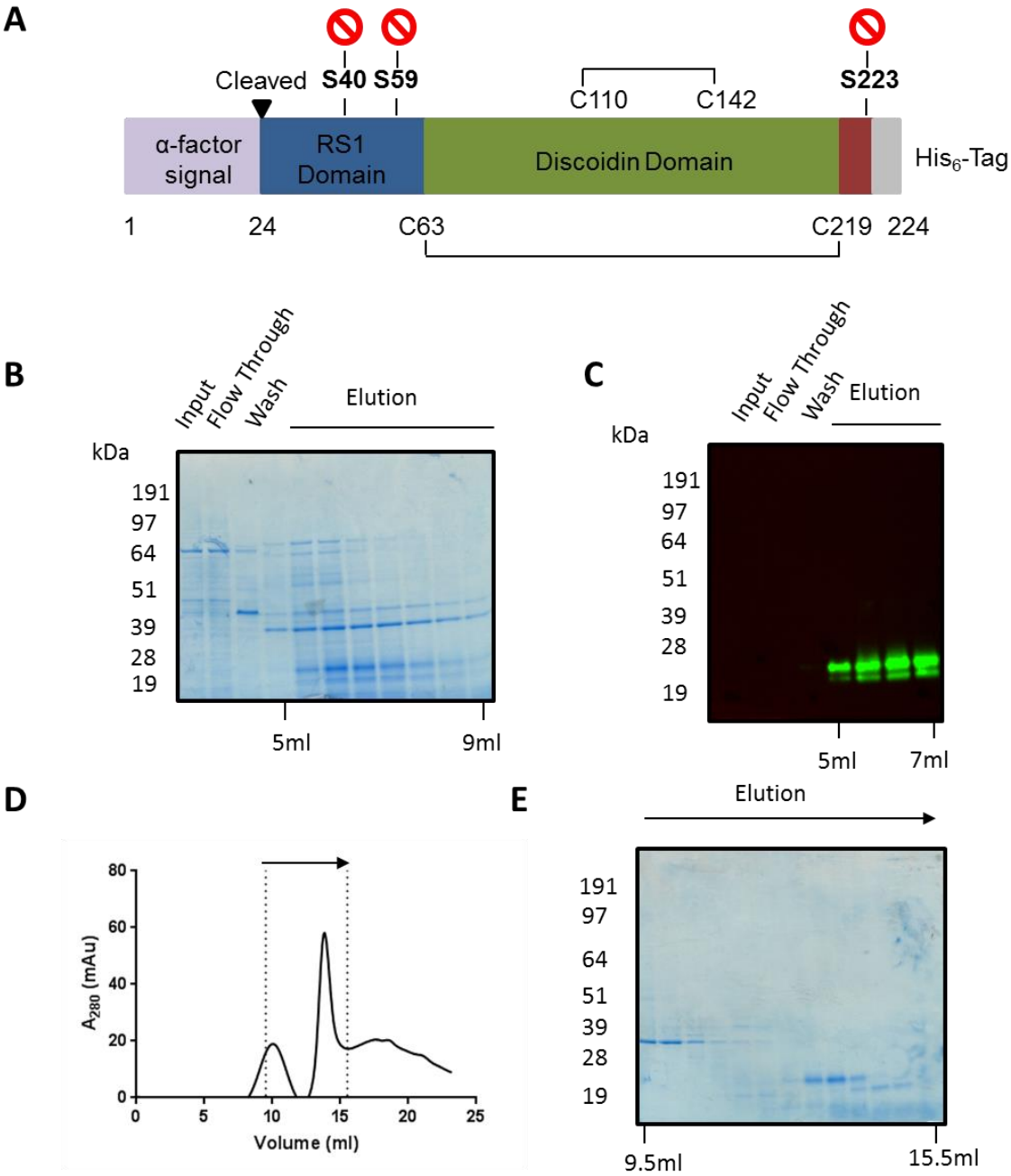

Figure 3.6 – Purification of C40S/C59S/C223S retinoschisin monomer. (**A**) Schematic of the C40S/C59S/C223S retinoschisin construct used, showing the positions of the domains. Intramolecular disulphides are marked with a (-) and the residues required for disulphide-mediated octamerisation which have been mutated to a serine marked. (**B**) Coomassie-stained reducing SDS-PAGE of Ni-NTA purification of recombinant, C40S/C59S/C223S retinoschisin showing input, flow through, wash and elution fractions. (**C**) Anti-His western blotting analysis (under reducing conditions) of Ni-NTA affinity purification of C40S/C59S/C223S retinoschisin. (**D**) SEC purification of C40S/C59S/C223S retinoschisin, highlighted area is further analysed in (**E**). (**E**) Coomassie-stained reducing SDS-PAGE analysis of C40S/C59S/C223S retinoschisin purification.

3.3.2 SAXS Analysis of the C40S/C59S/C223S Retinoschisin Monomer

The purification of triple mutant monomers allowed for investigation of the low resolution solution structure of the construct exploiting SAXS of the purified protein. SAXS analysis (between 0.025Å^{-1} and 0.225Å^{-1} q range) revealed a non-aggregating species with a linear Guinier region showing small residuals throughout the region (Figures 3.7A, Bi and Bii).

Guinier analysis revealed an R_g of 31Å for the C40S/C59S/C223S construct, highly similar to that observed for the wild-type protein. Furthermore, similar to the wild-type protein, the C40S/C59S/C223S construct also had a similar profile in the dimensionless Kratky plot to that of a folded protein, with a similar shift of the peak away from the globularity crosshairs, suggesting that the removal of the disulphide-bond forming cysteine residues does not alter the elongated shape of the protein (Figure 3.7C). However, comparison of the wild-type and C40S/C59S/C223S SAXS curves (Figures 3.4 and 3.7) shows some differences in the higher q regions, also observed in the Kratky plots (Figures 3.5C and 3.7C). Such differences may arise due to the lower concentration of the mutant protein (performed at 1.0 mg/ml compared to 1.9 mg/ml for the wild-type protein) which may lead to differences at higher spatial frequencies due to differences in signal to noise ratio. Also, at these higher spatial frequencies, any differences in the buffer subtraction (which may have arisen due to the different expression systems used for the wild-type and mutant protein) of the two samples may cause differences between the profiles. Furthermore, as the protein molecules studied are of low molecular weight, a higher concentration may be required to make a more accurate comparison in the higher q regions and examine if any differences observed are significant.

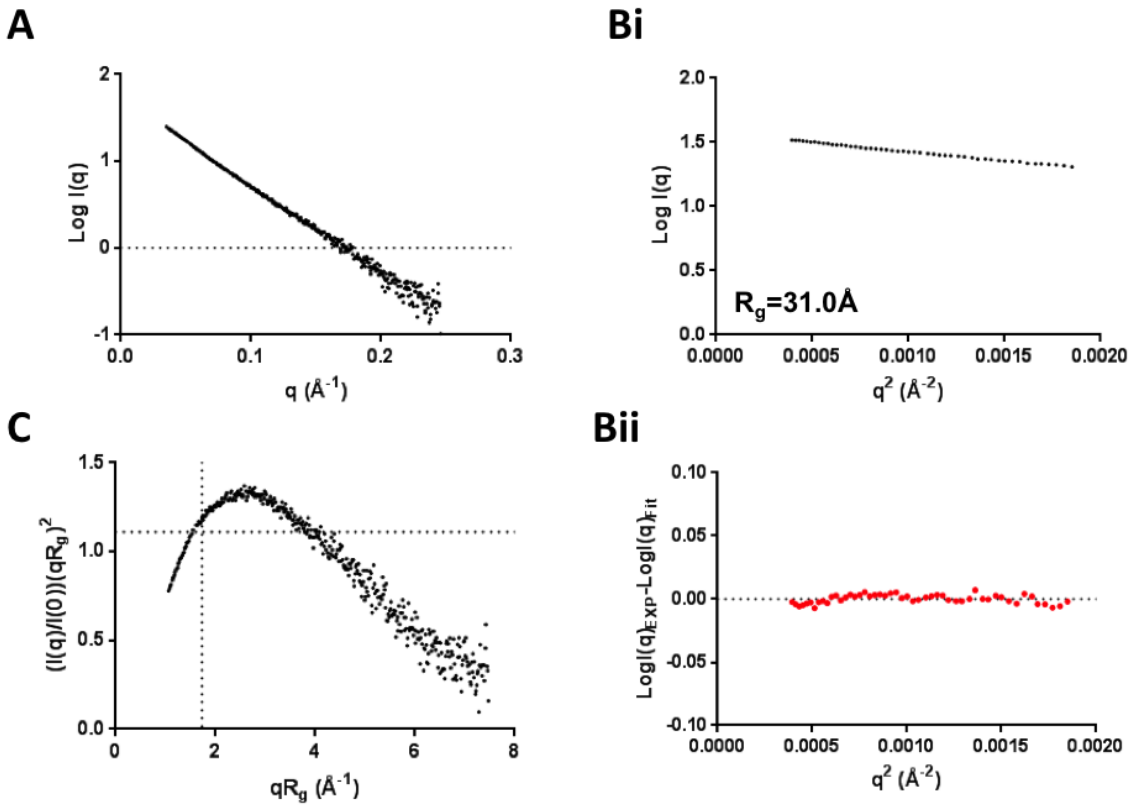

Figure 3.7 – SAXS analysis of purified C40S/C59S/C223S retinoschisin monomer. (**A**) One-dimensional SAXS profile showing the log of X-ray scattering intensity (LogI) as a function of the scattering vector q. (**Bi**) Guinier plot (LogI vs. q^2) of the low q region, showing a Radius of Gyration (R_g) value of 31 Å for the C40S/C59S/C223S retinoschisin monomer. (**Bii**) Plotted residuals ($LogI(q)_{EXP}$-$LogI(q)_{FIT}$) for the Guinier region. (**C**) Normalized Kratky plot ($((I(q)/I(0))(qR_g)^2$ vs. qR_g) showing a folded peak. Shown are the cross-hairs for globularity of the protein fold (1.1 vs. √3), this plot suggests a folded, elongated structure.

3.3.3 Shape Determination and Volumetric Modelling of C40S/C59S/C223S Retinoschisin Monomer from SAXS Analysis

P(r) determination for the triple mutant construct had a similar profile as previously observed for the wild-type monomer, with the majority of observed distances between 25Å and 55Å with a connected tail extending to greater distances (Figure 3.8A). Inverse Fourier transform of the triple mutant P(r) distribution revealed a regularized scatter profile which agreed well with the experimental scatter profile (Figure 3.8B). P(r) analysis calculated a similar D_{max} value of 118Å, with the small increase in the D_{max} potentially caused by a small amount of aggregate in the sample or a low signal to noise ratio in the data. DAMMIF reconstruction (Figure 3.8C) produced a highly similar molecular shape as previously observed for the wild-type monomer (Figure 3.5C). A single elongated projection from a central globular region was observed, with an overall flat extended structure. The structure was observed to fit the data well (Figure 3.8Di) with small residuals observed for the fit between the model and the experimental data (Figure 3.8Dii). Furthermore, the models had a NSD value of 0.624, suggesting that this represented a unique solution. These data suggest that the cysteine residues have a limited influence on the overall structure.

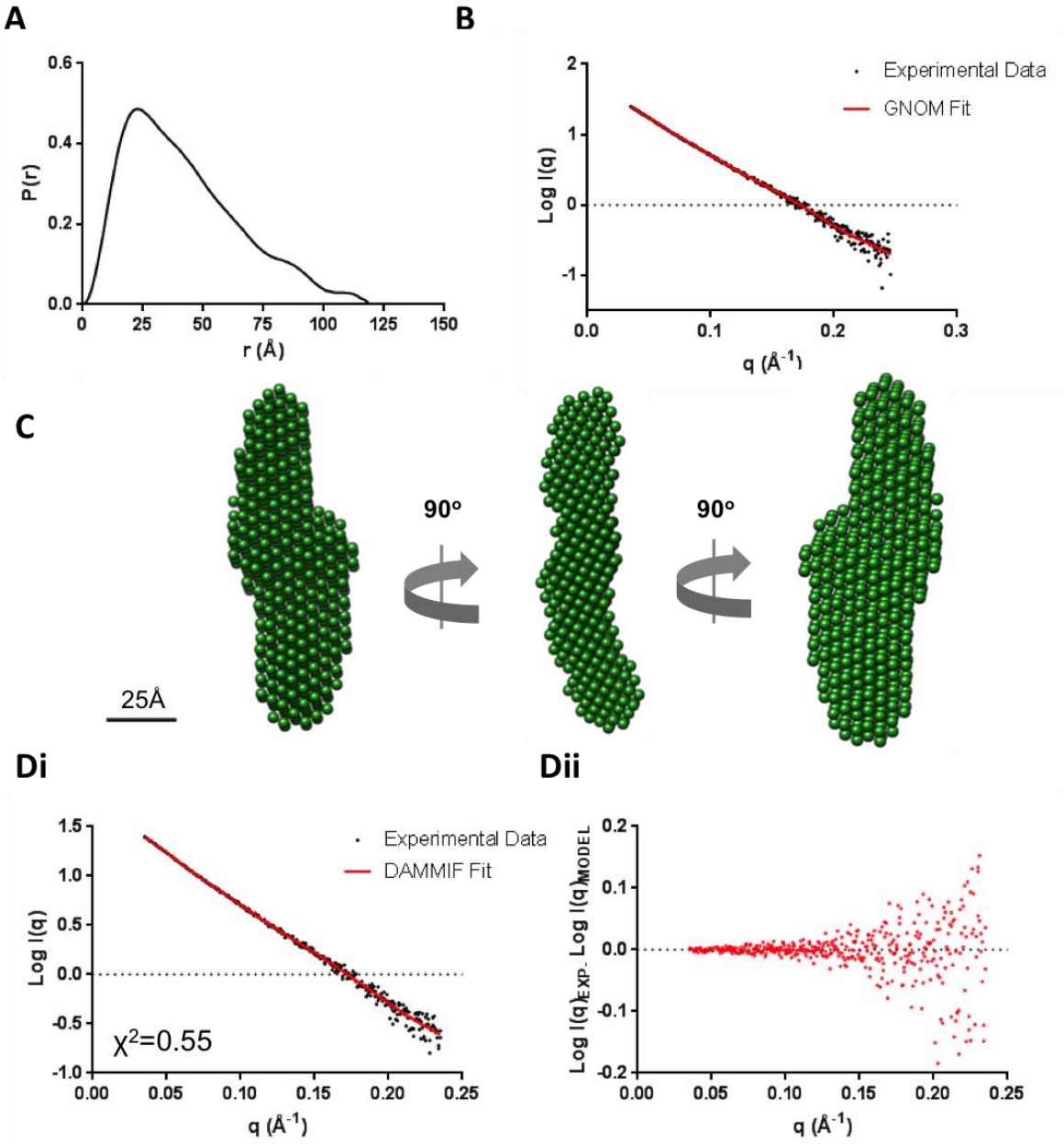

Figure 3.8 –SAXS structural determination of the C40S/C59S/C223S monomer. (**A**) Pair-distance distribution function (P(r)) of the C40S/C59S/C223S retinoschisin monomer. The D_{max} is calculated as 118Å. (**B**) The one-dimensional retinoschisin monomer scatter curve with the GNOM P(r) normalized fit overlayed. (**C**) DAMMIF volumetric bead modelling showing the determined low resolution molecular shape of the C40S/C59S/C223S retinoschisin monomer. (**Di**) Normalized DAMMIF fit overlayed the one-dimensional SAXS scatter profile, showing a χ^2 fit to the data of 0.55. (**Dii**) Plotted residuals of the normalized DAMMIF fit to the SAXS scatter profile.

3.4 The Solution Structure of the Retinoschisin Discoidin Domain

3.4.1 Expression and Purification of the Retinoschisin Discoidin Domain

To further probe the internal structure of the retinoschisin monomer, C-terminally His_6-tagged retinoschisin discoidin domain (Figure 3.9A) was expressed in yeast. The presence of only the discoidin domain was again confirmed through sequencing of the construct (Appendix 4). The secreted protein was purified from the media using Ni-NTA affinity chromatography. Elute fractions were enriched in a species migrating at

approximately 19 kDa (Figure 3.9B) which had anti-His_6 antibody reactivity (Figure 3.9C). However, a large amount of contamination was present in Ni-affinity elutes and further SEC purification was carried out (Figure 3.9D). SEC purification produced a large polydisperse peak (Figure 3.9D) with SDS-PAGE of elute fractions across this peak revealing the presence of many contaminant species (Figure 3.9E). However, later fractions (16-17ml elution volume) were enriched in the 19 kDa species previously observed to be His-reactive (Figure 3.9E). This confirmed the expression and purification of the domain, however despite the improved purification, the sample was still contaminated with a protein product of approximately 30 kDa.

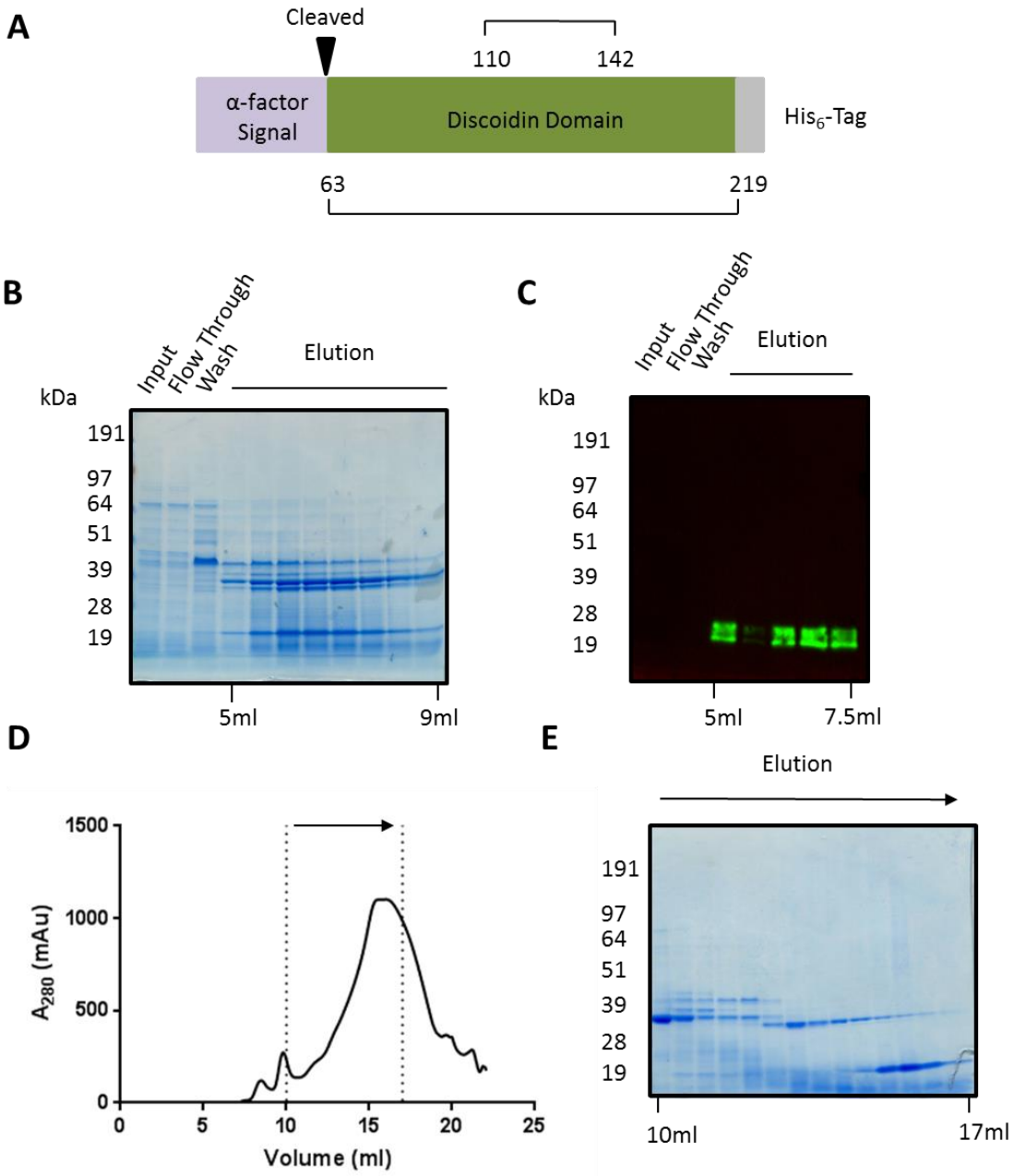

Figure 3.9 – Purification of retinoschisin discoidin domain from *P. pastoris*. (**A**) Schematic diagram of the retinoschisin discoidin domain construct, showing the positions of the domains. Intramolecular disulphides are marked with a (-). (**B**) Coomassie-stained reducing SDS-PAGE of Ni-NTA purification of recombinant, discoidin domain with input, flow through, wash and elution fractions. (**C**) Anti-His western blotting analysis (under reducing conditions) of Ni-NTA affinity purification of the discoidin domain. (**D**) SEC purification of the discoidin domain, highlighted area is further analysed in (**E**). (**E**) Coomassie-stained reducing SDS-PAGE analysis of the retinoschisin discoidin domain purification.

3.4.2 SAXS Analysis of the Retinoschisin Discoidin Domain

In order to remove this contaminating species, the discoidin domain elute fractions were subject to a further SEC purification step during the SAXS experiment. This approach allows for the separation of species using a SEC step immediately before injection into the X-Ray beam (Figure 3.10A). Protein was monitored via A_{280} immediately before the X-ray beam. The SEC employed for the discoidin domain allowed for further purification,

generating a single species eluted as a symmetrical peak (Figure 3.10B) directly into the SAXS experiment. SAXS analysis was confined between 0.075Å^{-1} to 0.275Å^{-1} q range (Figure 3.10C). Guinier analysis (Figures 3.10Di and Dii) determined a smaller R_g of 15.6Å, with the R_g normalized Kratky analysis (Figure 3.10E) indicating a folded and more globular (yet still slightly elongated) conformation, as shown by the smaller displacement of the peak from the 1.1 vs. $\sqrt{3}$ crosshairs.

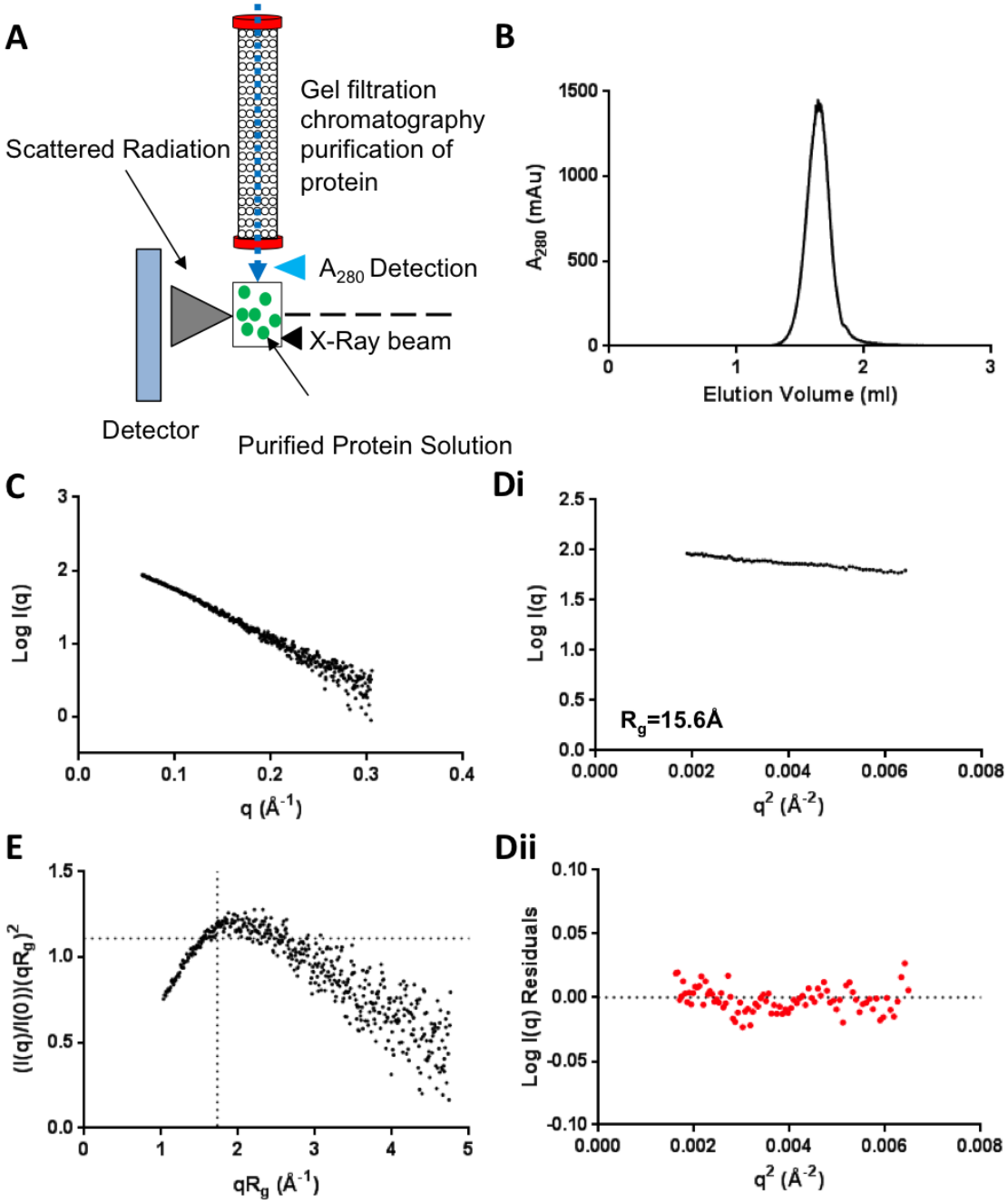

Figure 3.10 – SAXS analysis of purified retinoschisin discoidin domain. (**A**) Schematic for the SEC-SAXS experiment with separation of the protein carried out on a Superdex200 3.2 column with protein monitored using A_{280} (**B**) A_{280} of purified discoidin domain immediately before SAXS measurement. (**C**) One-dimensional SAXS profile showing the log of X-ray scattering intensity (LogI) as a function of the scattering vector q. (**Di**) Guinier plot (LogI vs. q^2) of the low q region, showing a Radius of Gyration (R_g) value of 15.6 Å for the discoidin domain. (**Dii**) Plotted residuals ($LogI(q)_{EXP}$-$LogI(q)_{FIT}$) for the Guinier region. (**E**) Normalized Kratky plot ($((I(q)/I(0))(qR_g)^2$ vs. qR_g). Shown are the cross-hairs for globularity of the protein fold (1.1 vs. √3).

3.4.3 Shape Determination and Volumetric Modelling of the Retinoschisin Discoidin Domain from SAXS Analysis

P(r) determination further revealed the smaller, more globular structure of the discoidin domain. The P(r) distribution had a typical profile associated with a globular protein with the absence of the large extension out to higher distances. As a result, the D_{max} value of 55Å reflects a more compact protein (Figures 3.11A and B). DAMMIF volumetric bead modelling (averaged and filtered from 17 individual iterations) was consistent with this, generating a small, globular conformation with a low NSD value of 0.556 (Figure 3.11C). Comparison of the model to the experimental data further showed a good fit between the data and the constructed model (Figure 3.11Di) with small residuals observed for the fit (Figure 3.11Dii) with a low X^2 value of 0.58. Overall, these data reveal a more globular, less extended shape for the discoidin domain, suggesting the elongated character shown may be due to the Rs1 domain being highly extended.

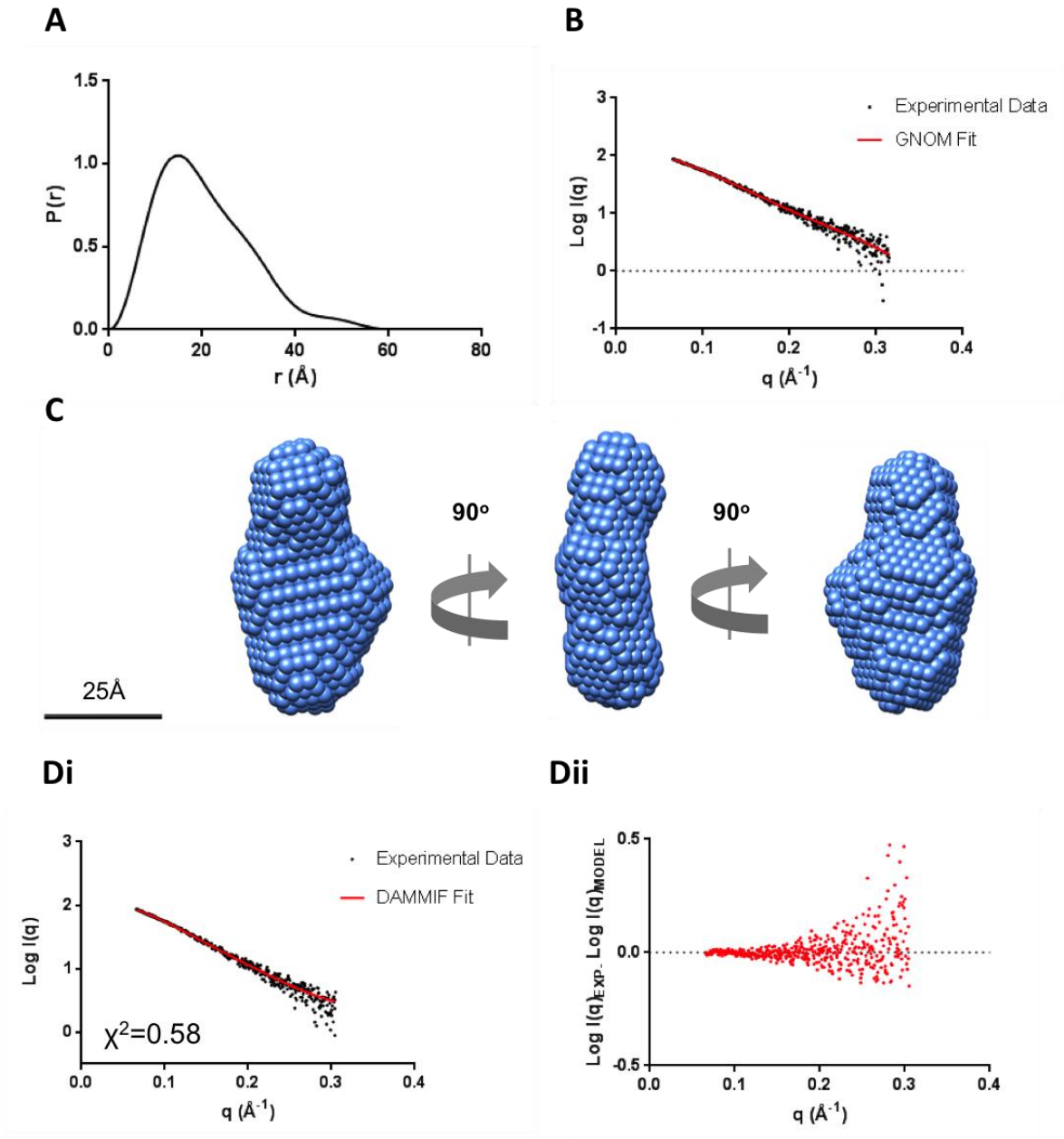

Figure 3.11 –SAXS structural determination of the retinoschisin discoidin domain. (**A**) Pair-distance distribution function (P(r)) of the discoidin domain, with a D_{max} of 55Å. (**B**) The one-dimensional discoidin domain scatter curve with the GNOM P(r) normalized fit overlayed. (**C**) DAMMIF volumetric bead modelling showing the determined low resolution molecular shape of the discoidin domain. (**Di**) Normalized DAMMIF fit overlayed the one-dimensional SAXS scatter profile, showing a χ^2 fit to the data of 0.58. (**Dii**) Plotted residuals of the normalized DAMMIF fit to the SAXS scatter profile.

3.5 Comparison of Wild-Type, Triple Mutant and Discoidin Domain SAXS Structures

Comparison of the P(r) distributions for the wild-type and triple mutant retinoschisin monomers confirmed the similar shape observed for both species (Figure 3.12A). Both molecules possessed a highly similar profile, with only a small difference in the x-intercepts, indicating the slightly increased D_{max} observed for the triple mutant. A more dramatic structural difference was however observed upon comparison of the discoidin domain and wild-type retinoschisin monomer P(r) distributions (Figure 3.12B). The

discoidin domain has a significantly shorter D_{max} as shown by the smaller x-intercept with respect to the wild-type retinoschisin monomer distribution. Here, the longer distances can be attributed to the presence of the Rs1 domain, which is adopting a highly elongated shape. Indeed, comparison of the discoidin domain and wild-type retinoschisin bead models (Figure 3.12C) revealed that the discodin domain forms the globular core of the molecule, with the extended projection representing the N-terminal Rs1 domain.

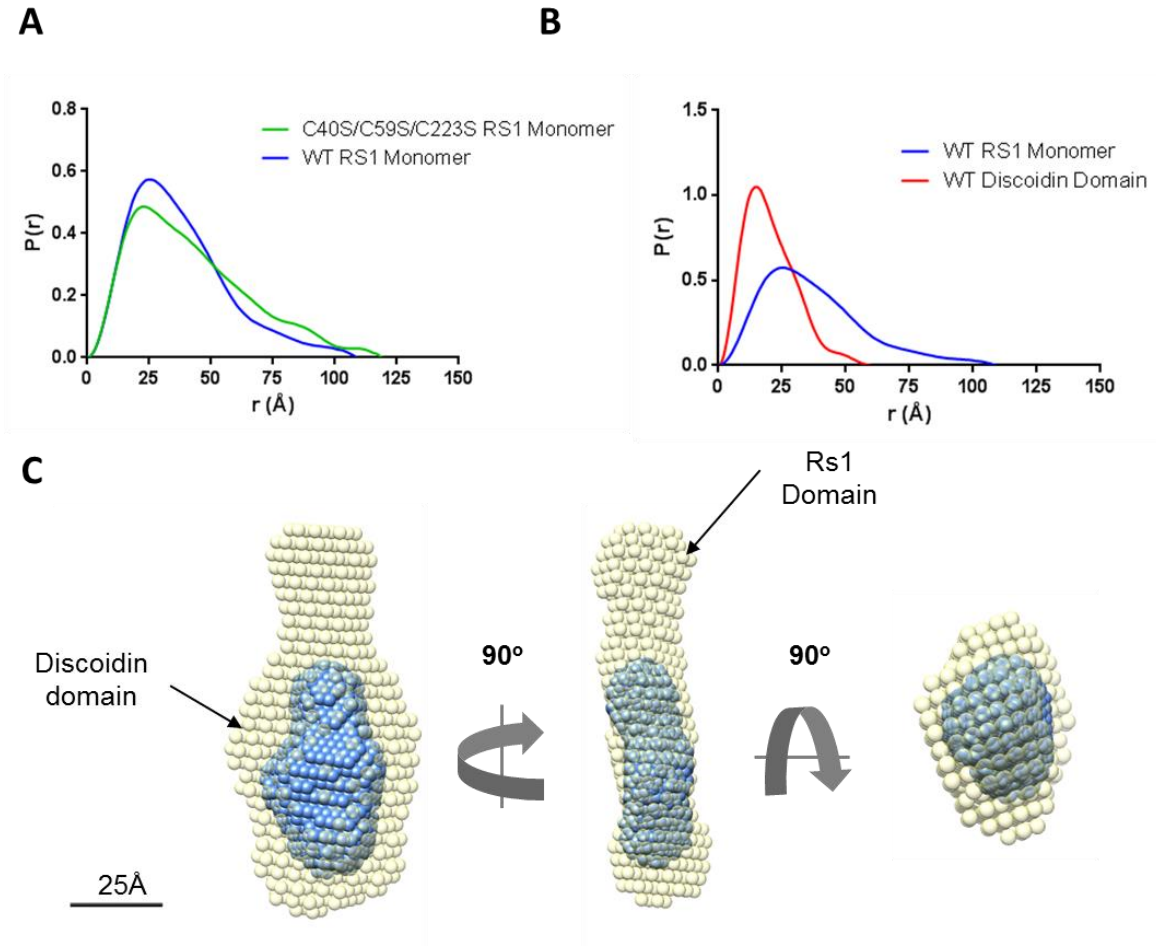

Figure 3.12 – SAXS structural comparison of the wild-type retinoschisin monomer, C40S/C59S/C223S retinoschisin monomer and the discoidin domain. (**A**) Comparison of the P(r) distribution functions for the wild-type and C40S/C59S/C223S retinoschisin monomer. (**B**) Comparison of the P(r) distribution functions for the wild-type retinoschisin monomer and the discoidin domain. (**C**) Comparison of the averaged, filtered DAMMIF volumetric bead models for the wild-type retinoschisin monomer and discoidin domain showing the relative locations of the discoidin and Rs1 domains in the full length retinoschisin molecule.

3.6 Discussion

In summary, wild-type human retinoschisin was expressed and purified from HEK293-EBNA cells, allowing for structural analyses of the retinoschisin molecule. Retinoschisin was secreted as a non-glycosylated protein which formed disulphide-dependent oligomers. Indeed MALS analysis revealed that retinoschisin was expressed from the mammalian expression system as a mixture of monomer, dimer and octamers. However, despite the markedly different molecular weights observed for each state (200, 52 and 24 kDa) the species showed relatively close elution volumes in SEC purification (Figure

3.2C). This may be potentially due to the overall molecular size not increasing as markedly as the molecular weight upon octamerisation. Further structural analysis of the retinoschisin octamer complex will be discussed in the following chapters.

Solution structural analysis of the retinoschisin monomer revealed a globular character with hydrodynamic (Figure 3.3) and SAXS analyses (Figures 3.4 and 3.5). Further SAXS analysis and volumetric modelling of the discoidin domain (which constitutes 75% of the overall retinoschisin sequence) revealed that this elongated structure may be due to the Rs1 domain adopting a highly extended conformation. Indeed, the discoidin domain adopted a more globular structure (Figures 3.10 and 3.11) with comparison between the wild-type monomer structure and the discoidin domain revealing that the central core density observed in the retinoschisin monomer represented the discoidin domain, with the Rs1 domain forming an extended projection from this structure (Figures 3.12B and C). This observation was consistent to previous predictions of the monomeric structure of retinoschisin. Using homology modelling and molecular dynamics, Sergeev *et al* predicted that the Rs1 domain forms a disordered extension from the discoidin domain (Sergeev, Caruso et al. 2010). These analyses experimentally support this prediction. Through extending away from the globular volumes of the discoidin domains, the Rs1 domains would be able to interact, forming a ring-like structure without inducing significant steric clashing between the discoidin domains. Therefore, such a structure would be compatible with octamer formation, analogous to the multimerisation of many 'wedge' shaped molecules.

In order to determine whether the purified monomer was indeed representative of the species which octamerises *in vivo* to form the mature retinoschisin octamer or an oligomerisation-incompetent form, the structure of the C40S/C59S/C223S was determined using SAXS. These residues are required for disulphide-mediated oligomerisation with their loss leading to loss of octamer secretion in HEK293 cell expression systems (Wu, Wong et al. 2005). Exploiting SAXS analysis, purified C40S/C59S/C223S retinoschisin monomer was observed to have the same R_g, a highly similar D_{max} value and P(r) distribution (Figures 3.7, 3.8 and 3.12A) when compared with the wild-type monomer. Volumetric modelling using DAMMIF further revealed a highly similar shape (Figures 3.5C and 3.8C). Together, these data suggest that the disulphides in the Rs1 domain have a limited influence on the monomer structure, with the purified monomer representing the form previously predicted by Sergeev *et al (Sergeev, Caruso et al. 2010)*.

4 Results Chapter 2: Characterisation of the Wild-Type Retinoschisin Octamer Structure

Retinoschisin is secreted from photoreceptors as an octamer, which represents the fully assembled, functional molecule in the retina. As a result, we sought to characterise the structure of the octameric molecule. To this end, the structure was investigated using a combinatorial approach of MALS, AUC and single particle analysis.

4.1 Hydrodynamic Analysis of Purified Wild-type Retinoschisin Octamer

After purification from the HEK293-EBNA cells shown in figure 3.2, octameric retinoschisin was subject to hydrodynamic characterisation. Previous observations using size-exclusion chromatography had suggested the octamer may have similar hydrodynamic parameters as the monomeric form (Figure 3.2C) with elution of the ~200 kDa complex, only 5ml earlier than the monomeric form (24 kDa) despite the large mass difference between the octamer and monomer (of approximately 170 kDa). The ability of both species to be separated in the non-void volume on a small size-exclusion chromatography column (Superdex 75 10/300GL) suggested that the octamer was a relatively compact molecule, possibly due to tight arrangement of the domains in the oligomer. Indeed, MALS and AUC analysis of the purified octamer revealed a molecule with a hydrodynamic radius of approximately 5nm (Figure 4.1) suggesting an approximate doubling of the hydrodynamic radius with an observed increase of 2.5nm compared to the monomer (Figure 3.3). Despite this, the octameric molecule maintained a globular conformation with an f/f_0 value of 1.33, therefore there is a relatively modest size increase observed upon octamerisation of retinoschisin monomers (Figure 4.1Bii). The approximate agreement between the MALS and AUC data suggested the presence of a monodisperse, compact octameric retinoschisin structure, consistent with previous size-exclusion chromatography observations.

Ai **Aii**

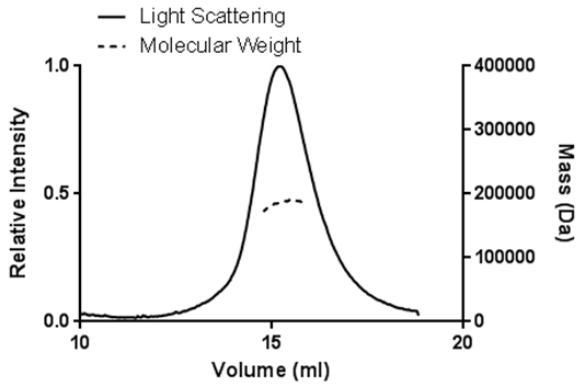

Molecular Weight (kDa)	187
Hydrodynamic Radius (nm)	5.8
Polydispersity	1.000

Bi **Bii**

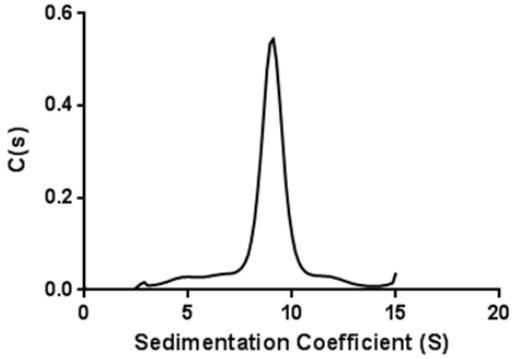

Molecular Weight (kDa)	180
Sedimentation Coefficient (S)	9.38
Hydrodynamic Radius (nm)	5.1
f/f_0	1.33

Figure 4.1 – Hydrodynamic Analysis of purified wild-type retinoschisin octamer. (**Ai**) SEC-MALS analysis of wild-type retinoschisin octamer. (**Aii**) Extracted hydrodynamic values from SEC-MALS analysis. (**Bi**) AUC analysis of wild-type retinoschisin octamer analysed using model-based continuous distribution (C(s)). (**Bii**) Hydrodynamic parameters obtained from AUC analysis.

4.2 Negative Stain Electron Microscopy of the Retinoschisin Octamer

The hydrodynamic for the retinoschisin molecule suggested a compact arrangement of domains within the mature retinoschisin octamer. In order to investigate this, negative stain electron microscopy was employed. Dilute, purified retinoschisin octamer preparations were subject to negative staining, with subsequent imaging revealing monodisperse molecules (Figure 4.2A) with a ‘ring’ like structure (Figure 4.2A, inset). Reference-free classification of the resulting particle set confirmed this ring-like shape with class averages (Figure 4.2B) showing an eight-fold symmetric arrangement of subunits in a central ring structure. Indeed, this symmetry was apparent in the Eigen images representing the principal components within the data (Figure 4.2C). Furthermore, autocorrelational comparison of ‘top’ reference-free class averages showed a pronounced eight-fold symmetry, with autocorrelational peaks observed every eighth of a rotation (45 degree rotation), again strongly suggesting eight-fold symmetry (Figure 4.2D). Closer inspection of the class averages revealed the ring to have a reduced contrast towards the centre of the molecule, due potentially to a reduction in the electron density of this region

or due to a less ordered region which is possibly refractory to averaging (Figure 4.2B). Aside from the observed eight-fold symmetric arrangement of domains, additional classes were observed which resembled the 'side' of this molecule (Figure 4.2B). These classes appear flat in appearance, suggesting a highly planar arrangement of subunits in the octameric propeller. Octamer molecules had an apparent bias towards 'top' orientations, with the observed side views representing a minority of particles within the data set. This may be due to preferential interactions between the carbon support and the protein molecule. As a result, it was not possible to determine a three-dimensional structure from the negative-stain data and cryo-EM was employed for three-dimensional structural determination.

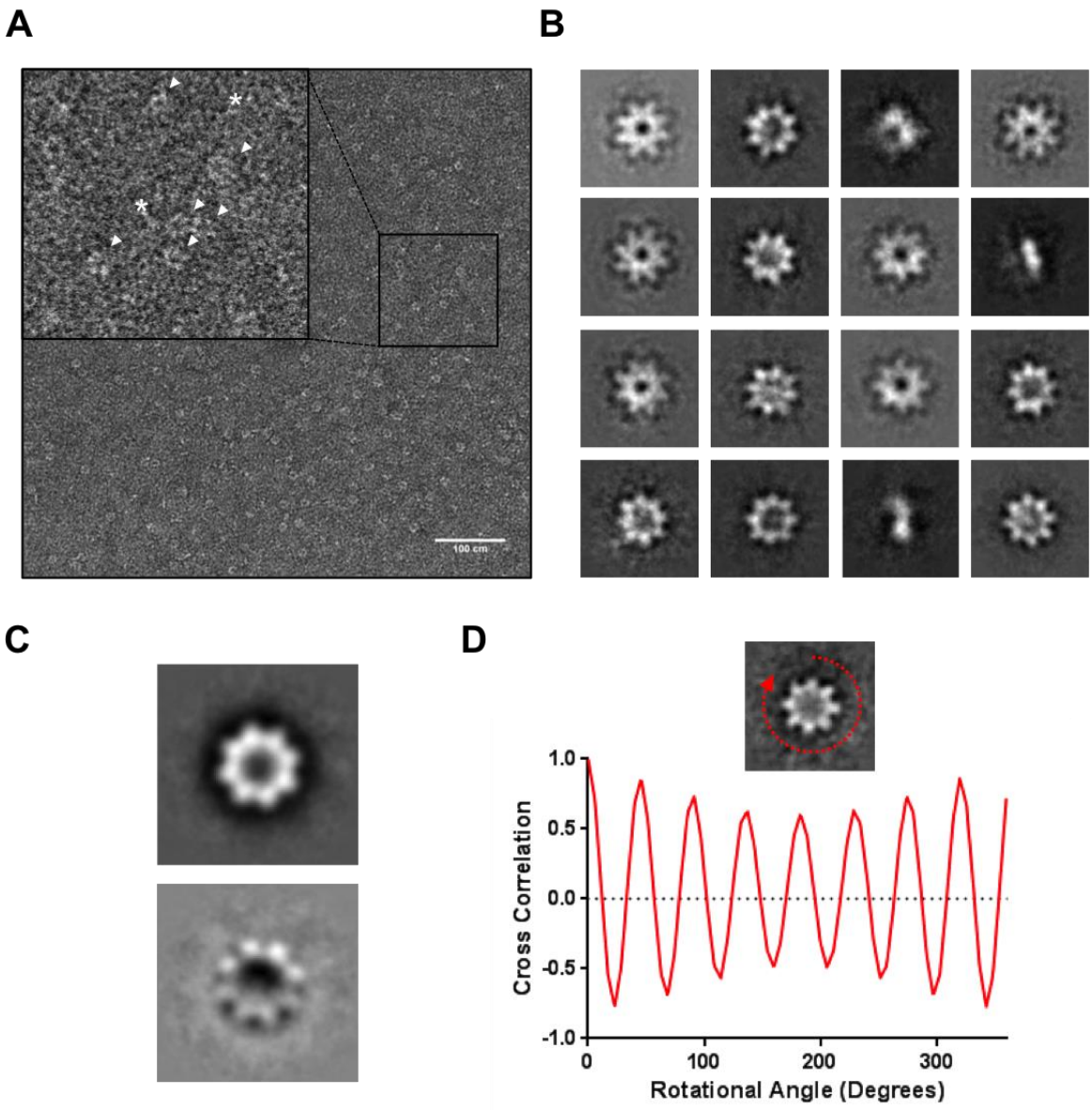

Figure 4.2 – Negative-stain microscopy of purified wild-type retinoschisin octamer. (**A**) Representative micrograph with a field of dispersed particles. 'Top' views are denoted with (Δ) and 'side' views with (*). (**B**) Reference-free class averages generated from the particle set using EMAN2.0. Only single-stack molecules are observed with a clearly eight-fold symmetrical ring structure. (**C**) Two Eigen images showing eightfold symmetry in the particle set. (**D**) Auto-correlational analysis of the showed reference-free class average.

4.3 The Structure of the Retinoschisin Dimer of Octamers

4.3.1 Solution Characterisation of Retinoschisin Dimer of Octamers Formation

To allow for cryo-EM structural determination, retinoschisin octamer samples were subject to centrifugal concentration to allow for visualization in vitreous ice. Subsequent nativePAGE analysis of the concentrated retinoschisin octamer sample at 0.1mg/ml revealed two species which were reactive with the anti-His_6 antibody, therefore representing recombinant protein (Figure 4.3). The lower species (migrating at approximately 242 kDa molecular weight) appeared to show an octameric species, which had previously been observed to have a molecular weight of approximately 190 kDa (Figure 3.2C and 4.1A). The additional species was observed to migrate between 480 and 720 kDa, suggesting the formation of a higher order oligomer. Therefore, this suggests that octameric retinoschisin self assembles into a novel, non-covalently stabilized, higher-order oligomer possibly in a concentration-dependent manner.

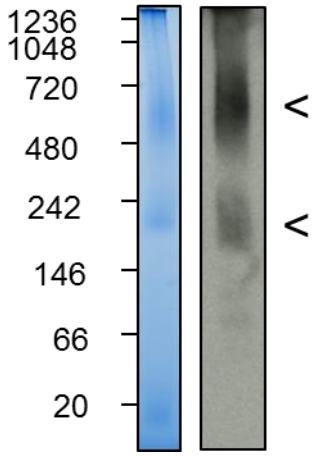

Figure 4.3 – Higher oligomerisation of the wild-type retinoschisin octamer in solution. NativePAGE analysis of purified wild-type retinoschisin at 0.1mg/ml concentration. Shown is a coomassie-stained gel together with a α-His_6 western blot, showing 2 His-reactive species.

4.3.2 Cryo-EM of the Retinoschisin Dimer of Octamers

In order to further characterise both the structure of the retinoschisin octamer and the observed higher order oligomer formed by the octamer in solution, purified retinoschisin octamer samples were imaged by cryo-EM. Imaging in vitreous ice allowed for visualization of the protein in a mixture of random orientations, overcoming the anisotropy observed within the negative-stain data set. In order to reach a higher resolution structural characterisation, wild-type retinoschisin was imaged in vitreous ice under cryo conditions in an FEI Technai F30 microscope fitted with a Gatan K2 Summit direct electron counting camera at STRUBI. The dose of $25e^-/Å^2$ was fractionated over 25 frames at 0.1 second/frame. Initial and final frames were discarded due to beam-induced sample movements (Brilot, Chen et al. 2012, Campbell, Cheng et al. 2012, Russo and Passmore

2014) and accumulative radiation damage (Scheres 2014) respectively, both of which combine to reduce the maximum possible resolution of the structural determination. Following this, drift correction allowed for the effect of particle drift during beam exposure to be reduced, allowing for a significant increase in the resolution at which retinoschisin structure could be determined. Shown in figure 4.4A is a representative view of retinoschisin octamers imaged in vitreous ice using a DDD detector. Subsequent reference-free classification of the particles revealed a characteristic 'propeller' structure (Figure 4.4B) previously observed under negative-stain conditions (Figure 4.2). Also, a mixture of single-layered and double-layered 'side' views were observed in the initial micrographs and following particle classification (Figures 4.4B and C). Comparison of these structures with the highly planar 'side' views observed for the octameric complex under negative-stain conditions (Figure 4.2B) suggests that these views represent a two stacked octamer rings, forming a dimer of octamers upon concentration of the octamers in solution. Therefore, the higher-order oligomer observed in nativePAGE represents a 16-mer complex formed by the dimerization of two octamers. This mixed population of single-stacked octamer and double-stacked hexadecamer particle sets were separated using the three-dimensional classification procedure available in the RELION 1.4 software suite (Figure 4.5).

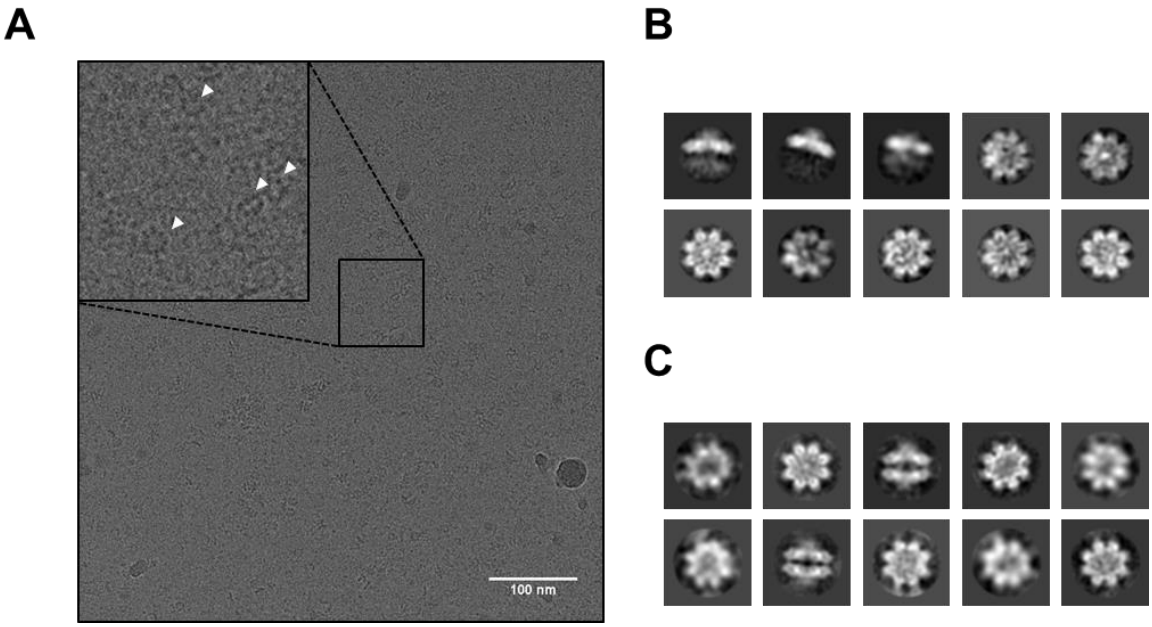

Figure 4.4 –Cryo-EM of the wild-type retinoschisin octamer and dimers of octamers. (**A**) Representative field of wild-type octamer particles imaged in vitreous ice under cryo conditions using the Gatan K2 Summit direct electron counting camera. Both 'top' and 'side' views are apparent in the data (inset). (**B**) Reference-free class averages of the wild-type retinoschisin octamers, and (**C**) dimers of octamers following separation of each particle set using three-dimensional class averaging, box size: 24nm, 1.6Å/pix.

The particle set was subjected to five iterative rounds of two-dimensional reference-free classification to remove 'bad' or damaged particles from the dataset which would work to compromise the maximum possible resolution. This significantly reduced the particle

number (Figure 4.5). Using a D8 symmetrical retinoschisin dimer of octamers previously resolved from this entire data set using EMAN 2.0 (which reached a lower resolution) (Figure 4.5) as a reference structure, three-dimensional classification was carried out into two classes with C8 symmetry applied. This allowed for separation of the octamer from the hexadecamer structures (Figure 4.5) generating two distinct particle populations which could be refined with their respective class structures to generate the final, refined model for each state. Shown in figures 4.4B and C are reference-free class averages of each separated particle set, showing two distinct structures for the octamer (Figure 4.4B) and hexadecamer (Figure 4.4C) states, showing good separation of the two particle sets.

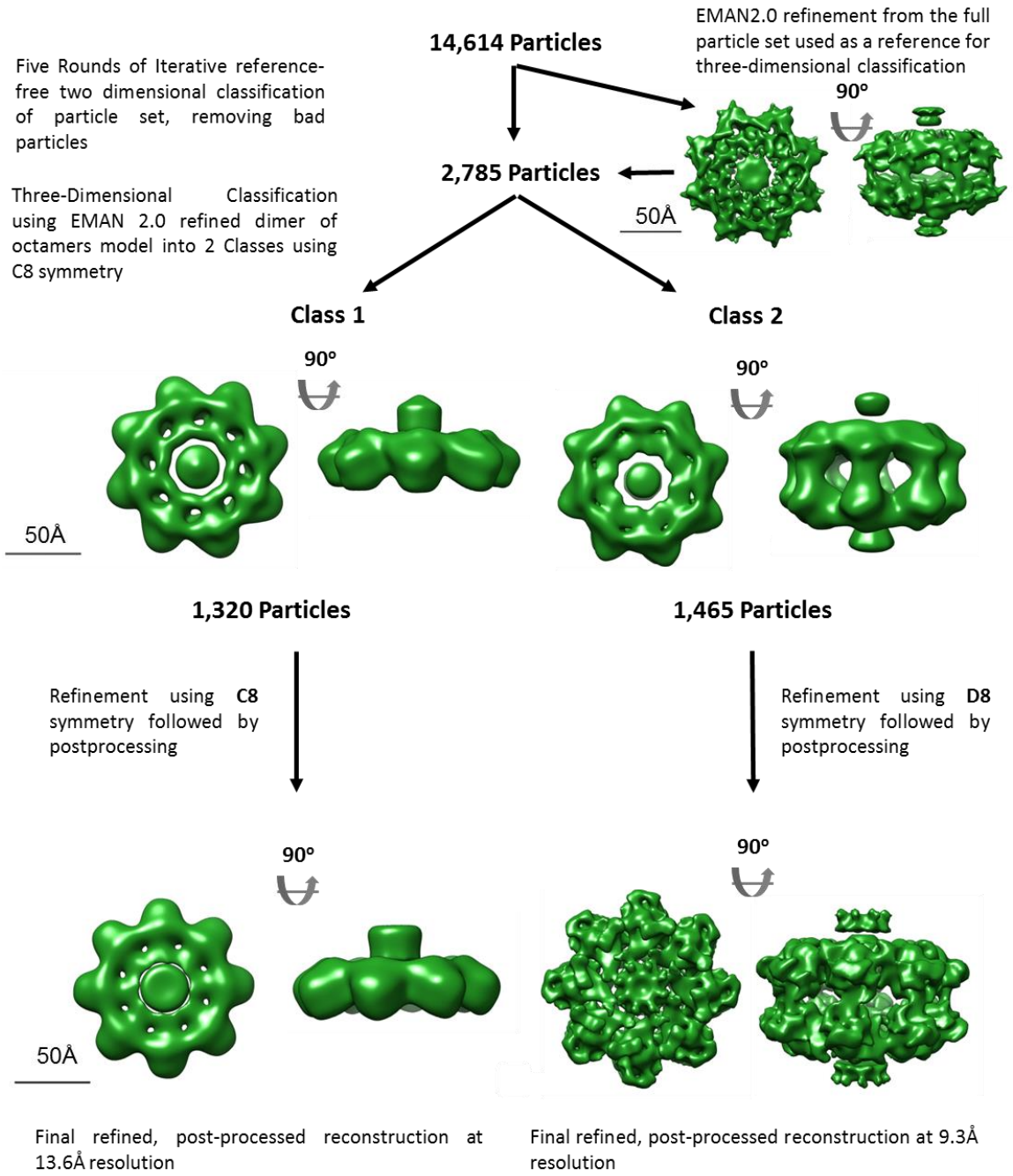

Figure 4.5 – Procedure for separating wild-type octamer and dimer of octamers. Poor quality particles are first removed using iterative rounds of two-dimensional classification. The structure calculated previously using EMAN2.0 was used as a reference for three-dimensional classification into two distinct classes using C8 symmetry. Following separation into octamer and hexadecamer species, further refinement (using C8 and D8 symmetry respectively) and postprocessing determined the final structure for both oligomers.

Following this refinement procedure, the structure of the retinoschisin wild-type octamer was resolved. Consistent with previous negative-stain analysis and reference-free class averages, the retinoschisin octamer had a pronounced planar propeller shape, likely consisting of a ring of discoidin domains (Figure 4.6A). Indeed, comparison of the discoidin domain volumetric model calculated following SAXS analysis of the isolated domain (Figure 3.11C) showed a good fit between the bead model and the octamer electron density (Figure 4.6B). As observed for negative-stain class averages, there

appeared to be a loss of density in the centre of the molecule, with a single, diffuse density observed in this region in the class averages for both the octamer and hexadecamer model (Figures 4.4B and C). These regions therefore likely represent a disordered, low density region, preventing full reconstruction. The coalescence of the Rs1 domains at the centre of the molecule, at the symmetry axis, generates the disconnected density observed in the class averages (Figures 4.4B and C) and final refined model (Figure 4.6). Overall, the resulting structure reached a modest resolution of 13.6Å at the gold standard FSC criterion (0.143) (Figure 4.7A) with good distribution of Euler angles observed (Figure 4.7B).

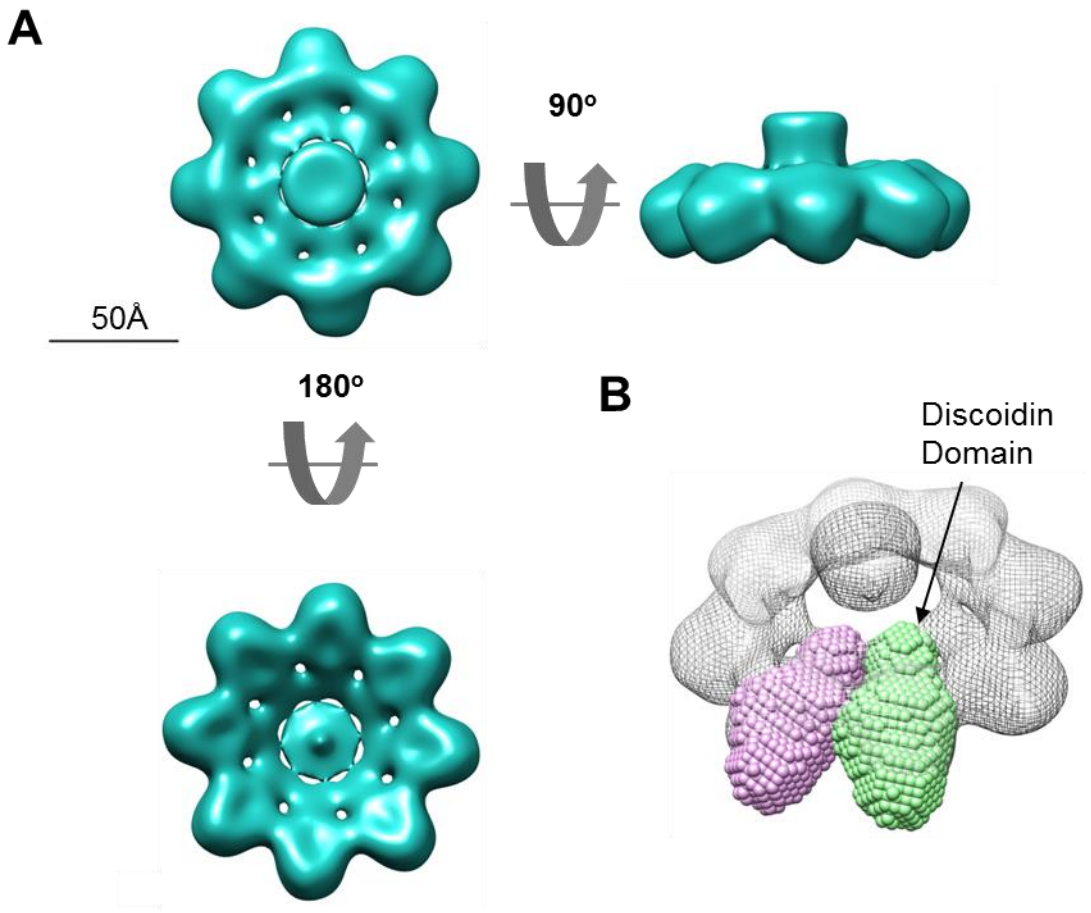

Figure 4.6 – Cryo-EM structure of the wild-type retinoschisin octamer. (**A**) The structure of the wild-type retinoschisin octamer at 13.6Å resolution with a pronounced propeller shape. (**B**) Fitting of the discoidin domain volumetric bead models calculated from SAXS analysis of the isolated discoidin domain fitted to the volume proposed to represent the discoidin domain.

The retinoschisin dimer of octamers was observed to be formed of two retinoschisin octamers dimerizing in an apparent face-to-face orientation, with small contacts formed between opposing discoidin domains (Figure 4.8A). The small contact interface appears sufficient to allow for efficient and stable dimerization, even at modest concentrations, and as a result likely represents a highly avid interaction, with the eight contacts synergizing to produce a stable dimerization interface. Inspection of the internal structure of the hexadecamer observed pronounced structural features. The octamer is constructed of two

concentric rings, an outer ring of discoidin domain volumes together with an inner ring of much smaller density. Additionally, within each discoidin domain, a central cavity was observed (Figure 4.8B). This may represent the gap in the highly conserved β-sandwich structure observed in numerous discoidin domains (Macedo-Ribeiro, Bode et al. 1999, Pratt, Shen et al. 1999, Carafoli, Bihan et al. 2009). Such internal features were observable due to the improved resolution of the dimer of octamers model. Gold standard FSC analysis of the structure revealed a final resolution of 9.3Å at 0.143 FSC (Figure 4.9A) with a good Euler coverage (Figure 4.9B). Despite both the octamer and dimer of octamer models being refined from comparatively sized data sets, the hexadecamer achieved significantly higher resolution compared to the retinoschisin octamer due to the higher, dihedral (D8) symmetry of the hexadecamer, reducing the total number of euler angles that are required to be represented in the particle set (Figure 4.9B). Nevertheless, the ability to collect a mixture of 'top', 'side' and 'intermediate' views allowed for improved model construction.

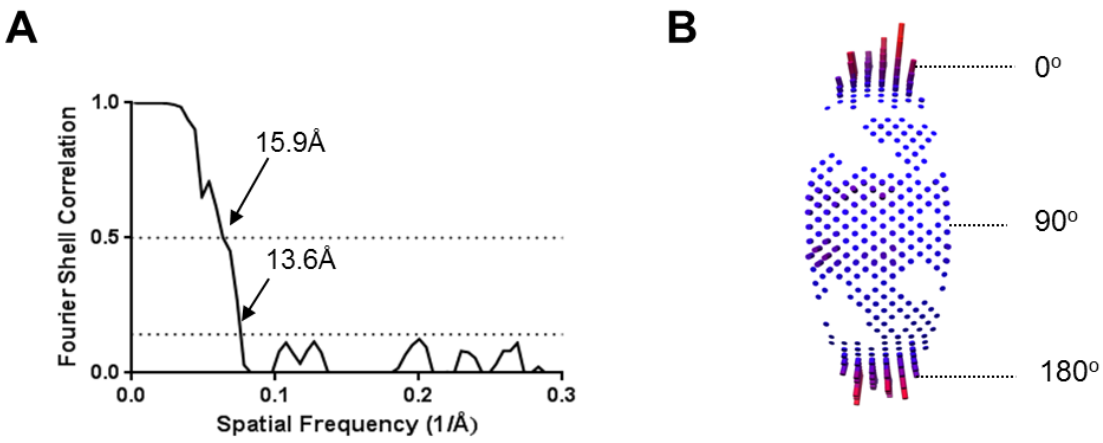

Figure 4.7 – Resolution assessment of the wild-type octamer structure. (**A**) Gold-standard Fourier shell correlation (FSC) of the wild-type octamer model, the calculated resolutions at 0.5 and 0.143 FSC criteria are shown. (**B**) Euler angle distribution of all particles used for calculating the octamer structure (C8 symmetry), relative heights of columns represent relative particle numbers for each angle, red columns denote angles with a high number of particles, with blue showing angles with relatively lower particle numbers.

However, the observed lack of structure in the central Rs1 domain region suggests that the resolution of the model is unlikely to be high in these regions, with local resolution fluctuations within the molecule. To assess this, ResMap-H2 analysis was employed (Kucukelbir, Sigworth et al. 2014). This procedure was applied to the wild-type dimer of octamers structure with the resolution distribution shown in figure 4.9C. Despite the overall resolution of 9.3Å calculated from 0.143 FSC, a large number of voxels were observed both at higher (6 - 8Å) and lower resolutions (10 - 15Å). Mapping of this revealed a distribution in which the higher observed resolutions were found in the core of the discoidin domain volume with lower resolutions observed towards the propeller tips (Figure 4.9D). Previously, it has been shown that the central β-sandwich structure which

stabilized the domain was highly rigid and conserved (Kiedzierska, Smietana et al. 2007). The observation of the highest resolutions in this core region of the discoidin domain volume is consistent with these previous observations. Furthermore, consistent with the observed lack of structure in the Rs1 domain regions observed in the reference-free class averages (Figures 4.4B and C) and loss of density in the subsequent reconstructions (Figures 4.6 and 4.8), the disconnected density possessed a markedly reduced resolution (Figure 4.9D). Again, this suggests the presence of disorder or flexibility.

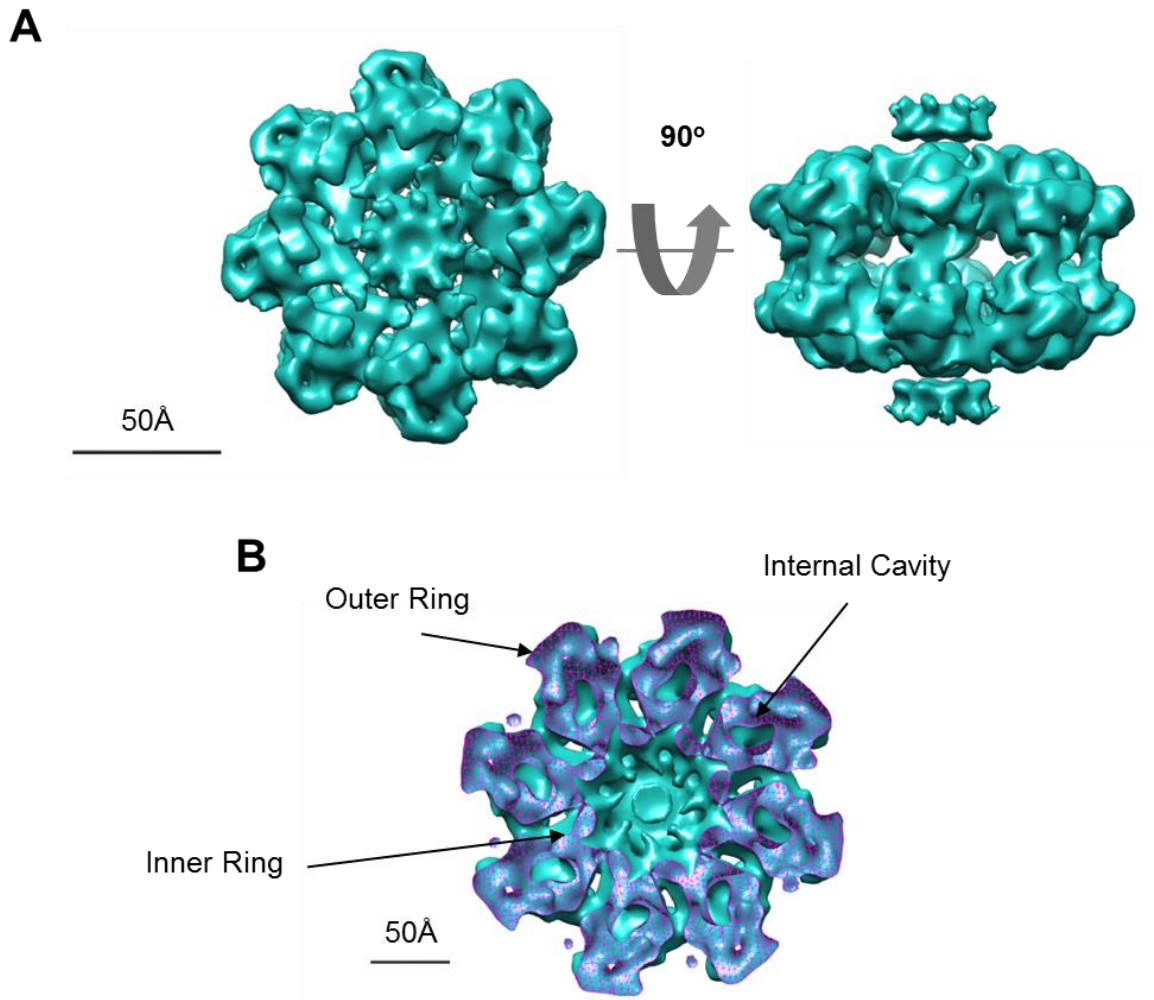

Figure 4.8 – Cryo-EM structure of the wild-type retinoschisin dimer of octamers. (**A**) The structure of the wild-type retinoschisin hexadecamer complex at 9.3Å resolution showing a distinct double-stacked propeller structure. (**B**) Volume slice through the hexadecamer, showing the internal structure consisting of an inner ring, with a cavity observed within each discoidin domain in the outer ring of the propeller.

Solution of the structures of the wild-type retinoschisin octamer and dimer of octamers allowed for investigation into potential conformational changes which may be induced upon octamer-dimerization. Using UCSF Chimera, the single octamer structure was fitted to the hexadecamer structure (Figure 4.10). This fitting observed high similarity in the structure of the retinoschisin octamer and one half of the dimer of octamers. As a result, this confirms the lack of gross conformational change of the retinoschisin octamer upon

dimerization and the assembled octamer presents a stable dimerization interface which facilitates the formation of the hexadecamer.

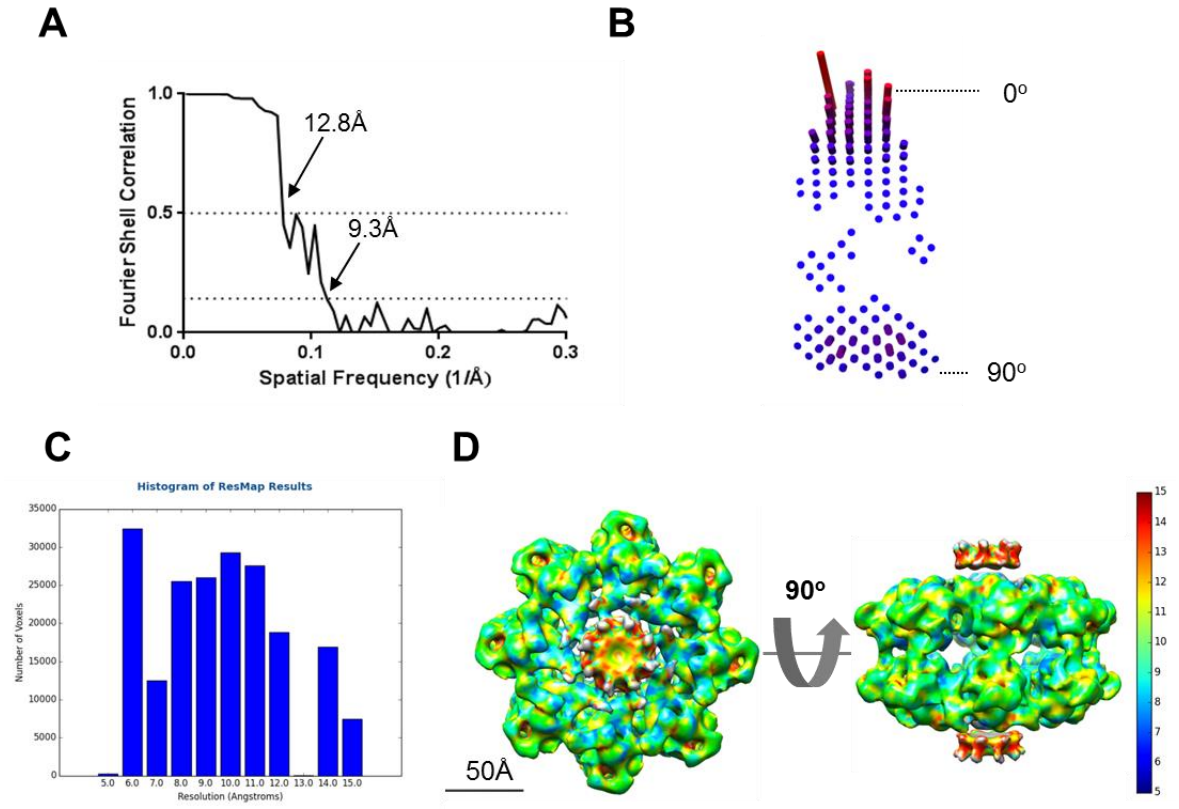

Figure 4.9 – Resolution estimation of the wild-type dimer of octamers complex. (**A**) Gold-standard Fourier shell correlation (FSC) of the wild-type octamer model, the calculated resolutions at 0.5 and 0.143 FSC criteria are shown. (**B**) Euler angle distribution of all particles used for calculating the octamer structure (D8 symmetry), relative heights of columns represent relative particle numbers for each angle, red columns denote angles with a high number of particles, with blue showing angles with relatively lower particle numbers. (**C**) ResMap-H2 analysis of the local resolution distribution within the wild-type model. Shown is a histogram of the number of voxels observed in the unfiltered half-models used for analysis in the resolution range sampled by ResMap-H2. (**D**) The wild-type hexadecamer structure rendered according to the observed local resolution within each region, as determined by ResMap-H2 analysis.

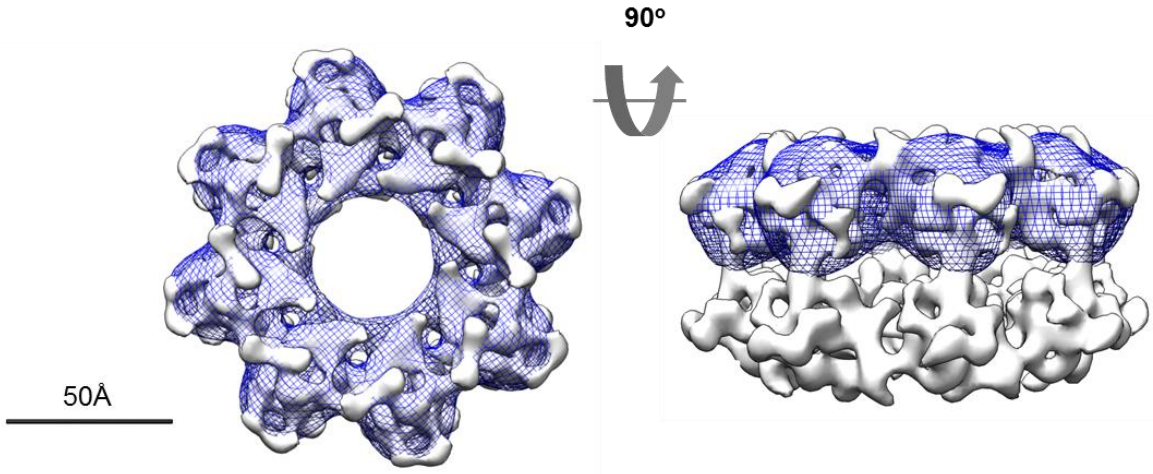

Figure 4.10 – Comparison of wild-type octamer and hexadecamer structures. Shown is the octamer structure at 13.6Å resolution (*blue mesh*) fitted to the hexadecamer structure (*white*) shown at 9.3Å resolution. Shown is a lack of major conformational change induced in the octamer structure upon dimerisation to form the hexadecameric oligomer.

4.4 Investigating the Hand and Subunit Structure of the Wild-Type Retinoschisin Dimer of Octamers

4.4.1 Retinoschisin Discoidin Domain Homology Model Construction

In order to investigate the hexadecamer structure, a homology model of the wild-type retinoschisin discoidin domain was constructed using the PHYRE2 webserver for fitting to the hexadecamer map (Kelley, Mezulis et al. 2015). As previously reported, the constructed homology model possessed the central eight-stranded β-sandwich structure consisting of two anti-parallel β-sheets, with three projecting spike regions thought to be essential in discoidin domain function (Figures 4.11A and B). Following cysteine bond insertion and energy minimization but prior to fitting to the retinoschisin hexadecamer structure, the homology model was assessed for stereochemical quality using the PROCHECK server. The resulting Ramachandran plot suggested a native protein fold is observed in the homology model. The vast majority of the residues were found in energetically permissible regions of the plot (97.8% of total residues), with just 3 residues from the total 157 disallowed (Figures 4.11C and D). Furthermore, calculation of the theoretical model-independent varaibles using the ScÅtter program gave an R_g of 15.4Å and a D_{max} of 53Å, very close to the values experimentally determined for the discoidin domain (Figures 3.10 and 3.11).

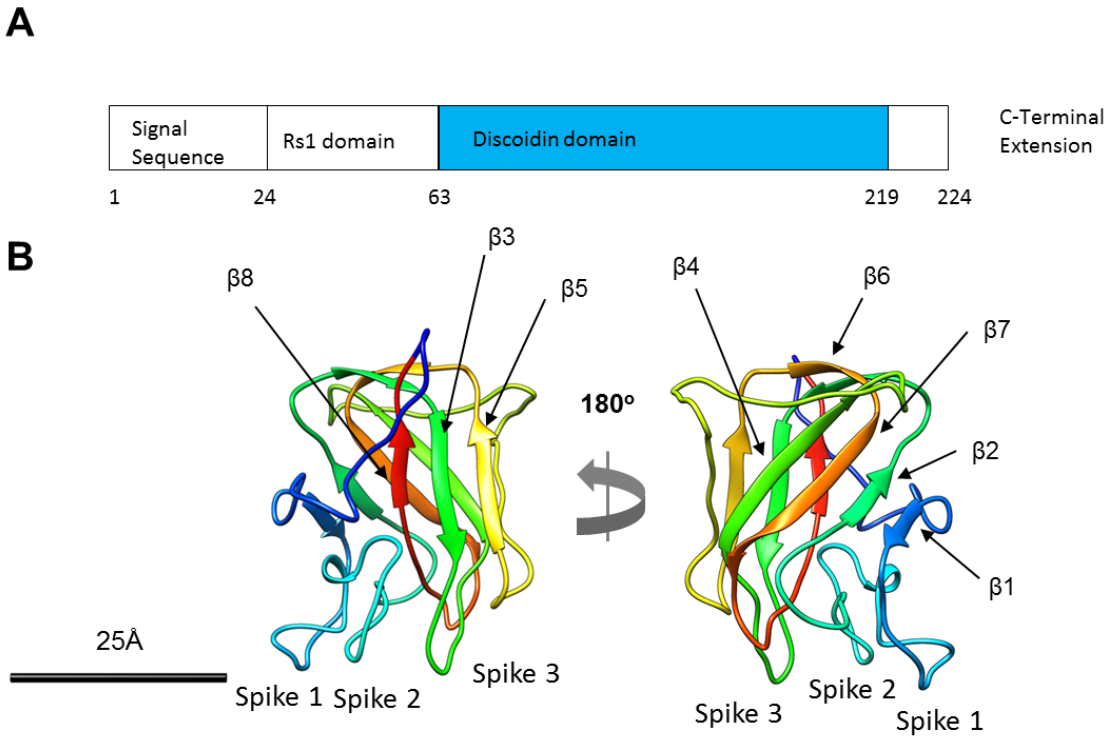

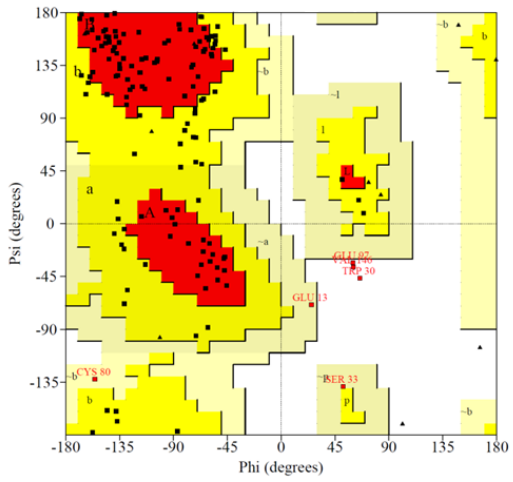

D

Residues in Most Favoured Regions	91	65.9%
Residues in Additional Allowed Regions	41	29.7%
Residues in Generously Allowed Regions	3	2.2%
Residues in Disallowed Regions	3	2.2%

Figure 4.11 – Construction of the wild-type discoidin domain homology model. (**A**) The modelled discoidin domain region highlighted in the schematic of the retinoschisin monomer sequence (*blue*) showing the considerable sequence proportion represented by the discoidin domain. (**B**) The discoidin domain homology model produced by Phyre2 webserver, with the major β-strands and spike regions labelled. (**C**) Ramachandran plot of the homology model stereochemistry, with relative proportions of residues found in energetically favourable and disallowed regions shown in (**D**).

4.4.2 Fitting the Discoidin Domain Homology Model to the Hexadecamer Subunit Structure and Hexadecamer Hand Determination

Subsequent fitting of this structure to the hexadecamer model was carried out using the DockEM program (Roseman 2000). Both the retinoschisin hexadecamer map and a calculated volume for the homology model were filtered to 9.5Å resolution, followed by the fitting into the hexadecamer structure at this resolution. This step prevented potential

noise in the hexadecamer map affecting the positioning of the domain within the structure. The fitting was performed as a global search of the density map with the search object, allowing for both translational and rotational searches, with the resulting fits scored according to both the cross correlational coefficient between the search object and the local fitted density and the number of standard deviations that the correlation value for this fit is observed to be over the mean of all fits calculated during the search. This procedure was followed for both the initial hand produced following refinement and the opposing hand (Figure 4.12). Due to the lack of handedness information present within each projected image of the molecule, such comparison to atomic models not only allows for determination of the correct hand of the density map, but is also required to produce an accurate quasi-atomic model of the retinoschisin complex. Indeed, such an atomic model-based approach to hand determination has been shown before with fitting of X-ray crystallography determined asymmetric unit structures to cryo-EM determined structures of rhinoviruses (Olson, Kolatkar et al. 1993), parvoviruses (Wikoff, Wang et al. 1994) and ΦX174 viruses (Ilag, Olson et al. 1995) used to determine the absolute hand of the virus capsid structure. As a result, this approach was employed for the retinoschisin hexadecamer structure due to the asymmetry observed in the discoidin domain homology model. Shown in figures 4.12A and B are the top five non-equivalent fits to both hands of the hexadecamer structure, with the respective correlation values and the number of standard deviations the observed fit is above the mean. Comparison of these individual fits (fits i-x) revealed a single fit that was of higher agreement than all other observed fits (Figure 4.12A, fit (i)). This fit had a higher correlation value than the corresponding highest correlated fit to the opposing hand of the structure (Figure 4.12B, fit (vi)), with closer comparison of these fits showing greater visual agreement between the initial hand and the discoidin domain homology model (Figure 4.13). This fit had good agreement with the model volume (Figure 4.13A) with the corresponding fit to the opposing hand (Figure 4.13B) showing regions of empty volume, regions of the homology model which protruded from the density map and β-strands crossing the central cavity in the Discoidin domain density. Together these observations suggest that the refinement selected the correct hand of the retinoschisin structure.

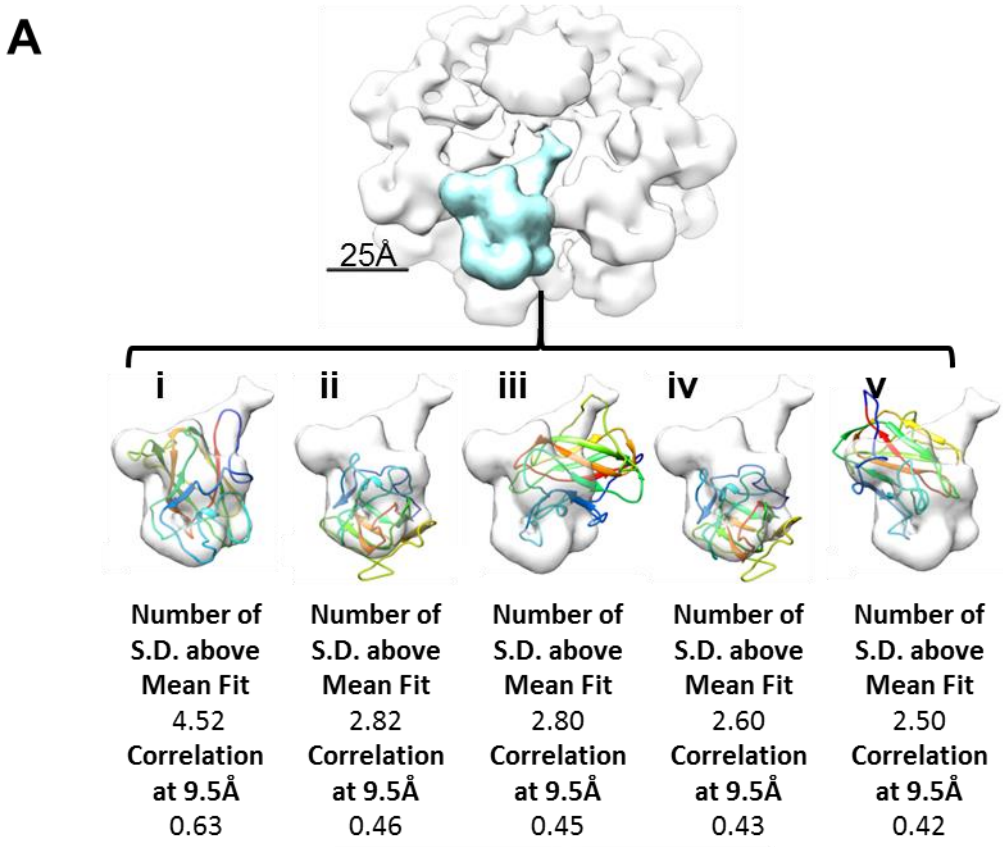

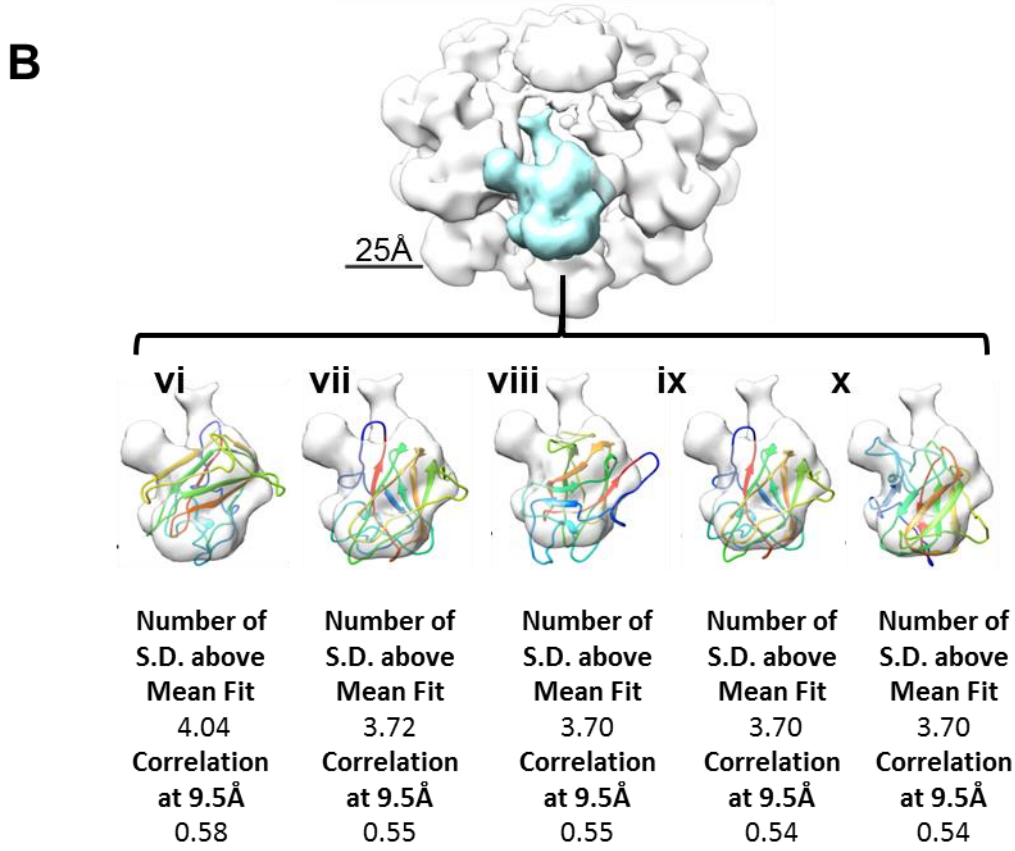

Figure 4.12 – DockEM Rigid body fitting of the wild-type discoidin domain into the (**A**) initial hand and (**B**) mirror hand of the dimer of octamers structure. Shown in blue is a single repeating subunit of the structure filtered at 9.5Å, into which the wild-type homology model was fitted. All fits were scored for significance (the number of standard deviations above the mean for all fits) and the correlation value at 4.5Å resolution. Shown are the top 5 non-equivalent fits for the initial (i-v) and mirror (vi-x) hands.

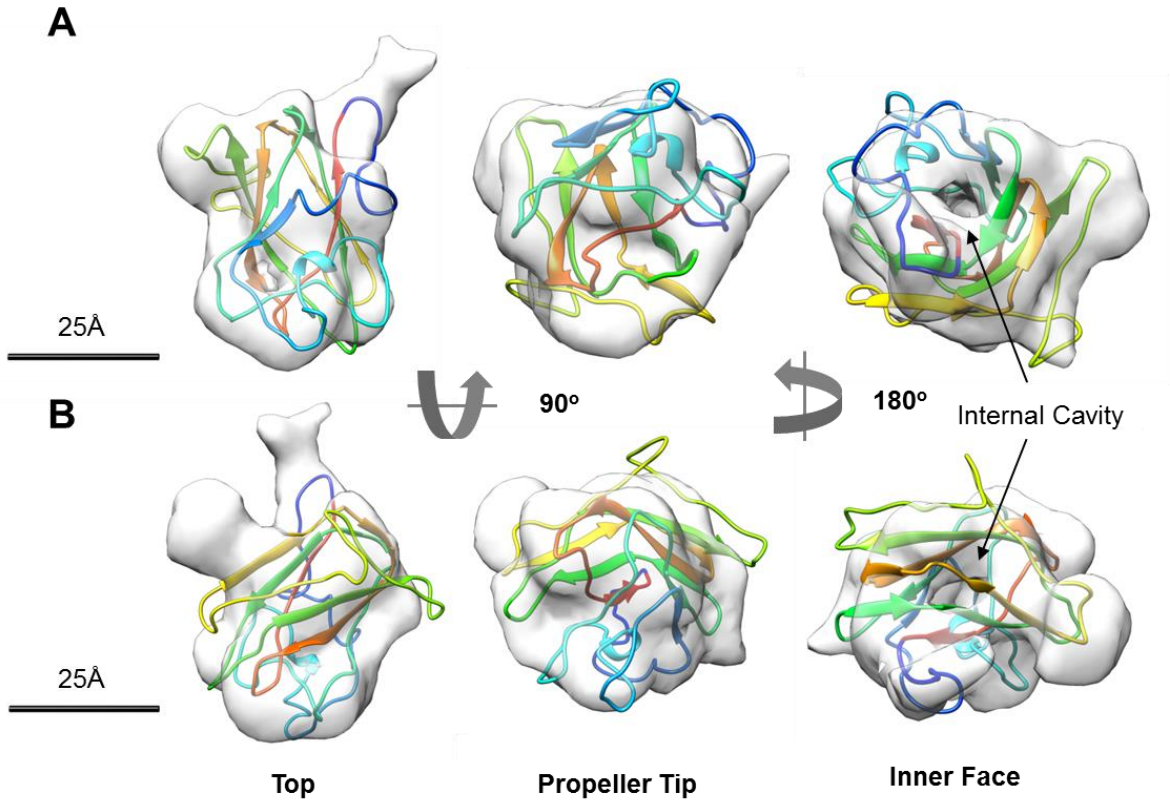

Figure 4.13 – Comparison between the DockEM fits of the initial hand and mirror hand. (**A**) The highest correlated fit of the initial hand and (**B**) the mirror hand to a single repeating subunit of each map, in each case the position of the inner cavity within the discoidin domain volume is marked.

4.4.3 The Quasi-Atomic Model for the Retinoschisin Dimer of Octamers

Following determination of the correct hand of the retinoschisin model, the highest quality fit was optimized by using the symmetrical fitting procedure in UCSF Chimera, allowing for preservation of the observed eight-fold symmetry observed within the octameric arrangement of the discoidin domains (Figures 4.2C and D). This yielded a final fit with a correlation of 0.9 at 9.5Å resolution, as assessed by UCSF Chimera. This allowed for construction of a quasi-atomic model of the assembled retinoschisin dimer of octamers (Figure 4.14A). This model reflected the highly planar structure previously observed for the retinoschisin octamer, with fitting of all sixteen subunits allowing for the identification of both interfaces within the octamer between the adjacent discoidin domains (intra-octamer interface) and between dimerizing octamers (inter-octamer interface). Shown in figure 4.14B, the intra-octamer interface is formed from the loop between β4 and β5 in one subunit contacting a surface consisting of the N-terminal region, spike 2 and strands β3, β5 and β8 in the adjacent molecule. In contrast, the contact interface between the octamer rings involved a lower proportion of the domain, with a smaller interaction interface. This site consisted of three main regions: the loops between β4 and β5, and β5 and β6 with another contribution from β7 (Figure 4.14C). In each instance, the loop between β4 and β5 appeared to form an integral part of both binding interfaces, we

speculate it could be potentially linking both interfaces, such that octamerisation may induce a conformational change in this loop region which then forms a stable interaction interface to facilitate further oligomerisation. However, in each case, the precise regions and residues involved in any interaction could not be accurately identified due to the limited resolution of the hexadecamer map, as a result, the identified regions represent an approximation of the binding interfaces.

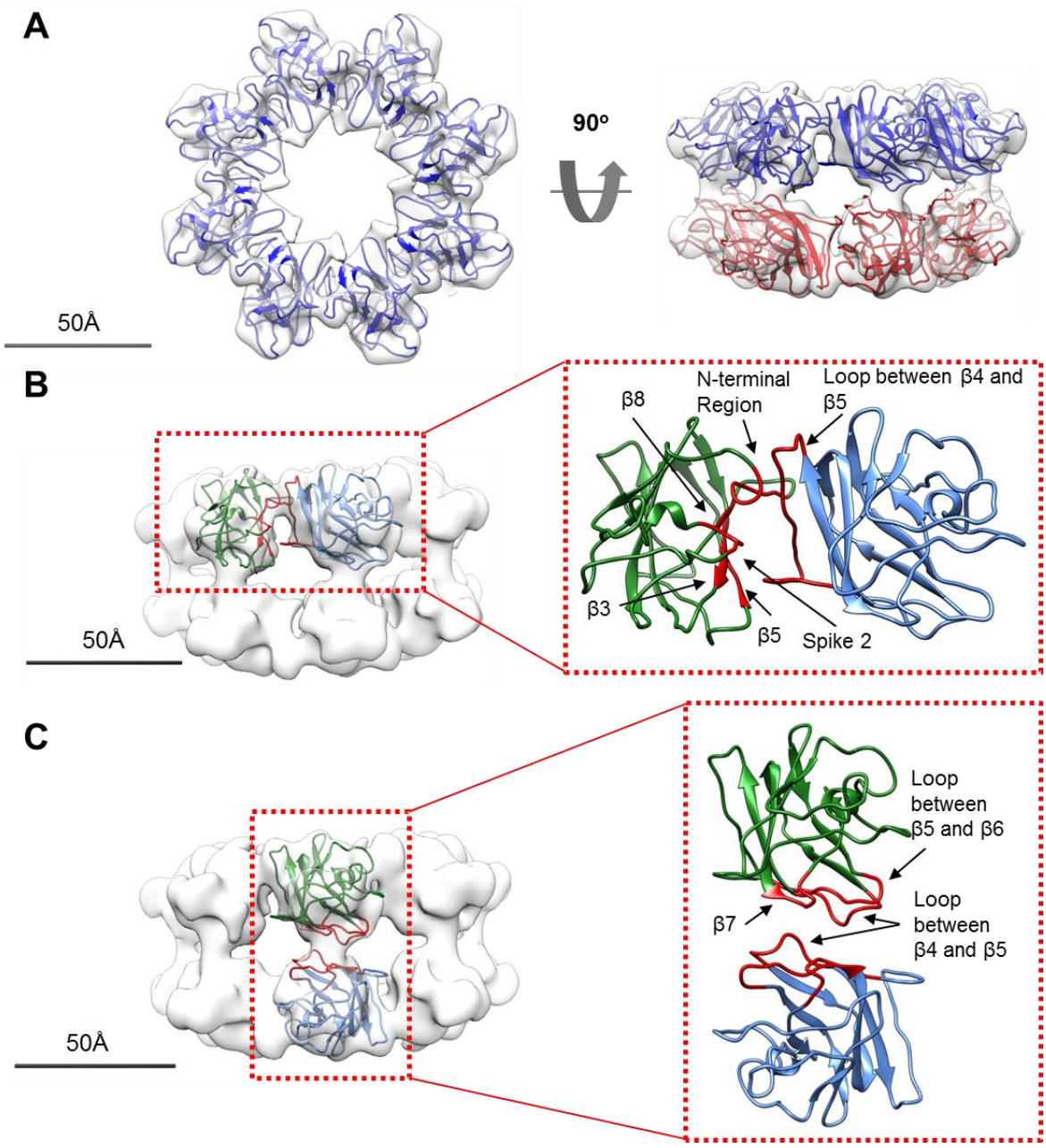

Figure 4.14 – The quasi-atomic model of the wild-type retinoschisin dimer of octamers. (**A**) The quasi-atomic model of the retinoschisin dimer of octamers with all fitted subunits shown. Subunits from opposing octamers in the dimer are coloured red and blue. (**B**) Investigation of the intra-octamer interface between adjacent discoidin domains, with interface regions shown in red (inset). (**C**) Investigation of the inter-octamer interface, with the contact sites between the rings shown in red (inset).

4.5 Discussion

In conclusion, wild-type retinoschisin octamer could be purified from the HEK293-EBNA system in sufficient quantities for structural analysis. Consistent with the observation of the retinoschisin octamer eluting from size-exclusion chromatography close to the elution volumes of the dimer and monomer despite the large difference in molecular weights (Figure 3.2C), MALS and AUC analysis revealed a compact octameric structure. Analysis of the frictional coefficient ratio (f/f_0 of 1.33) and the hydrodynamic radius (~5nm) suggested that the previously observed extended monomers assemble tightly to give only a modest increase in the octamer hydrodynamic size compared to the monomer (Figure 4.1). Indeed, negative stain microscopy revealed a tight octamer ring structure of individual subunits which possessed a striking eightfold symmetry, with a highly planar profile. Structural determination from this negative-stain analysis however was not possible due to significant orientation bias of the octamers into a 'top' orientation, suggesting the presence of a favourable interaction between the 'underside' of the retinoschisin octamers and the charged surface of the grid (Figure 4.2).

Therefore to allow for the structure of the retinoschisin octamer to be determined, the protein was analysed in the solution state, to remove the effects of any potential artefactual interactions between the grid substrate and the protein sample. However, this analysis required higher protein concentrations, with subsequent concentration of retinoschisin octamers revealing a higher order oligomer which was determined to represent a dimer of octamers together with a smaller population of planar retinoschisin octamers (Figure 4.3). Cryo-EM analysis reveled this double-stacked planar arrangement of two octamers assembled in a non-covalent manner (Figures 4.4). Exploitation of the latest DDD detectors together with the new maximum likelihood and three-dimensional classification methods (employed in the RELION 1.4 software suite), both distinct particle sets representing octamer and hexadecamer could be separated and resolved (Figure 4.5). Visualization of the octamer structure at 13.6Å resolution revealed the expected 'ring' of discoidin domains forming the flat octamer structure (Figure 4.6). Dimerization of this produced a double-stacked ring hexadecamer structure (visualized at 9.3Å resolution), formed through a small yet stable contact site between each opposing sets of discoidin domains (Figure 4.8). The small interaction interface suggests that this may represent an avidity type interaction requiring multiple clustered contact sites to be present to form this structure. In both structures the Rs1 domain appeared to produce a low contrast diffuse density in the reference-free class averages (Figures 4.4B and C) which could not be reconstructed into the three-dimensional structure (Figures 4.6A and 4.8A). This may reflect a lack of ordered structure in this region. Indeed, SAXS analysis of the retinoschisin monomer showed that despite the small size of this region, the domain adopted a highly extended structure (Figures 3.12B and C), suggesting that the centre of the molecule may

be highly flexible or not assemble in a symmetrical arrangement, preventing efficient averaging of these densities into a discrete density.

Comparison of the octamer with the hexadecamer structure indicated little conformational change in the retinoschisin octamer upon dimerization (Figure 4.10), suggesting that the formation of the octamer also produces a stable dimerization interface for construction of the hexadecamer structure. Fitting of the homology model representing the discoidin domain allowed for the correct hand to be assigned to the hexadecamer (Figure 4.12), with the unambiguous positioning of the domain in the hexadecamer allowing for subsequent construction of a quasi-atomic model (Figure 4.14). Here, the tight assembly of the subunits was apparent with a 'lock and key' like insertion, with the projection of the loop between β4 and β5 into the apparent binding site on the adjacent domain, consisting of β3, β5, β8 and the N-terminal region (Figure 4.14B). However, consistent with the observations within the density maps, the contact between the octamer rings in the fitted atomic models was small, consisting of three small regions of the discoidin domain (Figure 4.14C). In each interface, the spikes were found to have minimal participation, consistent with their role in mediating other, intermolecular interactions in homologous proteins. Therefore, this suggests that the loops with their lack of participation in the stabilizing interfaces may have a separate, distinct function.

Comparison of analyses at different concentrations suggested that the higher-order hexadecamer appears to self-assemble in an apparent concentration-dependent fashion. At lower concentrations (of ~20µg/ml), MALS and AUC analyses observed a highly monodisperse sample with a molecular weight of ~190 kDa, suggestive of a pure octamer complex (Figure 4.1). Furthermore, imaging of this sample under negative-stain conditions at this concentration revealed only planar 'side' views (Figure 4.2B), however, it is possible that the high 'top' bias in this data set may prevent detection of a small number of hexadecamer molecules. However, concentration of the sample (to concentrations of ~100µg/ml) revealed a marked amount of dimerized octamer particles in both nativePAGE and cryo-EM analysis (Figures 4.3 and 4.4), in stark contrast to analyses at lower concentration. As a result, we hypothesize that the retinoschisin octamer is able to self-assemble into a hexadecamer complex, which due to the stable nature of the assembly and the fact that retinoschisin exists immobilized on opposing membranes, may form *in vivo* and represent the fully-assembled, physiologically relevant species.

From the observation of this self-assembly we propose a model for retinoschisin structure in the mammalian retina. Previously, gold-labelled immuno-EM of endogenous retinoschisin in fixed mice retinal sections displayed a clear clustering of retinoschisin molecules on the outer leaflet of the plasma membrane of photoreceptor inner segments.

In wild-type animals, the photoreceptors are closely spaced in a characteristic columnar arrangement of cells, with retinoschisin found between the cells, forming additional structures which appeared to span the gap between the cells and make contact with both adjacent membranes. This suggested the presence of a physical linker being formed by retinoschisin (Vijayasarathy, Takada et al. 2007). Indeed, deletion of retinoschisin in *Rs1h*$^{-/-}$ mice led to a loss of tight clustering of these cells, with large cavities formed between the cells (Vijayasarathy, Takada et al. 2007). Furthermore, the participation of known binding partners for retinoschisin in this structural support has also been observed. The Na/K-ATPase was previously shown sufficient to drive membrane association of retinoschisin in HEK293 cell systems, with deletion of the ATP1B2 in mice models leading to a reduction of membrane association of retinoschisin (Friedrich, Stohr et al. 2011). However, more recently, antibodies raised against endogenous retinoschisin gave intense staining also at the surface of synaptic terminal membranes at the synapse between photoreceptors and bipolar cells (Ou, Vijayasarathy et al. 2015). This region, in the outer plexiform layer of the retina, represents the first synaptic transmission of the light stimulus signal from the photoreceptors to the bipolar cells, initiating the stimulus decoding process in the retina. This signal transduction relies on a host of integral membrane complexes on both the pre and post-synaptic membranes (Hoon, Okawa et al. 2014). Principal among these is the L-type voltage gated calcium ion channel CaV1.3, a retinal specific isoform which has been previously established as a binding partner for retinoschisin (Shi, Jian et al. 2009). Knockout of retinoschisin in the synaptic mouse model described by Ou et al. led to loss of pre-synaptic localisation of CaV1.3 on the pre-synaptic membrane, with loss of normal membrane localisation. This correlated with dysregulation of calcium ion gradients in the rod photoreceptor cells. Interestingly, this also correlated with a loss of membrane localisation of TRPM1, mGluR6 and the rest of the signalling machinery (including RGS11, Gβ5 and $G_{\alpha 0}$) on the post-synaptic bipolar cell (Ou, Vijayasarathy et al. 2015). This was followed by diffusion of these components into the cell body, away from the synaptic termini leading to a deterioration of the signal transduction at this synapse, characteristic in XLRS sufferers (Vincent, Robson et al. 2013) and retinoschisin null mice (Zeng, Takada et al. 2004, Min, Molday et al. 2005, Kjellstrom, Bush et al. 2007). However, re-introduction of wild-type retinoschisin using AAV8 vectors led to rescue of the synaptic localisation of the signalling machinery simultaneously on opposing pre and post-synaptic membranes, with a following increase in synaptic signalling (Ou, Vijayasarathy et al. 2015).

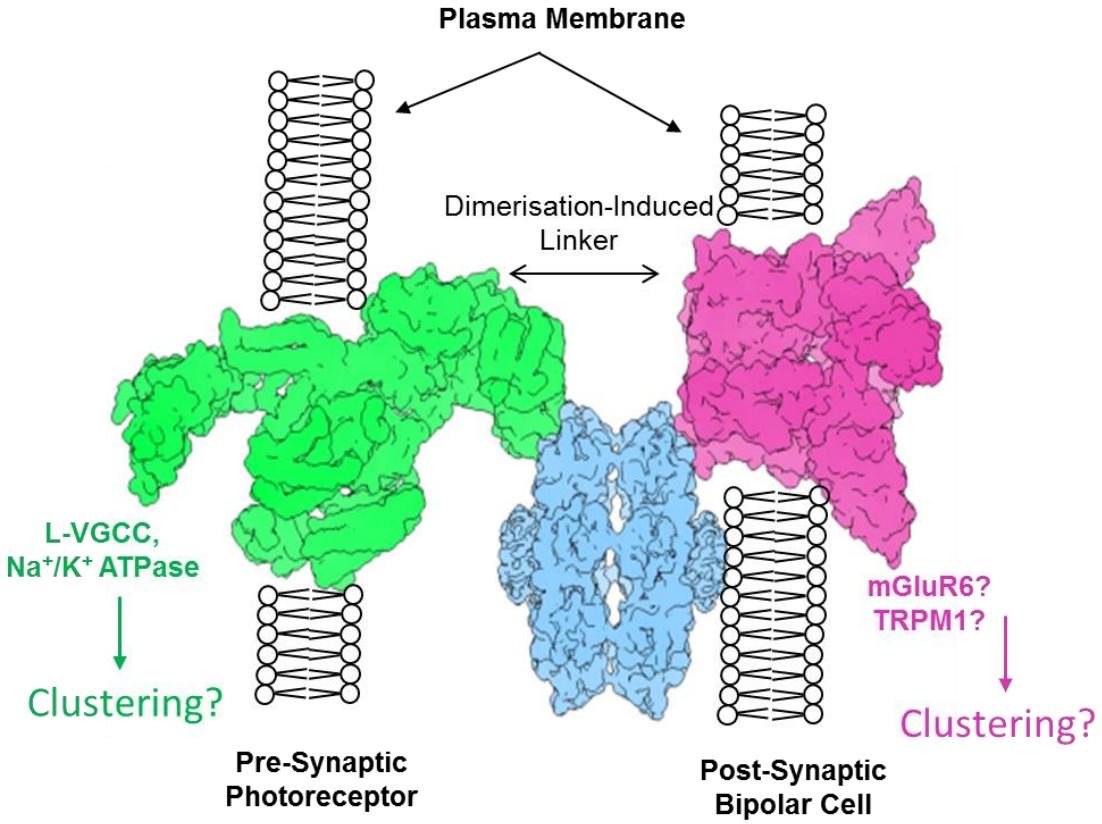

Figure 4.15 – Model for retinoschisin function at the photoreceptor-bipolar cell synapse. Concentration-dependent octamerisation of immobilised retinoschisin octamers on opposing membranes allows for the formation of physical linkers between the membranes. This allows for co-localisation and co-ordinate regulation of membrane complexes at the surface of each cell, with the high valency of the retinoschisin molecule potentially clustering the binding partners. This may allow for the formation of 'signalling clusters which could allow for more efficient neurotransmission across the synapse.

Together, these studies suggest retinoschisin is able to co-ordinately regulate the membrane localisation of binding partners on opposing membranes. In the proposed model, shown in figure 4.15, this co-ordinate regulation would be achieved via stable octamer dimerization at the membrane surface. Here, retinoschisin immobilized on each membrane through binding to integral membrane components would be brought into close interaction, increasing the local concentration of the protein, driving concentration-dependent hexadecamer formation. This would generate symmetrical physical linkers between cells which could maintain close association of photoreceptors (between cells) and also maintain signalling machinery clustered at the photoreceptor-bipolar cell synapse. As well as providing a structural linker at the synapse, the potential clustering of signaller and signal receptor together may increase the efficiency of neurotransmission at this synapse. This would point towards a possible dual function for retinoschisin within the retina, a structural and also signal tuning function. Indeed, it has been observed that correction of the fluid filled cysts in mice model and human XLRS patients using carbonic anhydrase inhibitors, lead to normal laminar architecture being re-established (Apushkin and Fishman 2006, Walia, Fishman et al. 2009, Genead, Fishman et al. 2010, Collison, Genead et al. 2014), but did not correlate with an increase in the visual processing

capacity of the retina (Khandhadia, Trump et al. 2011, Zhour, Bolz et al. 2012). We suggest that this phenotype is due to a loss of the additional synaptic coupling function of retinoschisin between photoreceptor and bipolar cells, potentially required for efficient signalling.

In each case, this model requires retinoschisin to be quite promiscuous in its binding partner, with multiple diverse binding partners implicated. This could be achieved through retinoschisin exploiting the common glycosylated character of the ectodomains of binding partners, with retinoschisin previously being demonstrated as a galactose-specific lectin (Dyka, Wu et al. 2008). Indeed, the 'spike' regions of the retinoschisin discoidin domain are positioned away from the interfaces required for complex assembly, projecting into the propeller tips of the octamer suggesting they may have an additional function, such as mediating inter-protein interactions and membrane localisation of the octamer via carbohydrate binding. Such binding mode would exploit the octameric character of the retinoschisin molecule, generating a highly multi-valent 'core' onto which the signalling machinery could be clustered and arranged. Also, through adopting this simple molecular function, retinoschisin would be able to perform both functions of retinal structural maintenance and synaptic signalling regulation in the retina as a function of the localisation of the protein within the retinal tissue.

Recently, the findings of this study have been confirmed. Wild-type retinoschisin was observed by Tolun et al. to form paired octamer rings in a hexadecamer complex, which could be sandwiched between adjacent cell membranes, forming a stabilizing 'array' of retinoschisin dimers of octamers (Tolun, Vijayasarathy et al. 2016). However, despite these recent structural insights, the precise molecular function remains elusive, with biochemical and mutational analysis required to confirm a mechanism of function.

5 Results Chapter 3: Structural Characterisation of R141H Retinoschisin

It has been well established that the vast majority of XLRS-associated mutations lead to the intracellular retention and loss of secretion of the retinoschisin octamer (Wang, Waters et al. 2002, Wu and Molday 2003, Wang, Zhou et al. 2006, Dyka and Molday 2007, Walia, Fishman et al. 2009, Vijayasarathy, Sui et al. 2010). However, a small subset has been identified which can still be secreted yet cause disease, therefore representing a functionally defective octameric complex (Wang, Zhou et al. 2006). Such mutants may allow for the identification of functional sites within the molecule, yielding potentially informative insights into the mechanism of retinoschisin function. To this end, the structure of the R141H mutant monomer and octamer was investigated. This mutant has previously been shown to lead to alterations in both ligand binding (Dyka, Wu et al. 2008) and alter the activity of binding partners at the membrane (Shi, Jian et al. 2009). As a result, the alteration induced by this mutation was investigated using a combination of MALS, AUC, SAXS, protein stability analyses and electron microscopy.

5.1 Purification of R141H Retinoschisin

As previously described for the wild-type retinoschisin (Figure 3.1), R141H retinoschisin was expressed from the pCEP-Pu/AC7 expression construct, with purification via the C-terminal His_6-tag. R141H retinoschisin secreted into the medium was purified using Ni-affinity chromatography. Shown in figure 5.1A, a protein product migrating at approximately 25 kDa under reducing conditions was eluted from the Ni-affinity column, which was reactive with the anti-His_6 antibody (Figure 5.1B). This recombinant species showed disulphide-dependent oligomerisation, with western blotting against the His-tag during non-reducing SDS-PAGE analysis showing a mixture of dimer and higher order oligomeric species (Figures 5.1B). Size-exclusion chromatography, removing the observed contamination in His-elutes observed three major species expressed for the mutant construct (Figures 5.1C), with tryptic digest mass spectrometry confirming the identity of the species migrating at 25 kDa as retinoschisin (Figure 5.1D). The peptide corresponding to the mutation site was not observed in the mass spectrometry data. To confirm the mutation of the retinoschisin construct, intact mass spectrometry of the purified monomer was carried out (Figure 5.1E). Purified wild-type retinoschisin monomer showed two species, with the species migrating at 24934.16 Da representing the retinoschisin sequence with five additional N-terminal residues from the BM40 signal sequence. This was in good agreement with the theoretical molecular weight of this construct (within 0.1 Da agreement). The additional species observed at 25268.71 Da, however, was unable to be accurately assigned to a retinoschisin sequence. As a result, this may represent a form which has been modified with a small molecule adduct or has

altered N-terminal processing. As a result, the molecular weight corresponding to unmodified retinoschisin was defined as 24934.16 Da. Measurement of the R141H yielded a molecular mass of 24915.39 Da, which agreed with the theoretical mass of the retinoschisin sequence with both the R to H mutation and five additional N-terminal amino acids from the BM40 sequence inserted (to within 0.1 Da agreement). Indeed, the mass difference observed between the two constructs (of 18.8Da) corresponds closely to the mass difference between an arginine and histidine amino acid (19.1 Da).

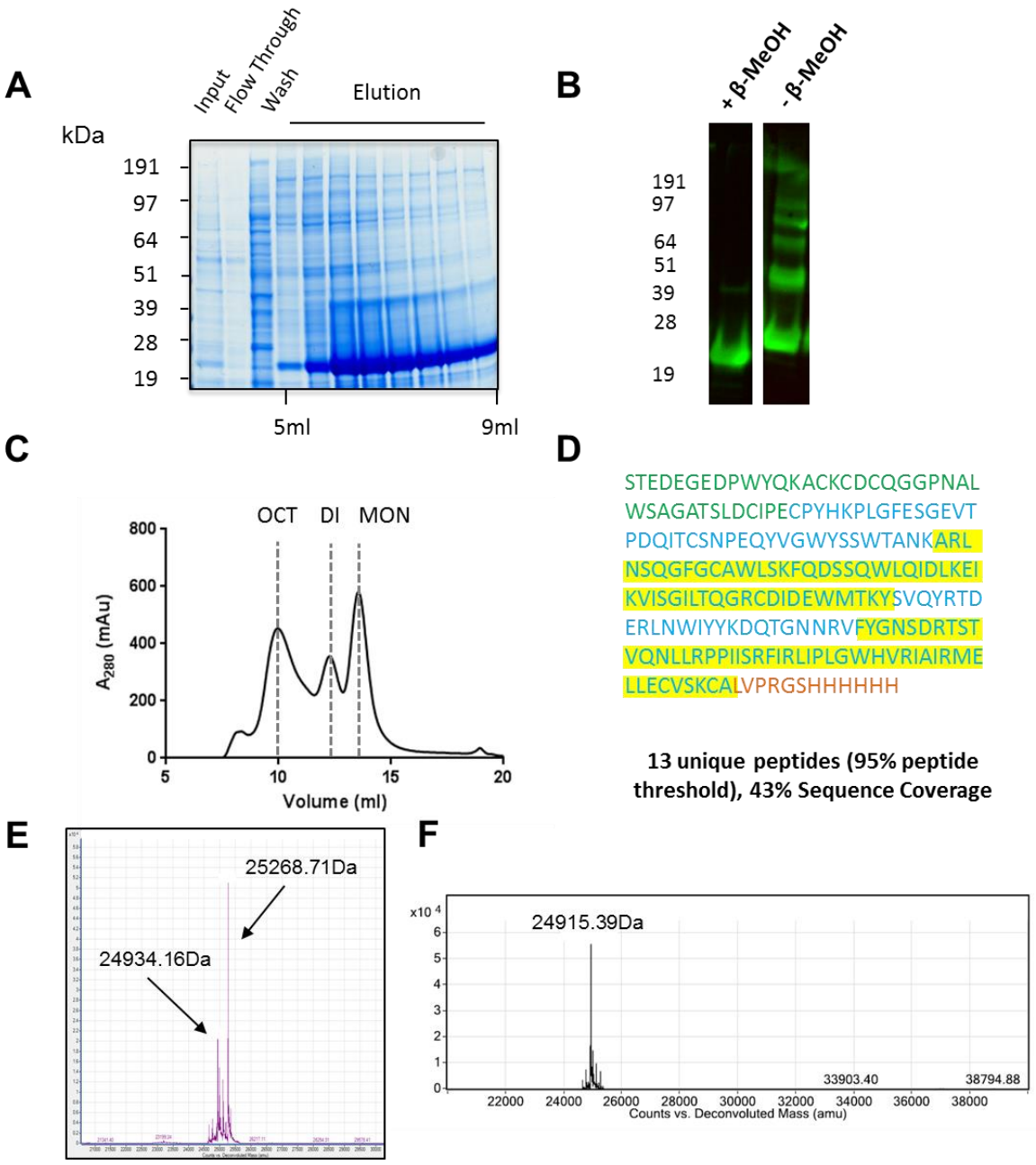

Figure 5.1 – Purification of R141H retinoschisin from HEK293-EBNA cell system. (**A**) Coomassie-stained reducing SDS-PAGE of Ni-NTA purification of recombinant, R141H retinoschisin showing input, flow through, wash and elution fractions. (**B**) Western blotting against the C-terminal His_6-tag carried out under reducing (+β-MeOH) and non-reducing (-β-MeOH) conditions, showing disulphide-dependent oligomerisation of the recombinant protein. (**C**) Size Exclusion Chromatography of His-purified R141H retinoschisin, showing three main species of octamer (OCT), dimer (DI) and monomer (MON) purified from the HEK293-EBNA system. (**D**) Tryptic-digest mass spectrometry identification of the major purified species, confirming retinoschisin identity. Shown in yellow are the peptides observed during mass spectrometry analysis. Regions of the construct sequence are shown; Rs1 domain (green), discoidin domain (blue) and thrombin cleavage site together with His-tag (orange). (**E**) Intact mass spectrometry of purified wild-type monomer , showing two species of 24934.16 Da and 25268.71 Da. (**F**) Intact Mass Mass-Spectrometry analysis of purified R141H retinoschisin monomer, showing a main species with a molecular weight of 24915.39 Da.

5.2 Hydrodynamic Characterisation of R141H Retinoschisin

5.2.1 Hydrodynamic Characterisation of the R141H Monomer

Initially, the structure of the R141H mutant monomer was probed using hydrodynamic measurements. MALS (Figures 5.2A and B) and AUC analyses (Figures 5.2C and D) reported similar hydrodynamic values for the monomer, with an $S_{(20,w)}$ of 2.5, a difference of 0.1S compared to the wild-type protein (Figures 3.3Bi and Bii). Similarly, the reported R_h values for both AUC and MALS analysis corresponded to those for the wild-type construct. The R_h of the mutant was 2.7nm from MALS, (Figures 5.2A and B) close to the wild-type 2.8nm (Figures 3.3A and B). The AUC data also showed good agreement for the mutant 2.3nm R_h (Figure 5.2B), similar to the 2.4nm for the wild-type (Figure 3.3Bii). Indeed, the similarity between the two constructs was highlighted through comparison of the sedimentation profiles, with both purified preparations showing a similar continuous distribution following sedimentation (Figure 5.2E).

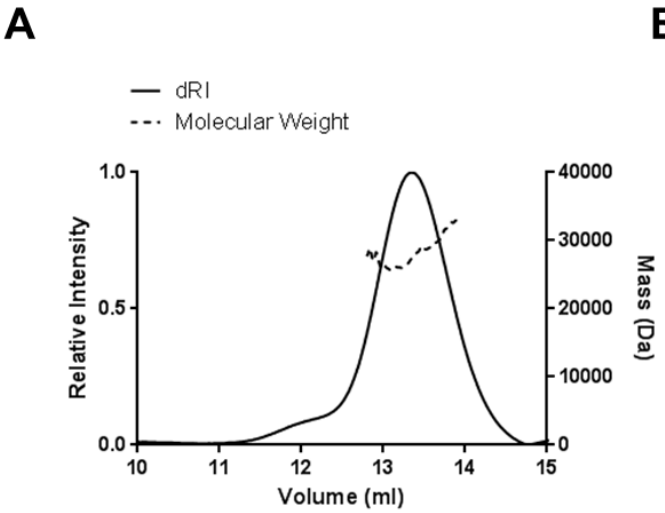

B

Molecular Weight (kDa)	28.6
Hydrodynamic Radius (nm)	2.7
Polydispersity	1.005

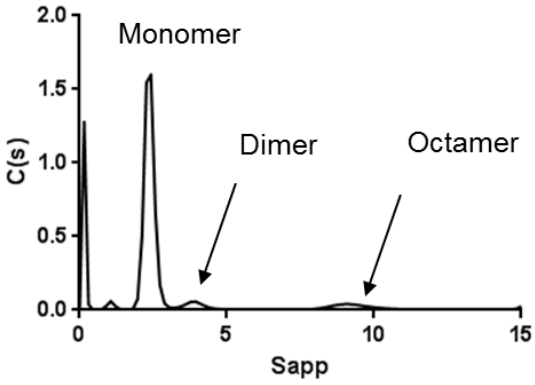

D

Molecular Weight (kDa)	25
Sedimentation Coefficient ($S_{(20,w)}$)	2.5
Hydrodynamic Radius (nm)	2.3
f/f_0	1.21

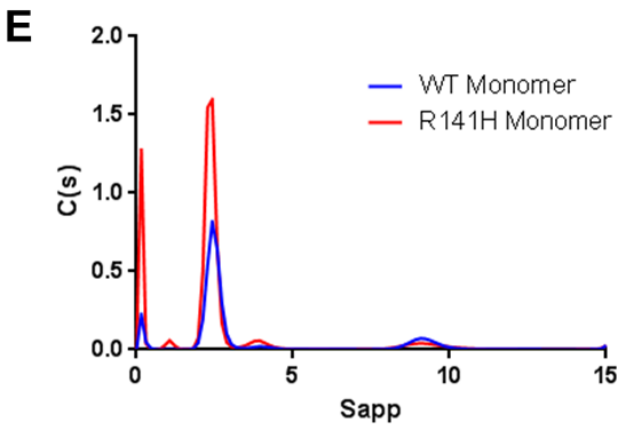

Figure 5.2 – Hydrodynamic analysis of purified R141H retinoschisin monomer. (**A**) SEC-MALS analysis of R141H retinoschisin monomer. (**B**) Extracted hydrodynamic values from SEC-MALS analysis. (**C**) AUC analysis of R141H retinoschisin monomer analysed using model-based continuous distribution (C(s)). (**D**) Hydrodynamic parameters obtained from AUC analysis. (**E**) C(s) distribution comparison between the wild-type and R141H monomers.

5.2.2 Hydrodynamic Characterisation of the R141H Octamer

To investigate if the R141H mutation alters the structure following assembly into the octameric form, the purified mutant octamer was analysed. MALS analysis of purified R141H octamer had an R_h of 5.5nm (Figures 5.3A and B), showing 0.3nm difference from

the wild-type (Figures 4.1A and B). Similarly, AUC analysis corroborated this observation, with a difference of 0.4S in the $S_{(20,w)}$ value and 0.1nm in the R_h (Figures 5.3C and D and 4.1C and D). Indeed, as observed for the comparison between the wild-type and mutant monomers, mutant and wild-type octamers had a very similar continuous distribution in the sedimentation profile (Figure 5.3E). As a result, hydrodynamic analyses suggested that R141H does not induce any gross conformational change in either the monomer or octamer.

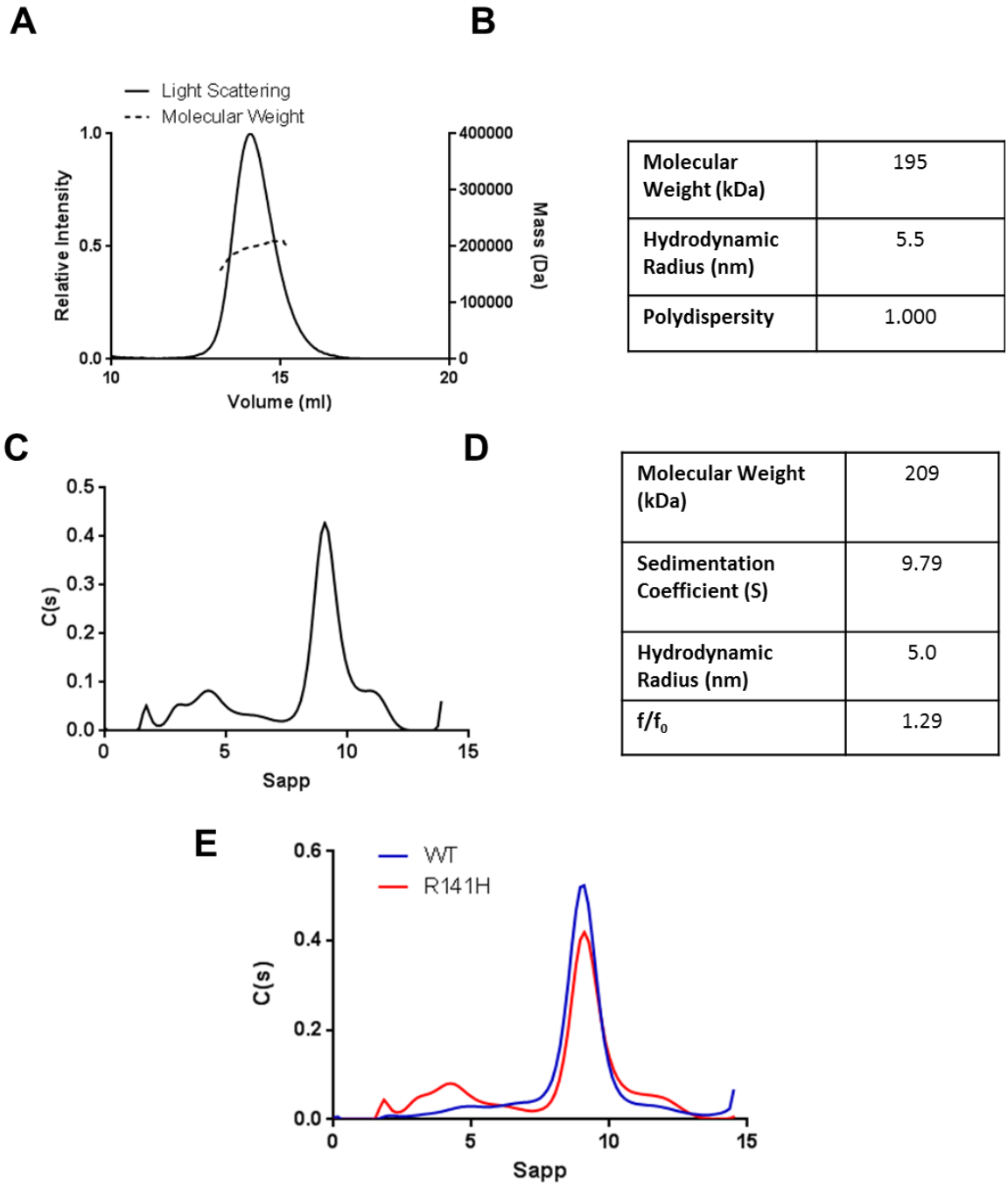

Molecular Weight (kDa)	195
Hydrodynamic Radius (nm)	5.5
Polydispersity	1.000

Molecular Weight (kDa)	209
Sedimentation Coefficient (S)	9.79
Hydrodynamic Radius (nm)	5.0
f/f_0	1.29

Figure 5.3 – Hydrodynamic analysis of purified R141H retinoschisin octamer. (**A**) SEC-MALS analysis of R141H retinoschisin octamer. (**B**) Extracted hydrodynamic values from SEC-MALS analysis. (**C**) AUC analysis of R141H retinoschisin octamer analysed using model-based continuous distribution (C(s)). (**D**) Hydrodynamic parameters obtained from AUC analysis. (**E**) (s) distribution comparison between the wild-type and R141H octamers.

5.3 Comparative Stability Analysis between the wild-type and R141H Retinoschisin

5.3.1 Comparative Stability of wild-type and R141H Monomers

In the absence of a conformational alteration, the stability of the mutant complex was probed to determine if the mutation destabilized the protein fold. To this end, purified wild-type and R141H monomer was subject to a temperature ramp experiment, in which exposure to high temperatures induced unfolding of the protein, with the thermostability of the protein expressed as the Unfolding Temperature (T_m), the temperature at which 50% of the protein sample is unfolded (Vieille and Zeikus 2001). Shown in figure 5.4A is the measured intrinsic fluorescence of the wild-type and mutant monomers as a function of increasing temperature. Here, the unfolding reaction is followed using the Barycentric Mean Fluorescence (BCM) of the protein constructs. This is defined as:

$$BCM = \frac{\Sigma\, I(\lambda) \cdot \lambda}{\Sigma \mathrm{I}(\lambda_{all})}$$

where *I(λ)* was the fluorescence intensity at wavelength (*λ*). Here, the sum of the product between each wavelength and the fluorescence intensity at each wavelength is divided by the sum of total fluorescence across all wavelengths ($\Sigma \mathrm{I}(\lambda_{all})$), calculating the 'centre of mass' (barycentre) of the fluorescence signal (Garstka, Fish et al. 2015). This tends to increase upon protein unfolding due to exposure of the fluorescent tryptophans and tyrosines to the solvent. T_m was defined at the first differential peak in the BCM signal, giving a measure of protein stability (Figure 5.4B) (Garstka, Fish et al. 2015). In both cases, the wild-type and mutant retinoschisin had highly similar melting temperatures of approximately 60^{o}C, suggesting that the mutation did not destabilize the retinoschisin monomer. This was corroborated with an independent measure of protein stability, using Differential Scanning Fluorimetry (DSF). This method relies on the use of the dye Sypro Orange, which binds to exposed hydrophobic regions of proteins upon unfolding (Pantoliano, Petrella et al. 2001, Niesen, Berglund et al. 2007). This binding interaction induces an increase in the fluorescence intensity of the dye, with the differential of this increasing signal over a temperature ramp experiment defining the T_m (Pantoliano, Petrella et al. 2001). Similar to the BCM-based analysis, the DSF analysis (Figure 5.4C) determined a melting temperature of 61^{o}C for both wild-type and R141H monomers (summarized in figure 5.4D). Consistent with the thermostability assays, static light scattering at 473nm (which detects the presence of large aggregates) of both wild-type and mutant protein expressed as a function of increasing temperature did not show any increase in the aggregation propensity of the retinoschisin monomer upon mutation (Figure 5.4E).

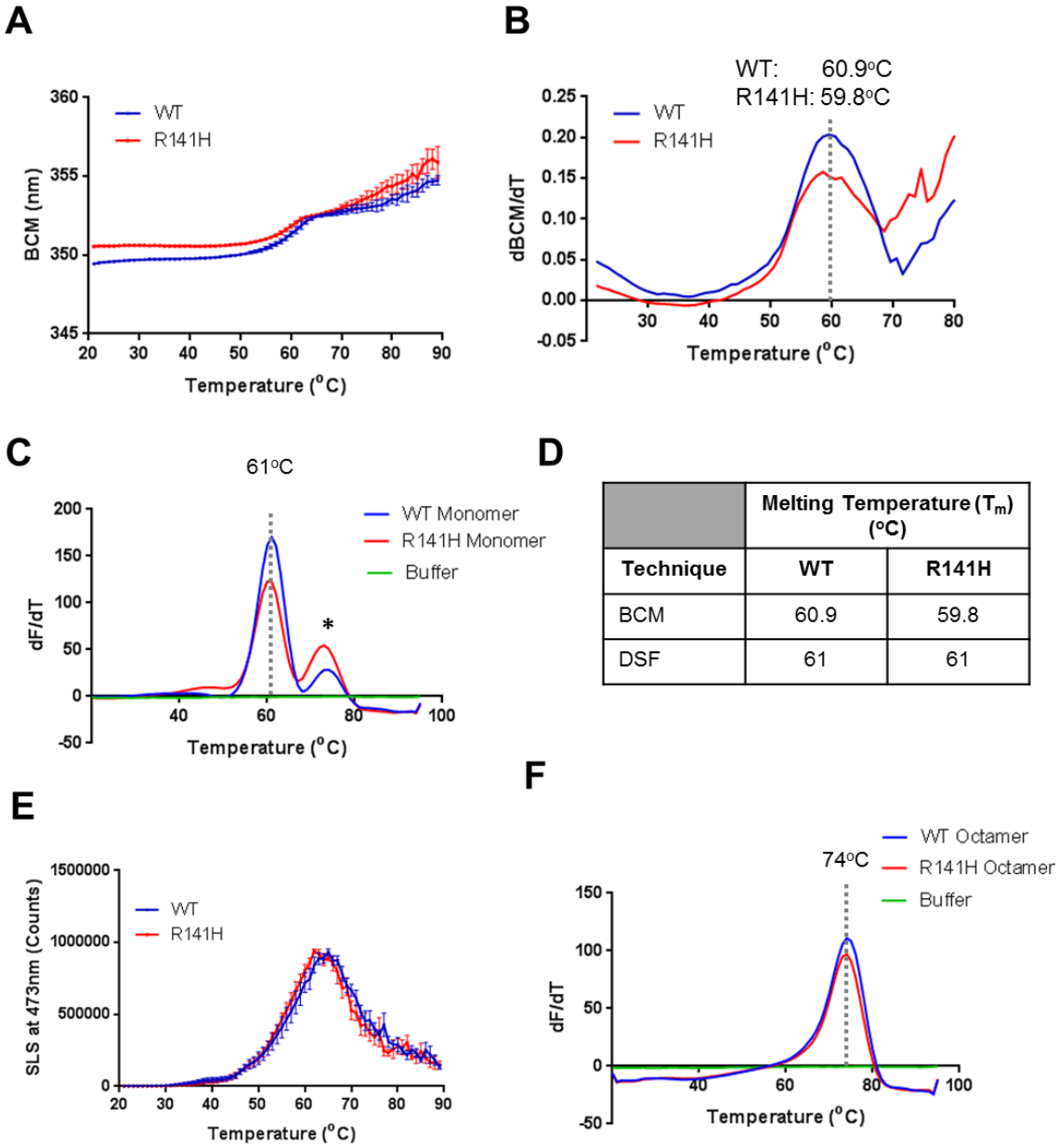

Figure 5.4 – Comparative thermal stability of wild-type and R141H retinoschisin. (**A**) Barycentric Mean Intrinsic fluorescence of purified wild-type and R141H monomers during heating from 20°C to 90°C, showing the unfolding reaction of both proteins (n=7). (**B**) The mean differential of the observed unfolding reaction, with the measured melting temperature marked (n=7). (**C**) Differential scanning fluorescence of the purified wild-type and R141H monomers, having the same melting temperature for both proteins (n=5). (*) denotes contaminating octamer. (**D**) Tabulated melting temperatures for both constructs determined by each technique. (**E**) Static Light Scattering (SLS) profiles of wild-type and R141H monomers revealing similar aggregation characteristics (n=5). (**F**) Differential scanning fluorescence of the purified wild-type and R141H octamers, showing the same melting temperature for both proteins (n=5).

5.3.2 Comparative Stability of wild-type and R141H Octamers

Despite the lack of effect on the retinoschisin fold, it was possible that the mutation was sufficient to induce destabilization of the octameric complex through alteration of binding interfaces between the monomers. To this end, the DSF approach was exploited to compare the thermostability of wild-type and R141H octamers. As shown in figure 5.4F, both wild-type and mutant octamers had the same T_m of 74°C with the same single

transition. Taken together these data suggests that the R141H mutation does not affect the stability of the retinoschisin fold or oligomers.

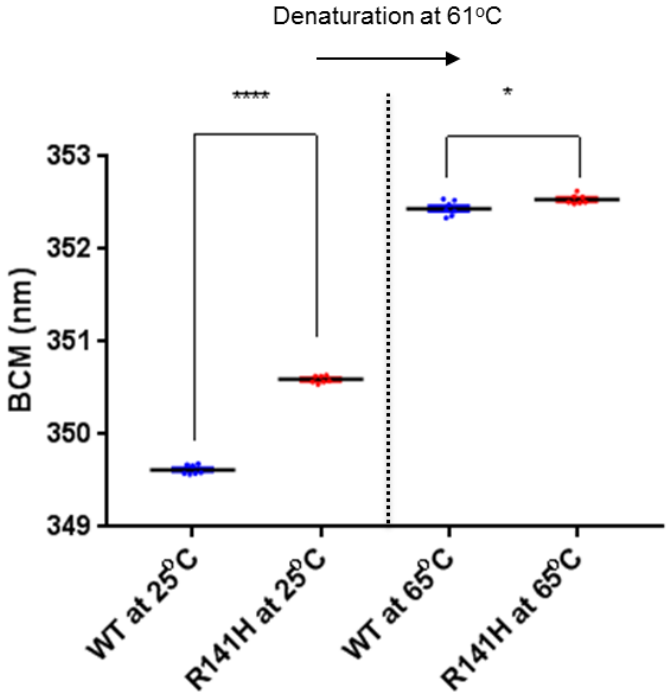

Figure 5.5 – Comparison of BCM values of wild-type and R141H retinoschisin At 25°C folded, monodisperse retinoschisin monomers show a difference of 1.1nm, with denatured samples showing a difference of 0.1nm in observed BCM values (n=7). Experimental values are shown with the mean (bold line) SEM (error bars).

5.4 Comparative Intrinsic Fluorescence Analysis of wild-type and R141H Monomers

During the monomer unfolding reaction, wild-type monomers had a larger BCM value than R141H monomers before unfolding, which was lost after denaturation at 61°C, with an average BCM difference of 1.1nm reduced to 0.1nm following unfolding (Figures 5.4A and 5.5). This is indicative of an alteration in the chemical environment of the fluorescent tryptophans in the folded state and may represent a subtle conformational change. Indeed, increased BCM measurements are indicative of increased solvent exposure with such an increase used previously to distinguish between different conformations with different tryptophan solvent exposure in the human protein disulphide isomerase (Wang, Chen et al. 2010). Consistent with this, on average there was increased fluorescence intensity observed for the mutant construct throughout the excitation spectrum (240-305nm) (Figures 5.6Ai and Aii). Comparison of the fluorescence intensity was carried out at 295nm excitation wavelength to evaluate the emission which arises due to the tryptophan residues, with the R141H mutant showing a raised emission intensity (Figure 5.6B). This increase suggested there was a decrease in fluorescence quenching caused by increased solvent exposure of tryptophan residues. Indeed, analysis of the solvent

accessible surface area (SASA) of the wild-type retinoschisin discoidin domain was carried out. This approach rolls a sphere (with a radius of 1.4Å, equivalent to that of water) over the Van der Waals surface of each residue in 'slices' through the atomic structure without penetrating through the atoms. The path drawn by the centre of this probe is an arc which defines as the solvent accessible surface area, with the length of this arc giving a quantitative measure of solvent accessibility of that residue (Lee and Richards 1971). This analysis (performed in Chimera) revealed that two of the seven tryptophans in the domain (W110 and W147) were found to be buried and both were found close to the R141 mutation site, being found on spikes 2 and 3 respectively (Figure 5.6C). As a result, we hypothesize that the R141H mutation induces a small conformational change in the loop or 'spike' regions of the discoidin domain, with the disulphide-bonded nature of spikes 2 and 3 allowing for subtle alterations in spike 3 to be transmitted further across all the loops. These spike regions were observed in the propeller 'tips' in the wild-type hexadecamer model (Figure 4.14) suggesting that this may represent an alteration in a surface-exposed binding site. However, this region was also close to the contacts with other octamer molecules in the hexadecamer facilitating octamer dimerization (Figure 4.14). Mutation and subtle conformational alteration in this region this may be sufficient to alter hexadecamer formation, which could potentially lead to pathology.

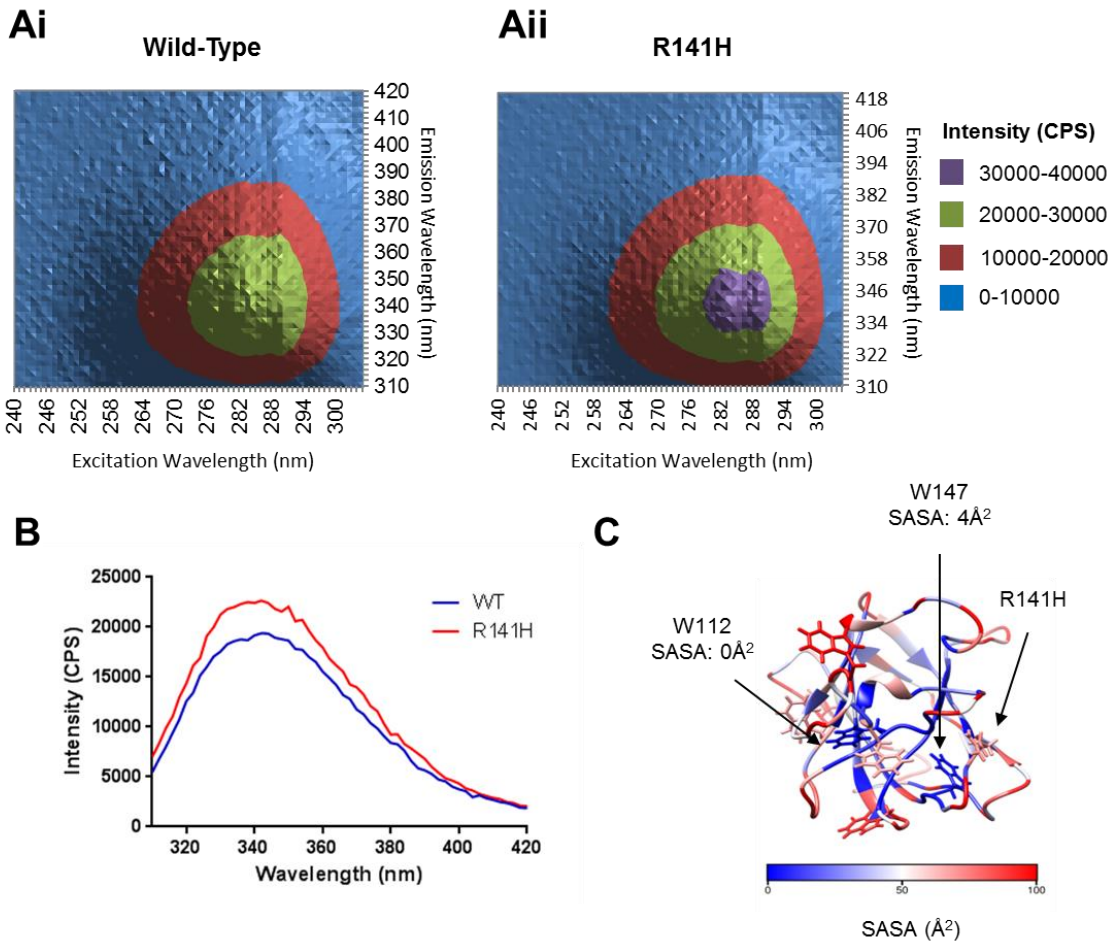

Figure 5.6 – Comparison of wild-type and R141H retinoschisin intrinsic fluorescence. (**Ai**) Three-dimensional spectra showing emission intensity (over 310-420nm wavelength range) through a range (240-305nm) of excitation wavelengths for wild-type and (**Aii**) R141H monomers. (**B**) Two-dimensional intrinsic fluorescence spectra of wild-type and R141H retinoschisin monomers, showing intensity of fluorescence emission following excitation at 295nm (n=3). (**C**) Homology model of wild-type retinoschisin discoidin domain rendered for Surface Accessible Surface Area (SASA). Marked are the positions of tryptophans responsible for intrinsic fluorescence.

5.5 Structural Characterisation of the R141H Retinoschisin Octamer

5.5.1 Negative-Stain Electron Microscopy of the R141H Octamer

To further characterise the effect of the R141H mutation on the retinoschisin complex, the structure of the R141H octamer was probed using negative-stain electron microscopy (Figure 5.7A). Alignment and classification using the EMAN2.0 software suite revealed a propeller-like eightfold-symmetrical arrangement of discoidin domains projecting from a core with apparent reduced density (Figure 5.7B), as seen for the wild-type octamer (Figure 4.2). Also, as observed for wild-type retinoschisin the R141H octamer also had bias towards the 'top' orientation preventing further structural analysis of the octameric complex.

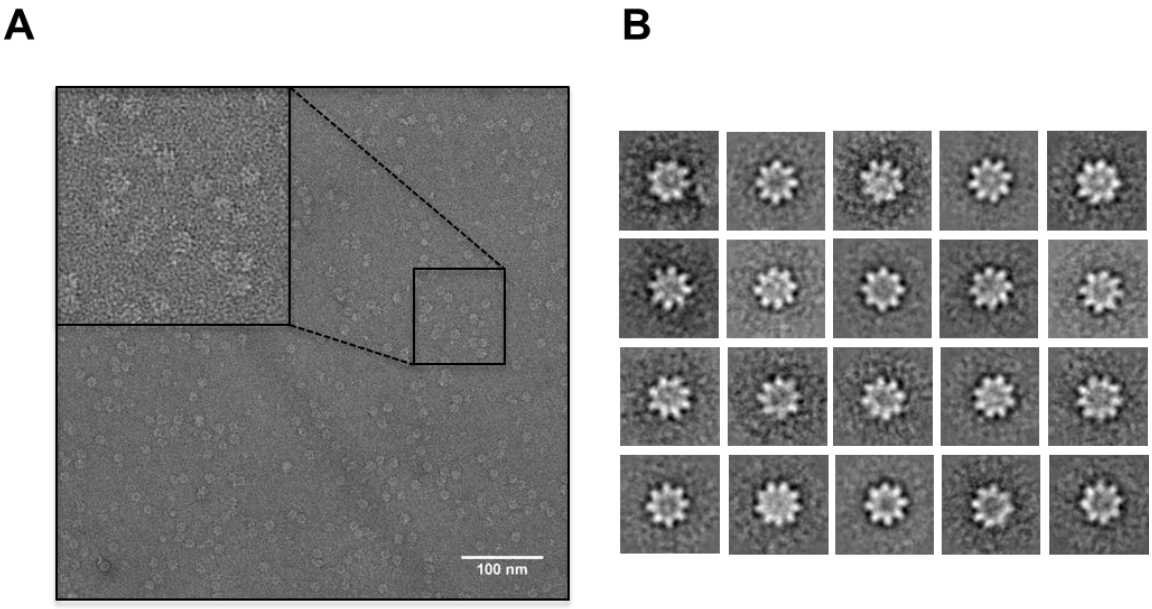

Figure 5.7 – Negative stain electron microscopy of R141H retinoschisin octamer. (**A**) Representative field of octamer particles with a five-fold magnified section (inset). (**B**) Reference-free class averages of R141H retinoschisin octamer particles, only 'top' views are shown, box size 33nm, 3.5Å/pix.

5.5.2 Cryo-EM of the R141H Octamer

To investigate whether the R141H affected the ability of the R141H octamer to form the dimer of octamers complex, the structure of the mutant was investigated in solution. Centrifugal concentration of purified R141H octamer to ~100µg/ml was followed by nativePAGE analysis (Figure 5.8A). As observed for the wild-type (Figure 4.3), concentrated R141H octamer was able to produce an anti-His antibody reactive, higher oligomeric variant approximately double in molecular weight to the octameric species (migrating above 242 kDa). This suggested that the R141H mutation did not prevent octamer dimerization. Subsequent imaging under Cryo-EM conditions using a Gatan K2 Summit DDD camera and FEI Krios I microscope and reference-free classification in RELION 1.4 revealed a similar double-stacked structure (Figures 5.8B and C). These data were subsequently refined using EMAN and the RELION 1.4 software suite following a similar protocol to that adopted in figure 4.5 for the wild-type particle set, outlined in figure 5.9. Initially, the full particle set was aligned and classified using EMAN2.0, revealing the 'double-stacked' hexadecamer structure. Therefore, the particle set was refined using the D8 symmetry operator and used as an initial model for RELION 1.4 three-dimensional classification (shown in figure 5.9). To generate the final model, the manually picked particle set was subject to five rounds of two-dimensional reference-free classification this time in RELION 1.4 to remove 'bad' or damaged particles. The resulting reduced particle set was further three-dimensionally classified using a D8 symmetrical dimer of octamers structure determined previously from the particle set using EMAN2.0 which was filtered to 30Å resolution. The D8 symmetry observed in the class averages (Figure 5.8C) and the

lack of octamer monomer classes observed in the particle set allowed for classification using this symmetry operator. Indeed, three-dimensional classification into two distinct classes using C8 symmetry with the hexadecamer initial model, as performed for the wild-type DDD dataset (Figure 4.5) generated two hexadecameric classes, unlike the wild-type set where such classification separated the octamer and hexadecamer populations (Appendix 6). This suggested a lack of octamers in the particle set. Therefore, the data set was classified into two D8 classes to sample the variation. However, in contrast to the relatively large variation observed between the wild-type classes (Figure 4.5), little variation was observed between the classes. The major variable region observed between the classes was the central region, which was refractory to two dimensional classification (generating a diffuse density in class sum images) (Figures 4.4B and C, 5.8C). However, the ring of discoidin domains appeared to have a low level of inter-class variation. As a result, the particle sets representing each class were combined and refined against class 2 (Figure 5.9).

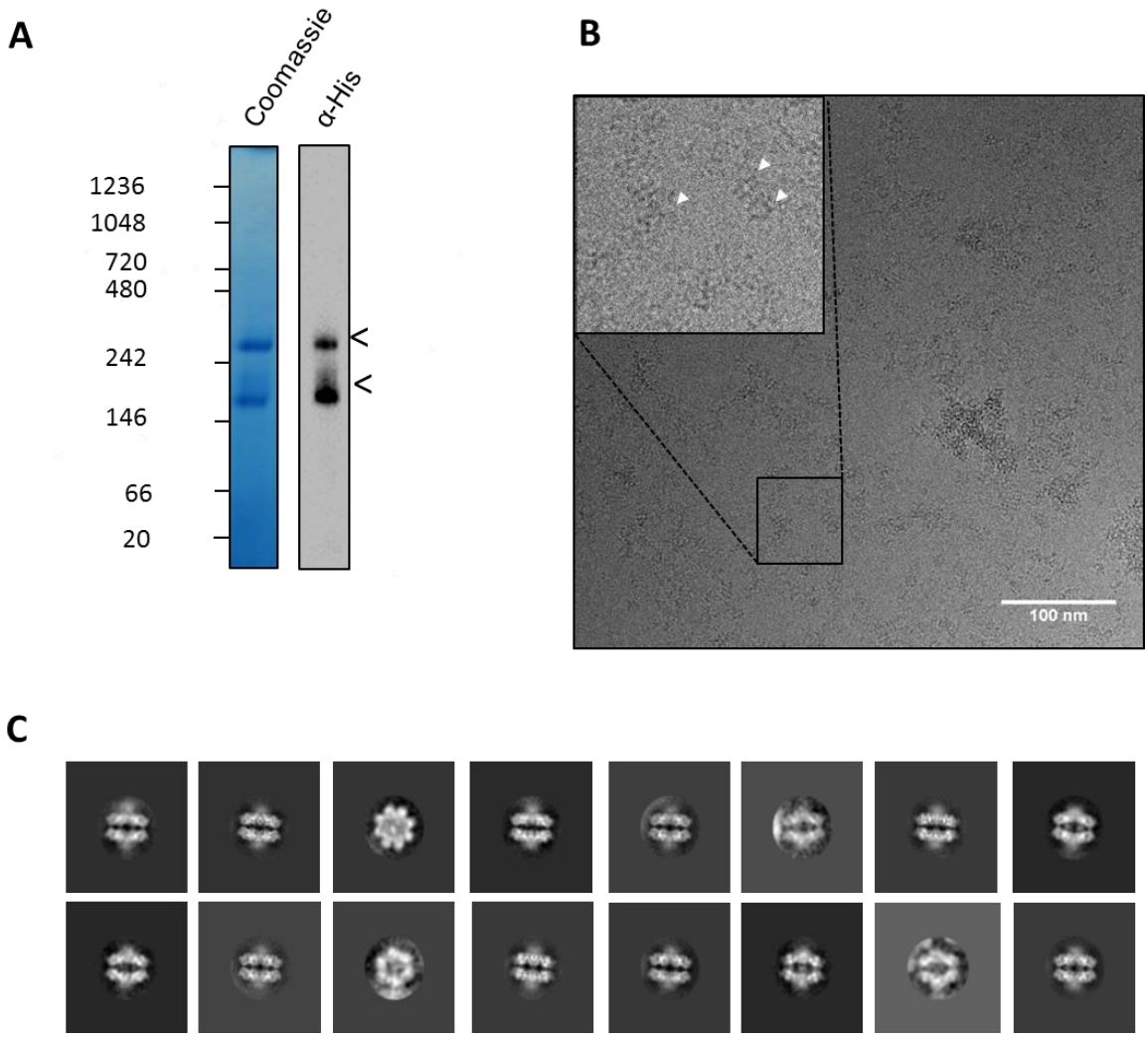

Figure 5.8 – Cryo-EM of the R141H retinoschisin dimer of octamers (**A**) NativePAGE analysis of purified R141H octamer at 0.1mg/ml. (**B**) Representative field of R141H octamer particles imaged in vitreous ice under cryo conditions using the Gatan K2 Summit direct electron counting camera. Both 'top' and 'side' views are apparent in the data (inset). (**C**) Reference-free class averages of the R141H retinoschisin dimer of octamers, box size: 24nm, 1.6Å/pix.

Refinement of the three-dimensional classes with the smaller particle sets which classified with them both gave a lower resolution reconstruction (Appendix 5) possibly due to a lower signal to noise ratio in the discoidin domain regions. Full particle set refinement generated an intermediate resolution map with high noise levels generated by the central Rs1 domains (Figures 5.9 and 5.10B). Subsequent masking out of this region using a soft Gaussian mask generated in RELION 1.4 allowed for a further improvement generating a final refined structure of the hexadecamer at 4.2Å resolution at 0.143 FSC (Figures 5.9, 5.10A and B). The resolution achieved reflected a good Euler distribution in the dataset (Figure 5.10C), however, a bias towards 'side' particle orientations was observed.

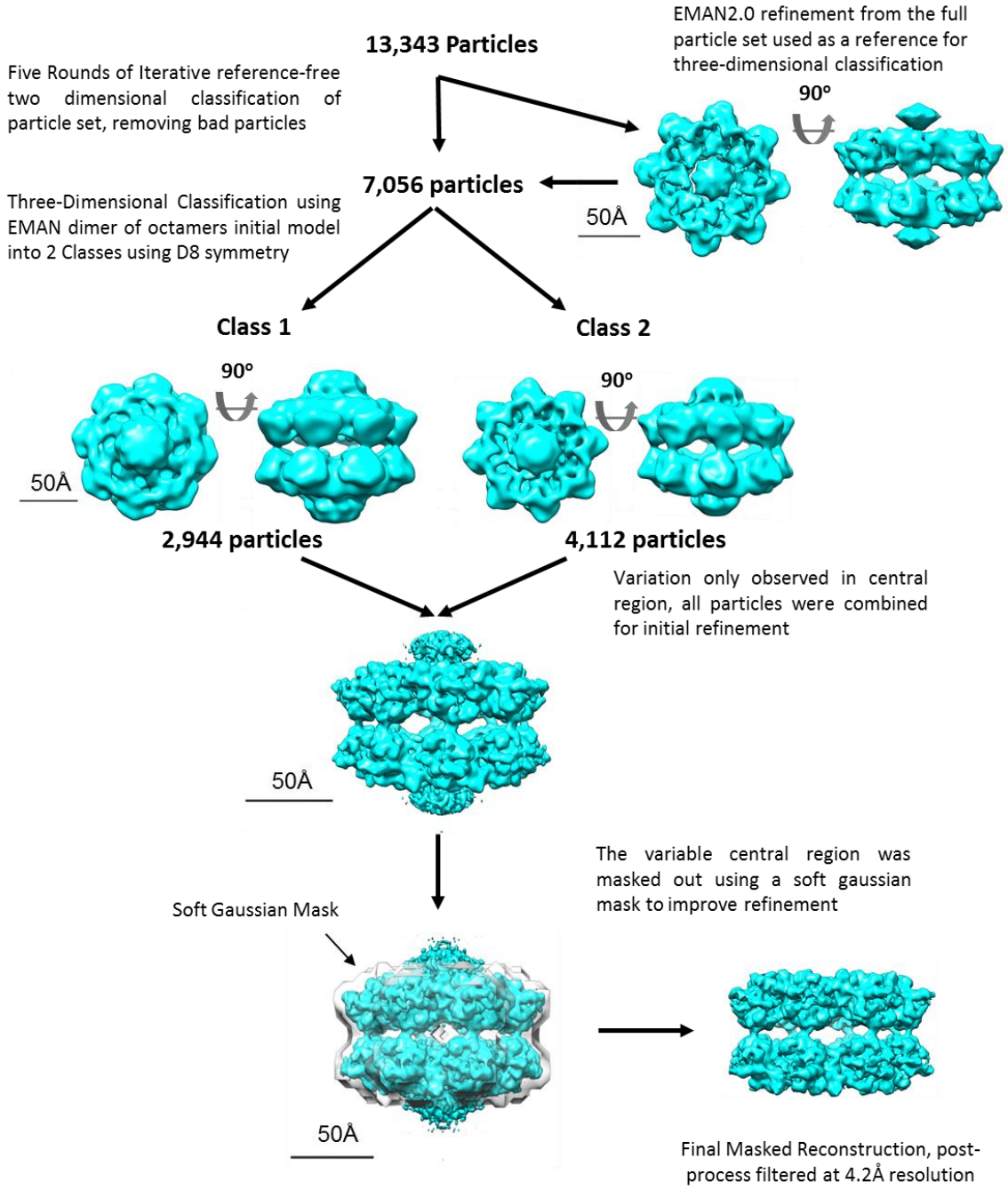

Figure 5.9 – Procedure for refinement of the R141H dimer of octamers using the RELION. Poor quality particles are first removed using iterative rounds of two-dimensional classification. The structure calculated previously using EMAN2.0 was used as a reference for three-dimensional classification into two distinct classes. Variation was only observed in the central Rs1 domain region, so this was masked out using a Gaussian soft mask for final refinement.

Cryo-EM confirmed a similar shape for the R141H dimer of octamers, however, migration of this mutant under nativePAGE conditions was markedly different to the wild-type protein, producing sharp bands (Figure 5.8A) in contrast to the broad bands observed for the wild-type (Figure 4.3). Protein migration under nativePAGE conditions is influenced both by the molecular size, shape and the surface charge of the protein. As both wild-type and R141H retinoschisin octamers have been purified under the same conditions, are at the same concentration, have been analysed under the same gel conditions at a constant

pH and are observed to possess the same gross molecular shape, this suggests that the mutation is potentially affecting the surface charge of the protein.

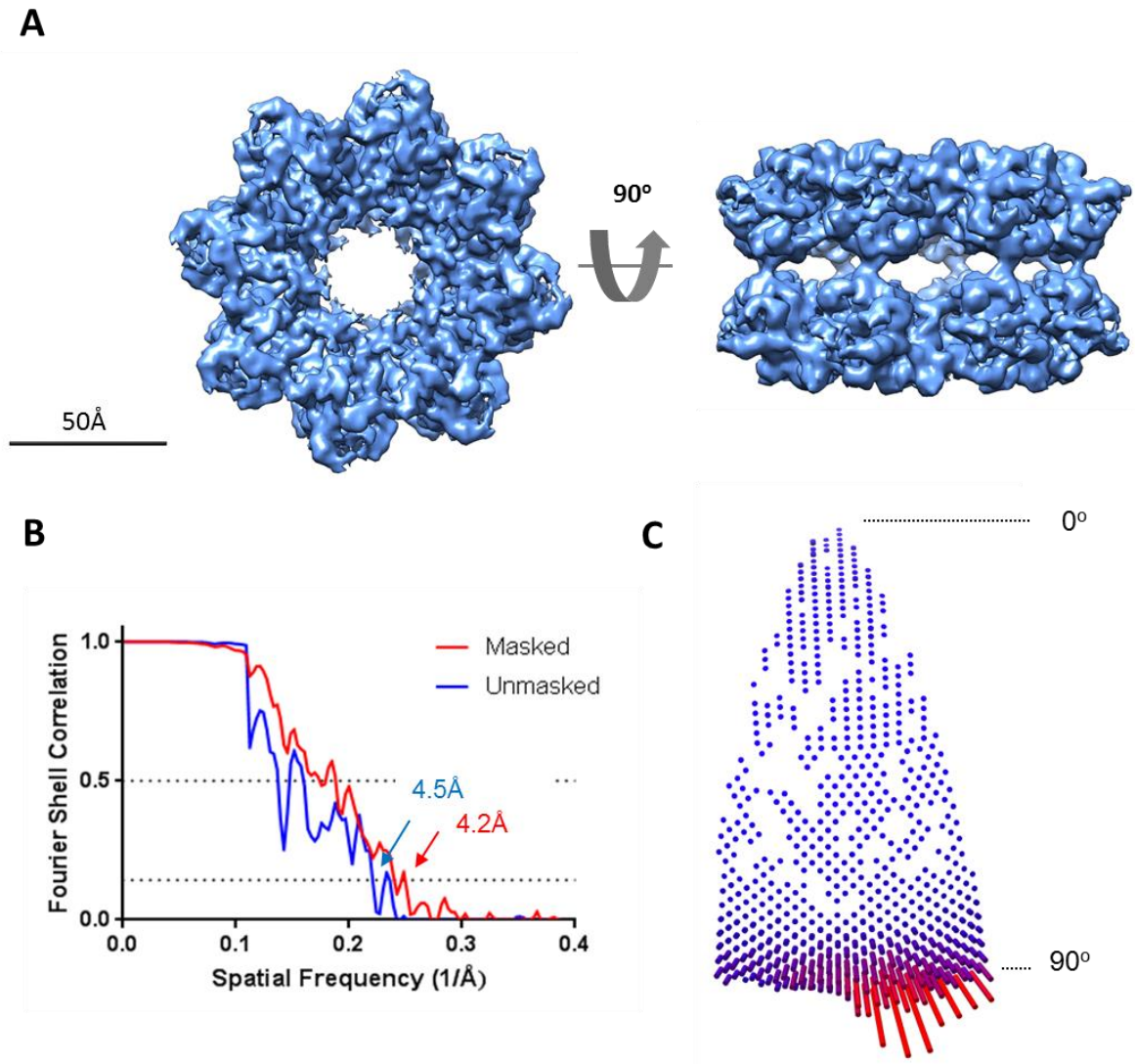

Figure 5.10 – Cryo-EM analysis of the R141H dimer of octamers. (**A**) Three-dimensional reconstruction at 4.2Å resolution of the R141H dimer of octamers. Shown is the final, masked reconstruction. (**B**) FSC resolution estimations of the masked and unmasked reconstructions, resolutions are reported at 0.143 FSC. (**C**) Euler angle distribution of the final, refined R141H model.

With both the higher resolution and the masking of the Rs1 domain regions, local resolution variations within the discoidin domain volume could be investigated. Employing ResMap-H2 analysis, a large proportion of the density was observed to be between 4.5 - 5Å resolution, consistent with the value reported at 0.143 FSC. However, a proportion of the voxels in the unfiltered models were observed at lower resolutions of 6 - 8Å (Figure 5.11A). Mapping of this distribution onto the refined R141H structure revealed these lower resolution regions to be present at the propeller tips, where the spike regions had been previously observed in the wild-type structure (Figure 4.14). This suggested that this region of the protein may be flexible, further suggested by the broken density observed in the map (Figure 5.11B, marked with an arrow).

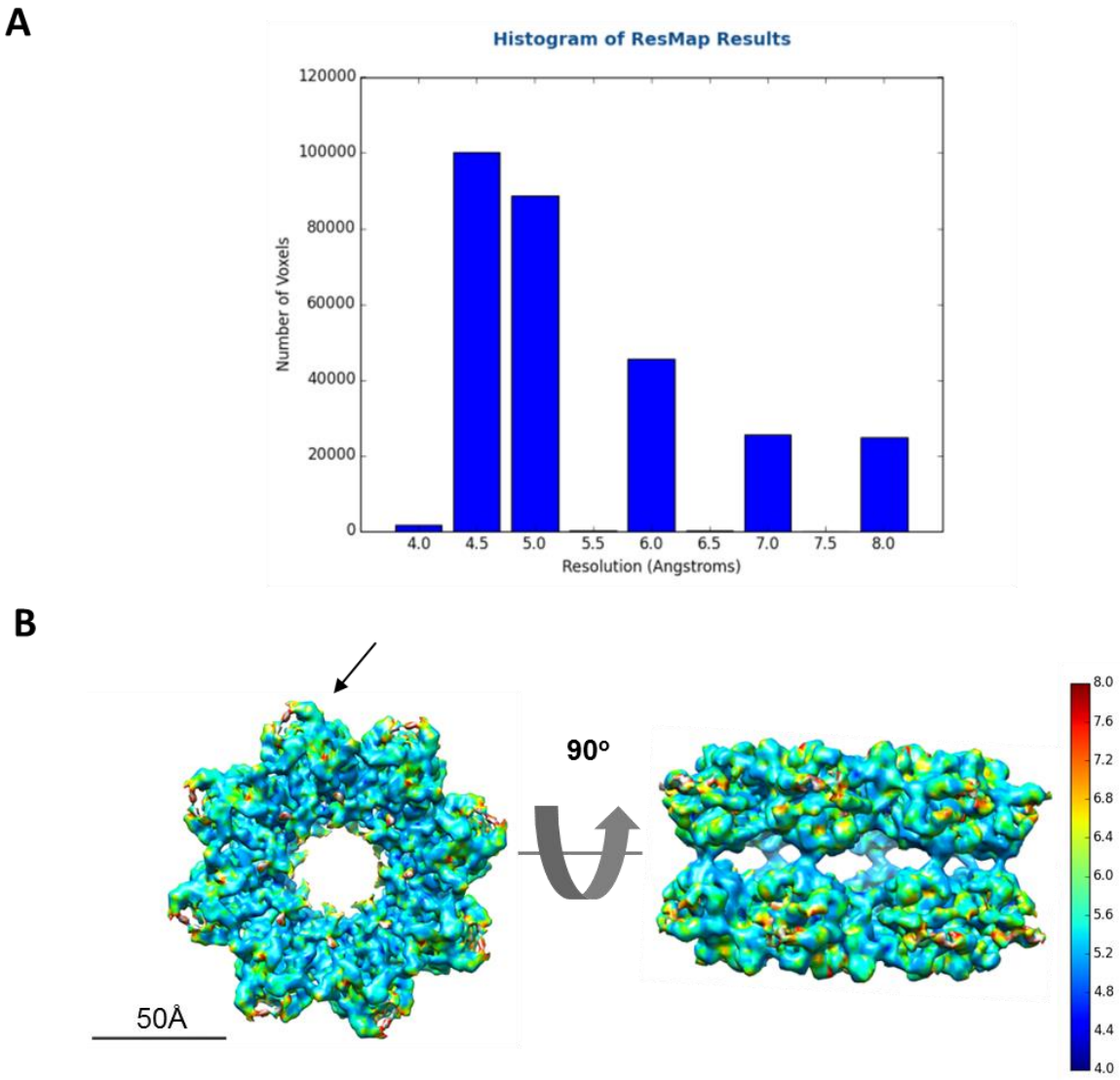

Figure 5.11 – ResMap-H2 local resolution determination for the R141H hexadecamer (**A**) A histogram of the number of voxels observed in the unfiltered half-models used for analysis in the resolution range sampled by ResMap-H2. (**B**) The R141H hexadecamer structure rendered according to the observed local resolution within each region, as determined by ResMap-H2 analysis.

5.6 Quasi-Atomic Model Construction of the R141H Dimer of Octamers

5.6.1 Model-Based Hand Determination of the R141H Dimer of Octamers Map

The enhanced resolution achieved within this data set allowed for accurate docking of the discoidin domain into the structure and determination of a more accurate quasi-atomic model. To this end, a homology model containing the R141H mutation was constructed, with comparison to the wild-type model confirming a lack of dramatic conformational change, with only differences observed within the spike regions (Appendix 7). Exploiting the same approach as for wild-type hand determination (Figures 4.12 and 4.13), the R141H discoidin domain homology model was fitted to the initial hand and the mirror hand of the R141H hexadecamer model following a DockEM global rigid-body search of the

structures at 4.5Å resolution (Appendices 8 and 9). As observed for the wild-type structure, the best fit was observed as the highest correlated fit to the initial hand (Appendix 8, fit (i)), with improved significance, correlation coefficients and visual agreement than observed with the highest correlated fit to the mirror structure (Appendix 9 fit (vi)).

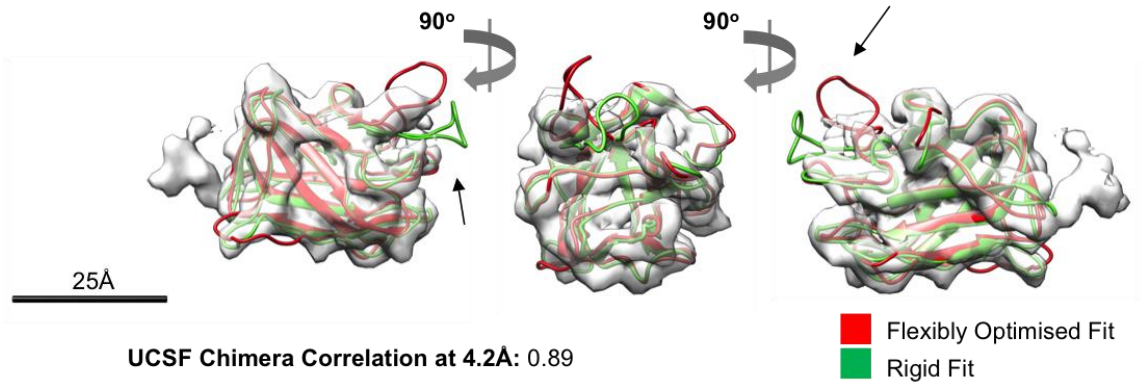

Figure 5.12 –FlexEM flexible fitting of the R141H discoidin domain. Shown in a single subunit density. Overlayed are the initial rigid body fit performed in DockEM (red) and the final, flexibly optimised fit following four iterations of FlexEM (green). The region (spike 1) observed to move during flexible fitting is marked with an arrow.

5.6.2 Flexible Optimisation of the Fitted R141H Discoidin Domain

The improved resolution of the R141H map allowed for the flexible optimization of the homology model structure to the experimentally determined density. Initially, the DockEM fit was optimized in UCSF Chimera using the symmetrical fitting option and subject to molecular dynamics based flexible fitting optimization using the FlexEM program at 4.2Å resolution. As shown in figure 5.12, this did not induce a large change in the positioning of the domain within the density, suggesting that the initial rigid-body fit allowed for an accurate representation of the atomic structure. However, movement was observed in the loop regions (Figure 5.12, marked with an arrow). Spike 1 was observed to move substantially, however, this is unlikely to be accurate due to this region having both lower local resolution and broken density (Figure 5.11B). Therefore, this suggests that Spike 1 may be a flexible region of the hexadecamer, projecting from the extreme tip of the propeller. However, the densities for the other regions appeared well defined and placed accurately. The flexible fitting procedure was followed by an energy minimization step using UCSF Chimera, with the final reported correlation of 0.89 at 4.2Å resolution. Furthermore, this procedure improves the stereochemistry of the homology model. Comparison of the R141H homology model stereochemistry before and after flexible fitting optimization using Ramachandran plots revealed no introduction of energetically unfavourable Φ/Ψ bond angle combinations following flexible fitting (Figure 5.13).

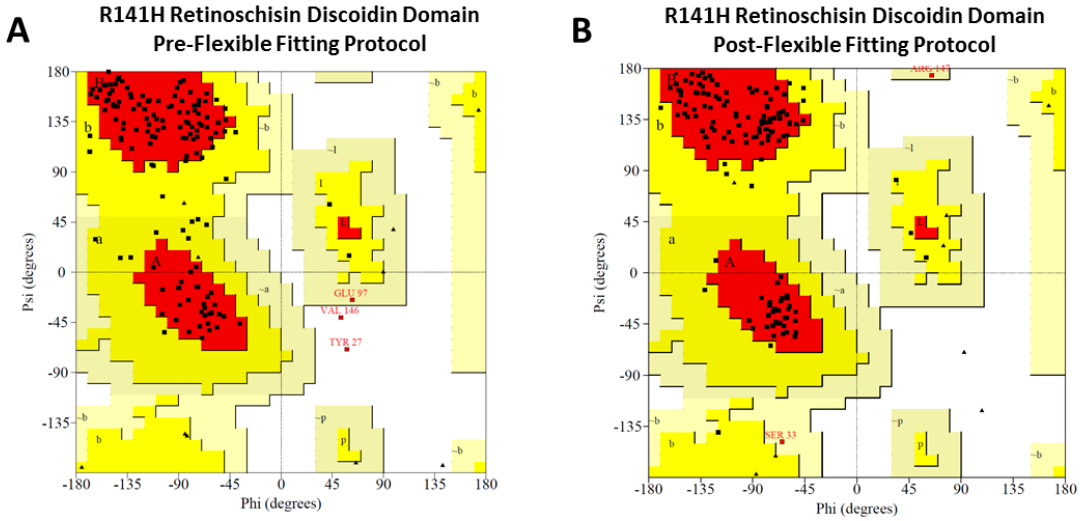

Residues in Most Favoured Regions	83.3%
Residues in Additional Allowed Regions	14.5%
Residues in Generously Allowed Regions	0.7%
Residues in Disallowed Regions	1.4%

Residues in Most Favoured Regions	88.4%
Residues in Additional Allowed Regions	10.1%
Residues in Generously Allowed Regions	1.4%
Residues in Disallowed Regions	0.0%

Figure 5.13 – Stereochemistry of the R141H discoidin domain before and after FlexEM (**A**) A Ramachandran plot of the φ/ψ angle combinations observed in the homology model before fitting and (**B**) following the flexible fitting protocol. In each case, the proportions of residues found in energetically favourable and unfavourable regions are shown.

5.6.3 Identification of Domain and Secondary Structure within the R141H Dimer of Octamers

The improved resolution of the R141H map allowed construction of a quasi-atomic model, shown in figure 5.14A. Shown in figure 5.14B is the fitting of a single domain to the repeating domain volume in the hexadecamer map. The enhanced resolution allowed for the positions of the individual β-strands (Figure 5.14B, inset) and the loop regions situated at the propeller tips to be determined.

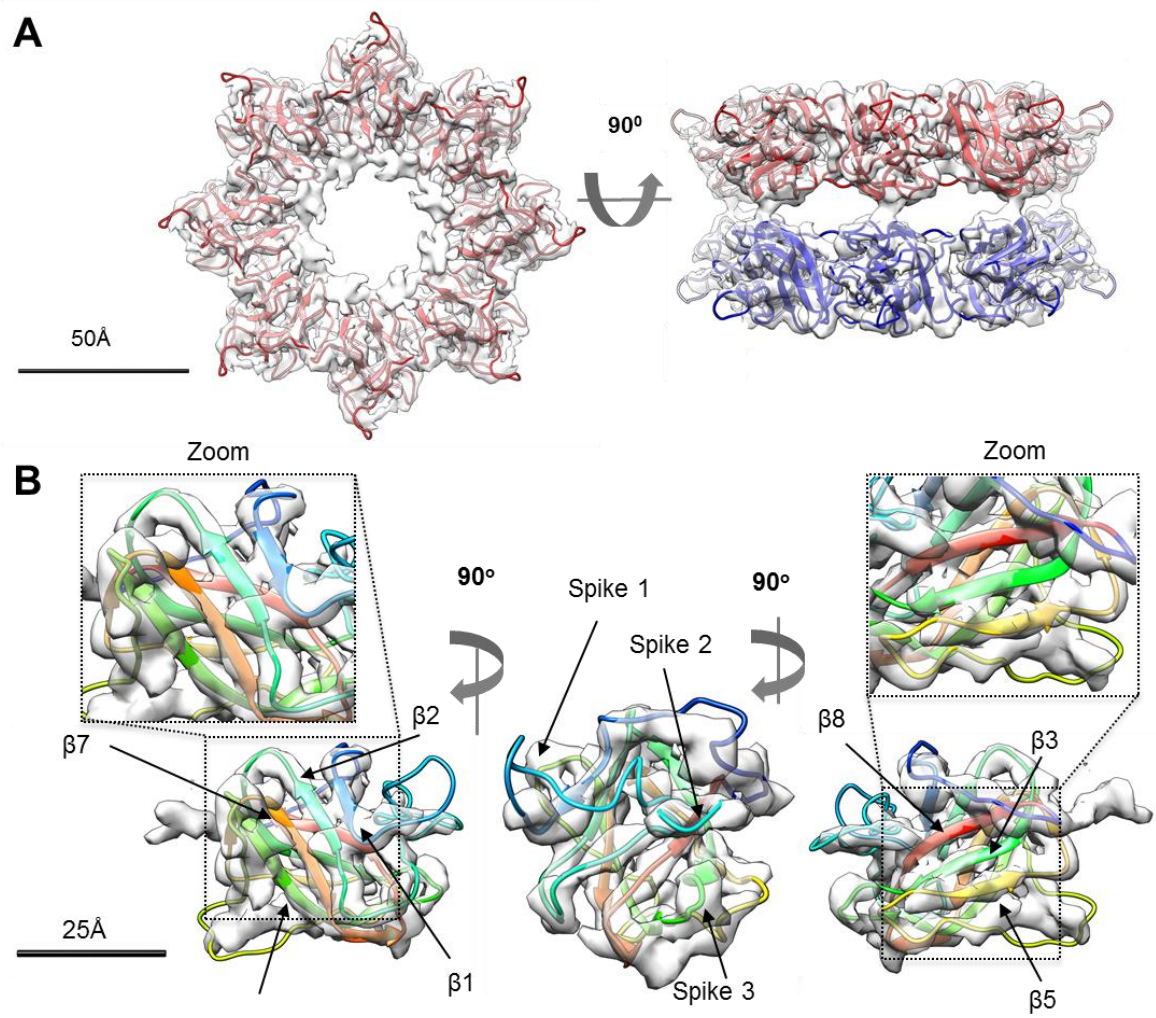

Figure 5.14 – The quasi-atomic model of the R141H retinoschisin dimer of octamers. (**A**) The hexadecamer quasi-atomic model shown fitted to the electron density map determined by Cryo-EM. Subunits of individual octamers forming the hexadecameric assembly are marked in red and blue. (**B**) The final, flexibly optimised fit shown on a single subunit of the retinoschisin complex. The positions of the β-strands and spike regions identified in the structure are marked, with resolution of all β-strands observed in the electron density (*zoom*).

Furthermore, construction of this model allowed for the positions of other less well-resolved regions of the map to be determined. Fitting of the discoidin domains into the hexadecamer structure revealed an additional region of density unoccupied by the homology model (Figure 5.15A). This region represented the inner ring of density, previously observed in the wild-type dimer of octamers model (Figure 4.8B). Closer inspection of this region revealed that it represented the octamerising C59-C223 disulphide linkages required for oligomerisation (Wu, Wong et al. 2005). Shown in figure 5.15B is the proposed positioning of these regions and disulphide bonding pattern.

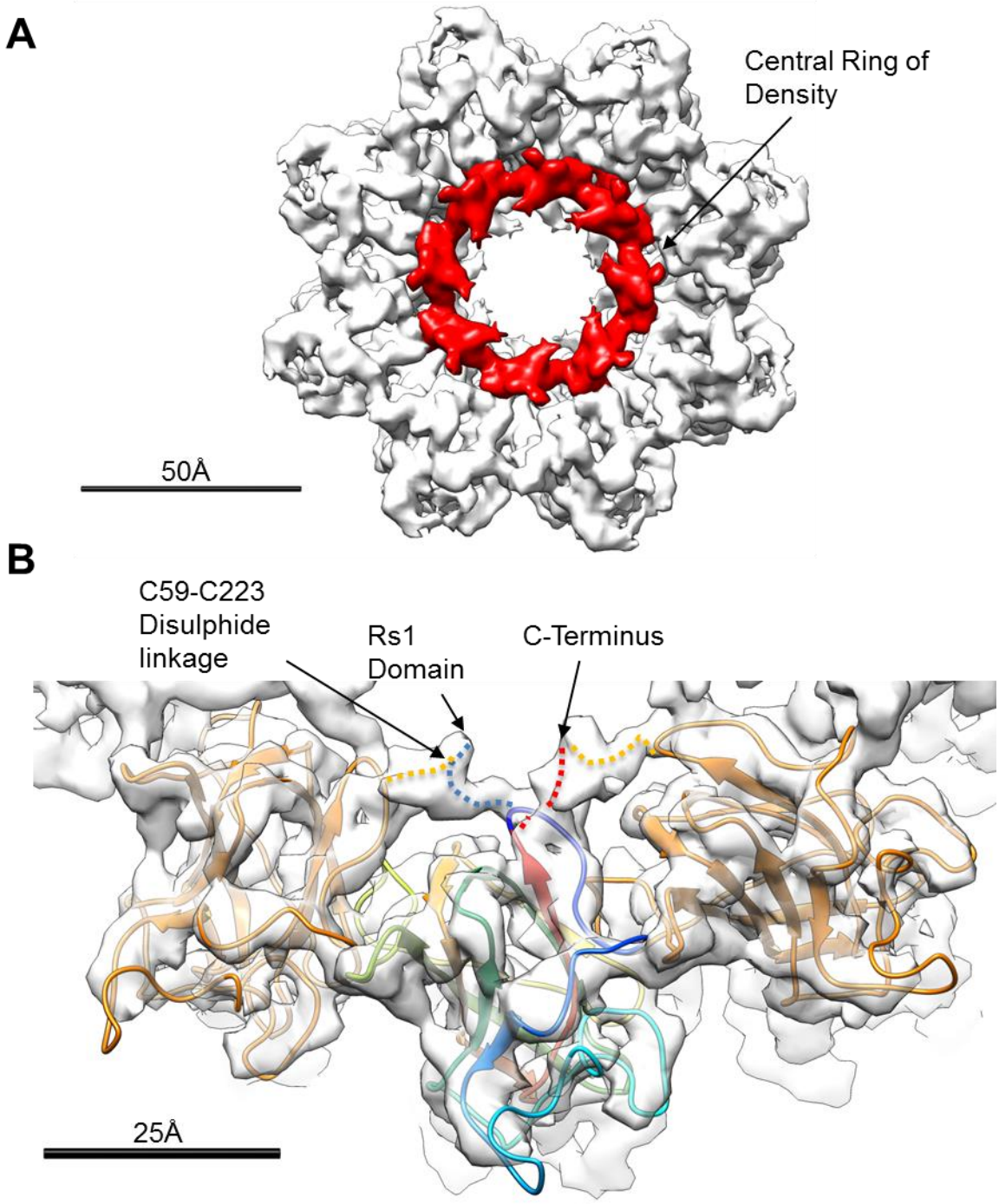

Figure 5.15 – Identification of the stabilising ring of C59-C223 disulphide linkages. (**A**) The central ring of density observed in the retinoschisin structure, positioned concentrically to the discoidin domains (red). (**B**) Fitted discoidin domains in the octamer ring, with the proposed positions of the N-terminal Rs1 domains, C-terminal extensions and the C59-C223 disulphide linkages between them.

5.6.4 Interface Identification in the R141H Dimer of Octamer

A significant benefit of the enhanced resolution is the ability to identify interfaces within the complex. Two interfaces are present within the dimer of octamers, the interface between adjacent discoidin domains within the octamer (the intra-octamer interface) and the interface between the octamer rings (the inter-octamer interface). The quasi-atomic model was analysed using the PDBePISA which identifies residues involved in protein-protein

interfaces using the buried surface area in the interface calculated for each residue. Shown in figure 5.16A, regions involved in both interfaces were identified, with a cluster of interface residues between β4 and β5. Mapping identified intra-octamer interface residues identified the hot spot as the loop between β4 and β5 which projected onto an interface made from the N-terminus, spike 2, β5 and β8 of the adjacent domain (Figure 5.16B). Closer inspection of the density in this region identified three distinct connecting densities (Figure 5.16C, numbered 1-3) which represented the contacts formed between the loop between β4 and β5 and the N-terminal region (contact 1), spike 2 (contact 2) and β5 (contact 3), with interacting residues marked (Figure 5.16C). In contrast to the intra-octamer interface, the inter-octamer interface was less substantial, with three contact sites identified. Again, the loop between β4 and β5 produced a single contact site, alongside β7 and β4 (Figure 5.16D).

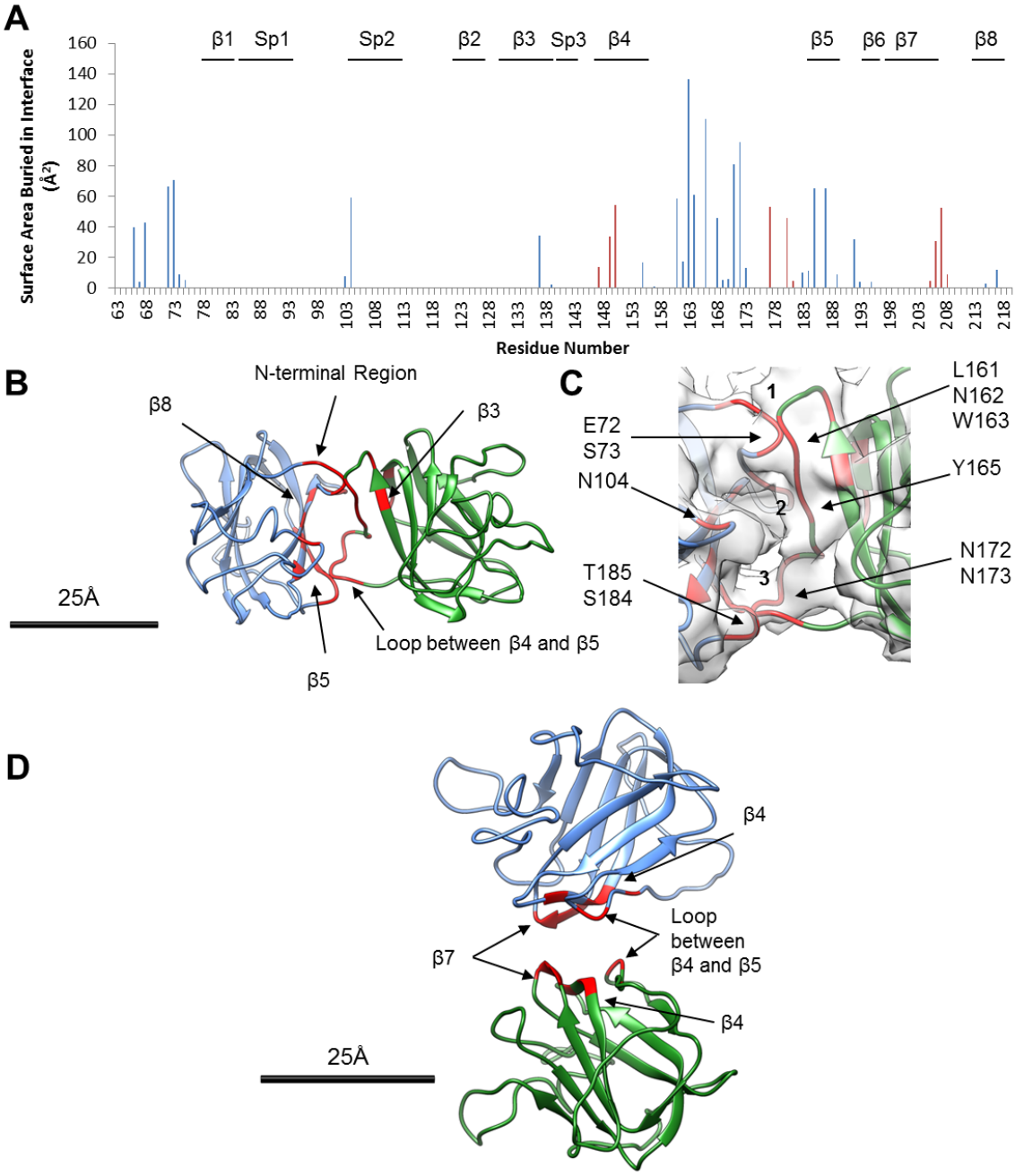

Figure 5.16 – Mapping of discoidin domain interfaces in the quasi-atomic model. (**A**) PDBePISA analysis of fitted subunits. Residues which contribute surface area to the intra-octamer interface are shown in blue, with residues involved in the inter-octamer interface highlighted in red. (**B**) The observed intra-octamer interface between subunits with residues identified by PDBePISA shown in red. (**C**) The intra-octamer interface contains 3 main contact points, with residues in these regions highlighted. (**D**) The inter-octamer interface, with PDBePISA-identified complexing residues shown in red.

5.6.5 Mutational Mapping onto the R141H Quasi-Atomic Model

Quasi-atomic model construction allowed for the effects of previously uncharacterised XLRS-associated mutations on the structure of fully assembled retinoschisin. All identified XLRS-associated mutations have been previously deposited into the Leiden Open Variation Database (LOVD). These mutations were screened to select for conservative mutations which did not affect a cysteine residue (important in the folding of retinoschisin),

had conservative BLOSUM62 substitution matrix scores (of -1 and above) or were previously predicted to have a negligible effect on retinoschisin folding (Sergeev, Caruso et al. 2010, Sergeev, Vitale et al. 2013). Table 5.1 summarizes the disease-associated mutations which satisfied these requirements. The identified mutations were mapped onto the quasi-atomic model and were found to cluster into two distinct interface regions (with 77% of all conservative mutations found in these regions), which were classified as class I and class II mutations. Class I mutations mapped to the intra-octamer interface, with conservative mutations found in each region identified in the interface by PDBePISA analysis (Figure 5.17A). Despite the conservative nature of these mutations, the mapping to this interface suggests that they will prevent octamerisation and possibly even secretion. Indeed, the conservative mutations E72K (Wu and Molday 2003), N104K (Wang, Zhou et al. 2006) and T185K (Dyka and Molday 2007) (all found in the contact sites between the adjacent domains) have been previously shown to cause intracellular retention of retinoschisin. As a result, we predict this phenotype for the other class I mutations mapping between the discoidin domains (Figure 5.17A).

Another class of disease-associated mutations, named class II, were found to cluster at the contact between the octamers. As shown in figure 5.17B all three contact sites identified by PDBePISA between the octamers were mutated in the disease state. Such mutations may work to destabilize the hexadecamer state, suggesting that pathology of these mutations is associated with affecting hexadecamer formation. Therefore, this suggests that the dimer of octamers structure may be physiologically relevant, with its loss associated with the development of XLRS.

Seven of the identified mutants were not identified by PDBePISA as in an interface region. Four of these mutated residues (Q124, D126, I133 and Q154) were found on both β3 and β4, and therefore may also alter the intra-octamer interface. An additional mutated residue, L113, was found on spike 2 and may alter the conformation of this loop which forms part of the intra-octamer interface. The remaining mutated positions, I199 and R200, have been shown previously to be part of (or in close proximity to) a ‘conserved triad’ in the retinoschisin discoidin domain which consists of W122-R200-W163. Molecular dynamics simulations have previously suggested that these residues are important to maintain the stability of the discoidin domain fold. Therefore, even mild mutations at these sites may not be tolerated (Fraternali, Cavallo et al. 2003).

Residue	Mutation(s)	BLOSUM62 Matrix Score
G70	G70S	-1
E72	E72K	+1
	E72O	+2
	E72A	-1
	E72D	+2
S73	S73P	-1
A101	A101P	-1
R102	R102O	+1
L103	L103F	0
N104	N104K	0
L113	L113F	0
O124	O124R	+1
D126	D126H	-1
I133	I133F	0
I136	I136T	-1
T138	T138A	0
R141	R141H	0
	R141O	+1
D145	D145H	-1
E146	E146K	+1
O154	O154R	+1
D158	D158N	+1
K167	K167N	0
G178	G178D	-1
N179	N179D	+1
T185	T185K	-1
P192	P192T	-1
	P192S	-1
	P192A	-1
P193	P193S	-1
I195	I195V	+3
R197	R197H	0
I199	I199T	-1
R200	R200H	0
H207	H207O	0
	H207D	-1
R209	R209H	0
R213	R213O	+1
E215	E215K	+1

Table 5.1 – Residues (non-cysteine) with one or more conservative mutations associated with XLRS. Mutations were identified using the Leiden Open Variation Database (http://grenada.lumc.nl/LOVD2/eye/variants.php?action=search_unique&select_db=RS1) and structural affects predicted using the BLOSUM62 substitution matrix. Values of -1 and above were considered conservative mutations.

The R141H mutation was also not in an interface region. R141 was found to project into the propeller tips away from either interface, suggesting that alteration at this site may affect an additional functional site, as this mutation although pathogenic has little impact on the molecule structure.

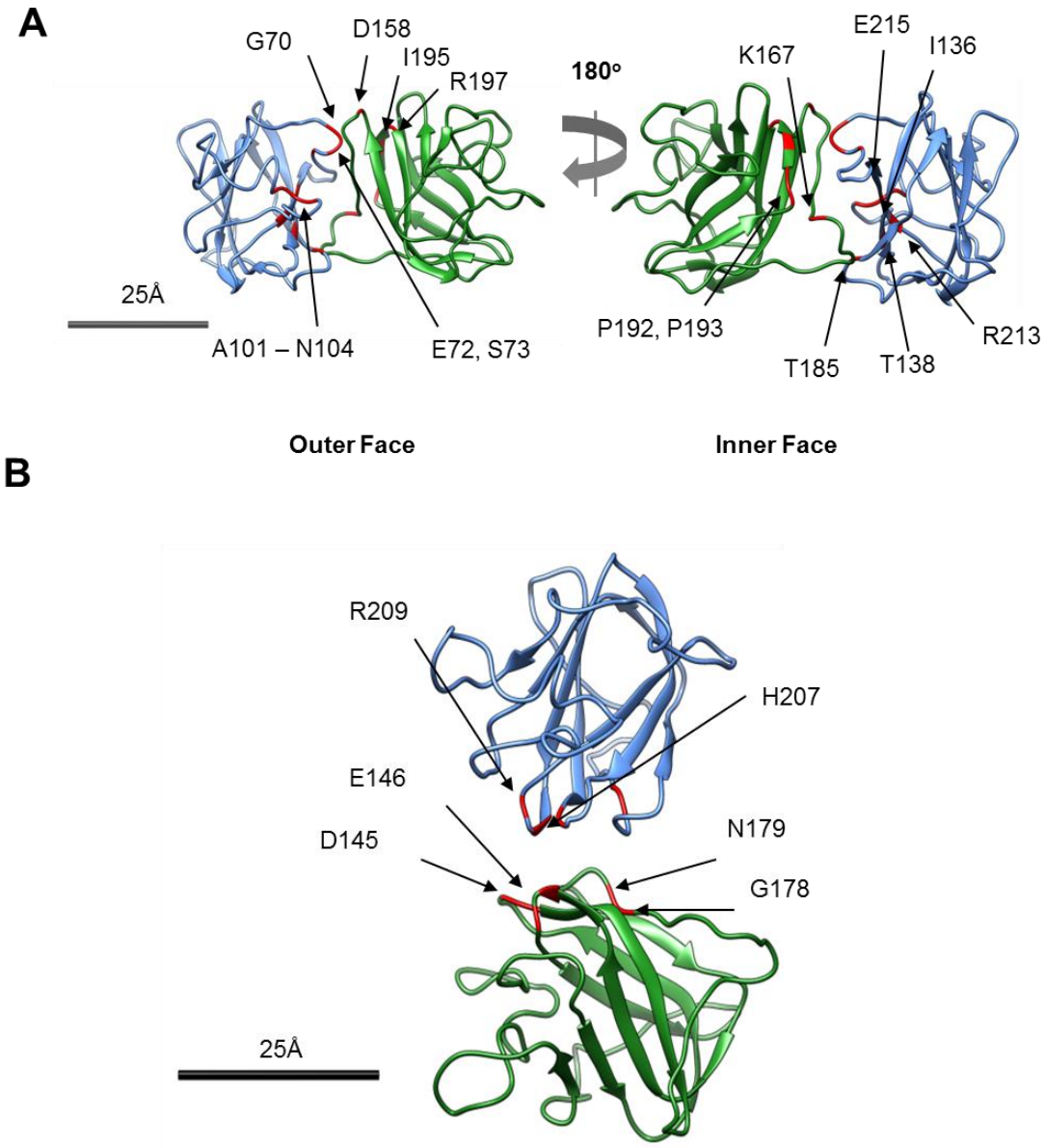

Figure 5.17 – Mapping XLRS-associated mutations on the hexadecamer. (**A**) Class I mutations of conservative, non-cysteine mutations mapped to the intra-octamer interface between adjacent discoidin domains in the octamer structure. (**B**) Class II mutations mapped to the inter-octamer interface between the octamers assembled into the hexadecamer oligomer.

5.7 Comparison Between the Wild-Type and R141H Dimer of Octamers

Recently, Tolun et al. have resolved the structure of the wild-type retinoschisin dimer of octamers to an equivalent resolution of 4.1Å (Tolun, Vijayasarathy et al. 2016), confirming the structure determined by this study. As a result, this afforded the opportunity for structural comparison between the wild-type and disease-associated mutant. The R141H structure determined by this study was fitted to the wild-type map deposited in the

Electron Microscopy Data Bank (EMDB, accession number emd_6425) using DockEM. Initially, both maps were filtered to 5Å resolution to prevent any noise present in either map affecting the fitting. This was followed by an exhaustive global search of the wild-type density with the R141H map. Initially the search was conducted over a range of magnification factors with a coarse angular sampling to find the factor at which both structures were comparable. This was followed by a finer one degree angular search with the highest correlated fit visualized in UCSF Chimera. As shown in figure 5.18, both structures were highly similar, with no obvious conformational differences between the wild-type and the mutant structure. As a result, the alteration in the intrinsic fluorescence observed between the purified wild-type and mutant monomers may represent a very subtle change which possibly cannot be resolved due to the local drop in resolution at the propeller tips. Indeed, local resolution in this region was assessed as 8Å (Figure 5.11B), and therefore the maps may be too resolution limited in this region to distinguish any subtle difference, or the difference may be associated with a loss of rigidity within the structure in this region.

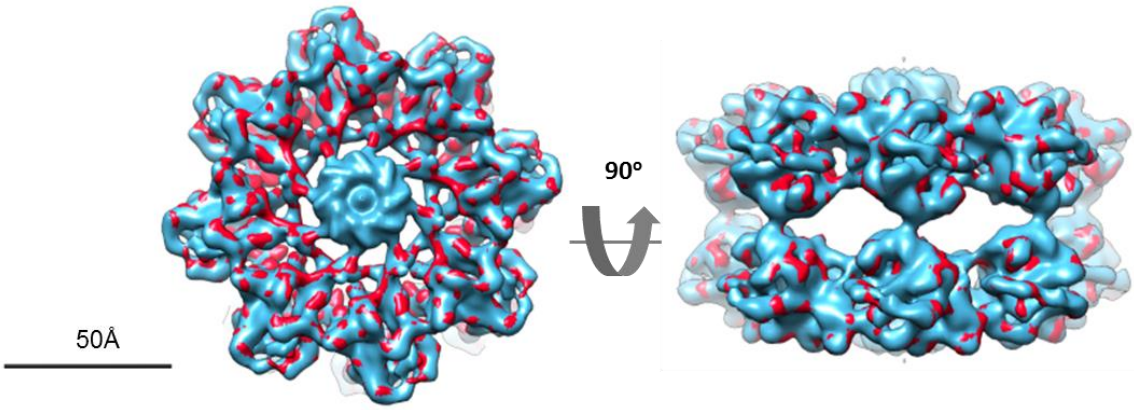

Figure 5.18 – DockEM comparison between the R141H retinoschisin hexadecamer structure (red) and the wild-type structure (emd_6425) (blue). Both maps are filtered at 5 Å for comparison.

5.8 Discussion

Expression and purification of R141H mutant retinoschisin allowed for analysis of the effect of this disease-associated mutation on the retinoschisin structure (Figure 5.1). Comparison of wild-type and mutant hydrodynamics and stability showed that the mutation did not lead to a gross conformational change or destabilize either the protein fold or assembled octameric structure (Figures 5.2, 5.3 and 5.4). Furthermore, R141H did not affect the ability of the octamers to dimerize, generating a similar hexadecameric structure as observed for the wild-type (Figure 5.8). As a result, the R141H does not lead to a large alteration in the overall retinoschisin structure. From this, we hypothesized that the mutation was more subtle, possibly confined to a small region of the protein which may have functional significance.

Indeed, despite the lack of gross alterations, purified monomeric R141H mutant had both raised BCM values (Figure 5.5) and increased fluorescence intensity (Figure 5.6) consistent with an increased solvent exposure of tryptophans in the structure (Wang, Chen et al. 2010). Analysis of the discoidin domain showed that five of the seven tryptophans in this domain were predicted to be solvent exposed. However, the remaining two were found to be buried (W110 and W147 found on spikes 2 and 3 respectively) and close to the R141 mutational site on spike 3 (Figures 5.6C and 5.19A). Therefore, we hypothesize that R141H induces a small alteration in the conformation of spike 3 which could also be translated to spike 2 via the disulphide bond between them (Wu, Wong et al. 2005), leading to a subtle reorganization which exposes one or more of the two buried tryptophans to the solvent, hence leading to increased intrinsic fluorescence of these tryptophans. This alteration may be small enough that it cannot be detected even at subnanometre resolutions of around 8Å at these spike regions (Figure 5.11) or may lead to another alteration through increasing the flexibility of this region preventing formation of a stable interface or through alteration of surface charge. Indeed, such an alteration was suggested by the change in the migration of the R141H mutant in nativePAGE gels despite the very similar shape and concentration of the proteins (Figures 5.8A and 4.3). Furthermore, modelling suggested that R141 was found in a surface-exposed, positively charged region of the domain, with mutation to a histidine possibly reducing the positive change which may be sufficient to abrogate binding to another protein or ligand (Figure 5.19B). Indeed, mutation of this residue has been associated with loss of galactose binding (Dyka, Wu et al. 2008) and changes in the channel gating kinetics of the L-VGCC binding partner (Shi, Jian et al. 2009) found on the photoreceptor membrane (Ko, Liu et al. 2008). This coupled with the solvent accessibility and the positioning of spike 3 at the propeller tips, away from interfaces (Figure 5.14B) required for complex assembly suggests that R141H may affect an inter-molecular binding site which may be required for membrane anchorage of the octameric complex. However, this remains a preliminary hypothesis and requires further study. In order to elucidate the effect of this mutation, complex structures of retinoschisin together with L-VGCC should be solved with the effect of the mutation on the binding affinity for this binding partner investigated.

In addition, despite the intrinsic fluorescence data suggesting a subtle alteration, it cannot be ruled out that there is a change in the Rs1 domains as two tryptophans are found here. Intact mass measurements confirmed the presence of this region in both wild-type and R141H monomers (Figure 5.1E and F). However, SAXS (Figure 3.12) and Cryo-EM analysis (Figure 5.8C) suggested that this region is extended and possibly flexible, and as a result, tryptophan burial in this region appears unlikely. However, to further investigate the nature of the alteration, the dynamics and conformations of the discoidin domain loop regions should be probed with higher resolution. Nuclear Magnetic Resonance (NMR)

analysis of purified monomers would allow for such investigation. Such study requires large quantities of material which can be labeled with ^{15}N and ^{13}C, with bacterial expression systems ideal for such 'doped' protein production. This may be challenging for retinoschisin due to the presence of disulphide bonds, however, bacterial systems allowing for high expression and structural analysis of disulphide bonded mammalian proteins have been developed, such as the CyDisCo (Matos, Robinson et al. 2014, Alanen, Walker et al. 2015) and Origami (DE3) (Blumenschein, Friedrich et al. 2007) strains. Such production of retinoschisin monomer would allow for the dynamics of the loops to be probed following residue assignment. Using comparative model-free analysis of the NMR signal decay in the wild-type and mutant, the signal for each residue could be assigned a generalized order-parameter (S^2) with drops in this value suggestive of an increase in flexibility. With the flexibility also characterised through assignment of τ_e (to describe picosecond to nanosecond timescale motion) or R_{ex} (to describe microsecond to millisecond timescale motion) to any flexible regions (Cole and Loria 2002). Such comparison would allow the effect of the R141H mutant on dynamics of the loop regions to be investigated, with also the potential for high resolution structural analysis to investigate any subtle conformational alterations.

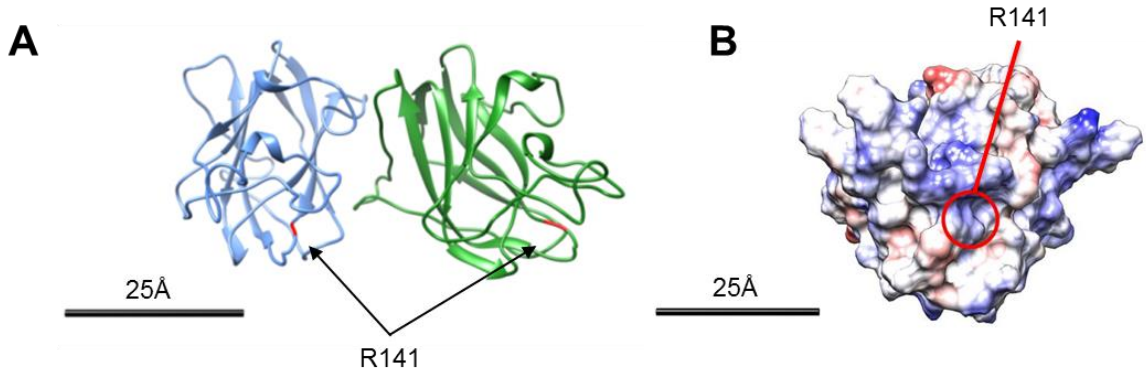

Figure 5.19 – The position of the R141H mutation in the dimer of octamers. (**A**) The position of R141 on spike 3, projecting out at the propeller tips away from complexing interfaces. (**B**) The surfaces charge of the wild-type discoidin domain homology model showing in the wild-type structure, R141 is found in a positively charged surface area.

Cryo-EM structural analysis of the R141H dimer of octamers however allowed for mapping of XLRS-associated mutations onto the fully assembled hexadecameric structure through construction of a quasi-atomic model (Figure 5.14). Selection of conservative mutations which were not predicted to affect protein folding was performed to identify functional regions. Mapping of these mutations identified two clusters of conservative mutations (Class I at the intra-octamer interface and Class II at the inter-octamer interface). Class I mutations were predicted to prevent octamer formation, and possibly prevent secretion of retinoschisin. Indeed, this was observed for three class I mutations: E72K, N104K and T185K (Wu and Molday 2003, Wang, Zhou et al. 2006, Dyka and

Molday 2007), despite molecular dynamics simulations predicting a small affect of these mutations on the discoidin domain fold (Sergeev, Caruso et al. 2010). As a result, we predict that other uncharacterised mutations found at this interface will lead to loss of octamer secretion. Class II mutations were found clustered at all the contact sites identified between the octamers. The disease association of these mutations and conservative nature suggested that alteration of octamer dimerization may lead to pathology, suggesting that hexadecamer formation may be physiologically relevant. Indeed, two mutations found in class II (H207Q and R209H) were found to be secreted as octamers (Wang, Zhou et al. 2006), suggesting that these mutations do not affect the assembly of the retinoschisin octamer. To further investigate class II mutations, H207Q was further studied and is discussed in the next chapter.

6 Results Chapter 4: Structural Characterisation of H207Q Retinoschisin

The observation that H207 formed part of the inter-octamer interface led to the hypothesis that this residue was important in hexadecamer formation. Indeed, H207 was previously observed to be a mutational 'hotspot' for XLRS-associated mutation, with the H207Q mutation still permitting secretion of assembled retinoschisin octamers (Wang, Zhou et al. 2006, Sergeev, Caruso et al. 2010). Therefore, we sought to characterise the effects of the H207Q mutation on retinoschisin structure using a combination of stability assays, negative-stain EM and nativePAGE analysis.

6.1 Expression and Purification of H207Q Retinoschisin

H207Q retinoschisin was expressed from the pCEP-Pu/AC7 expression construct, with purification via the C-terminal His_6-tag as before (Figures 3.1 and 5.1). H207Q retinoschisin migrated as a band at approximately 28 kDa, previously observed for both wild-type and R141H retinoschisin (Figure 6.1A). This band was His-reactive and formed redox-sensitive higher order oligomers (Figure 6.1B), with SEC purification identifying three oligomers eluting at the same volumes as the octamer, dimer and monomer (Figure 6.1C) in both wild-type and R141H retinoschisin purifications (Figures 3.2C and 5.1C), consistent with the observation that H207Q does not affect retinoschisin assembly. In order to confirm the presence of the H207Q mutation in the expressed protein, purified monomer was subject to intact mass spectrometry. The molecular mass of 24,926.07Da (Figure 6.1D) shows good agreement with the predicted molecular weight of the H207Q retinoschisin sequence with five additional N-terminal residues remaining from the BM40 signal sequence (to within 1 Da). Furthermore, the difference in the molecular weights between H207Q and wild-type monomers (8.1 Da) is equivalent to the mass difference between a single histidine and glutamine residue (9 Da), suggesting the presence of the H207Q mutation in the purified protein.

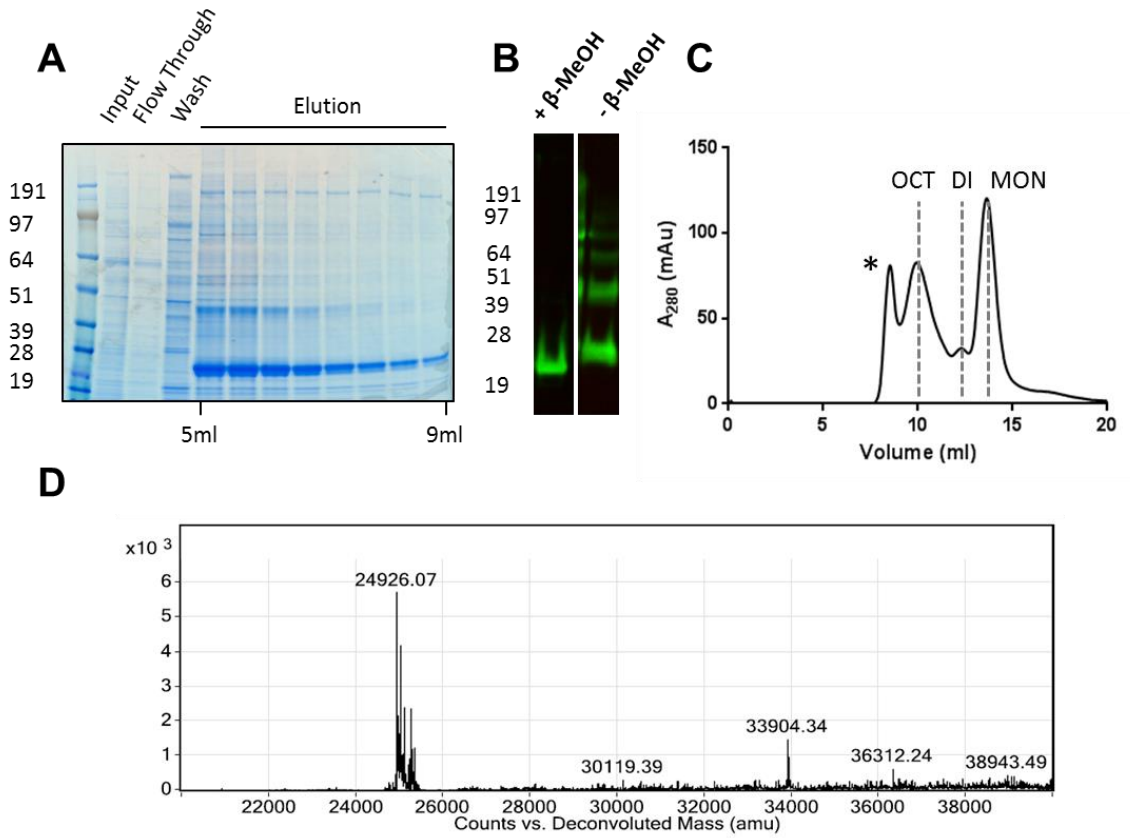

Figure 6.1 – Purification of H207Q retinoschisin from HEK293-EBNA cell system. (**A**) Coomassie-stained reducing SDS-PAGE of Ni-NTA purification of recombinant, H207Q retinoschisin with input, flow through, wash and elution fractions. (**B**) Western blotting against the C-terminal His_6-tag carried out under reducing (+β-MeOH) and non-reducing (-β-MeOH) conditions showing disulphide-dependent oligomerisation of the recombinant protein. (**C**) Size exclusion chromatography of His-purified H207Q retinoschisin, there are three main oligomers of octamer (OCT), dimer (DI) and monomer (MON) purified from the HEK293-EBNA system. (**D**) Intact Mass Mass-Spectrometry analysis of purified H207Q retinoschisin monomer, with a main species with a molecular weight of 24926.07 Da.

6.2 Comparative Stability of H207Q and Wild-Type Retinoschisin Monomers

To probe the effect of the H207Q mutation, the stability of the monomer fold was investigated. Purified H207Q and wild-type monomer unfolding was monitored during a temperature ramp experiment, with unfolding monitored via the increasing BCM values for each construct. As shown in figure 6.2A, H207Q monomer BCM values increase at lower temperatures than the wild-type construct, with the differentials of each peak showing a 5^oC reduction in the T_m for the mutant monomer (Figure 6.2B). This drop in comparative stability was also observed by DSF (Figures 6.2C and 6.2D) suggesting that the H207Q mutation reduces the stability of the retinoschisin fold.

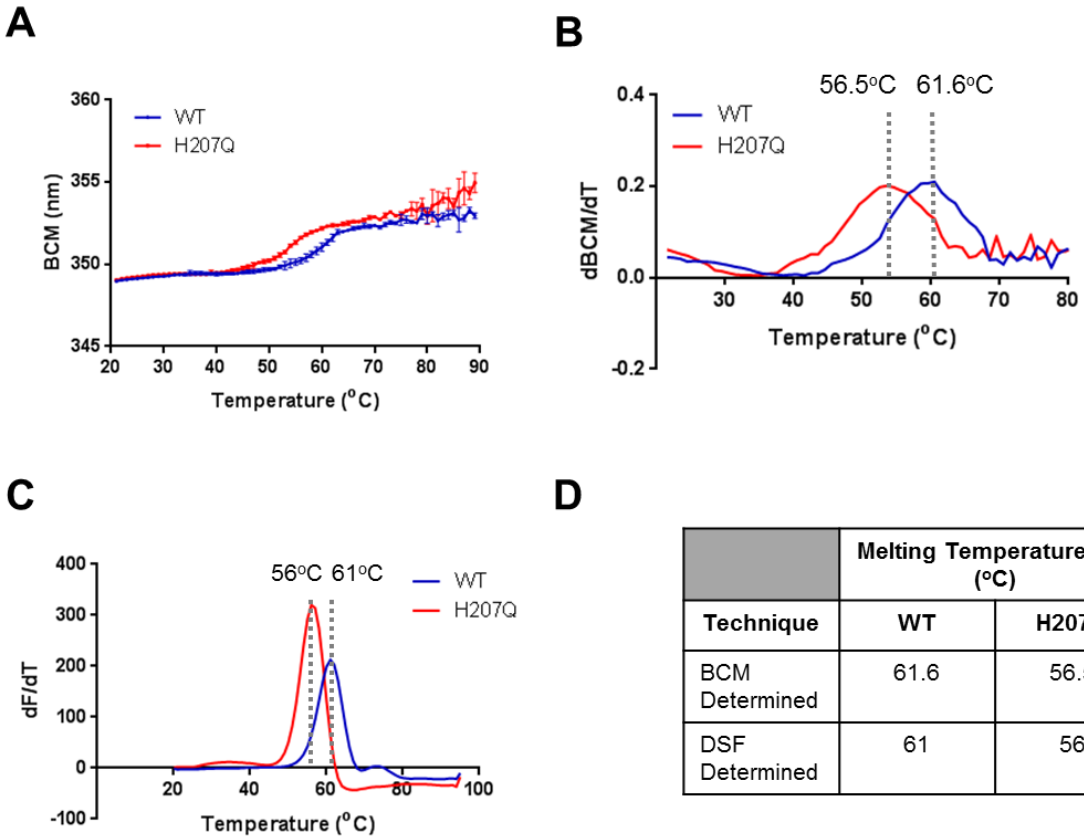

	Melting Temperature (T_m) (°C)	
Technique	**WT**	**H207Q**
BCM Determined	61.6	56.5
DSF Determined	61	56

Figure 6.2 – Comparative thermal stability of wild-type and H207Q monomers (**A**) Barycentric Mean intrinsic fluorescence of purified wild-type and H207Q monomers during heating from 20°C to 90°C, showing the unfolding reaction of both proteins (n=3). (**B**) The mean differential of the observed unfolding reaction, with the measured melting temperature marked (n=3). (**C**) Differential scanning fluorescence of the purified wild-type and H207Q monomers, showing the different melting temperature for both proteins (n=5). (**D**) Tabulated melting temperatures for both constructs determined by each technique.

Consistent with this finding, purified H207Q monomer also had a greater aggregation propensity than the wild-type monomer. Aggregation was observed to occur at lower temperatures than the wild-type monomer, with aggregation onset observed at 43.5°C for H207Q, compared with 46.2°C for the wild-type (Figure 6.3). Together, these data suggest that the H207Q mutation destabilizes retinoschisin, producing a protein more prone to unfolding and aggregation.

A

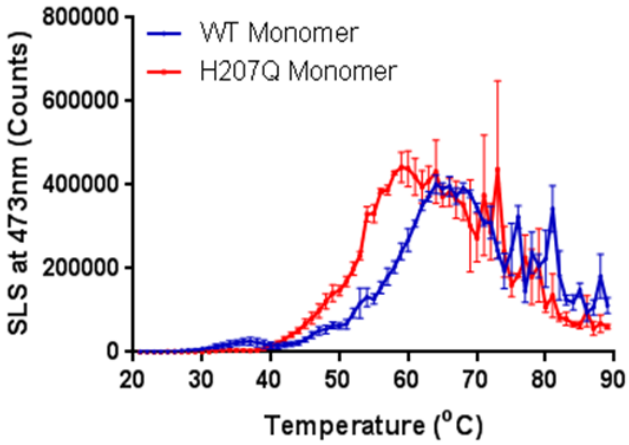

B

Aggregation Temperature (T_{agg}) (°C)	
WT	**H207Q**
46.2	43.5

Figure 6.3 – Aggregation of wild-type and H207Q retinoschisin monomers. (**A**) Static Light Scattering (SLS) profiles of wild-type and H207Q monomers revealing more rapid aggregation of the H207Q protein (n=3). (**B**) Aggregation temperatures for wild-type and R141H retinoschisin monomers.

6.3 Structural Characterisation of the H207Q Octamer

In order to determine if the destabilization observed for the H207Q monomer led to an alteration in the octamer, the structure of the octamer was investigated. Negative stain EM of purified H207Q octamer shows the same planar, propeller-like octameric arrangement of subunits as shown in the reference-free class averages (Figures 6.4A and B). Despite the apparent lack of quarternary structure alteration, the H207Q octamer was less stable as measured by DSF, with a 6°C reduction in the T_m of the octamer when compared to both wild-type and R141H retinoschisin (Figures 6.4C and 5.4F). This suggests that the destabilization observed in the monomeric state persists into the octamer. However, the position of the residue in the inter-octamer interface (Figure 5.17B) suggested that mutation at this site may have a detrimental impact on the ability of the octamers to dimerize, potentially preventing octamer dimerization. To test this, purified H207Q octamer was analysed at 0.1mg/ml concentration using nativePAGE. As observed for both wild-type and R141H retinoschisin, H207Q octamer formed two oligomeric species, migrating at approximately 200 and 400-500 kDa molecular weight, consistent with the presence of both octamers and dimers of octamers. Therefore, this suggests that the H207Q is still able to form hexadecameric complexes which may be less stable.

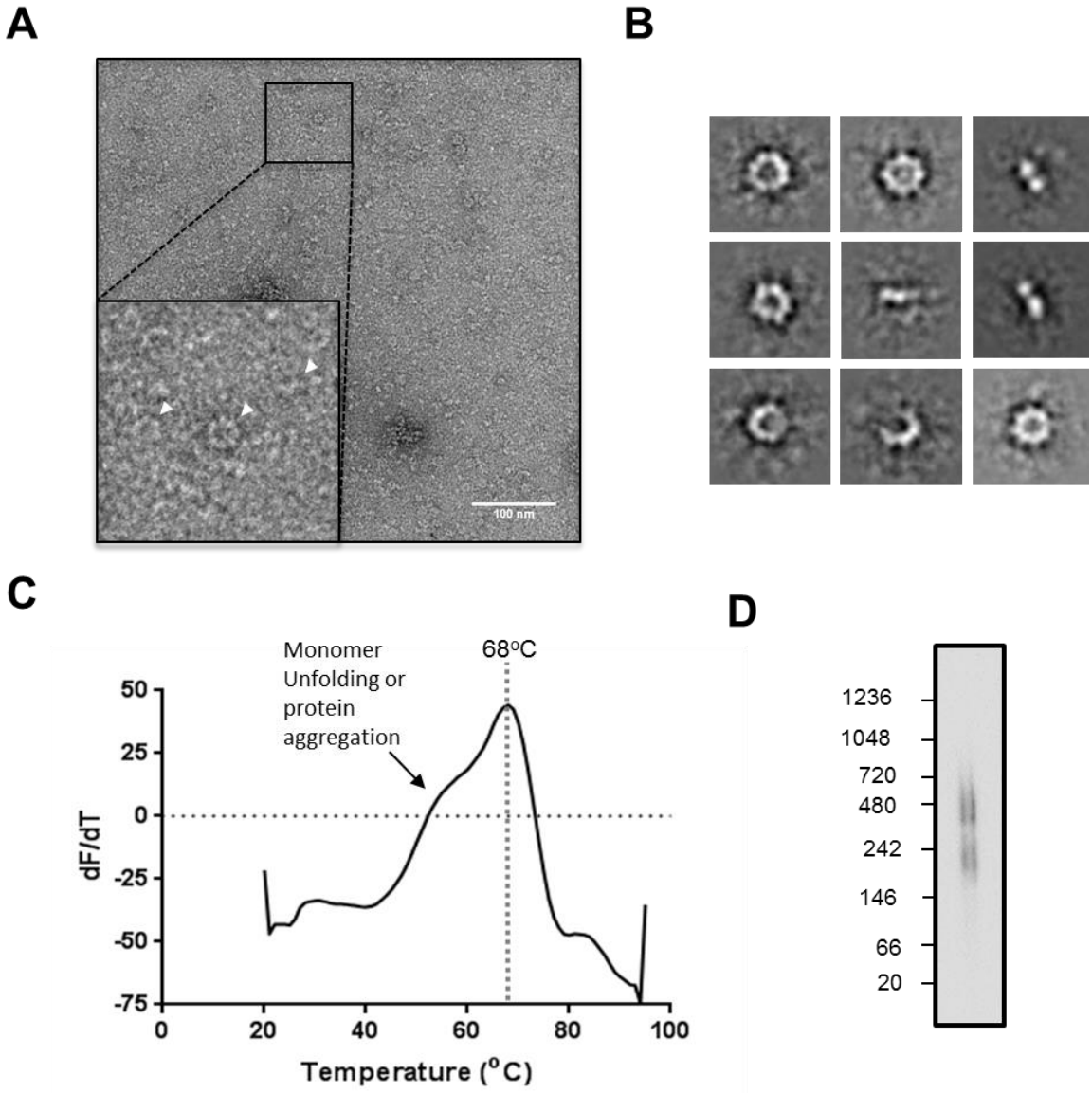

Figure 6.4 – Characterisation of the H207Q octamer. (**A**) Representative field of H207Q octamer particles imaged following negative staining, octamer particles were readily identified (inset). (**B**) Reference-free class averages of purified H207Q octamer particles, box size: 35nm, 2.8Å/pix. (**C**) Averaged DSF profile for the unfolding of purified H207Q octamer (n=5). The calculated T_m is marked. (**D**) NativePAGE of purified H207Q octamer at 0.1mg/ml concentration. Shown are two distinct species representing octamer and dimer of octamers.

6.4 Discussion

In summary, H207Q mutant retinoschisin could be purified from the HEK293-EBNA mammalian cell expression system as both fully assembled octamers and as individual monomers (Figure 6.1), as previously observed (Wang, Zhou et al. 2006). Whilst the mutation did not affect the ability of the retinoschisin construct to assemble into both octameric and hexadecameric complexes, in each case the protein was significantly destabilized compared to the wild-type (Figures 6.2 and 6.3).

The observation that the H207Q disease-associated mutation both maintained octameric secretion (Wang, Zhou et al. 2006) and was found as a class II mutation at the interface between the octamer rings (Figure 5.17B), suggested that the pathology may arise from altering or preventing octamer dimerization. NativePAGE analysis confirmed that H207Q octamers were able to self-assemble into a higher order oligomer, consistent with formation of the hexadecamer (Figure 6.4D). This is unsurprising as PDBePISA analysis identified three contact sites between the octamers in the R141H structure (Figure 5.16B), as a result, H207Q may result in either loss or alteration of only a single site, potentially weakening but not preventing the interaction. Currently, the lack of structural data on the H207Q hexadecameric state prevents the interpretation of the effect of this mutation on this state. It is possible that the mutation lowers the affinity of binding between the rings or leads to a conformational alteration in the octamer which masks or disrupts a functional site. However, strikingly, the H207Q mutation appeared to significantly destabilize both the monomer and octamer. As a result, we hypothesise that the mutation leads to a general destabilization of retinoschisin higher-order oligomers which, in turn, leads to a loss of structural support through either a reduction in secretion or a less durable structural support which is more prone to aggregation or unfolding once secreted.

From these mutational observations, the effects of the different identified classes of conservative, disease-associated missense mutations can be hypothesized using the model proposed for retinoschisin function (Figure 6.5). In this model, class I mutations found at the intra-octamer interface would be predicted to prevent octamer formation, whereas class II mutations would alter octamer dimerization and destabilize the inter-octamer interface required to couple the opposing membranes. In this model the R141H mutation would lead to an alteration at the propeller tips which would affect the interaction between retinoschisin and integral membrane proteins (possibly via binding to the glycosylation of the ectodomains) in the opposing membranes. In each case, the mutations would affect an interface essential for retinoschisin function, leading to the onset of pathology.

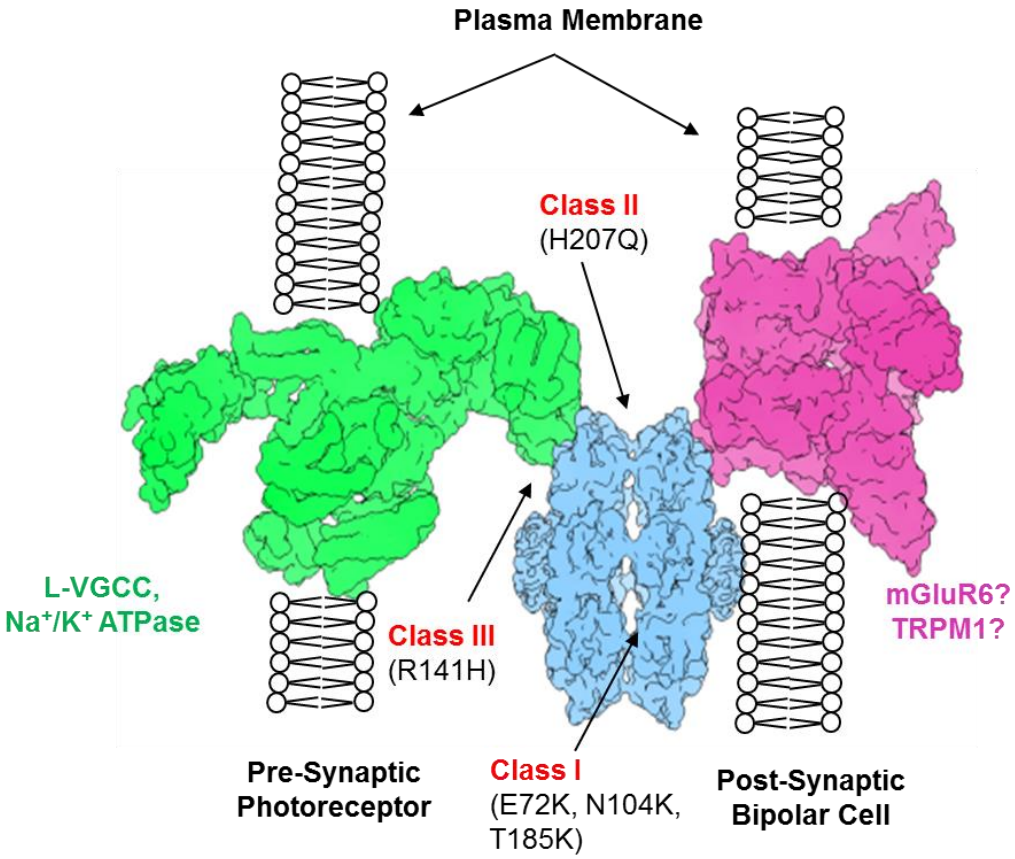

Figure 6.5 – The potential effects of the characterised mutations on the proposed model for retinoschisin function. In this model, the H207Q mutation potentially destabilises the hexadecamer structure preventing coupling between opposing membranes. In contrast, the R141H mutation potentially disrupts a binding site in the propeller tips required for retinoschisin membrane association.

7 Final Discussion

In summary, this study aimed to both structurally characterise the retinoschisin monomer and octamer and then investigate the effects of XLRS-associated mutations on this structure. To this end, retinoschisin was expressed and secreted in HEK293-EBNA cells, producing both monomeric and octameric retinoschisin in adequate quantities to allow for structural characterisation.

7.1 Characterisation of the Monomer Nano-Structure

Previously, investigation of the structure of the retinoschisin monomer had been limited to the discoidin domain, with numerous homology models constructed of this structure (Fraternali, Cavallo et al. 2003, Wu and Molday 2003, Wang, Zhou et al. 2006, Sergeev, Caruso et al. 2010, Sergeev, Vitale et al. 2013). The structure of the N-terminal Rs1 domain remained elusive due to the lack of reliable sequence homology of this region with any other observed sequence (Sauer, Gehrig et al. 1997, Molday, Kellner et al. 2012). This had stifled further characterisation of the full molecule with previous studies citing insufficient material to allow for full structural characterisation (Molday, Kellner et al. 2012). As a result Sergeev et al. employed molecular dynamics simulations of a discoidin domain homology model with the Rs1 domain sequence, predicting a highly extended form for this region (Sergeev, Caruso et al. 2010). Therefore, employing both hydrodynamic and SAXS analyses, we sought to characterise the nanostructure of the retinoschisin monomer and determine the conformation of the Rs1 domain region.

Both MALS and AUC analyses suggested that monomeric, wild-type retinoschisin was globular (Figure 3.3), however, higher resolution analysis afforded by SAXS revealed that this was an elongated structure, consisting of a smaller projection from a globular ‘core’ (Figures 3.4 and 3.5). However, *in vivo*, monomeric retinoschisin is secreted as an octamer, therefore the secreted monomer is potentially an artefactual ‘oligomerisation-incompetent’ monomer caused by non-native intramolecular disulphide bond formation, induced by the high expression levels. SAXS analysis of the C40S/C59S/C223S triple mutant confirmed a highly similar structure to the wild-type, suggesting the elongated shape is not dependent on the octamerising cysteine residues in the N and C-termini (Figure 3.8). Comparison of the wild-type monomer structure to the discoidin domain suggested that the elongated character of the molecule was due to the presence of the Rs1 domain, with the discoidin domain possessing a more globular shape (Figure 3.12). As a result, we suggest that the structure of the retinoschisin monomer consists of a globular ‘core’ of the folded discoidin domain with a highly extended projection consisting mainly of the Rs1 domain. These data are consistent with the structure predicted by Sergeev and colleagues using molecular dynamics approaches (Sergeev, Caruso et al.

2010). We hypothesize that the projection of the Rs1 domains away from the globular core allows for efficient octamerisation of the subunits as the ‘wedge’ shape allows for the monomers to closely associate and form disulphide bonds in the centre of the octamer without inducing steric clashing between the larger, adjacent discoidin domains.

7.2 Characterisation of the Octamer Structure

Indeed, this tight association of the subunits in the retinoschisin octamer was shown both by hydrodynamics and negative stain EM (Figures 4.1 and 4.2). The subunits octamerised forming a highly planar ‘propeller’ structure, which (likely due to the highly planar nature of the molecule) showed preferential orientation on the carbon support of the grid. Analysis in solution at higher concentrations overcame this orientation bias, showing that in solution retinoschisin self-assembled into a dimer of octamers, which was observed for wild-type and XLRS-associated (R141H and H207Q) mutants (Figures 4.3, 4.4, 5.8 and 6.4). Structural analysis of the hexadecameric structure together with the retinoschisin octamer suggested little conformational change upon octamer dimerization, suggesting that the octamer produced a stable interface for hexadecamer construction (Figure 4.10). Furthermore, cryo-EM of the dimer of octamers suggested this complex formed due to the formation of many small interactions, building a stable complex through a highly avid overall interaction (Figure 5.10).

Such stable association of the octamers allowed for a model of retinoschisin function within the retina to be hypothesized. Here, concentration-driven hexadecamer formation between adjacent, immobilized retinoschisin octamers on opposing cells is hypothesized to form stable ‘linkers’ (Figure 4.15). This would allow retinoschisin to maintain the highly packed arrangement of cells in the retina, however, the formation of this complex at the photoreceptor-bipolar cell synapse could also allow for retinoschisin to co-ordinately regulate the localisation of the pre and post-synaptic signalling machinery as previously observed (Ou, Vijayasarathy et al. 2015). Therefore, together, through hexadecamer formation retinoschisin could potentially allow for more efficient synaptic signalling through clustering of the synaptic machinery. Indeed, the highly valent eight-fold binding sites could facilitate such clustering at the membrane, allowing for supramolecular re-organization at the synapse. Such ‘dual-function’ of retinoschisin in this model of general structural maintenance throughout the retina and as a signalling ‘tuner’ at the synapse could be achieved through exploiting the lectin binding capability of retinoschisin (Dyka, Wu et al. 2008), allowing it to complex with a host of integral membrane proteins throughout the retina through binding to their glycosylated ectodomains. Indeed, different glycosylated integral membrane binding partners (such as Na/K-ATPase and L-VGCC complexes) have been previously identified as important in anchoring retinoschisin to the

photoreceptor membrane (Molday, Wu et al. 2007, Shi, Jian et al. 2009, Friedrich, Stohr et al. 2011), consistent with this hypothesis.

However, whilst this study proposes this 'hexadecamer model' for retinoschisin function, an additional model has been proposed previously to explain retinoschisin action. In this model, the ability of retinoschisin to bind to ion channels at the plasma membrane suggests that it may have a role in osmotic homeostasis in the retina, with loss of retinoschisin causing dysregulation and fluid build-up which induces cystic cavity formation (Molday, Kellner et al. 2012). Indeed, carbonic anhydrase inhibitors (such as acetazolomide and dorzolomide), which inhibit carbonic anhydrase on the apical membrane of the retinal pigment epithelium inducing acidification of the retinal tissue and enhancing the rate of fluid export from the retinal tissue (Wolfensberger 1999), have been used in XLRS treatment. This reduction in intraocular pressure has been shown to reduce the schisis cavities in XLRS-sufferers (Apushkin and Fishman 2006, Walia, Fishman et al. 2009, Thobani and Fishman 2011, Collison, Genead et al. 2014, Rocha Cabrera, Pareja Rios et al. 2014, Sadaka and Sisk 2016). However, the reduction of fluid in the retina does not appear sufficient to rescue the neurotransmission in the retina (Khandhadia, Trump et al. 2011, Zhour, Bolz et al. 2012) and restore normal visual acuity as seen for AAV8-mediated retinoschisin re-introduction in mice models (Zeng, Takada et al. 2004, Min, Molday et al. 2005, Kjellstrom, Bush et al. 2007, Janssen, Min et al. 2008). As a result, this suggests that retinoschisin may have another as yet unidentified function. As a result, further functional and structural charactersiation of retinoschisin *in vivo* is required to determine the mechanism of retinoschisin action.

This study contributes to the wider goal of understanding the basis of retinal cell adhesion and the maintenance of the photoreceptor-bipolar cell synapse, where retinoschisin localises. Currently, a number of proteins have been implicated in the support of the synapse between the photoreceptors and bipolar cells, however, the precise mechanism by which these proteins work remain elusive. Indeed, direct linkage between the photoreceptor and bipolar cell membranes (as hypothesized for retinoschisin function by this study) has been proposed before. The proteins α-dystroglycan and β-dystroglycan have been identified as important in maintaining synapse structure, linking dystrophin and the photoreceptor cytoskeleton to the laminin interphotoreceptor extracellular matrix (Ibraghimov-Beskrovnaya, Ervasti et al. 1992, Talts, Andac et al. 1999, Mercer and Thoreson 2011), as previously proposed for retinoschisin (Steiner-Champliaud, Sahel et al. 2006). However, the highly glycosylated character of α-dystroglycan also allows it to complex with pikachurin, another extracellular factor (Sato, Omori et al. 2008), with reduction of the glycan-dependent interaction between these proteins leading to loss of retinal structure (Kanagawa, Omori et al. 2010, Hu, Li et al. 2011). Analogous to

retinoschisin, no post-synaptic binding partners have been identified for pikachurin (Mercer and Thoreson 2011), with the existence of these binding partners hypothesized due to the disruption of the outer plexiform layer in pikachurin knockout mice (Kanagawa, Omori et al. 2010). Similarly, another such physical linker has been proposed for MAGI proteins. Here, pre-synaptic MAGI proteins interact with sidekick-2 in the synapse which also complexes with the post-synaptic MAGI proteins, allowing for a large complex to form, spanning the synapse (Yamagata and Sanes 2010). However, the splitting of the retina at the outer plexiform layer in XLRS patients suggests that retinoschisin is also a critical structural component. In this study, we propose that association of the retinoschisin hexadecamer with both pre and post-synaptic integral membrane proteins could form a new linkage which is important in maintaining synapse structure. However, the ability of retinoschisin to diffuse throughout the retina and attach to other membrane factors may allow it to also form additional linkers throughout the retina maintaining the normal laminar structure.

Indeed, the observation that loss of retinoschisin in *Rs1h*$^{-/y}$ mice models also led to the splitting of adjacent photoreceptors suggests the presence of a 'dual-role', whereby hexadecamer formation here on the basolateral membranes may allow for tight association of columnar photoreceptors (Vijayasarathy, Takada et al. 2007). This may represent a general adhesive function that it may serve throughout the retina. However, whilst retinoschisin diffuses throughout the retina, mutation of this protein appears to affect only the outer retina, suggesting that this may be the main region of retinoschisin function (Yang, Lee et al. 2014). However, it cannot be ruled out that retinoschisin functions in other cell layers. Throughout the retina there are many other protein complexes regulating cell-cell interactions, often in a cell-type specific manner. There are regulated repulsive (arising from for example semaphorins and plexins, Megf10 and 11 and protocadherins) and adhesive (such as Dscam, Sidekick1 and Sidekick2) interactions combining to regulate retinal structure (Hoon, Okawa et al. 2014). Also, an extensive supportive extracellular matrix is observed in the retina, with a distinct matrix, the interphotoreceptor matrix, observed around the photoreceptor cell layer (Al-Ubaidi, Naash et al. 2013, Ishikawa, Sawada et al. 2015). As a result, retinoschisin may form one type of adhesive interaction amongst a host of others, and as a result, the contribution of retinoschisin to structural integrity with other cell types and other cell layers outside the outer layers is unknown, and may be challenging to investigate due to potential functional redundancy with other adhesive molecules or the extracellular matrix.

Alongside the putative adhesion function of retinoschisin in this context, we also hypothesize that retinoschisin may also be able to cluster or organize membrane binding partners to allow for efficient synaptic signalling. Indeed, such organization of signalling

machinery has been observed at this synapse. PSD-95, an intracellular PDZ-domain containing protein is found at the intracellular surface of the pre-synaptic membrane. Here, it is known to be important in organizing integral membrane complexes such as PMCA (Aartsen, Arsanto et al. 2009) and TMEM16B (Stohr, Heisig et al. 2009). However, the action of PSD-95 is localized to the pre-synaptic membrane as it occurs intracellularly, whereas in the proposed model, retinoschisin may be able to carry out such a clustering role extracellularly on both the pre and post-synaptic membranes simultaneously. Together, in this hypothesis, retinoschisin would be able to carry out two of the previously identified principal functions of extracellular matrix proteins at the photoreceptor-bipolar cell synapse, linkage and membrane complex organisation, simultaneously.

However, whilst this structural observation of retinoschisin has been confirmed by other studies (Bush, Setiaputra et al. 2016, Tolun, Vijayasarathy et al. 2016), currently, the proposed model remains a hypothesis, with further functional characterisation required *in vivo*. Furthermore, other functions such as retinoschisin-mediated cellular linkages to the retinal extracellular matrix cannot be ruled out.

7.3 Mutational Analysis of the Retinoschisin Dimer of Octamers

The resolution of the dimer of octamers cryo-EM structure allowed for construction of a quasi-atomic model of retinoschisin. This, in turn allowed for the effects of previously uncharacterised XLRS-associated mutations on the fully assembled complex to be investigated. Previously, mapping of these mutations was limited to homology models of the isolated discoidin domain, with such studies identifying disease-associated mutations with little predicted effect on this structure, (Sergeev, Caruso et al. 2010, Sergeev, Vitale et al. 2013) suggesting that these mutations may alter retinoschisin assembly or inter-molecular interactions. Therefore, mutations were selected from the LOVD database which had conservative BLOSUM62 substitution matrix scores (above -1) or were previously predicted to have limited effect on retinoschisin folding (Sergeev, Caruso et al. 2010, Sergeev, Vitale et al. 2013). Mapping of these mutations revealed two clusters of conservative mutations at the intra-octamer interface between adjacent discoidin domains (Class I) and the inter-octamer interface between the octamer rings (Class II). Class I mutations were predicted to prevent octamer formation, with three XLRS-associated mutations (E72K, N104K and T185K) found at the contact sites between the domains, preventing secretion of retinoschisin (Wu and Molday 2003, Wang, Zhou et al. 2006, Dyka and Molday 2007) despite the predicted lack of effect on discoidin domain folding. As a result, we predict that the other currently uncharacterised Class I mutations will either lead to secretion of monomeric retinoschisin or loss of secretion. However, whilst these studies predict the effect of these mutations, the effect on secretion and oligomerisation needs to

be investigated in a cell-based system, as performed for other mutants, before these structural observations can be confirmed.

Class II mutations however, had been previously observed to maintain octameric secretion. Both H207Q and R209H were secreted from HEK 293-EBNA cells as octamers (Wang, Zhou et al. 2006), suggesting that pathology may rise from disruption of the octamer dimerization interface. As a result, the hexadecamer may have functional significance, with alteration of this structure leading to disease. This is consistent with the hypothesized model for retinoschisin function.

In addition to the identified clusters, another mutated site was identified. R141H is mutated on spike 3, away from either interface. This is consistent with the lack of assembly defects for this mutant and suggested that this may represent an intermolecular binding interface. Indeed, mutation at this site was associated with both loss of galactose binding affinity and an alteration of the channel binding kinetics of the L-VGCC binding partner on photoreceptor membranes (Dyka, Wu et al. 2008, Shi, Jian et al. 2009). As a result, the effect of this mutation was investigated. Despite the apparent functional significance, the R141H mutation introduced little structural alteration, with only small conformational change detected by intrinsic fluorescence spectroscopy, which may represent a subtle reorganization of the discoidin domain spikes. This may induce an alteration of the structure or the dynamics of the region which in turn affects a binding interface. Indeed, alterations in the migration of the R141H in nativePAGE suggested that there could be a change in the charge distribution of the molecule; however, the effect of this mutation on the structure must be more closely investigated in order to determine the nature of the alteration. Furthermore, whilst we hypothesize that this region represents a binding site, this has not been confirmed. Therefore, binding studies and mapping of interaction sites with known binding partners is required to investigate the effect of this mutation.

In addition to the characterisation of the R141H mutation, the effect of the XLRS-associated H207Q mutation (identified as a class II mutation in the retinoschisin structure) was investigated. Consistent with previous studies (Wang, Zhou et al. 2006), this was secreted as an octamer from HEK 293-EBNA cells which assembled into the planar propeller shape, with nativePAGE suggesting the formation of a dimer of octamers. This suggests that despite the presence of this mutation in the inter-octamer interface, this mutation is not sufficient to prevent octamer dimerization. This may be due to binding by the other contact sites, however, this may generate a less stable dimerization interface. Indeed, despite the low predicted effect of this mutation, it caused a marked reduction in the stability of both the monomer and the octamer, suggesting that any complex formed

by the H207Q mutant would be less stable and more prone to unfolding and aggregation, which may also be observed for other Class II mutations. This raises a potential challenge for the development of therapeutics for patients carrying these disease-associated mutations. Previously, Dyka et al. showed that expression and secretion of wild-type retinoschisin octamers was unaffected by the co-expression of aggregating XLRS-associated mutants in HEK293 cells. However, co-expression of wild-type with R141H mutants led to co-assembly of mutant and wild-type protein to form chimeric octamers which may be non-functional (Dyka and Molday 2007). The assembly of the H207Q mutant into the characteristic propeller shape suggested that this may also occur for the H207Q mutant. This is relevant for the current ongoing clinical trail for the reintroduction of wild-type retinoschisin into the eyes of XLRS sufferers using AAV vectors (https://clinicaltrials.gov/ct2/show/NCT02317887?term=xlrs&rank=5). In sufferers with the H207Q mutation, less stable chimeric complexes may be formed which are non-functional. Furthermore, if this effect is seen for all class II mutations, this may lead to a greater number of patients than previously thought who may not be able to be treated using this approach. As a result, the effects of the Class II mutations on the retinoschisin structure and the formation of chimeras must be investigated to determine if the observed detabilisation for the H207Q mutant is characteristic of mutations at this site. Furthermore, the ability of these mutants to form chimeras and the stability of these complexes must be tested.

7.4 Future Directions

Following from this study, future work should be arranged into two main areas: to investigate the proposed model for retinoschisin action and to further characterise the effects of XLRS-associated mutations on retinoschisin structure.

7.4.1 Investigating the Proposed Model for Retinoschisin Function at the Photoreceptor-Bipolar Cell Synapse

In order to investigate the hypothesized model for retinoschisin function, the presence of the dimer of octamers must be confirmed *in vivo*. Towards this aim, the presence of the dimer of octamers could be investigated using tomography of photoreceptor-bipolar synapses or of purified photoreceptor membranes. The retinoschisin molecules could be extracted from the tomograms and the structure solved using sub-tomogram averaging. This may be challenging due to the relatively small size of the retinoschisin complex, however, the improved imaging afforded by the next generation of DDD cameras may allow for structural resolution.

Furthermore, to investigate the model, the interaction of L-VGCC with retinoschisin should be investigated. Currently retinoschisin has been shown to interact with a site in the N-terminal 500 residues of the CaV 1.3 channel (Shi, Jian et al. 2009). However the nature of this interaction is not known and could be either a protein-protein interaction or mediated via retinoschisin binding to the glycosylation of the channel. Indeed, the $\alpha_2\delta$ subunit is highly glycosylated and may represent a retinoschisin binding site (Davies, Hendrich et al. 2007). Therefore, binding studies should be performed with glycosylated and deglycosylated channel subunits and in the presence of free competing oligosaccharides to further map the binding site. Furthermore, such binding assays may be used to investigate the effect of the R141H mutation on the binding affinity and complex formation with the L-VGCC N-terminal region.

The identified region of L-VGCC bound by retinoschisin is still large, encompassing a single repetitive unit of six transmembrane alpha helices and extracellular loops in CaV 1.3, spanning from the periphery of the channel to the central pore (Wu, Yan et al. 2015). A structure of retinoschisin complexed to CaV 1.3 would allow for the binding sites on both proteins to be localized and the effect of the R141H mutation could be assessed from the complex structure. Previously, this mutation was also found to affect the circadian regulation of the L-VGCC channel, which was required for circadian regulation of retinoschisin (Ko, Liu et al. 2008). A complex structure would allow for the presence of any conformational changes or other regulatory mechanisms used by retinoschisin to regulate channel gating kinetics to be investigated through comparison to the structure of the homologous CaV 1.1 channel solved using cryo-EM (Wu, Yan et al. 2015).

As part of the hypothesized model, the high valency of the retinoschisin hexadecamer suggested that retinoschisin may be able to cluster signalling machinery at the photoreceptor-bipolar cell synapse, allowing for more efficient signalling. This could be investigated using super resolution microscopy. Indeed, the use of photoactivatable localisation microscopy (PALM) allowed for the identification of clusters of a small (56 kDa) membrane localized Src-related protein Lck and another Src kinase conjugated to the photo-convertible fluorescent protein tdEdos in the plasma membrane (Owen, Rentero et al. 2010). Furthermore, exploiting another super-resolution method, direct stochastic optical reconstruction microscopy (dSTORM) using Cy dye conjugated anit-phosphorylated LAT antibodies, phosphorylated Linker for Activation of T-cells (LAT) microclusters in the T-cell immunological synapse could be imaged (Owen, Rentero et al. 2010). Employing this approach in cells co-expressing L-VGCCs and retinoschisin could allow for investigation if retinoschisin is sufficient to drive membrane clustering of these channels.

In order to investigate the presence of a synapse-spanning linker at the synapse, it is important to identify a post-synaptic binding partner for retinoschisin. The observation of loss of synaptic localisation of TRPM1 and mGluR6 integral membrane proteins (Ou, Vijayasarathy et al. 2015) suggests these may be candidates for any hypothesized interaction. This should be investigated using co-immunoprecipitation and co-localisation of both proteins, with any identified interaction possibly investigated biophysically using surface plasmon resonance (SPR) of purified proteins or protein fragments of the proposed binding partner.

7.4.2 Investigating the Effects of Mutation on Retinoschisin Structure

The mutational characterisation of retinoschisin should be continued to characterise the effects of the mapped mutations on the retinoschisin structure. From the positions of the Class I mutations, we predicted that these mutations would lead to loss of octamerisation and possibly secretion, as observed for the E72K, N104K and T185K mutations. Employing a cell based assay, the secretion and octamerisation of each mutant should be characterised using western blotting in reducing and non-reducing conditions of cell medium and lysates to determine the effect of each mutation on complex assembly.

The secretion and oligomerisation of the uncharacterised mutations in the class II mutations should also be investigated to determine if all disease-associated mutants here are still capable of forming octamers and if the mutants are destabilized like H207Q retinoschisin. As observed for the R141H mutant, the ability of the class II mutants to co-assemble with co-expressed wild-type retinoschisin should be investigated to determine if the use of gene therapy for patients carrying these mutations is compromised by co-assembly of the mutant and wild-type protein, as predicted for the R141H mutant (Dyka and Molday 2007). Moreover, if the destabilization observed for H207Q is common to all class II mutations, this may represent a common difficulty in gene therapy-based treatment for all class II mutations as these mutations could lead to the formation of unstable chimeras in patients.

The observation that the H207Q mutant still formed dimers of octamers suggested that there is more than one important contact which drives octamer dimerization, with three contacts identified by PDBePISA analysis (Figure 5.16). In order to identify the residues required for contact, residues in each of the contact sites could be mutated simultaneously, with the formation of the dimer of octamers in the these double and triple mutants assessed using nativePAGE. Furthermore, cryo-EM structural investigation of the H207Q octamer could be carried out to identify any induced conformational change. This may break interactions at the inter-octamer interface which may reduce the affinity of

binding between the octamers. Such lowering of binding affinity could also be investigated using molecular dynamics simulations of the constructed quasi-atomic model for the hexadecamer. The free energy of association of the octamers in explicit solvent could be simulated in the presence and absence of the mutation, with a reduction in the favourability of octamer association suggesting a lowered binding affinity. Moreover, the effect of class II mutations on the binding affinity between the octamers could also be investigated using sedimentation equilibrium, which could determine the K_d for association of the wild-type and mutant octamers.

The R141H mutation appears to affect another site away from either identified interface, with a small conformational change suggested by this study. This may occur in the spike regions of the discoidin domain which may be a new functional site in the molecule. As a result, the alteration should be more closely examined. Such investigation would require the use of high-resolution techniques such as X-ray crystallography or NMR spectroscopy to investigate any subtle conformational alteration or changes in the dynamics of this region. These studies could potentially complement structural and binding studies of retinoschisin in complex with L-VGCC, allowing for the origin of the alteration in the channel gating kinetics to be investigated. Due to the molecular size restriction of such analyses, NMR characterisation would be carried out on monomeric retinoschisin.

However, high-resolution analysis of retinoschisin structure will require higher purification yields. The production of sufficient quantities of retinoschisin for structural and biochemical characterisation has previously been challenging (Molday, Kellner et al. 2012). Employing a stable HEK293-EBNA expression system allowed for sufficient quantities of retinoschisin for cryo-EM analysis in this study. Other studies have exploited both stable and transient insect cell expression systems which have also given good yields, allowing for cryo-EM analysis (Dyka, Wu et al. 2008, Bush, Setiaputra et al. 2016, Tolun, Vijayasarathy et al. 2016). However, these yields still fall short of those required for X-ray crystallography and NMR analysis. This study also used the yeast expression system *Pichia pastoris* X-33 for the production of retinoschisin monomer. Whilst this gave enough material for hydrodynamic and SAXS analyses, again the yield was still not sufficient for higher resolution analysis and was also difficult to separate from contaminating species. Therefore, following from this study, a higher expression system could be developed using bacteria that facilitate disulphide bonding in expressed proteins such as Oragami (DE3) and CyDisCo strains. Use of bacteria would also allow for doping of the protein with heavy nitrogen and carbon isotopes required for NMR analysis.

NativePAGE also suggested that there was a change in the surface charge of the R141H octamer. Indeed, R141 is found in a surface-exposed, positively charged region of the

discoidin domain in the retinoschisin octamer. This could be relevant to any binding interactions and could be investigated using isoelectric focusing. A change in the mutant isoelectric point (pI) would support a change in the charge of the molecule, which may in turn alter an electrostatic interaction, leading to pathology.

7.5 Conclusions

This study has demonstrated that retinoschisin forms an elongated structure (due to the extension of the N-terminal Rs1 domain) which octamerises to form a highly planar, propeller octamer. Furthermore, at higher concentrations, the octamers self-assemble into dimers of octamers with no detectable conformational changes induced upon octamer dimerization. Using the hexadecamer structure, uncharacterised, disease-associated point mutations were mapped, identifying three distinct classes of XLRS-associated mutations which may affect assembly of the octamer (Class I), assembly of the hexadecamer (Class II) and an additional site in spike 3, which may alter an inter-molecular interaction site. Together, these structural findings, allowed for the hypothesis of a model for retinoschisin function in the retina. Work is still in the early stages towards that goal, with further structural and binding analyses of the wild-type and disease-associated mutants required both *in situ* and *in vitro* to further investigate the hypothesis.

8 References

Aartsen, W. M., J. P. Arsanto, J. P. Chauvin, R. M. Vos, I. Versteeg, B. N. Cardozo, A. L. Bivic and J. Wijnholds (2009). "PSD95beta regulates plasma membrane Ca2+ pump localization at the photoreceptor synapse." Mol Cell Neurosci **41**(2): 156-165.

Adrian, M., J. Dubochet, J. Lepault and A. W. McDowall (1984). "Cryo-electron microscopy of viruses." Nature **308**(5954): 32-36.

Al-Ubaidi, M. R., M. I. Naash and S. M. Conley (2013). "A perspective on the role of the extracellular matrix in progressive retinal degenerative disorders." Invest Ophthalmol Vis Sci **54**(13): 8119-8124.

Alanen, H. I., K. L. Walker, M. Lourdes Velez Suberbie, C. F. Matos, S. Bonisch, R. B. Freedman, E. Keshavarz-Moore, L. W. Ruddock and C. Robinson (2015). "Efficient export of human growth hormone, interferon alpha2b and antibody fragments to the periplasm by the Escherichia coli Tat pathway in the absence of prior disulfide bond formation." Biochim Biophys Acta **1853**(3): 756-763.

Alexander, K. R., C. S. Barnes and G. A. Fishman (2001). "High-frequency attenuation of the cone ERG and ON-response deficits in X-linked retinoschisis." Invest Ophthalmol Vis Sci **42**(9): 2094-2101.

Ali, S. and R. Seth (2013). "X-linked juvenile retinoschisis in females and response to carbonic anhydrase inhibitors: case report and review of the literature." Semin Ophthalmol **28**(1): 50-54.

Alitalo, T., J. Karna, H. Forsius and A. Delachapelle (1987). "X-Linked Retinoschisis Is Closely Linked to Dxs41 and Dxs16 but Not Dxs85." Clin Genet **32**(3): 192-195.

Antonicek, H., E. Persohn and M. Schachner (1987). "Biochemical and Functional-Characterization of a Novel Neuron-Glia Adhesion Molecule That Is Involved in Neuronal Migration." J Cell Biol **104**(6): 1587-1595.

Apaolaza, P. S., A. Del Pozo-Rodriguez, J. Torrecilla, A. Rodriguez-Gascon, J. M. Rodriguez, U. Friedrich, B. H. Weber and M. A. Solinis (2015). "Solid lipid nanoparticle-based vectors intended for the treatment of X-linked juvenile retinoschisis by gene therapy: In vivo approaches in Rs1h-deficient mouse model." J Control Release **217**: 273-283.

Apaolaza, P. S., D. Delgado, A. del Pozo-Rodriguez, A. R. Gascon and M. A. Solinis (2014). "A novel gene therapy vector based on hyaluronic acid and solid lipid nanoparticles for ocular diseases." Int J Pharm **465**(1-2): 413-426.

Apushkin, M. A. and G. A. Fishman (2006). "Use of dorzolamide for patients with X-linked retinoschisis." Retina- J Ret Vit Dis **26**(7): 741-745.

Apushkin, M. A., G. A. Fishman and A. S. Rajagopalan (2005). "Fundus findings and longitudinal study of visual acuity loss in patients with X-linked retinoschisis." Retina **25**(5): 612-618.

Bai, X. C., G. McMullan and S. H. Scheres (2015). "How cryo-EM is revolutionizing structural biology." Trends Biochem Sci **40**(1): 49-57.

Bai, X. C., C. Yan, G. Yang, P. Lu, D. Ma, L. Sun, R. Zhou, S. H. Scheres and Y. Shi (2015). "An atomic structure of human gamma-secretase." Nature **525**(7568): 212-217.

Bartesaghi, A., A. Merk, S. Banerjee, D. Matthies, X. Wu, J. L. Milne and S. Subramaniam (2015). "2.2 A resolution cryo-EM structure of beta-galactosidase in complex with a cell-permeant inhibitor." Science **348**(6239): 1147-1151.

Baumgartner, S., K. Hofmann, R. Chiquet-Ehrismann and P. Bucher (1998). "The discoidin domain family revisited: New members from prokaryotes and a homology-based fold prediction." Protein Sci **7**(7): 1626-1631.

Blanco, G. and R. W. Mercer (1998). "Isozymes of the Na-K-ATPase: heterogeneity in structure, diversity in function." Am J Physiol-Renal **275**(5): F633-F650.

Blumenschein, T. M., N. Friedrich, R. A. Childs, S. Saouros, E. P. Carpenter, M. A. Campanero-Rhodes, P. Simpson, W. Chai, T. Koutroukides, M. J. Blackman, T. Feizi, D. Soldati-Favre and S. Matthews (2007). "Atomic resolution insight into host cell recognition by Toxoplasma gondii." EMBO J **26**(11): 2808-2820.

Brenner, S. and R. W. Horne (1959). "A negative staining method for high resolution electron microscopy of viruses." Biochim Biophys Acta **34**: 103-110.

Brilot, A. F., J. Z. Chen, A. Cheng, J. Pan, S. C. Harrison, C. S. Potter, B. Carragher, R. Henderson and N. Grigorieff (2012). "Beam-induced motion of vitrified specimen on holey carbon film." J Struct Biol **177**(3): 630-637.

Buraei, Z. and J. Yang (2013). "Structure and function of the beta subunit of voltage-gated Ca(2)(+) channels." Biochim Biophys Acta **1828**(7): 1530-1540.

Bush, M., D. Setiaputra, C. K. Yip and R. S. Molday (2016). "Cog-Wheel Octameric Structure of RS1, the Discoidin Domain Containing Retinal Protein Associated with X-Linked Retinoschisis." PLoS One **11**(1): e0147653.

Byrne, L. C., B. E. Ozturk, T. Lee, C. Fortuny, M. Visel, D. Dalkara, D. V. Schaffer and J. G. Flannery (2014). "Retinoschisin gene therapy in photoreceptors, Muller glia or all retinal cells in the Rs1h-/- mouse." Gene Ther **21**(6): 585-592.

Campbell, M. G., A. Cheng, A. F. Brilot, A. Moeller, D. Lyumkis, D. Veesler, J. Pan, S. C. Harrison, C. S. Potter, B. Carragher and N. Grigorieff (2012). "Movies of ice-embedded particles enhance resolution in electron cryo-microscopy." Structure **20**(11): 1823-1828.

Carafoli, F., D. Bihan, S. Stathopoulos, A. D. Konitsiotis, M. Kvansakul, R. W. Farndale, B. Leitinger and E. Hohenester (2009). "Crystallographic Insight into Collagen Recognition by Discoidin Domain Receptor 2." Structure **17**(12): 1573-1581.

Chen, C. Y., C. W. Lin, C. Y. Chang, S. T. Jiang and Y. P. Hsueh (2011). "Sarm1, a negative regulator of innate immunity, interacts with syndecan-2 and regulates neuronal morphology." J Cell Biol **193**(4): 769-784.

Cheng, Y. F. (2015). "Single-Particle Cryo-EM at Crystallographic Resolution." Cell **161**(3): 450-457.

Cole, R. and J. P. Loria (2002). "Evidence for flexibility in the function of ribonuclease A." Biochemistry **41**(19): 6072-6081.

Collison, F. T., M. A. Genead, G. A. Fishman and E. M. Stone (2014). "Resolution of mid-peripheral schisis in x-linked retinoschisis with the use of dorzolamide." Ophthalmic Genet **35**(2): 125-127.

Crowther, R. A., L. A. Amos, J. T. Finch, D. J. De Rosier and A. Klug (1970). "Three dimensional reconstructions of spherical viruses by fourier synthesis from electron micrographs." Nature **226**(5244): 421-425.

Danev, R. and W. Baumeister (2016). "Cryo-EM single particle analysis with the Volta phase plate." Elife **5**.

Danev, R. and K. Nagayama (2010). "Phase plates for transmission electron microscopy." Methods Enzymol **481**: 343-369.

Davies, A., J. Hendrich, A. T. Van Minh, J. Wratten, L. Douglas and A. C. Dolphin (2007). "Functional biology of the alpha(2)delta subunits of voltage-gated calcium channels." Trends Pharmacol Sci **28**(5): 220-228.

de la Torre, J. G., M. L. Huertas and B. Carrasco (2000). "Calculation of hydrodynamic properties of globular proteins from their atomic-level structure." Biophys J **78**(2): 719-730.

De Rosier, D. J. and A. Klug (1968). "Reconstruction of three dimensional structures from electron micrographs." Nature **217**(5124): 130-134.

De Waard, M., C. A. Gurnett and K. P. Campbell (1996). "Structural and functional diversity of voltage-activated calcium channels." Ion Channels **4**: 41-87.

Dejong, P. T. V. M., E. Zrenner, G. J. Vanmeel, J. E. E. Keunen and D. Vannorren (1991). "Mizuo Phenomenon in X-Linked Retinoschisis - Pathogenesis of the Mizuo Phenomenon." Arch Ophthalmol **109**(8): 1104-1108.

Delgado, D., A. del Pozo-Rodriguez, M. A. Solinis, M. Aviles-Triqueros, B. H. Weber, E. Fernandez and A. R. Gascon (2012). "Dextran and protamine-based solid lipid nanoparticles as potential vectors for the treatment of X-linked juvenile retinoschisis." Hum Gene Ther **23**(4): 345-355.

den Dunnen, J. T., T. Kraayenbrink, M. van Schooneveld, E. van de Vosse, P. T. V. M. de Jong, J. B. ten Brink, E. Schuurman, N. Tijmes, G. J. B. van Ommen, A. A. B. Bergen, G. Andolfi, E. Montini, Y. Li, C. Oudet, H. Bolz, J. Kaplan, U. Orth, A. Gal, A. Hanauer, A. M. Bardelli, C. Ayuso, F. J. Diaz, P. Bitoun, V. Ventruto, A. Ballabio, B. Franco, K. T. Hiriyanna, E. L. Bingham, C. McHenry, H. Pawar, C. Coats, T. Darga, J. E. Richards, P. A. Sieving, L. Huopaniemi, A. Rantala, T. Rosenberg, N. Dahl, A. Wright, A. de la Chapelle, T. Alitalo, S. Lenzner, B. Brunner, S. Feil, B. Niesler, U. Schulz, A. Pinckers, A. Blankennagel, K. Ruether, U. Kellner, G. Rappold, H. H. Ropers, V. Kalscheuer, W. Berger, D. Trump, S. M. Walpole, A. Nicolaou, S. A. Gaythor, D. Pimenides, N. D. L. George, U. T. Moore, J. R. W. Yates and R. Consortium (1998). "Functional implications of the spectrum of mutations found in 234 cases with X-linked juvenile retinoschisis (XLRS)." Hum Mol Genet **7**(7): 1185-1192.

Dhingra, A., A. Lyubarsky, M. S. Jiang, E. N. Pugh, L. Birnbaumer, P. Sterling and N. Vardi (2000). "The light response of ON bipolar neurons requires G alpha(o)." J Neurosci **20**(24): 9053-9058.

Dubochet, J., M. Adrian, J. J. Chang, J. C. Homo, J. Lepault, A. W. McDowall and P. Schultz (1988). "Cryo-electron microscopy of vitrified specimens." Q Rev Biophys **21**(2): 129-228.

Durand, D., C. Vives, D. Cannella, J. Perez, E. Pebay-Peyroula, P. Vachette and F. Fieschi (2010). "NADPH oxidase activator p67(phox) behaves in solution as a multidomain protein with semi-flexible linkers." J Struct Biol **169**(1): 45-53.

Dyka, F. M. and R. S. Molday (2007). "Coexpression and interaction of wild-type and missense RS1 mutants associated with X-linked retinoschisis: its relevance to gene therapy." Invest Ophthalmol Vis Sci **48**(6): 2491-2497.

Dyka, F. M., W. W. Wu, T. A. Pfeifer, L. L. Molday, T. A. Grigliatti and R. S. Molday (2008). "Characterization and purification of the discoidin domain-containing protein retinoschisin and its interaction with galactose." Biochemistry **47**(35): 9098-9106.

Ebert, S., K. Weigelt, Y. Walczak, W. Drobnik, R. Mauerer, D. A. Hume, B. H. Weber and T. Langmann (2009). "Docosahexaenoic acid attenuates microglial activation and delays early retinal degeneration." J Neurochem **110**(6): 1863-1875.

Eksandh, L., S. Andreasson and M. Abrahamson (2005). "Juvenile X-linked retinoschisis with normal scotopic b-wave in the electroretinogram at an early stage of the disease." Ophthalmic Genet **26**(3): 111-117.

Erickson, H. P. and A. Klug (1970). "Fourier Transform of an Electron Micrograph - Effects of Defocussing and Aberrations, and Implications for Use of Underfocus Contrast Enhancement." Berichte Der Bunsen-Gesellschaft Fur Physikalische Chemie **74**(11): 1129-&.

Faruqi, A. R. and R. Henderson (2007). "Electronic detectors for electron microscopy." Curr Opin Struct Biol **17**(5): 549-555.

Frank, J., M. Radermacher, P. Penczek, J. Zhu, Y. Li, M. Ladjadj and A. Leith (1996). "SPIDER and WEB: processing and visualization of images in 3D electron microscopy and related fields." J Struct Biol **116**(1): 190-199.

Franke, D. and D. I. Svergun (2009). "DAMMIF, a program for rapid ab-initio shape determination in small-angle scattering." J App Crystallogr **42**: 342-346.

Fraternali, F., L. Cavallo and G. Musco (2003). "Effects of pathological mutations on the stability of a conserved amino acid triad in retinoschisin." FEBS Lett **544**(1-3): 21-26.

Friedrich, U., H. Stohr, D. Hilfinger, T. Loenhardt, M. Schachner, T. Langmann and B. H. Weber (2011). "The Na/K-ATPase is obligatory for membrane anchorage of retinoschisin, the protein involved in the pathogenesis of X-linked juvenile retinoschisis." Hum Mol Genet **20**(6): 1132-1142.

Garstka, M. A., A. Fish, P. H. N. Celie, R. P. Joosten, G. M. C. Janssen, I. Berlin, R. Hoppes, M. Stadnik, L. Janssen, H. Ovaa, P. A. van Veelen, A. Perrakis and J. Neefjes (2015). "The first step of peptide selection in antigen presentation by MHC class I molecules." Proc Natl Acad Sci U S A **112**(5): 1505-1510.

Gehrig, A., A. Janssen, F. Horling, C. Grimm and B. H. Weber (2006). "The role of caspases in photoreceptor cell death of the retinoschisin-deficient mouse." Cytogenet Genome Res **115**(1): 35-44.

Gehrig, A., T. Langmann, F. Horling, A. Janssen, M. Bonin, M. Walter, S. Poths and B. H. Weber (2007). "Genome-wide expression profiling of the retinoschisin-deficient retina in early postnatal mouse development." Invest Ophthalmol Vis Sci **48**(2): 891-900.

Gehrig, A., K. White, B. Lorenz, M. Andrassi, S. Clemens and B. H. Weber (1999). "Assessment of RS1 in X-linked juvenile retinoschisis and sporadic senile retinoschisis." Clin Genet **55**(6): 461-465.

Gehrig, A. E., R. Warneke-Wittstock, C. G. Sauer and B. H. Weber (1999). "Isolation and characterization of the murine X-linked juvenile retinoschisis (Rs1h) gene." Mamm Genome **10**(3): 303-307.

Genead, M. A., G. A. Fishman and S. Walia (2010). "Efficacy of sustained topical dorzolamide therapy for cystic macular lesions in patients with X-linked retinoschisis." Arch Ophthalmol **128**(2): 190-197.

Genead, M. A., S. Pasadhika and G. A. Fishman (2009). "Retinal nerve fibre layer thickness analysis in X-linked retinoschisis using Fourier-domain OCT." Eye (Lond) **23**(5): 1019-1027.

George, N. D., J. R. Yates, K. Bradshaw and A. T. Moore (1995). "Infantile presentation of X linked retinoschisis." Br J Ophthalmol **79**(7): 653-657.

George, N. D., J. R. Yates and A. T. Moore (1995). "X linked retinoschisis." Br J Ophthalmol **79**(7): 697-702.

Gleghorn, L. J., D. Trump and N. J. Bulleid (2010). "Wild-type and missense mutants of retinoschisin co-assemble resulting in either intracellular retention or incorrect assembly of the functionally active octamer." Biochem J **425**(1): 275-283.

Gloor, S., H. Antonicek, K. J. Sweadner, S. Pagliusi, R. Frank, M. Moos and M. Schachner (1990). "The Adhesion Molecule on Glia (Amog) Is a Homolog of the Beta-Subunit of the Na,K-Atpase." J Cell Biol **110**(1): 165-174.

Grayson, C., S. N. Reid, J. A. Ellis, A. Rutherford, J. C. Sowden, J. R. Yates, D. B. Farber and D. Trump (2000). "Retinoschisin, the X-linked retinoschisis protein, is a secreted photoreceptor protein, and is expressed and released by Weri-Rb1 cells." Hum Mol Genet **9**(12): 1873-1879.

Grigorieff, N. (2007). "FREALIGN: high-resolution refinement of single particle structures." J Struct Biol **157**(1): 117-125.

Harauz, G. and F. P. Ottensmeyer (1983). "Direct three-dimensional reconstruction for macromolecular complexes from electron micrographs." Ultramicroscopy **12**(4): 309-319.

Henderson, R. (1995). "The potential and limitations of neutrons, electrons and X-rays for atomic resolution microscopy of unstained biological molecules." Q Rev Biophys **28**(2): 171-193.

Hildebrand, G. D. and A. R. Fielder (2011). "Anatomy and Physiology of the Retina." Pediatric Retina: 39-65.

Hiriyanna, K. T., E. L. Bingham, B. M. Yashar, R. Ayyagari, G. Fishman, K. W. Small, D. V. Weinberg, R. G. Weleber, R. A. Lewis, S. Andreasson, J. E. Richards and P. A. Sieving (1999). "Novel mutations in XLRS1 causing retinoschisis, including first evidence of putative leader sequence change." Human Mutation **14**(5): 423-427.

Hoon, M., H. Okawa, L. Della Santina and R. O. Wong (2014). "Functional architecture of the retina: development and disease." Prog Retin Eye Res **42**: 44-84.

Hu, H., J. Li, Z. Zhang and M. Yu (2011). "Pikachurin interaction with dystroglycan is diminished by defective O-mannosyl glycosylation in congenital muscular dystrophy models and rescued by LARGE overexpression." Neurosci Lett **489**(1): 10-15.

Huopaniemi, L., J. Fellman, A. Rantala, A. Eriksson, H. Forsius, A. De la Chapelle and T. Alitalo (1999). "Skewed secondary sex ratio in the offspring of carriers of the 214G > A mutation of the RS1 gene." Anna Hum Genet **63**: 521-533.

Huopaniemi, L., A. Rantala, E. Tahvanainen, A. de la Chapelle and T. Alitalo (1997). "Linkage disequilibrium and physical mapping of X-linked juvenile retinoschisis." Am J Hum Genet **60**(5): 1139-1149.

Iannaccone, A., M. Mura, F. M. Dyka, M. L. Ciccarelli, B. M. Yashar, R. Ayyagari, M. M. Jablonski and R. S. Molday (2006). "An unusual X-linked retinoschisis phenotype and biochemical characterization of the W112C RS1 mutation." Vision Res **46**(22): 3845-3852.

Ibraghimov-Beskrovnaya, O., J. M. Ervasti, C. J. Leveille, C. A. Slaughter, S. W. Sernett and K. P. Campbell (1992). "Primary structure of dystrophin-associated glycoproteins linking dystrophin to the extracellular matrix." Nature **355**(6362): 696-702.

Ilag, L. L., N. H. Olson, T. Dokland, C. L. Music, R. H. Cheng, Z. Bowen, R. McKenna, M. G. Rossmann, T. S. Baker and N. L. Incardona (1995). "DNA packaging intermediates of bacteriophage phi X174." Structure **3**(4): 353-363.

Ishikawa, M., Y. Sawada and T. Yoshitomi (2015). "Structure and function of the interphotoreceptor matrix surrounding retinal photoreceptor cells." Exp Eye Res **133**: 3-18.

Jacques, D. A. and J. Trewhella (2010). "Small-angle scattering for structural biology--expanding the frontier while avoiding the pitfalls." Protein Sci **19**(4): 642-657.

Janssen, A., S. H. Min, L. L. Molday, N. Tanimoto, M. W. Seeliger, W. W. Hauswirth, R. S. Molday and B. H. Weber (2008). "Effect of late-stage therapy on disease progression in AAV-mediated rescue of photoreceptor cells in the retinoschisin-deficient mouse." Mol Ther **16**(6): 1010-1017.

Johnson, B. A., N. Aoyama, N. H. Friedell, S. Ikeda and A. Ikeda (2008). "Genetic modification of the schisis phenotype in a mouse model of X-linked retinoschisis." Genetics **178**(3): 1785-1794.

Johnson, B. A., B. S. Cole, E. E. Geisert, S. Ikeda and A. Ikeda (2010). "Tyrosinase is the modifier of retinoschisis in mice." Genetics **186**(4): 1337-1344.

Jowitt, T. A., A. D. Murdoch, C. Baldock, R. Berry, J. M. Day and T. E. Hardingham (2010). "Order within disorder: aggrecan chondroitin sulphate-attachment region provides new structural insights into protein sequences classified as disordered." Proteins **78**(16): 3317-3327.

Kanagawa, M., Y. Omori, S. Sato, K. Kobayashi, Y. Miyagoe-Suzuki, S. Takeda, T. Endo, T. Furukawa and T. Toda (2010). "Post-translational maturation of dystroglycan is necessary for pikachurin binding and ribbon synaptic localization." J Biol Chem **285**(41): 31208-31216.

Kaplan, J. H. (2002). "Biochemistry of Na,K-ATPase." Annu Rev Biochem **71**: 511-535.

Karlstetter, M., C. Nothdurfter, A. Aslanidis, K. Moeller, F. Horn, R. Scholz, H. Neumann, B. H. Weber, R. Rupprecht and T. Langmann (2014). "Translocator protein (18 kDa) (TSPO) is expressed in reactive retinal microglia and modulates microglial inflammation and phagocytosis." J Neuroinflammation **11**: 3.

Karlstetter, M., Y. Walczak, K. Weigelt, S. Ebert, J. Van den Brulle, H. Schwer, R. Fuchshofer and T. Langmann (2010). "The novel activated microglia/macrophage WAP domain protein, AMWAP, acts as a counter-regulator of proinflammatory response." J Immunol **185**(6): 3379-3390.

Kelley, L. A., S. Mezulis, C. M. Yates, M. N. Wass and M. J. Sternberg (2015). "The Phyre2 web portal for protein modeling, prediction and analysis." Nat Protoc **10**(6): 845-858.

Kellner, U., S. Brummer, M. H. Foerster and A. Wessing (1990). "X-linked congenital retinoschisis." Graefes Arch Clin Exp Ophthalmol **228**(5): 432-437.

Khan, N. W., J. A. Jamison, J. A. Kemp and P. A. Sieving (2001). "Analysis of photoreceptor function and inner retinal activity in juvenile X-linked retinoschisis." Vision Res **41**(28): 3931-3942.

Khandhadia, S., D. Trump, G. Menon and A. J. Lotery (2011). "X-linked retinoschisis maculopathy treated with topical dorzolamide, and relationship to genotype." Eye **25**(7): 921-927.

Kiedzierska, A., K. Smietana, H. Czepczynska and J. Otlewski (2007). "Structural similarities and functional diversity of eukaryotic discoidin-like domains." Biochim Biophys Acta **1774**(9): 1069-1078.

Kikhney, A. G. and D. I. Svergun (2015). "A practical guide to small angle X-ray scattering (SAXS) of flexible and intrinsically disordered proteins." FEBS Lett **589**(19): 2570-2577.

Kitamura, E., Y. E. Gribanova and D. B. Farber (2011). "Regulation of retinoschisin secretion in Weri-Rb1 cells by the F-actin and microtubule cytoskeleton." PLoS One **6**(6): e20707.

Kjellstrom, S., R. A. Bush, Y. Zeng, Y. Takada and P. A. Sieving (2007). "Retinoschisin gene therapy and natural history in the Rs1h-KO mouse: long-term rescue from retinal degeneration." Invest Ophthalmol Vis Sci **48**(8): 3837-3845.

Ko, M. L., Y. Liu, L. Shi, D. Trump and G. Y. Ko (2008). "Circadian regulation of retinoschisin in the chick retina." Invest Ophthalmol Vis Sci **49**(4): 1615-1621.

Koike, C., T. Obara, Y. Uriu, T. Numata, R. Sanuki, K. Miyata, T. Koyasu, S. Ueno, K. Funabiki, A. Tani, H. Ueda, M. Kondo, Y. Mori, M. Tachibana and T. Furukawa (2010). "TRPM1 is a component of the retinal ON bipolar cell transduction channel in the mGluR6 cascade." Proc Natl Acad Sci U S A **107**(1): 332-337.

Kotova, S., C. Vijayasarathy, E. K. Dimitriadis, L. Ikonomou, H. Jaffe and P. A. Sieving (2010). "Retinoschisin (RS1) interacts with negatively charged lipid bilayers in the presence of Ca2+: an atomic force microscopy study." Biochemistry **49**(33): 7023-7032.

Kraus, D., M. Karlstetter, Y. Walczak, D. Hilfinger, T. Langmann and B. H. F. Weber (2011). "Retinal expression of the X-linked juvenile retinoschisis (RS1) gene is controlled by an upstream CpG island and two opposing CRX-bound regions." BBA-Gene Regulatory Mechanisms **1809**(4-6): 245-254.

Krissinel, E. and K. Henrick (2007). "Inference of macromolecular assemblies from crystalline state." J Mol Biol **372**(3): 774-797.

Kucukelbir, A., F. J. Sigworth and H. D. Tagare (2014). "Quantifying the local resolution of cryo-EM density maps." Nat Methods **11**(1): 63-65.

Kuhlbrandt, W. (2014). "Biochemistry. The resolution revolution." Science **343**(6178): 1443-1444.

Langmann, T., S. Ebert, Y. Walczak, K. Weigelt, M. U. Ehrengruber, T. Stiewe and B. H. Weber (2009). "Induction of early growth response-1 mediates microglia activation in vitro but is dispensable in vivo." Neuromolecular Med **11**(2): 87-96.

Langmann, T., C. C. L. Lai, K. Weigelt, B. M. Tam, R. Warneke-Wittstock, O. L. Moritz and B. H. F. Weber (2008). "CRX controls retinal expression of the X-linked juvenile retinoschisis (RS1) gene." Nucleic Acids Res **36**(20): 6523-6534.

Laue, T. M., B. Shah, T. M. Ridgeway and S. L. Pelletier (1992). "Computer-aided interpretation of analytical sedimentation data for proteins."

Lee, B. and F. M. Richards (1971). "The interpretation of protein structures: estimation of static accessibility." J Mol Biol **55**(3): 379-400.

Lee, C. C., A. Kreusch, D. McMullan, K. Ng and G. Spraggon (2003). "Crystal structure of the human neuropilin-1 b1 domain." Structure **11**(1): 99-108.

Leschziner, A. E. and E. Nogales (2006). "The orthogonal tilt reconstruction method: an approach to generating single-class volumes with no missing cone for ab initio reconstruction of asymmetric particles." J Struct Biol **153**(3): 284-299.

Li, X., P. Mooney, S. Zheng, C. R. Booth, M. B. Braunfeld, S. Gubbens, D. A. Agard and Y. Cheng (2013). "Electron counting and beam-induced motion correction enable near-atomic-resolution single-particle cryo-EM." Nat Methods **10**(6): 584-590.

Liao, M., E. Cao, D. Julius and Y. Cheng (2013). "Structure of the TRPV1 ion channel determined by electron cryo-microscopy." Nature **504**(7478): 107-112.

Lin, L., O. Huai, M. D. Huang, B. Furie and B. C. Furie (2007). "Crystal structure of the bovine lactadherin C2 domain, a membrane binding motif, shows similarity to the C2 domains of factor V and factor VIII." J Mol Biol **371**(3): 717-724.

Ludtke, S. J., P. R. Baldwin and W. Chiu (1999). "EMAN: Semiautomated software for high-resolution single-particle reconstructions." J Struct Biol **128**(1): 82-97.

Macedo-Ribeiro, S., W. Bode, R. Huber, M. A. Quinn-Allen, S. W. Kim, T. L. Ortel, G. P. Bourenkov, H. D. Bartunik, M. T. Stubbs, W. H. Kane and P. Fuentes-Prior (1999). "Crystal structures of the membrane-binding C2 domain of human coagulation factor V." Nature **402**(6760): 434-439.

Magyar, J. P., U. Bartsch, Z. Q. Wang, N. Howells, A. Aguzzi, E. F. Wagner and M. Schachner (1994). "Degeneration of neural cells in the central nervous system of mice deficient in the gene for the adhesion molecule on Glia, the beta 2 subunit of murine Na,K-ATPase." J Cell Biol **127**(3): 835-845.

Mansergh, F., N. C. Orton, J. P. Vessey, M. R. Lalonde, W. K. Stell, F. Tremblay, S. Barnes, D. E. Rancourt and N. T. Bech-Hansen (2005). "Mutation of the calcium channel gene Cacna1f disrupts calcium signaling, synaptic transmission and cellular organization in mouse retina." Hum Mol Genet **14**(20): 3035-3046.

Masland, R. H. (2012). "The neuronal organization of the retina." Neuron **76**(2): 266-280.

Matos, C. F., C. Robinson, H. I. Alanen, P. Prus, Y. Uchida, L. W. Ruddock, R. B. Freedman and E. Keshavarz-Moore (2014). "Efficient export of prefolded, disulfide-bonded recombinant proteins to the periplasm by the Tat pathway in Escherichia coli CyDisCo strains." Biotechnol Prog **30**(2): 281-290.

McMullan, G., A. T. Clark, R. Turchetta and A. R. Faruqi (2009). "Enhanced imaging in low dose electron microscopy using electron counting." Ultramicroscopy **109**(12): 1411-1416.

McMullan, G., A. R. Faruqi, R. Henderson, N. Guerrini, R. Turchetta, A. Jacobs and G. van Hoften (2009). "Experimental observation of the improvement in MTF from backthinning a CMOS direct electron detector." Ultramicroscopy **109**(9): 1144-1147.

Mendoza-Londono, R., K. T. Hiriyanna, E. L. Bingham, F. Rodriguez, B. S. Shastry, A. Rodriguez, P. A. Sieving and M. L. Tamayo (1999). "A Colombian family with X-linked juvenile retinoschisis with three affected females finding of a frameshift mutation." Ophthalmic Genet **20**(1): 37-43.

Menke, M. N., G. T. Feke and T. Hirose (2011). "Effect of aging on macular features of X-linked retinoschisis assessed with optical coherence tomography." Retina **31**(6): 1186-1192.

Mercer, A. J. and W. B. Thoreson (2011). "The dynamic architecture of photoreceptor ribbon synapses: cytoskeletal, extracellular matrix, and intramembrane proteins." Vis Neurosci **28**(6): 453-471.

Mertens, H. D. and D. I. Svergun (2010). "Structural characterization of proteins and complexes using small-angle X-ray solution scattering." J Struct Biol **172**(1): 128-141.

Min, S. H., L. L. Molday, M. W. Seeliger, A. Dinculescu, A. M. Timmers, A. Janssen, F. Tonagel, N. Tanimoto, B. H. Weber, R. S. Molday and W. W. Hauswirth (2005). "Prolonged recovery of retinal structure/function after gene therapy in an Rs1h-deficient mouse model of x-linked juvenile retinoschisis." Mol Ther **12**(4): 644-651.

Mindell, J. A. and N. Grigorieff (2003). "Accurate determination of local defocus and specimen tilt in electron microscopy." J Struct Biol **142**(3): 334-347.

Molday, L. L., D. Hicks, C. G. Sauer, B. H. Weber and R. S. Molday (2001). "Expression of X-linked retinoschisis protein RS1 in photoreceptor and bipolar cells." Invest Ophthalmol Vis Sci **42**(3): 816-825.

Molday, L. L., W. W. Wu and R. S. Molday (2007). "Retinoschisin (RS1), the protein encoded by the X-linked retinoschisis gene, is anchored to the surface of retinal photoreceptor and bipolar cells through its interactions with a Na/K ATPase-SARM1 complex." J Biol Chem **282**(45): 32792-32801.

Molday, R. S. (2007). "Focus on molecules: retinoschisin (RS1)." Exp Eye Res **84**(2): 227-228.

Molday, R. S., U. Kellner and B. H. Weber (2012). "X-linked juvenile retinoschisis: clinical diagnosis, genetic analysis, and molecular mechanisms." Prog Retin Eye Res **31**(3): 195-212.

Molthagen, M., M. Schachner and U. Bartsch (1996). "Apoptotic cell death of photoreceptor cells in mice deficient for the adhesion molecule on glia (AMOG, the beta 2-subunit of the Na, K-ATPase)." J Neurocytol **25**(4): 243-255.

Morgans, C. W., J. M. Zhang, B. G. Jeffrey, S. M. Nelson, N. S. Burke, R. M. Duvoisin and R. L. Brown (2009). "TRPM1 is required for the depolarizing light response in retinal ON-bipolar cells." Proc Natl Acad Sci U S A **106**(45): 19174-19178.

Morth, J. P., B. P. Pedersen, M. S. Toustrup-Jensen, T. L. Sorensen, J. Petersen, J. P. Andersen, B. Vilsen and P. Nissen (2007). "Crystal structure of the sodium-potassium pump." Nature **450**(7172): 1043-1049.

Nguyen, T. H., W. P. Galej, X. C. Bai, C. Oubridge, A. J. Newman, S. H. Scheres and K. Nagai (2016). "Cryo-EM structure of the yeast U4/U6.U5 tri-snRNP at 3.7 A resolution." Nature **530**(7590): 298-302.

Niesen, F. H., H. Berglund and M. Vedadi (2007). "The use of differential scanning fluorimetry to detect ligand interactions that promote protein stability." Nature Prot **2**(9): 2212-2221.

Nomura, A., R. Shigemoto, Y. Nakamura, N. Okamoto, N. Mizuno and S. Nakanishi (1994). "Developmentally regulated postsynaptic localization of a metabotropic glutamate receptor in rat rod bipolar cells." Cell **77**(3): 361-369.

O'Neill, L. A. and A. G. Bowie (2007). "The family of five: TIR-domain-containing adaptors in Toll-like receptor signalling." Nat Rev Immunol **7**(5): 353-364.

Olson, N. H., P. R. Kolatkar, M. A. Oliveira, R. H. Cheng, J. M. Greve, A. McClelland, T. S. Baker and M. G. Rossmann (1993). "Structure of a human rhinovirus complexed with its receptor molecule." Proc Natl Acad Sci U S A **90**(2): 507-511.

Orlova, E. V. and H. R. Saibil (2011). "Structural Analysis of Macromolecular Assemblies by Electron Microscopy." Chem Rev **111**(12): 7710-7748.

Ou, J., C. Vijayasarathy, L. Ziccardi, S. Chen, Y. Zeng, D. Marangoni, J. G. Pope, R. A. Bush, Z. Wu, W. Li and P. A. Sieving (2015). "Synaptic pathology and therapeutic repair in adult retinoschisis mouse by AAV-RS1 transfer." J Clin Invest **125**(7): 2891-2903.

Owen, D. M., C. Rentero, J. Rossy, A. Magenau, D. Williamson, M. Rodriguez and K. Gaus (2010). "PALM imaging and cluster analysis of protein heterogeneity at the cell surface." J Biophotonics **3**(7): 446-454.

Pantoliano, M. W., E. C. Petrella, J. D. Kwasnoski, V. S. Lobanov, J. Myslik, E. Graf, T. Carver, E. Asel, B. A. Springer, P. Lane and F. R. Salemme (2001). "High-density miniaturized thermal shift assays as a general strategy for drug discovery." J Biomol Screen **6**(6): 429-440.

Pardue, M. T. and N. S. Peachey (2014). "Mouse b-wave mutants." Doc Ophthalmol **128**(2): 77-89.

Park, T. K., Z. Wu, S. Kjellstrom, Y. Zeng, R. A. Bush, P. A. Sieving and P. Colosi (2009). "Intravitreal delivery of AAV8 retinoschisin results in cell type-specific gene expression and retinal rescue in the Rs1-KO mouse." Gene Ther **16**(7): 916-926.

Peachey, N. S., J. N. Pearring, P. Bojang, M. E. Hirschtritt, G. Sturgill-Short, T. A. Ray, T. Furukawa, C. Koike, A. F. X. Goldberg, Y. Shen, M. A. McCall, S. Nawy, P. M. Nishina and R. G. Gregg (2012). "Depolarizing bipolar cell dysfunction due to a Trpm1 point mutation." J Neurophysiol **108**(9): 2442-2451.

Pettersen, E. F., T. D. Goddard, C. C. Huang, G. S. Couch, D. M. Greenblatt, E. C. Meng and T. E. Ferrin (2004). "UCSF Chimera--a visualization system for exploratory research and analysis." J Comput Chem **25**(13): 1605-1612.

Pimenides, D., N. D. George, J. R. Yates, K. Bradshaw, S. A. Roberts, A. T. Moore and D. Trump (2005). "X-linked retinoschisis: clinical phenotype and RS1 genotype in 86 UK patients." J Med Genet **42**(6): e35.

Poole, S., R. A. Firtel, E. Lamar and W. Rowekamp (1981). "Sequence and expression of the discoidin I gene family in Dictyostelium discoideum." J Mol Biol **153**(2): 273-289.

Prasad, A., R. Wagner and N. Bhagat (2006). "Vitreous hemorrhage as the initial manifestation of X-linked retinoschisis in a 9-month-old infant." J Pediatr Ophthalmol Strabismus **43**(1): 56-58.

Pratt, K. P., B. W. Shen, K. Takeshima, E. W. Davie, K. Fujikawa and B. L. Stoddard (1999). "Structure of the C2 domain of human factor VIII at 1.5 angstrom resolution." Nature **402**(6760): 439-442.

Putnam, C. D., M. Hammel, G. L. Hura and J. A. Tainer (2007). "X-ray solution scattering (SAXS) combined with crystallography and computation: defining accurate macromolecular structures, conformations and assemblies in solution." Q Rev Biophys **40**(3): 191-285.

Radermacher, M., T. Wagenknecht, A. Verschoor and J. Frank (1987). "Three-dimensional reconstruction from a single-exposure, random conical tilt series applied to the 50S ribosomal subunit of Escherichia coli." J Microsc **146**(Pt 2): 113-136.

Rambo, R. P. and J. A. Tainer (2011). "Characterizing Flexible and Intrinsically Unstructured Biological Macromolecules by SAS Using the Porod-Debye Law." Biopolymers **95**(8): 559-571.

Rambo, R. P. and J. A. Tainer (2013). "Super-resolution in solution X-ray scattering and its applications to structural systems biology." Annu Rev Biophys **42**: 415-441.

Rawson, S., M. G. Iadanza, N. A. Ranson and S. P. Muench (2016). "Methods to account for movement and flexibility in cryo-EM data processing." Methods **100**: 35-41.

Reid, S. N. and D. B. Farber (2005). "Glial transcytosis of a photoreceptor-secreted signaling protein, retinoschisin." Glia **49**(3): 397-406.

Reid, S. N., C. Yamashita and D. B. Farber (2003). "Retinoschisin, a photoreceptor-secreted protein, and its interaction with bipolar and muller cells." J Neurosci **23**(14): 6030-6040.

Renner, A. B., U. Kellner, B. Fiebig, E. Cropp, M. H. Foerster and B. H. Weber (2008). "ERG variability in X-linked congenital retinoschisis patients with mutations in the RS1 gene and the diagnostic importance of fundus autofluorescence and OCT." Doc Ophthalmol **116**(2): 97-109.

Rocha Cabrera, P., A. C. Pareja Rios, L. Cordoves Dorta, C. Mantolan Sarmiento and M. A. Serrano Garcia (2014). "A combination of topical and systemic carbonic anhydrase in the treatment of chromosome X-linked retinoschisis." Arch Soc Esp Oftalmol **89**(8): 320-323.

Rodriguez, F. J., A. Rodriguez, R. Mendoza-Londono and M. L. Tamayo (2005). "X-linked retinoschisis in three females from the same family: a phenotype-genotype correlation." Retina **25**(1): 69-74.

Roesch, M. T., C. C. Ewing, A. E. Gibson and B. H. Weber (1998). "The natural history of X-linked retinoschisis." Can J Ophthalmol **33**(3): 149-158.

Roseman, A. M. (2000). "Docking structures of domains into maps from cryo-electron microscopy using local correlation." Acta Crystallogr D **56**: 1332-1340.

Rosenthal, P. B. and R. Henderson (2003). "Optimal determination of particle orientation, absolute hand, and contrast loss in single-particle electron cryomicroscopy." J Mol Biol **333**(4): 721-745.

Russo, C. J. and L. A. Passmore (2014). "Electron microscopy: Ultrastable gold substrates for electron cryomicroscopy." Science **346**(6215): 1377-1380.

Sadaka, A. and R. A. Sisk (2016). "Dramatic regression of macular and peripheral retinoschisis with dorzolamide 2 % in X-linked retinoschisis: a case report." J Med Case Rep **10**(1): 142.

Saldana, M., J. Thompson, E. Monk, D. Trump, V. Long and E. Sheridan (2007). "X-linked retinoschisis in a female with a heterozygous RS1 missense mutation." Am J Med Genet A **143A**(6): 608-609.

Saleheen, D., A. Ali, S. Khanum, M. Z. Ozair, M. Zaidi, M. J. Sethi, N. Khan and P. Frossard (2008). "Molecular analysis of the XLRS1 gene in 4 females affected with X-linked juvenile retinoschisis." Can J Ophthalmol **43**(5): 596-599.

Sander, B., M. M. Golas and H. Stark (2005). "Advantages of CCD detectors for de novo three-dimensional structure determination in single-particle electron microscopy." J Struct Biol **151**(1): 92-105.

Sato, S., Y. Omori, K. Katoh, M. Kondo, M. Kanagawa, K. Miyata, K. Funabiki, T. Koyasu, N. Kajimura, T. Miyoshi, H. Sawai, K. Kobayashi, A. Tani, T. Toda, J. Usukura, Y. Tano, T. Fujikado and T. Furukawa (2008). "Pikachurin, a dystroglycan ligand, is essential for photoreceptor ribbon synapse formation." Nat Neurosci **11**(8): 923-931.

Sauer, C. G., A. Gehrig, R. Warneke-Wittstock, A. Marquardt, C. C. Ewing, A. Gibson, B. Lorenz, B. Jurklies and B. H. Weber (1997). "Positional cloning of the gene associated with X-linked juvenile retinoschisis." Nat Genet **17**(2): 164-170.

Scheres, S. H. (2010). "Classification of structural heterogeneity by maximum-likelihood methods." Methods Enzymol **482**: 295-320.

Scheres, S. H. (2012). "RELION: implementation of a Bayesian approach to cryo-EM structure determination." J Struct Biol **180**(3): 519-530.

Scheres, S. H. (2014). "Beam-induced motion correction for sub-megadalton cryo-EM particles." Elife **3**: e03665.

Scheres, S. H. (2016). "Processing of Structurally Heterogeneous Cryo-EM Data in RELION." Methods Enzymol **579**: 125-157.

Scheres, S. H. and S. Chen (2012). "Prevention of overfitting in cryo-EM structure determination." Nat Methods **9**(9): 853-854.

Scheres, S. H., H. Gao, M. Valle, G. T. Herman, P. P. Eggermont, J. Frank and J. M. Carazo (2007). "Disentangling conformational states of macromolecules in 3D-EM through likelihood optimization." Nat Methods **4**(1): 27-29.

Scheres, S. H., M. Valle, R. Nunez, C. O. Sorzano, R. Marabini, G. T. Herman and J. M. Carazo (2005). "Maximum-likelihood multi-reference refinement for electron microscopy images." J Mol Biol **348**(1): 139-149.

Scheres, S. H. W. (2012). "A Bayesian View on Cryo-EM Structure Determination." J Mol Biol **415**(2): 406-418.

Schuck, P. (2000). "Size-distribution analysis of macromolecules by sedimentation velocity ultracentrifugation and lamm equation modeling." Biophys J **78**(3): 1606-1619.

Sergeev, Y. V., R. C. Caruso, M. R. Meltzer, N. Smaoui, I. M. MacDonald and P. A. Sieving (2010). "Molecular modeling of retinoschisin with functional analysis of pathogenic mutations from human X-linked retinoschisis." Hum Mol Genet **19**(7): 1302-1313.

Sergeev, Y. V., S. Vitale, P. A. Sieving, A. Vincent, A. G. Robson, A. T. Moore, A. R. Webster and G. E. Holder (2013). "Molecular modeling indicates distinct classes of missense variants with mild and severe XLRS phenotypes." Hum Mol Genet **22**(23): 4756-4767.

Shi, L., K. Jian, M. L. Ko, D. Trump and G. Y. Ko (2009). "Retinoschisin, a new binding partner for L-type voltage-gated calcium channels in the retina." J Biol Chem **284**(6): 3966-3975.

Shinoda, K., H. Ohde, Y. Mashima, R. Inoue, S. Ishida, M. Inoue, S. Kawashima and Y. Oguchi (2001). "On- and off-responses of the photopic electroretinograms in X-linked juvenile retinoschisis." Am J Ophthalmol **131**(4): 489-494.

Sigworth, F. J. (1998). "A maximum-likelihood approach to single-particle image refinement." J Struct Biol **122**(3): 328-339.

Sigworth, F. J., P. C. Doerschuk, J. M. Carazo and S. H. Scheres (2010). "An introduction to maximum-likelihood methods in cryo-EM." Methods Enzymol **482**: 263-294.

Sikkink, S. K., S. Biswas, N. R. Parry, P. E. Stanga and D. Trump (2007). "X-linked retinoschisis: an update." J Med Genet **44**(4): 225-232.

Staffieri, S. E., L. Rose, A. Chang, J. N. De Roach, T. L. McLaren, D. A. Mackey, A. W. Hewitt and T. M. Lamey (2015). "Clinical and molecular characterization of females affected by X-linked retinoschisis." Clin Experiment Ophthalmol **43**(7): 643-647.

Steiner-Champliaud, M. F., J. Sahel and D. Hicks (2006). "Retinoschisin forms a multi-molecular complex with extracellular matrix and cytoplasmic proteins: interactions with beta2 laminin and alphaB-crystallin." Mol Vis **12**: 892-901.

Stoecker, K., K. Weigelt, S. Ebert, M. Karlstetter, Y. Walczak and T. Langmann (2009). "Induction of STAP-1 promotes neurotoxic activation of microglia." Biochem Biophys Res Commun **379**(1): 121-126.

Stohr, H., J. B. Heisig, P. M. Benz, S. Schoberl, V. M. Milenkovic, O. Strauss, W. M. Aartsen, J. Wijnholds, B. H. Weber and H. L. Schulz (2009). "TMEM16B, a novel protein with calcium-dependent chloride channel activity, associates with a presynaptic protein complex in photoreceptor terminals." J Neurosci **29**(21): 6809-6818.

Suloway, C., J. Pulokas, D. Fellmann, A. Cheng, F. Guerra, J. Quispe, S. Stagg, C. S. Potter and B. Carragher (2005). "Automated molecular microscopy: the new Leginon system." J Struct Biol **151**(1): 41-60.

Svergun, D. I. (1992). "Determination of the Regularization Parameter in Indirect-Transform Methods Using Perceptual Criteria." J App Crystallogr **25**: 495-503.

Svergun, D. I. (1999). "Restoring low resolution structure of biological macromolecules from solution scattering using simulated annealing." Biophys J **76**(6): 2879-2886.

Takada, Y., R. N. Fariss, M. Muller, R. A. Bush, E. J. Rushing and P. A. Sieving (2006). "Retinoschisin expression and localization in rodent and human pineal and consequences of mouse RS1 gene knockout." Mol Vis **12**: 1108-1116.

Takada, Y., R. N. Fariss, A. Tanikawa, Y. Zeng, D. Carper, R. Bush and P. A. Sieving (2004). "A retinal neuronal developmental wave of retinoschisin expression begins in ganglion cells during layer formation." Invest Ophthalmol Vis Sci **45**(9): 3302-3312.

Talts, J. F., Z. Andac, W. Gohring, A. Brancaccio and R. Timpl (1999). "Binding of the G domains of laminin alpha1 and alpha2 chains and perlecan to heparin, sulfatides, alpha-dystroglycan and several extracellular matrix proteins." EMBO J **18**(4): 863-870.

Tang, G., L. Peng, P. R. Baldwin, D. S. Mann, W. Jiang, I. Rees and S. J. Ludtke (2007). "EMAN2: an extensible image processing suite for electron microscopy." J Struct Biol **157**(1): 38-46.

Tantri, A., T. R. Vrabec, A. Cu-Unjieng, A. Frost, W. H. Annesley, Jr. and L. A. Donoso (2004). "X-linked retinoschisis: a clinical and molecular genetic review." Surv Ophthalmol **49**(2): 214-230.

Taylor, K. A. and R. M. Glaeser (1974). "Electron diffraction of frozen, hydrated protein crystals." Science **186**(4168): 1036-1037.

Taylor, K. A. and R. M. Glaeser (1976). "Electron microscopy of frozen hydrated biological specimens." J Ultrastruct Res **55**(3): 448-456.

Thobani, A. and G. A. Fishman (2011). "The Use of Carbonic Anhydrase Inhibitors in the Retreatment of Cystic Macular Lesions in Retinitis Pigmentosa and X-Linked Retinoschisis." Retina- J Ret Vit Dis **31**(2): 312-315.

Tolun, G., C. Vijayasarathy, R. Huang, Y. Zeng, Y. Li, A. C. Steven, P. A. Sieving and J. B. Heymann (2016). "Paired octamer rings of retinoschisin suggest a junctional model for cell-cell adhesion in the retina." Proc Natl Acad Sci U S A **113**(19): 5287-5292.

Topf, M., K. Lasker, B. Webb, H. Wolfson, W. Chiu and A. Sali (2008). "Protein structure fitting and refinement guided by cryo-EM density." Structure **16**(2): 295-307.

Troilo, H., A. V. Zuk, R. B. Tunnicliffe, A. P. Wohl, R. Berry, R. F. Collins, T. A. Jowitt, G. Sengle and C. Baldock (2014). "Nanoscale structure of the BMP antagonist chordin supports cooperative BMP binding." Proc Natl Acad Sci U S A **111**(36): 13063-13068.

Unwin, P. N. (1974). "Electron microscopy of the stacked disk aggregate of tobacco mosaic virus protein. II. The influence of electron irradiation of the stain distribution." J Mol Biol **87**(4): 657-670.

van Heel, M. (1984). "Multivariate statistical classification of noisy images (randomly oriented biological macromolecules)." Ultramicroscopy **13**(1-2): 165-183.

van Heel, M., G. Harauz, E. V. Orlova, R. Schmidt and M. Schatz (1996). "A new generation of the IMAGIC image processing system." J Struct Biol **116**(1): 17-24.

Vander Kooi, C. W., M. A. Jusino, B. Perman, D. B. Neau, H. D. Bellamy and D. J. Leahy (2007). "Structural basis for ligand and heparin binding to neuropilin B domains." Proc Natl Acad Sci U S A **104**(15): 6152-6157.

Vanheel, M. and J. Frank (1981). "Use of Multivariate Statistics in Analyzing the Images of Biological Macromolecules." Ultramicroscopy **6**(2): 187-194.

Vieille, C. and G. J. Zeikus (2001). "Hyperthermophilic enzymes: Sources, uses, and molecular mechanisms for thermostability." Microbiol Mol Biol R **65**(1): 1-+.

Vijayasarathy, C., M. A. Gawinowicz, Y. Zeng, Y. Takada, R. A. Bush and P. A. Sieving (2006). "Identification and characterization of two mature isoforms of retinoschisin in murine retina." Biochem Biophys Res Commun **349**(1): 99-105.

Vijayasarathy, C., R. Sui, Y. Zeng, G. Yang, F. Xu, R. C. Caruso, R. A. Lewis, L. Ziccardi and P. A. Sieving (2010). "Molecular mechanisms leading to null-protein product from retinoschisin (RS1) signal-sequence mutants in X-linked retinoschisis (XLRS) disease." Hum Mutat **31**(11): 1251-1260.

Vijayasarathy, C., Y. Takada, Y. Zeng, R. A. Bush and P. A. Sieving (2007). "Retinoschisin is a peripheral membrane protein with affinity for anionic phospholipids and affected by divalent cations." Invest Ophthalmol Vis Sci **48**(3): 991-1000.

Vincent, A., A. G. Robson, M. M. Neveu, G. A. Wright, A. T. Moore, A. R. Webster and G. E. Holder (2013). "A phenotype-genotype correlation study of X-linked retinoschisis." Ophthalmology **120**(7): 1454-1464.

Volkov, V. V. and D. I. Svergun (2003). "Uniqueness of ab initio shape determination in small-angle scattering." J App Crystallogr **36**: 860-864.

Walia, S., G. A. Fishman, R. S. Molday, F. M. Dyka, N. M. Kumar, M. A. Ehlinger and E. M. Stone (2009). "Relation of response to treatment with dorzolamide in X-linked retinoschisis to the mechanism of functional loss in retinoschisin." Am J Ophthalmol **147**(1): 111-115 e111.

Wang, C., S. Chen, X. Wang, L. Wang, A. K. Wallis, R. B. Freedman and C. C. Wang (2010). "Plasticity of human protein disulfide isomerase: evidence for mobility around the X-linker region and its functional significance." J Biol Chem **285**(35): 26788-26797.

Wang, T., C. T. Waters, A. M. Rothman, T. J. Jakins, K. Romisch and D. Trump (2002). "Intracellular retention of mutant retinoschisin is the pathological mechanism underlying X-linked retinoschisis." Hum Mol Genet **11**(24): 3097-3105.

Wang, T., A. Zhou, C. T. Waters, E. O'Connor, R. J. Read and D. Trump (2006). "Molecular pathology of X linked retinoschisis: mutations interfere with retinoschisin secretion and oligomerisation." Br J Ophthalmol **90**(1): 81-86.

Weber, B. H., H. Schrewe, L. L. Molday, A. Gehrig, K. L. White, M. W. Seeliger, G. B. Jaissle, C. Friedburg, E. Tamm and R. S. Molday (2002). "Inactivation of the murine X-linked juvenile retinoschisis gene, Rs1h, suggests a role of retinoschisin in retinal cell layer organization and synaptic structure." Proc Natl Acad Sci U S A **99**(9): 6222-6227.

Weigelt, K., W. Ernst, Y. Walczak, S. Ebert, T. Loenhardt, M. Klug, M. Rehli, B. H. Weber and T. Langmann (2007). "Dap12 expression in activated microglia from retinoschisin-deficient retina and its PU.1-dependent promoter regulation." J Leukoc Biol **82**(6): 1564-1574.

Wieacker, P., T. F. Wienker, B. Mevorah, B. Dallapiccola, K. E. Davies and H. H. Ropers (1984). "Linkage Relationships between Xg, Steroid Sulfatase (Sts) and Retinoschisis (Rs), Respectively, and a Cloned DNA-Sequence from the Distal Short Arm of the X-Chromosome." Cytogenet Cell Genet **37**(1-4): 608-608.

Wikoff, W. R., G. Wang, C. R. Parrish, R. H. Cheng, M. L. Strassheim, T. S. Baker and M. G. Rossmann (1994). "The structure of a neutralized virus: canine parvovirus complexed with neutralizing antibody fragment." Structure **2**(7): 595-607.

Wolfensberger, T. J. (1999). "The role of carbonic anhydrase inhibitors in the management of macular edema." Doc Ophthalmol **97**(3-4): 387-397.

Wu, J., Z. Yan, Z. Li, C. Yan, S. Lu, M. Dong and N. Yan (2015). "Structure of the voltage-gated calcium channel Cav1.1 complex." Science **350**(6267): aad2395.

Wu, J. W. and H. L. Liu (2012). "In silico Investigation of the Disease-Associated Retinoschisin C110Y and C219G Mutants." J Biomol Struct Dyn **29**(5): 1-23.

Wu, W. W. and R. S. Molday (2003). "Defective discoidin domain structure, subunit assembly, and endoplasmic reticulum processing of retinoschisin are primary mechanisms responsible for X-linked retinoschisis." J Biol Chem **278**(30): 28139-28146.

Wu, W. W., J. P. Wong, J. Kast and R. S. Molday (2005). "RS1, a discoidin domain-containing retinal cell adhesion protein associated with X-linked retinoschisis, exists as a novel disulfide-linked octamer." J Biol Chem **280**(11): 10721-10730.

Xu, J., L. L. Molday, R. S. Molday and M. V. Sarunic (2009). "In vivo imaging of the mouse model of X-linked juvenile retinoschisis with fourier domain optical coherence tomography." Invest Ophthalmol Vis Sci **50**(6): 2989-2993.

Xu, Y., A. Dhingra, M. E. Fina, C. Koike, T. Furukawa and N. Vardi (2012). "mGluR6 deletion renders the TRPM1 channel in retina inactive." J Neurophysiol **107**(3): 948-957.

Yamagata, M. and J. R. Sanes (2010). "Synaptic localization and function of Sidekick recognition molecules require MAGI scaffolding proteins." J Neurosci **30**(10): 3579-3588.

Yang, H. S., J. B. Lee, Y. H. Yoon and J. Y. Lee (2014). "Correlation between spectral-domain OCT findings and visual acuity in X-linked retinoschisis." Invest Ophthalmol Vis Sci **55**(5): 3029-3036.

Ye, G. J., E. Budzynski, P. Sonnentag, P. E. Miller, A. K. Sharma, J. N. Ver Hoeve, K. Howard, D. R. Knop and J. D. Chulay (2015). "Safety and Biodistribution Evaluation in Cynomolgus Macaques of rAAV2tYF-CB-hRS1, a Recombinant Adeno-Associated Virus Vector Expressing Retinoschisin." Hum Gene Ther Clin Dev **26**(3): 165-176.

Ye, G. J., T. Conlon, K. Erger, P. Sonnentag, A. K. Sharma, K. Howard, D. R. Knop and J. D. Chulay (2015). "Safety and Biodistribution Evaluation of rAAV2tYF-CB-hRS1, a Recombinant Adeno-Associated Virus Vector Expressing Retinoschisin, in RS1-Deficient Mice." Hum Gene Ther Clin Dev **26**(3): 177-184.

Yu, J., Y. Ni, P. A. Keane, C. Jiang, W. Wang and G. Xu (2010). "Foveomacular schisis in juvenile X-linked retinoschisis: an optical coherence tomography study." Am J Ophthalmol **149**(6): 973-978 e972.

Zeng, Y., Y. Takada, S. Kjellstrom, K. Hiriyanna, A. Tanikawa, E. Wawrousek, N. Smaoui, R. Caruso, R. A. Bush and P. A. Sieving (2004). "RS-1 Gene Delivery to an Adult Rs1h Knockout Mouse Model Restores ERG b-Wave with Reversal of the Electronegative Waveform of X-Linked Retinoschisis." Invest Ophthalmol Vis Sci **45**(9): 3279-3285.

Zhour, A., S. Bolz, C. Grimm, G. Willmann, A. Schatz, B. H. Weber, E. Zrenner and M. D. Fischer (2012). "In vivo imaging reveals novel aspects of retinal disease progression in Rs1h(-/Y) mice but no therapeutic effect of carbonic anhydrase inhibition." Vet Ophthalmol **15 Suppl 2**: 123-133.

Ziccardi, L., C. Vijayasarathy, R. A. Bush and P. A. Sieving (2012). "Loss of retinoschisin (RS1) cell surface protein in maturing mouse rod photoreceptors elevates the luminance

threshold for light-driven translocation of transducin but not arrestin." J Neurosci **32**(38): 13010-13021.

9 Appendices

9.1 Appendix 1

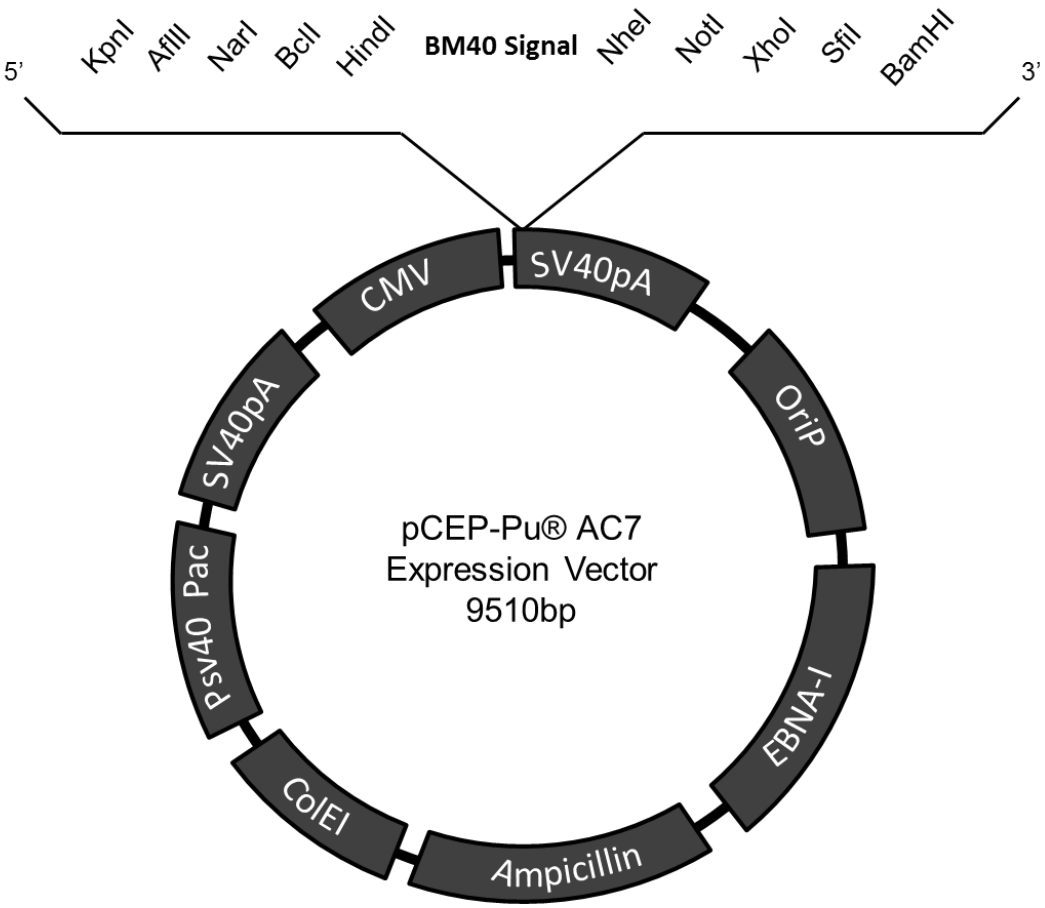

- **OriP/EBNA-I:** Eukaryotic origin of replication induced by EBNA-I allowing for maintenance of this plasmid in stably-transfected cell lines
- **Ampicillin:** Ampicillin resistance open reading frame
- **ColE1:** Bacterial origin of replication
- **PSV40:** Promoter for Pac in eukaryotic cells
- **Pac:** Puromycin resistance open reading frame
- **SV40pA:** 3' polyadenylation signal
- **CMV:** Construct promoter sequence
- **BM40:** Signal peptide for construct secretion in eukaryotic cell lines

Appendix 1 – The pCEP-Pu/Ac7 mammalian expression vector allowing for expression and secretion of retinoschisin constructs in stably transfected HEK293-EBNA cells.

9.2 Appendix 2

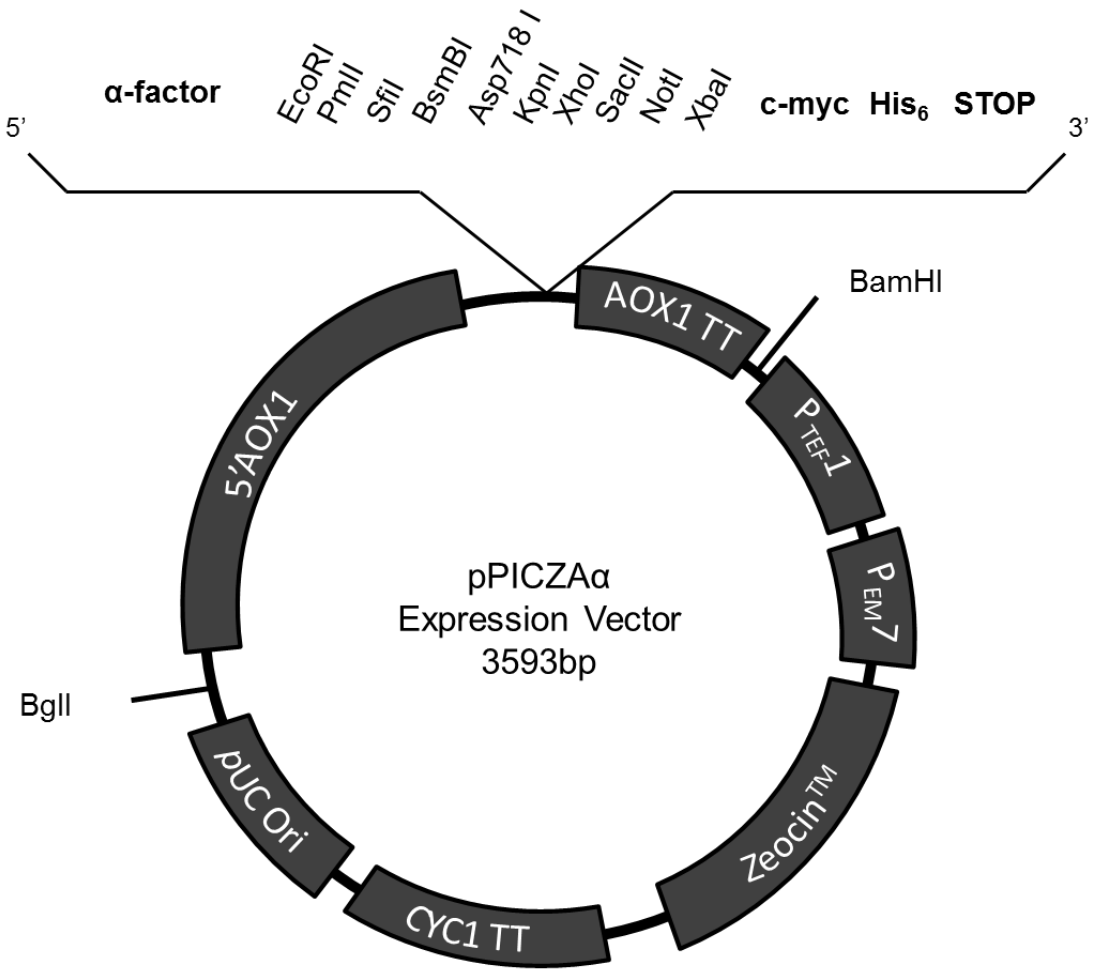

- **5' AOX1:** Construct promoter region
- **α-factor:** Signal sequence allowing for yeast secretion
- **AOX1 TT:** 3' polyadenyaltion signal
- **$P_{TEF}1$:** Transcription elongation factor 1, drives zeocin expression in yeast cells
- **$P_{EM}7$:** Synthetic prokaryotic promoter, drives zeocin expression in *E. coli*
- **Zeocin:** Zeocin resistance marker
- **CYC1 TT:** 3'polyadenylation signal for zeocin marker
- **pUC Ori:** Bacterial origin of replication

Appendix 2 – The pPICZAα *Pichia pastoris* expression vector allowing for expression and secretion of retinoschisin constructs in stably-transfected *Pichia pastoris* cells.

9.3 Appendix 3

A

R141H GeneArt® Gene-string

```
gccgccgctagcctctaccgaggatgaaggcgaggacccctggtaccaaaaagcatgcaag
  P  P  L  A  S  T  E  D  E  G  E  D  P  W  Y  Q  K  A  C  K
tgcgattgccaaggaggacccaatgctctgtggtctgcaggtgccacctccttggactgt
 C  D  C  Q  G  G  P  N  A  L  W  S  A  G  A  T  S  L  D  C
ataccagaatgcccatatcacaagcctctgggtttcgagtcaggggaggtcacaccggac
 I  P  E  C  P  Y  H  K  P  L  G  F  E  S  G  E  V  T  P  D
cagatcacctgctctaacccggagcagtatgtgggctggtattcttcgtggactgcaaac
 Q  I  T  C  S  N  P  E  Q  Y  V  G  W  Y  S  S  W  T  A  N
aaggcccggctcaacagtcaaggctttgggtgtgcctggctctccaagttccaggacagt
 K  A  R  L  N  S  Q  G  F  G  C  A  W  L  S  K  F  Q  D  S
agccagtggttacagatagatctgaaggagatcaaagtgatttcagggatcctcacccag
 S  Q  W  L  Q  I  D  L  K  E  I  K  V  I  S  G  I  L  T  Q
gggcactgtgacatcgatgagtggatgaccaagtacagcgtgcagtacaggaccgatgag
 G  H  C  D  I  D  E  W  M  T  K  Y  S  V  Q  Y  R  T  D  E
cgcctgaactggatttactacaaggaccagactggaaacaaccgggtcttctatggcaac
 R  L  N  W  I  Y  Y  K  D  Q  T  G  N  N  R  V  F  Y  G  N
tcggaccgcacctccacggttcagaacctgctgcggcccccatcatctcccgcttcatc
 S  D  R  T  S  T  V  Q  N  L  L  R  P  P  I  I  S  R  F  I
cgcctcatcccgctgggctggcacgtccgcattgccatccggatggagctgctggagtgc
 R  L  I  P  L  G  W  H  V  R  I  A  I  R  M  E  L  L  E  C
gtcagcaagtgtgccctggtgcccagaggcagccaccaccatcaccaccattagctcgag
 V  S  K  C  A  L  V  P  R  G  S  H  H  H  H  H  H  -  L  E
gccgcc
 A  A
```

B

H207Q GeneArt® Gene-string

```
gccgccgctagcctctaccgaggatgaaggcgaggacccctggtaccaaaaagcatgcaag
  P  P  L  A  S  T  E  D  E  G  E  D  P  W  Y  Q  K  A  C  K
tgcgattgccaaggaggacccaatgctctgtggtctgcaggtgccacctccttggactgt
 C  D  C  Q  G  G  P  N  A  L  W  S  A  G  A  T  S  L  D  C
ataccagaatgcccatatcacaagcctctgggtttcgagtcaggggaggtcacaccggac
 I  P  E  C  P  Y  H  K  P  L  G  F  E  S  G  E  V  T  P  D
cagatcacctgctctaacccggagcagtatgtgggctggtattcttcgtggactgcaaac
 Q  I  T  C  S  N  P  E  Q  Y  V  G  W  Y  S  S  W  T  A  N
aaggcccggctcaacagtcaaggctttgggtgtgcctggctctccaagttccaggacagt
 K  A  R  L  N  S  Q  G  F  G  C  A  W  L  S  K  F  Q  D  S
agccagtggttacagatagatctgaaggagatcaaagtgatttcagggatcctcacccag
 S  Q  W  L  Q  I  D  L  K  E  I  K  V  I  S  G  I  L  T  Q
gggcgctgtgacatcgatgagtggatgaccaagtacagcgtgcagtacaggaccgatgag
 G  R  C  D  I  D  E  W  M  T  K  Y  S  V  Q  Y  R  T  D  E
cgcctgaactggatttactacaaggaccagactggaaacaaccgggtcttctatggcaac
 R  L  N  W  I  Y  Y  K  D  Q  T  G  N  N  R  V  F  Y  G  N
tcggaccgcacctccacggttcagaacctgctgcggcccccatcatctcccgcttcatc
 S  D  R  T  S  T  V  Q  N  L  L  R  P  P  I  I  S  R  F  I
cgcctcatcccgctgggctgccaagtccgcattgccatccggatggagctgctggagtgc
 R  L  I  P  L  G  W  Q  V  R  I  A  I  R  M  E  L  L  E  C
gtcagcaagtgtgccctggtgcccagaggcagccaccaccatcaccaccattagctcgag
 V  S  K  C  A  L  V  P  R  G  S  H  H  H  H  H  H  -  L  E
gccgcc
 A  A
```

Appendix 3 – Sequences of the (**A**) R141H and (**B**) H207Q retinoschisin gene strings, subsequently cloned into the pCEP-Pu/Ac7 mammalian expression vector. Positions of the introduced point mutations are highlighted. Regions of the sequence are coloured according to the domain they encode. With the Rs1 domain (green), discoidin domain (blue), C-terminal extension (purple), thrombin cleavage site and His_6 tag (red) followed by the stop codon (orange).

9.4 Appendix 4

A

***Pichia pastoris* Wild-type GeneArt® Gene-string**

```
gccgccgaattctctactgaagatgaaggtgaggacccatggtatcaaaaggcttgtaag
 A  A  E  F  S  T  E  D  E  G  E  D  P  W  Y  Q  K  A  C  K
tgtgactgtcagggtggtccaaacgctttgtggtctgctggtgctacttccttggactgt
 C  D  C  Q  G  G  P  N  A  L  W  S  A  G  A  T  S  L  D  C
attccagaatgtccataccacaagccattgggtttcgaatccggtgaagttactccagac
 I  P  E  C  P  Y  H  K  P  L  G  F  E  S  G  E  V  T  P  D
cagatcacttgttccaacccagagcaatacgttggttggtactcttcctggactgctaac
 Q  I  T  C  S  N  P  E  Q  Y  V  G  W  Y  S  S  W  T  A  N
aaggctagattgaactcccagggttttggttgtgcttggttgtccaagttccaagactct
 K  A  R  L  N  S  Q  G  F  G  C  A  W  L  S  K  F  Q  D  S
tcccagtggttgcagatcgacttgaaagagatcaaggttatctccggtatcttgactcag
 S  Q  W  L  Q  I  D  L  K  E  I  K  V  I  S  G  I  L  T  Q
ggtagatgtgacattgacgagtggatgactaagtactccgttcagtacagaactgacgag
 G  R  C  D  I  D  E  W  M  T  K  Y  S  V  Q  Y  R  T  D  E
agattgaattggatctactacaaggaccagactggtaacaacagagttttctacggtaac
 R  L  N  W  I  Y  Y  K  D  Q  T  G  N  N  R  V  F  Y  G  N
tccgacagaacttccactgttcagaacttgttgagaccaccaatcatctccagattcatc
 S  D  R  T  S  T  V  Q  N  L  L  R  P  P  I  I  S  R  F  I
agattgatccctttgggttggcacgttagaatcgctatcagaatggagttgttggagtgt
 R  L  I  P  L  G  W  H  V  R  I  A  I  R  M  E  L  L  E  C
gtttccaagtgtgctcatcaccatcaccaccactaaccgcgggccgcc
 V  S  K  C  A  H  H  H  H  H  H  -  P  R  A  A
```

B

***Pichia pastoris* C40S/C59S/C223S GeneArt® Gene-string**

```
gccgccgaattctctactgaagatgaaggtgaggacccatggtatcagaaggcttgtaag
 A  A  E  F  S  T  E  D  E  G  E  D  P  W  Y  Q  K  A  C  K
tctgactgtcagggtggtccaaacgctttgtggtctgctggtgctacttctttggactcc
 S  D  C  Q  G  G  P  N  A  L  W  S  A  G  A  T  S  L  D  S
attccagaatgtccataccacaagccattgggtttcgaatccggtgaagttactccagac
 I  P  E  C  P  Y  H  K  P  L  G  F  E  S  G  E  V  T  P  D
cagatcacttgttccaacccagagcaatacgttggttggtactcttcctggactgctaac
 Q  I  T  C  S  N  P  E  Q  Y  V  G  W  Y  S  S  W  T  A  N
aaggctagattgaactcccagggttttggttgtgcttggttgtccaagttccaagactct
 K  A  R  L  N  S  Q  G  F  G  C  A  W  L  S  K  F  Q  D  S
tcccagtggttgcagatcgacttgaaagagatcaaggttatctccggtatcttgactcag
 S  Q  W  L  Q  I  D  L  K  E  I  K  V  I  S  G  I  L  T  Q
ggtagatgtgacattgacgagtggatgactaagtactccgttcagtacagaactgacgag
 G  R  C  D  I  D  E  W  M  T  K  Y  S  V  Q  Y  R  T  D  E
agattgaattggatctactacaaggaccagactggtaacaacagagttttctacggtaac
 R  L  N  W  I  Y  Y  K  D  Q  T  G  N  N  R  V  F  Y  G  N
tccgacagaacttccactgttcagaacttgttgagaccaccaatcatctccagattcatc
 S  D  R  T  S  T  V  Q  N  L  L  R  P  P  I  I  S  R  F  I
agattgatccctttgggttggcacgttagaatcgctatcagaatggagttgttggagtgt
 R  L  I  P  L  G  W  H  V  R  I  A  I  R  M  E  L  L  E  C
gtttccaagtctgctcatcaccatcaccaccactaaccgcgggccgcc
 V  S  K  S  A  H  H  H  H  H  H  -  P  R  A  A
```

Appendix 4 – Sequences of the codon-optimised (**A**) Wild-type and (**B**) C40S/C59S/C223S retinoschisin gene strings, subsequently cloned into the pPICZAα *Pichia pastoris* expression vector. The start site for the discoidin domain sequence cloned into the expression vector is marked with a red arrow in the wild-type sequence, with mutations in the triple mutant sequence marked. Regions of the sequence are coloured according to the domain they encode. With the Rs1 domain (green), discoidin domain (blue), C-terminal extension (purple), thrombin cleavage site and His_6 tag (red) followed by the stop codon (orange).

9.5 Appendix 5

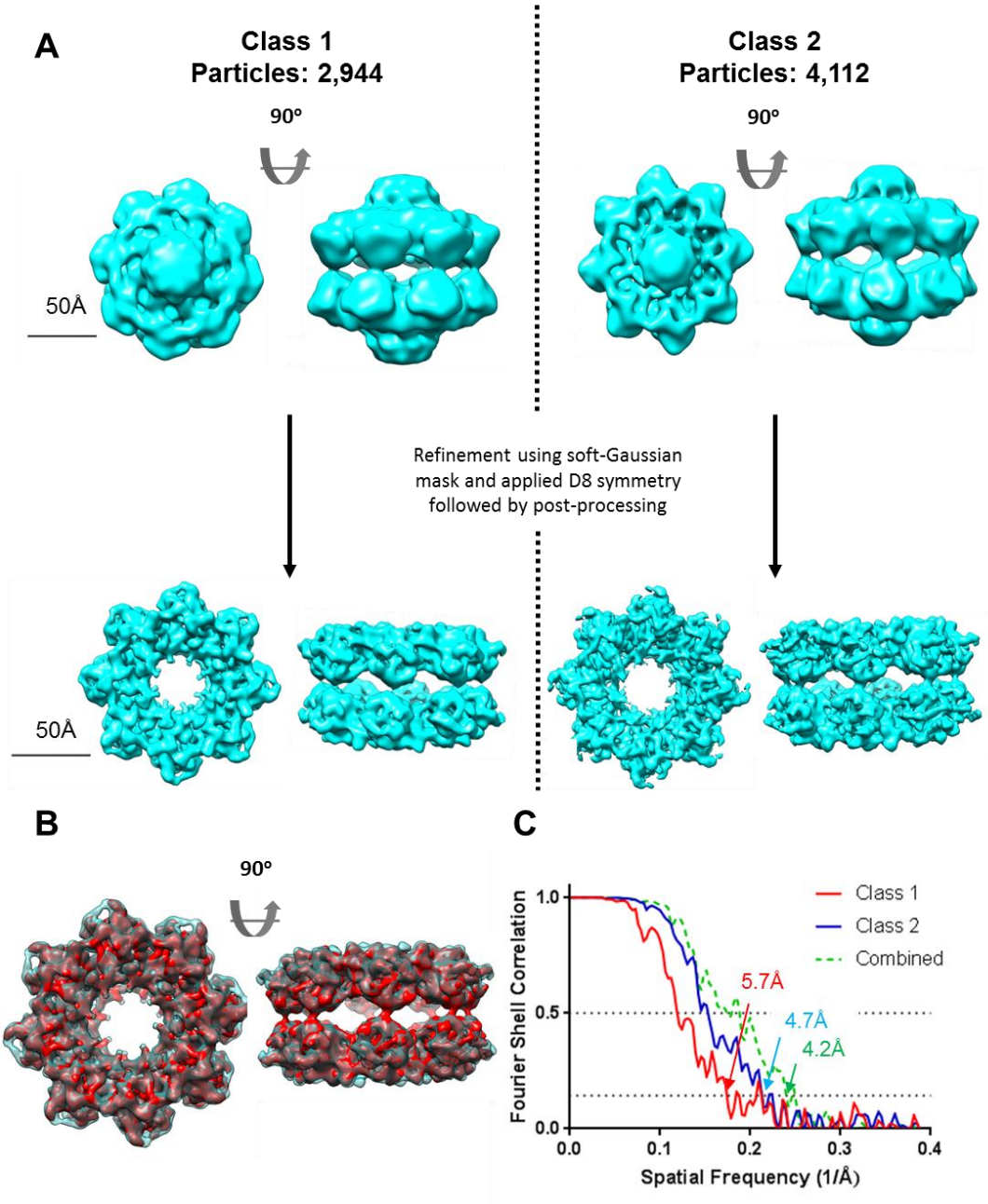

Appendix 5 – Masked refinement of three-dimensionally classified particle sets. (**A**) Refinement using the soft-Gaussian masking of the Rs1 domain region and D8 symmetry of the class 1 and 2 three-dimensional classes with their respective assigned particle sets, with the final post-processed model shown. (**B**) Comparison of both class-only refined models, fitted at 6Å-simulated resolution. Class 1 (transparent, blue) and class 2 (red) models are shown. UCSF Chimera calculated a correlation coefficient of 0.97 for the fit. (**C**) FSC resolution estimation of the each final model, compared with the final refined model produced through combination of these particle sets.

9.6 Appendix 6

Three-Dimensional Class 1

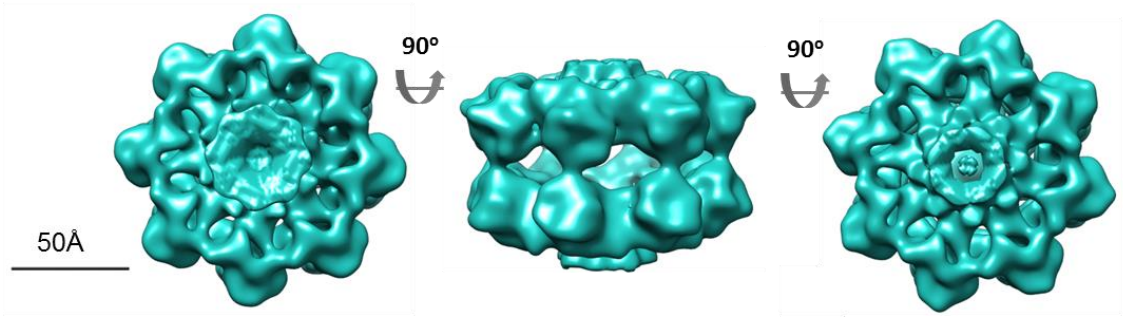

Three-Dimensional Class 2

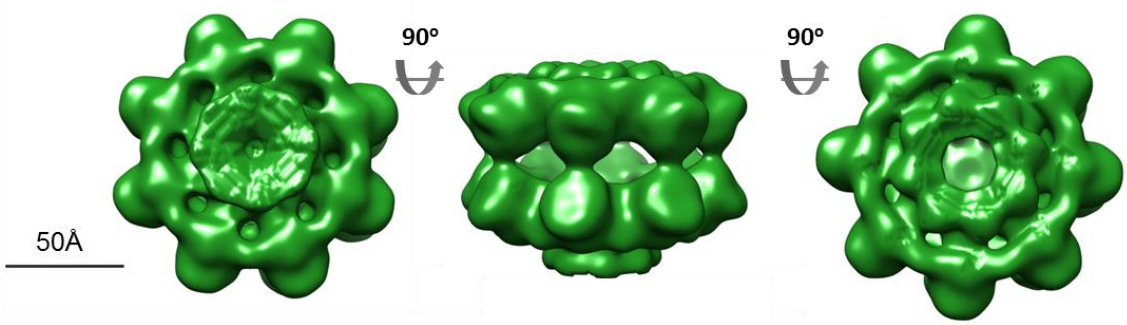

Appendix 6 – Three-dimensional classes of the final R141H particle set following classification using C8 symmetry. Both generated classes are shown.

9.7 Appendix 7

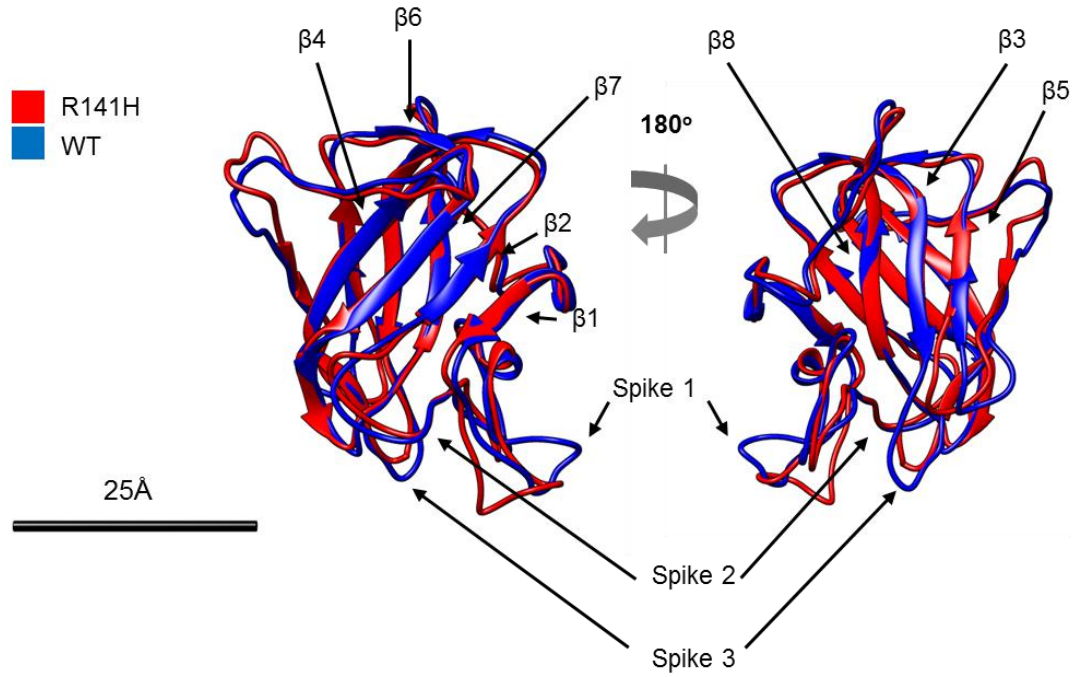

Appendix 7 – Construction of the R141H homology model. Shown is a structural alignment of wild-type and R141H homology models constructed using the Phyre2 webserver, marked are the major secondary structural elements of the discoidin domain. Overall both structures were observed to be highly similar with an RMSD value of 0.974Å over 137 atom pairs in the comparison, with a similar topology observed with slight differences in the spike regions.

9.8 Appendix 8

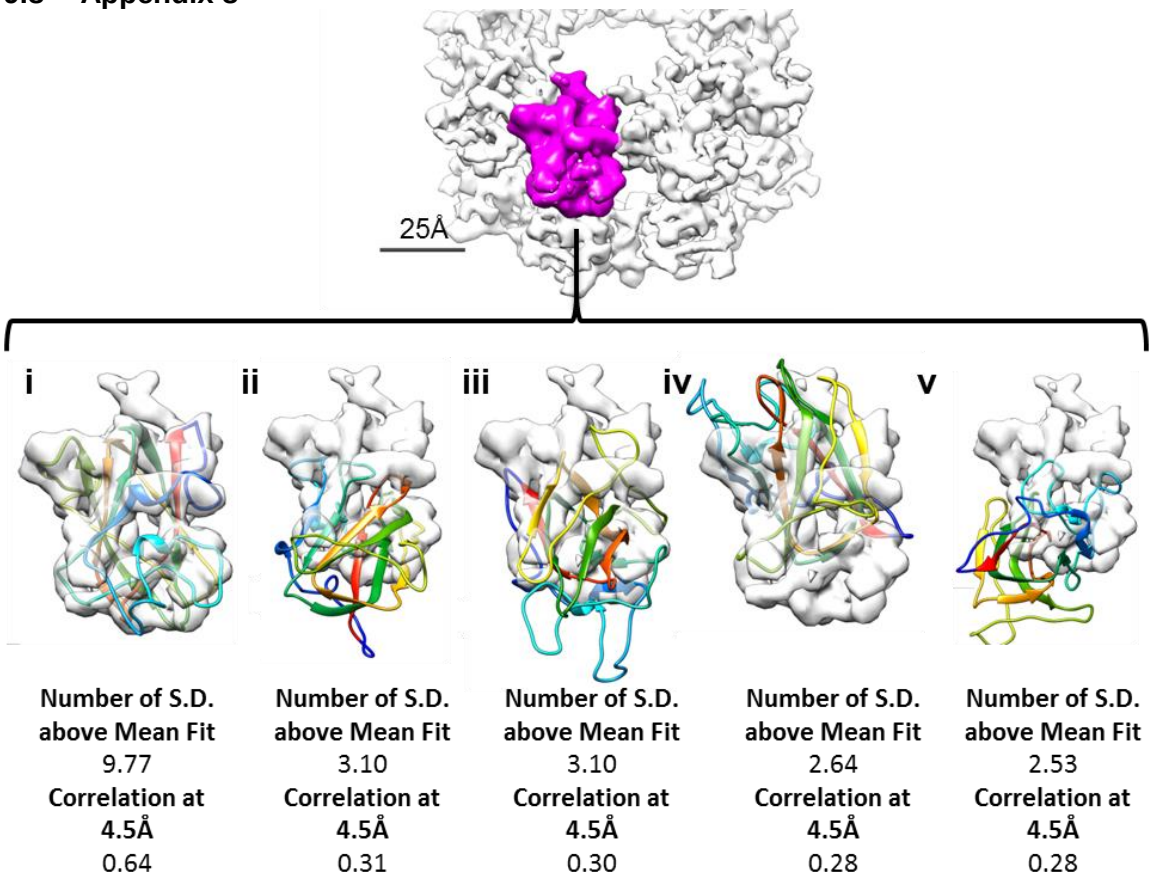

Appendix 8 – Rigid body fitting of the R141H discoidin domain into the hexadecamer structure. DockEM rigid body fitting to the R141H map. Shown in magenta is a single repeating subunit of the structure, into which the R141H homology model was fitted. All fits were scored for significance (the number of standard deviations above the mean for all fits) and the correlation value at 4.5Å resolution. Shown are the top 5 non-equivalent fits (i-v).

9.9 Appendix 9

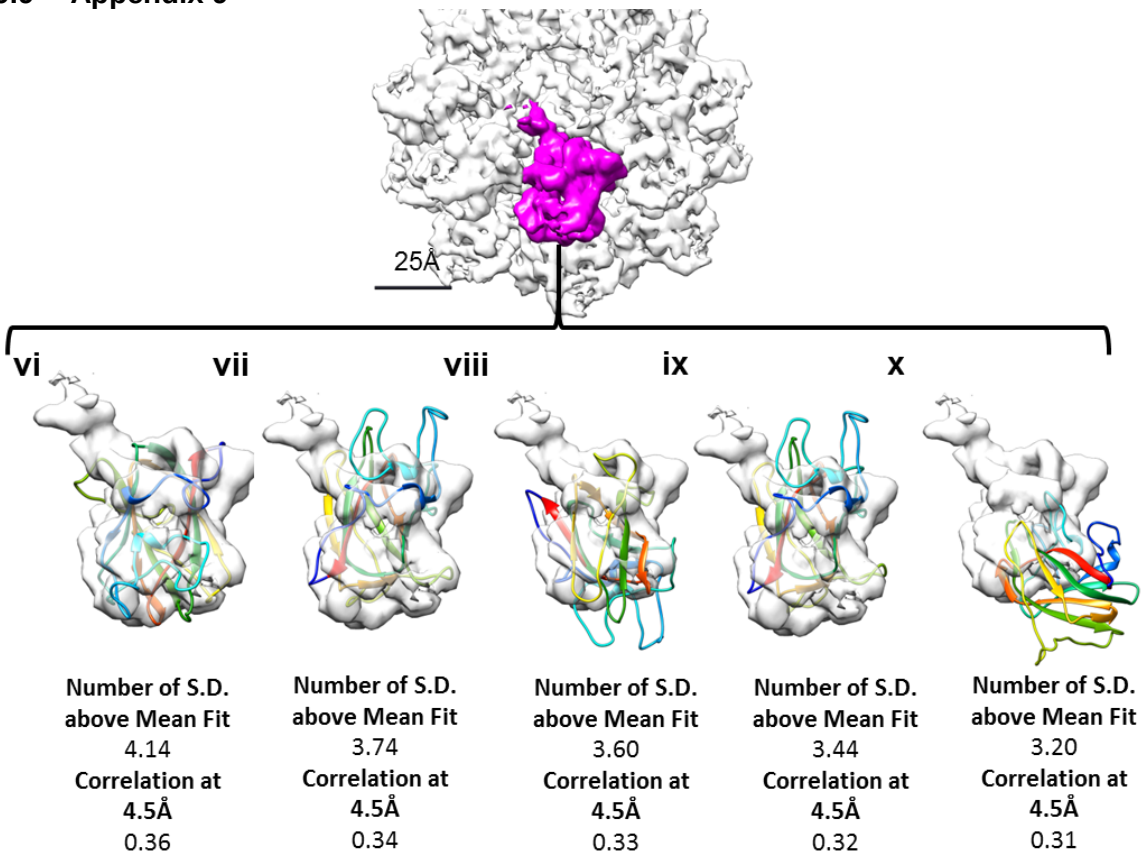

Appendix 9 – Model-based handedness determination of the R141H dimer of octamers. Shown is the mirrored hand of the hexadecamer structure, with a single repeating subunit highlighted (magenta). The top 5 non-equivalent hits to the mirrored retinoschisin structure (vi-x) are shown together with the fit scoring for significance (the number of standard deviations each observed fit is above the mean for all fits) and correlation at 4.5Å resolution.